

A Dissertation

entitled

Characterization and Application of Colloidal Nanocrystalline Materials for Advanced
Photovoltaics

by

Khagendra P. Bhandari

Submitted to the Graduate Faculty as partial fulfillment of the requirements for the
Doctor of Philosophy Degree in Physics

Dr. Randy J. Ellingson, Committee Chair

Dr. Victor Karpov, Committee Member

Dr. Michael Heben, Committee Member

Dr. Rupali Chandar, Committee Member

Dr. Terry Bigioni, Committee Member

Dr. Patricia R. Komuniecki, Dean
College of Graduate Studies

The University of Toledo
May 2015

Copyright 2015, Khagendra P. Bhandari

This document is copyrighted material. Under copyright law, no parts of this document may be reproduced without the expressed permission of the author.

An Abstract of
Characterization and Application of Colloidal Nanocrystalline Materials for Advanced
Photovoltaics

by

Khagendra P. Bhandari

Submitted to the Graduate Faculty as partial fulfillment of the requirements for the
Doctor of Philosophy Degree in Physics

The University of Toledo

May 2015

Solar energy is Earth's primary source of renewable energy and photovoltaic solar cells enable the direct conversion of sunlight into electricity. Crystalline silicon solar cells and modules have dominated photovoltaic technology from the beginning and they now constitute more than 90% of the PV market. Thin film (CdTe and CIGS) solar cells and modules come in second position in market share. Some organic, dye-sensitized and perovskite solar cells are emerging in the market but are not yet in full commercial scale. Solar cells made from colloidal nanocrystalline materials may eventually provide both low cost and high efficiency because of their promising properties such as high absorption coefficient, size tunable band gap, and quantum confinement effect. It is also expected that the greenhouse gas emission and energy payback time from nanocrystalline solar PV systems will also be least compared to all other types of PV systems mainly due to the least embodied energy throughout their life time.

The two well-known junction architectures for the fabrication of quantum dot based photovoltaic devices are the Schottky junction and heterojunction. In Schottky junction cells, a heteropartner semiconducting material is not required. A low work function metal is used as the back contact, a transparent conducting layer is used as the front contact, and the layer of electronically-coupled quantum dots is placed between these two materials. Schottky junction solar cells explain the usefulness of nanocrystalline materials for high efficiency heterojunction solar cells. For heterojunction devices, n-type semiconducting materials such as ZnO , CdS or TiO₂ have been used as suitable heteropartners.

Here, PbS quantum dot solar cells were fabricated using ZnO and CdS semiconductor films as window layers. Both of the heteropartners are sputter-deposited onto TCO coated glass substrates; ZnO was deposited with the substrate held at room temperature and for CdS the substrate was at 250 °C. Within this work, CdS was demonstrated for the first time as the heteropartner for a quantum dot absorber layer. Iron pyrite nanocrystal (NC) could not be used as an absorber layer in thin film solar cells because the material's very high free hole density rendered it nearly metallic in nature. However, the author discovered and demonstrated that an iron pyrite nanocrystal film functions well as a back contact buffer layer for CdTe solar cells. Performance of CdTe devices when using FeS₂/Au as back contact approaches that of a laboratory standard Cu/Au back contact.

To my parents and family.

Acknowledgements

I am truly indebted and thankful to my advisor Dr. Randy J. Ellingson for his encouragement, supervision and constant support throughout my research. This would not have been possible without his help. I am thankful to my committee members, Dr. Heben, Dr. Karpov, Dr. Chandar, and Dr. Bigioni for agreeing to be a part of the committee in evaluating my research every year and for their fruitful advice, their review of and comments on my dissertation.

My special thanks go to Mr. Paul Roland for help in light soaking measurements, assistance with the theoretical study of EQE and temperature dependent device performance. I am grateful to Dr. Sohee Jeong for UPS and XPS measurements. My special thanks also go to Dr. Defne Apul and Ms. Jennifer Collier for substantial contributions to our PV LCA project and publication. I would like to thank Mr. Corey Grice for his help in C-V measurements. I am thankful to Dr. Naba Paudel, Dr. Hasitha Mahabaduge, and Dr. Prakash Koirala for providing samples to complete my study and also for fruitful discussions. I am also thankful to Dr. Tienieke Dykstra for initial lab set up and helpful suggestions. I am also thankful to Mr. Neale Haugen, Dr. Rajendra Raj Khanal, Dr. Puruswottam Aryal, Dr. Riza Kaya and Mr. Zhaoning Song for helpful discussions.

My parents have been the constant source of inspiration throughout my life and I would not be here without their sacrifice and unconditional love. My children, Kevina and Rianna's love and affection, whilst patience and understandings of my wife Dr. Ranjita Nepal have been a great strength; without their support and encouragements I could not have finished this work.

Table of Contents

Abstract	iii
Acknowledgements	v
List of Tables	xiii
List of Figures	xv
List of Abbreviations	xxvi
List of Symbols.....	xxvii
1. Introduction.....	1
1.1 Summary and Motivation	1
1.2 Quantum dots for solar cells	4
1.3 Life cycle analysis of PV systems	9
1.4 Back contact for CdTe solar cells	11
1.5 Electronic energy alignment between two semiconductors.....	13
1.6 Dissertation Overview	15
2. General information on colloidal synthesis, optical and electronic properties of PbS and FeS₂ semiconductor nanocrystals and basic of solar cells.....	19
2.1 Introduction.....	19

2.2. Direct and indirect semiconductors	20
2.3 Crystal and band structure properties of bulk and quantum dot PbS.....	23
2.4 Crystal and band structure of iron pyrite	28
2.5 Size dependent band gap and quantum confinement of NCs	31
2.5.1 Density of states.....	31
2.5.2 Particle in infinite potential well.....	33
2.5.3 Excitons in a bulk semiconductor.....	34
2.5.4 Quantum confinement in quantum dots.....	34
2.6 General synthesis scheme of colloidal NCs (or QDs)	39
2.6.1 Surface passivation and charge recombination.....	42
2.7 Basic operational principles of solar cells	45
2.7.1 The PN junction.....	45
2.7.2 Solar cell external parameters.....	48
2.8 Conclusions.....	50
3. Synthesis, characterization and photovoltaic application of PbS quantum	
dots	53
3.1 Introduction.....	53
3.2 Experimental.....	54
3.2.1 Materials	54
3.2.2 PbS QD synthesis	54

3.3	Experimental results and discussion	56
3.3.1	Quantum dots synthesis	56
3.3.2	PbS QDs film fabrication.....	63
3.3.3	Photovoltaic device fabrication	69
3.4	Conclusions.....	95
4.	PbS-QD based thin film heterojunction solar cells using CdS as an n-type window layer.....	96
4.1	Introduction.....	96
4.2	Experimental.....	98
4.2.1	PbS quantum dot (QD) synthesis.....	98
4.2.2	Photovoltaic device fabrication	99
4.2.3	Device fabrication for Mott Schottky measurement.....	100
4.3	Results and Discussion	100
4.4	Conclusions	130
5.	Synthesis and Characterization of Iron Pyrite and Tin Disulfide Nanocrystals	132
5.1	Introduction.....	132
5.2	Experimental.....	135
5.2.1	Materials	135
5.2.2	Synthesis of FeS ₂ NCs.....	135

5.2.3	Synthesis of SnS ₂ Nanocrystals (NCs)	138
5.2.4	Fabrication of Films from FeS ₂ or SnS ₂ NCs	139
5.2.5	Characterization of FeS ₂ and SnS ₂ NCs	143
5.3	Results and Discussion	144
5.3.1	Iron pyrite NCs	144
5.3.2	Tin disulfide (SnS ₂) Nanocrystals (NCs).....	168
5.4	Conclusions.....	174
6.	Application of earth abundant iron pyrite nanocrystal as a copper-free back contact for polycrystalline CdTe thin film solar cells.....	175
6.1	Introduction.....	175
6.2	Experimental.....	178
6.2.1	Synthesis and film preparation of FeS ₂ NC.....	178
6.2.2	CdS/CdTe device fabrication.....	179
6.3	Results and Discussions.....	180
6.3.1	Characterization of thin films: FeS ₂ , CdS, CdTe and Au	180
6.3.2	Application of iron pyrite as a back contact.....	182
6.4	Conclusions.....	211
7.	Kelvin probe and photoelectron spectroscopy study of the electronic structure of metal and semiconductor thin films.....	213
7.1	Introduction.....	213

7.2 Kelvin Probe force microscopy	213
7.2.1 Theory and working principle	213
7.2.2 Sample preparation	216
7.2.3 Results and discussion	216
7.3 Ultraviolet Photoelectron Spectroscopy (UPS)	219
7.3.1 Introduction.....	219
7.3.2 Physical principle of UPS	220
7.3.3 Sample preparation	221
7.3.4 Electron energetics of semiconductor thin films	221
7.4 X-ray photoelectron spectroscopy	230
7.4.1 Introduction.....	230
7.4.2 Sample preparation	230
7.4.3 Elemental analysis on surfaces of CdS and PbS-films	231
7.4.4 Determination of the valence and conduction band offsets between CdS bulk and PbS QDs using XPS.....	235
7.5 Conclusions.....	247
8. Life cycle assessment (LCA) study of photovoltaic systems.....	249
8.1 Introduction.....	249
8.2 PV System Description.....	251
8.2.1 Classification of PV System	251

8.2.2 Fabrication of the light-absorbing films used in photovoltaic cells and modules.....	252
8.2.3 Methods of growing.....	254
8.2.4 Module design	256
8.2.5 Relevant Parameters	258
8.3 Methods.....	260
8.3.1 Collection of Literature.....	260
8.3.2 Criteria for Inclusion.....	261
8.3.3 EPBT and EROI Calculation	264
8.4 Results and Discussion	267
8.4.1 Embedded Energy.....	268
8.4.2 Energy Payback Time (EPBT)	273
8.4.3 Energy Return on Energy Invested (EROI).....	280
8.5 Conclusions.....	282
9. Conclusion and future work.....	284
9.1 Conclusions.....	284
9.2 Future work.....	289
9.2.1 Electron injection from colloidal PbS QDs into sputtered CdS thin films	289
9.2.2 Doping of PbS QDs using metal impurities	293

9.2.3 Multijunction (tandem) solar cells from PbS-QDs of different sizes .	302
9.2.4 FeS ₂ NC and low work function metal as back contact for CdTe solar cells	304
9.2.5 Size dependent study of FeS ₂ NCs using TRPL and TA.....	305
9.2.6 Synthesis and applications of other pyrite materials such as FeTe ₂ and FeSe ₂	305
References	306
Appendices	358
A. Solar cell performance of iron pyrite	358
B. Second derivative of JV curves when FeS ₂ /Au and Cu/Au were used as back contacts for CdTe devices prepared from CSS deposition methods.....	362
C. Derivatives of JV curves (light) when FeS ₂ (untreated)/Au, and FeS ₂ (treated)/Au were used as back contacts for sputtered CdS/CdTe solar cells.....	363

List of Tables

3.1	Performance parameters of Schottky junction solar cells when PbS-QDs of three different band gaps were used as absorber layers.....	76
3.2	Performance parameters of ZnO/PbS QD solar cells when PbS-QDs of five different band gaps were used as absorber layers.....	81
4.1	Parallel test results: CdS70/PbS792 solar cells.....	108
5.1	Instrumentation used in the process of characterization of FeS ₂ and SnS ₂ NCs.	143
5.2	Effect of annealing temperature and time on the FWHM of the (200) XRD peak measured for FeS ₂ NC films.....	159
5.3	Four point probe measurements: average thickness of the film = 3.5 μm.	161
5.4	Hall Measurements; average thickness of the films = 3.5 μm.	164
6.1	Average parameters for 15 CdTe solar cells in three different back contacts.....	185
6.2	Statistics of temperature dependent study of sputtered CdTe devices with FeS ₂ /Au as back contact; in each case, average and standard deviation of 15 cells were calculated.....	193
6.3	Average of 20 cells (two different back contacts in two device fabrication condition: sputtered and CSS).....	203
7.1	Work function measurement.....	229
7.2	Calculated parameters to satisfy equation (7.4).....	245
8.1	Module efficiencies used for harmonization.....	268

8.2	Mean unharmonized (U) and harmonized (H) parameters for each photovoltaic technology with the percentage difference.	277
8.3	Mean harmonized EPBT and EROI for Multiple Insolation values.	278

List of Figures

1-1	Growth of the photovoltaic in the world.	4
1-2	Research cell efficiency records prepared by NREL.	6
2-1	Direct and indirect bandgap semiconductors: absorption and emission of light.....	23
2-2	Electronic band structure of PbS. The minimum energy direct band gap is situated at L: L_1^6 $\rightarrow L_2^6$. The higher energy transition E3 can also be seen.	26
2-3	Crystal structure and Brillouin zone for rocksalt crystal of PbS with space group Fm3m showing four equivalent L points at the center of the faces.....	28
2-4	Iron pyrite crystal structure. Smaller dark spheres represent Fe and larger white spheres represent S atoms.	29
2-5	Energy bands of FeS ₂ are drawn for the pyrite structure. The orbital degeneracy of each level is represented in brackets and because of spin degeneracy is multiplied by 2.	30
2-6	Density of states in semiconductor structures in different dimensions.	32
2-7	Infinite square potential well.....	33
2-8	Schematic of a single QD with its surrounding matrix and the potential well for each of the three spatial dimensions, and the quantized energy levels of electrons and holes in a QD.	35
2-9	Energy levels of an exciton in a direct band gap semiconductor with conduction and valence bands at $E_g = 0$	37
2-10	Change in free energy with respect to the NC size, and growth rate with respect to the critical radius r^*	41

2-11	The I-V characteristics of a PN junction, and representation of a diode.....	46
2-12	J-V characteristic of a solar cell in the dark and under 1-Sun illumination. The area of the green rectangle represents the maximum power output.....	50
3-1	Photograph of a Schlenk line showing its various parts. Syntheses of QDs or NCs are performed in a nitrogen environment.....	55
3-2	Absorbance with respect to wavelength (nm) for PbS QD samples dispersed in hexane. Absorbance (OD) and photoluminescence (PL) spectra of a PbS-QD solution in hexane. .	60
3-3	Dependence of first exciton energy of QDs with size of the dots. Stokes shifts of various size QDs relative to the first exciton peaks (both in terms of energy in eV).	62
3-4	Possible ligand exchange procedure between oleic acid and 1,2-ethanedithiol (EDT) when making PbS QD film.....	64
3-5	Layer by layer dip coating process using hand dipping and dip coater	65
3-6	C-H vibrational modes of molecule in OA and EDT treated films. Red shift in the first exciton peak of the absorbance spectra from the QD film vs. solution.....	68
3-7	Device structure of a PbS-QD thin film Schottky junction solar cell. Band diagram in equilibrium with metal work function.....	71
3-8	Pattern ITO coated glass substrate and metal mask to deposit back contact.....	72
3-9	Current voltage characteristics of Schottky junction solar cells. Solid line represents light measurement and dash line represents dark measurement.....	73
3-10	External quantum efficiency of Schottky junction solar cells made from PbS QDs of ~3 nm diameter, corresponding to the first exciton absorption peak at 890 nm.	74
3-11	Current voltage characteristics of Schottky junction solar cells when PbS QDs of three different sizes were used as absorber layers.....	75

3-12	PbS-QD photovoltaic device architecture and non-equilibrium energy level alignment of ITO, ZnO, PbS-QD (2.5 nm diameter) and Au.....	77
3-13	Complete heterojunction devices prepared from PbS QD film as absorber layer.....	77
3-14	Measured current voltage characteristics under AM1.5G simulated solar illumination for a representative heterojunction device.....	78
3-15	External quantum efficiency of the representative ZnO/PbS-QD device; for comparison, the absorption spectrum of the QDs in solution are also shown.	80
3-16	J-V curves for five devices made from PbS-QDs with various diameters. V_{OC} was obtained high from smaller dots and low from larger dots whereas J_{SC} followed opposite trend.	80
3-17	J-V characteristics of ZnO window layer thickness effects on ZnO/PbS-QD devices (QD diameter = 2.6 nm).	82
3-18	Series and shunt resistance of PbS QD solar cells when the size of the QD is fixed but the thickness of window layer is varied.	83
3-19	Increase in J_{SC} and PCE with respect to time. No saturation was observed after a scan of four hours consisting of two thousand J-V curves.	85
3-20	V_{OC} and FF with respect to time (min). V_{OC} appears nearly constant over this time period.	86
3-21	Open circuit voltage and fill factor of the solar cells with respect to time (hour).....	86
3-22	J_{SC} and PCE of the solar cells with respect to time (hour); there is no indication of saturation of these values.	87
3-23	Current density in mA cm^{-2} is plotted with respect to open circuit voltage in Volts in the 1 st , 1500 th and 2999 th scan of light measurement.	88
3-24	J_{SC} and PCE with respect to time in minutes; it is seen that PCE is increasing until around 45 minutes.	89

3-25	EQE before and after the light soaking performance for when CdS and ZnO were used as window layers.	90
3-26	Decrease in series resistance and increase in shunt resistance with respect to time (min) when the window layer is CdS in heterojunction devices.....	91
4-1	Schematic of the PbS QD/CdS heterojunction solar cell, cross-sectional SEM of the PbS QD/CdS junction solar cell and schematic of the energy band diagram of solar cell.	101
4-2	X-ray diffraction (XRD) pattern for sputtered CdS thin film and transmission spectra of CdS thin films of varying thickness deposited on soda lime glass substrates.....	104
4-3	Current density-voltage (J-V) characteristics of a CdS/PbS-QD heterojunction solar cell recorded in the dark and under $100 \text{ mW}\cdot\text{cm}^{-2}$ simulated AM1.5 illumination.....	107
4-4	Real device with device structure of ITO/CdS/PbS QD/Au where PbS QD of size 2.5 nm was used to make ~ 200 nm thick layer of QD.	109
4-5	External quantum efficiency spectrum of the PbS-QD solar cell featured in Figure 4-1 from both theoretically and experimentally obtained data.....	111
4-6	Reflectance and transmittance of a stack of solar cell device obtained by using an optical model based on 2x2 transfer matrix.	113
4-7	Optical model calculation of the electric field strength and charge carrier generation rate with respect to film depth and wavelength.....	114
4-8	Theoretical study of the fraction of light absorbed within each layer. Note that the absorption within the CdS layer is separated from that of the PbS-QD layer.....	116
4-9	Theoretical study of the fraction of light absorbed within each layer. The blue curve shows the fraction of light absorbed within the CdS and PbS-QD layers.....	117
4-10	Dependence of V_{OC} , J_{SC} , FF and PCE on the diameter and effective band gap energy (the first exciton peak, E_g in eV) of PbS-QDs.	118

4-11	Dependence on window layer thickness of the performance of PbS-QDs solar cells. The PbS QD diameter was 2.6 nm, corresponding to the first exciton peak at 816 nm (1.52 eV).	120
4-12	Surface roughness of CdS films with respect to CdS thickness in nm.....	122
4-13	Surface roughness on PbS-QD films deposited onto CdS films of different thicknesses. .	123
4-14	Series and shunt resistances with respect to CdS thickness in nm; The PbS QD diameter was 2.6 nm.	125
4-15	Representative device performance evolution for more than sixty days; each datum point represents the average relative value change of six cells.	126
4-16	Mott-Schottky plot for PbS QD/Al Schottky junction showing the measured $\text{area}^2/\text{capacitance}^2$ data and the data adjusted to eliminate constant capacitance.....	129
4-17	Mott-Schottky plot for CdS/Ag Schottky junction showing the measured $\text{area}^2/\text{capacitance}^2$ data.	130
5-1	Chemical reaction for the synthesis of iron pyrite nanocrystals.	136
5-2	Surface passivation schematic of TOPO to FeS ₂ NC.....	138
5-3	Schematic of the removal of TOPO from the surface of the NCs by hydrazine treatment.	141
5-4	Optical absorbance and absorption coefficient spectra of as obtained NC solution and film of thickness ~150 nm.	145
5-5	Direct and indirect band gap calculation of FeS ₂ NC in film using optical absorbance spectra shown in Figure 5-4.	146
5-6	Absorbance spectra of as synthesized and hydrazine treated FeS ₂ NC films taken from FTIR measurement.	147
5-7	XRD spectrum of untreated and unsintered FeS ₂ NC film deposited by drop-cast using NCs of size ~130 nm.	148

5-8	XRD spectra in cases when oleylamine 1,2-hexanediol were used as coordinating solvents and oleylamine as non-coordinating solvent.....	149
5-9	Raman scattering spectrum of untreated and unsintered FeS ₂ NC in film deposited by drop-cast using NCs of size ~130 nm; NCs are capped with TOPO molecules.....	150
5-10	Raman spectrum when 1,2-hexanediol and oleylamine were used as surfactant and non-coordinating solvent respectively.	151
5-11	SEM image of untreated and unsintered FeS ₂ NC film deposited by drop-cast using NCs of size ~130 nm with magnification.....	153
5-12	SEM image of untreated and unsintered FeS ₂ NC films at magnification 40.0 k when using 1,2-hexanediol/OLA combination as surfactant and non-coordinating solvent.....	154
5-13	TEM image for TOPO capped FeS ₂ NCs and size distribution of the NCs as calculated using TEM images and <i>image-j</i> software with the help of Origin software.	154
5-14	EDX measurement of seven FeS ₂ NC films fabricated from distinct NC syntheses.	156
5-15	XRD spectra showing the effect of hydrazine and thermal annealing treatment and Raman spectrum for a film annealed at 540 °C for 1 hour.....	159
5-16	SEM micrographs of as deposited and hydrazine treated FeS ₂ NC films annealed at 540 °C for 3 hours, deposited using a layer by layer drop-cast method.....	160
5-17	Solar cell schematic when low free electron density CdS and very high free hole density FeS ₂ NC are heterointerfaced.....	165
5-18	Temperature dependent resistivity of the hydrazine-treated FeS ₂ NC film of thickness ~486 nm and 850 nm prepared on soda lime glass.....	166
5-19	Absorbance spectrum taken from spectrophotometer of SnS ₂ NC solution prepared in chloroform. The path length of the cuvette was 2 mm.....	169

5-20	Transmission spectrum of SnS ₂ spin coated film of thickness ~77 nm prepared on soda lime glass. This does not account for reflection losses.	169
5-21	Band gap calculation using Figure 5-19; the direct band gap of the material is found to be ~2.7 eV. The NCs were dispersed in chloroform and the path length of cuvette is 2 mm.	170
5-22	XRD pattern of SnS ₂ product prepared by heating the tetrakis (N, N-diethyldithiocarbamate) tin (IV) at 280 °C for 10 min.	171
5-23	Raman spectra of SnS ₂ prepared by heating tetrakis (N, N-diethyldithiocarbamate) tin (IV) at 280 °C for 10 minutes.	172
5-24	TEM and SEM images of SnS ₂ NCs; For TEM image, grapheme enhanced Cu grids were used and for SEM image, SnS ₂ film was prepared on glass.	173
5-25	EDS measurement of SnS ₂ NC film. Atomic and weight percentage of Sn and S are provided in tables.	173
6-1	Non-equilibrium band diagram of metal and semiconductors showing conduction and valence band positions relative to the vacuum level	181
6-2	Standard device structure and cross-sectional SEM images of CdTe thin film solar cells with FeS ₂ /Au as back contact.	184
6-3	Current density vs. bias voltage measurements of sputtered CdTe device with Au, Cu/Au, and FeS ₂ /Au back contacts obtained under simulated AM1.5G solar spectrum.	186
6-4	Two diode model equivalent circuit including a heterojunction diode between the CdS and CdTe films and Schottky junction diode between CdTe film and back contact metal.	187
6-5	EQE for sputtered CdTe devices with Au, Cu/Au and FeS ₂ /Au back contacts. The inset provides a zoomed view of EQE in the long wavelength cutoff region.	189
6-6	J-V curves when FeS ₂ thickness was varied from 0.35 μm to 1.5 μm. Performance parameters for each device are shown in the boxes.	191

6-7	Thermal stability test for sputtered CdTe device when FeS ₂ /Au was used as a back contact. Best cells' efficiencies at different temperature and time are provided in the graph.	193
6-8	Thermal stability test for sputtered CdTe device when Cu/Au was used as a back contact; best cells' efficiencies at different time scales are provided.	194
6-9	Thermal stability test for sputtered CdTe device when only Au was used as a back contact; best cells' efficiencies at different time scales are provided.	194
6-10	CdTe device was dipped into the hydrazine solution before depositing standard back contact to check the effect of hydrazine on CdTe.	196
6-11	Light intensity dependent current density of sputtered CdTe devices when Cu/Au and FeS ₂ /Au were used as back contacts.	197
6-12	Effect of light intensity on the efficiency and fill factor of sputtered CdTe devices when Cu/Au and FeS ₂ /Au were used as back contacts.	198
6-13	SEM image of FeS ₂ NCs at 10 kV accelerating potential and J-V curves when untreated FeS ₂ NC was used as a back contact for sputtered CdTe solar cells.	200
6-14	Current density voltage characteristics of CdTe devices, when the back contact is deposited as a combination of Cu/FeS ₂ /Au for both sputtered and CSS CdTe devices.	202
6-15	Typical EQE of cells before and after involving FeS ₂ NC as an interface layer for CSS deposited CdTe devices.	204
6-16	Temperature dependent J-V characteristics when standard Cu/Au is used as back contact for sputtered CdTe solar cell. Inset gives temperature dependent V _{OC}	206
6-17	Temperature dependent JV characteristics when treated-FeS ₂ /Au is used as back contact for sputtered CdTe solar cell. Inset gives temperature dependent V _{OC}	208
6-18	Temperature dependent JV characteristics when untreated-FeS ₂ /Au is used as back contact for sputtered CdTe solar cell. Inset gives temperature dependent V _{OC}	210

7-1	Work functions of the sample and the conducting tip before and after they are in contact; and an effect of an external bias (VDC) cancel the CPD.....	215
7-2	Work function of Au, CdS and PbS-QD films taken from KPFM measurement; Sample was scanned parallel to the edge.	217
7-3	Work function measured by KPFM through atomic steps on Au, bulk-CdS and PbS-QD films respectively.	218
7-4	Schematic showing the physics of ultraviolet photoelectron spectroscopy (UPS) and minimum and maximum KE of emitted photoelectrons.	220
7-5	UPS spectra for CdS film deposited on gold substrate. $E = 0$ on the Binding Energy axis corresponds to the Fermi energy, E_F	222
7-6	UPS spectra for CdS on Au and PbS QDs (diameter = 2.5 nm) on CdS for the qualitative analysis of emission behavior in two cases.....	224
7-7	The VBM position for CdS is at 2.0 ± 0.1 eV and for PbS QD is at 0.6 ± 0.1 eV.	225
7-8	UPS spectrum of CdS plotted as counts/s with respect to kinetic energy. The relation between spectrum width, $h\nu$ and work function (WF) is numerically illustrated.....	228
7-9	UPS spectra of PbS-QD film of two different thicknesses plotted as counts/s with respect to kinetic energy.	229
7-10	The S 2p, O 1s and Pb 4f XPS spectra for the EDT capped PbS QD films and the S 2p, O 1s and Cd 3d XPS spectra for the sputtered CdS film deposited on gold coated substrates.	233
7-11	Core level survey spectra of 70 nm layer of CdS, 200 nm PbS-QD and 70 nm CdS/12 nm PbS-QD composite films each of them were deposited on TEC15 glass substrate.	238
7-12	Photoemission spectra of Cd and Pb core levels measured after each layer of PbS-QD deposition onto the CdS thin film	239

7-13	The schematic band diagram of the interface between CdS and PbS-QD film. The CL binding energies of CdS and PbS-QD film are also shown.	240
7-14	XPS binding energy spectra of separate CdS-bulk and PbS-QD films and PbS-QD/CdS-bulk heterojunction in the region of the Pb 4f and Cd 3d core levels.	242
7-15	XPS and UPS binding energy spectra for CdS. Letters 'a' and 'b' represent the BE difference between the Cd 3d core level and the VBM.....	244
7-16	XPS and UPS binding energy spectra for PbS-QD. Letters 'c' and 'd' denote the BE difference between Pb 4f CL and the VBM.....	245
7-17	Energy band diagram of CdS/PbS-QD heterojunction interface. All parameters as obtained from the measurement are labeled and expressed in eV.	246
8-1	Technologies included in this study and their estimated percentage of market share. These market share percentages were published in 2013.	252
8-2	a-Si solar cell in "superstrate" (p-i-n) and "substrate"(n-i-p)configurations.	254
8-3	Schematic of a typical CdTe solar cell in superstrate configuration.	255
8-4	A schematic cross-sectional view of a typical substrate configuration CIGS solar cell. ...	256
8-5	A schematic representation of a module showing 36 crystalline silicon PV cells connected in series.	257
8-6	Module and BOS mean (μ) and standard deviation (σ) of embedded primary energy with error bars representing one standard deviation.	269
8-7	Correlation between the embedded energy and publication date of various PV types.	270
8-8	Mean embedded energy values reported by the collected references with error bars representing one standard deviation for the manufacturing of BOS.	272
8-9	Unharmonized (U) and harmonized (H) EPBT for crystalline silicon solar cells. The number of scenarios included is shown in parentheses after the technology name.	274

8-10	Unharmonized (U) and harmonized (H) EPBT for thin film solar cells. The number of scenarios included is shown in parentheses after the technology name.....	276
8-11	Efficiency values from the studies that passed all screening as well as the ones that did not pass the year 2000 cutoff criteria, most recent, best lab and theoretical efficiencies.....	279
8-12	Mean harmonized EROI with error bars representing standard deviation. The number of values for each module type is included in parentheses.....	281
9-1	Valence and conduction band levels of various sizes of PbS QDs and CdS films with respect to vacuum level.....	290
9-2	The absorbance spectra of PbS QDs (solid green lines), with diameter of 4.7 nm, and the PbS QD-CdS composite (solid blue lines).	291
9-3	The absorbance spectra of PbS QDs (solid green lines), with diameter of 3.0 nm, film and the PbS QD-CdS composite film (solid blue lines).....	292
9-4	Absorbance and photoluminescence spectra of silver doped and undoped PbS QDs of first exciton peak at ~870 nm and ~1238 nm.	295
9-5	Absorbance spectra of doped (copper) and undoped PbS 870 size QDs.	297
9-6	EDS Spectra for doped and undoped PbS QDs. Horizontal axis is energy in keV.....	300
9-7	XRD diffractograms for both doped and undoped QD films; The PbS QDs crystal structure corresponds to the PbS bulk fcc rock salt structure.	301
9-8	Multijunction quantum dot solar cell device structure.....	303
9-9	Current voltage characteristics of CdS/CdTe solar cells when FeS ₂ NC/Al is used as a back contact.	305

List of Abbreviations

AR	Auger Recombination
CdTe	Cadmium Telluride
CIGS	Copper Indium Gallium Diselenide
CBM	Conduction Band Minimum
CQD	Colloidal Quantum Dot
CVD	Chemical Vapor Deposition
DFT	Density Functional Theory
EPBT	Energy Payback Time
EROI	Energy Return on Energy Invested
EDT	1,2-ethanedithiol
FIB	Focused Ion Beam
FTIR	Fourier Transform Infrared Spectroscopy
FWHM	Full Width at Half Maximum
GHG	Greenhouse Gas
GW	Gigawatt
HOMO	Highest Occupied Molecular Orbital
HRT	High Resistive Transparent
KPFM	Kelvin Probe Force Measurement
LUMO	Lowest Unoccupied Molecular Orbital
MBE	Molecular Beam Epitaxy
MW	Megawatt
MEG	Multiple Exciton Generation
NC	Nanocrystal
NREL	National Renewable Energy laboratory
OD	Optical Density
PV	Photovoltaic
PL	Photoluminescence
PCE	Photo-conversion Efficiency
QD	Quantum Dot
SEM	Scanning Electron Microscopy
TEM	Transmission Electron Microscopy
TWh	Terawatt Hour
TMS	Hexamethyldisilathaine or Bis (trimethylsilyl) sulfide
TOPO	Trioctylphosphine Oxide
UPS	Ultraviolet Photoelectron Spectroscopy
VBM	Valence Band Maximum
XPS	X-ray Photoelectron Spectroscopy

List of Symbols

a	Lattice constant
a_B	Exciton Bohr radius
d	Diameter
e	Electron
h	Plank's constant
\AA	Unit of thickness
A	Absorbance
K	Degrees Kelvin
R	Reflection
T	Transmission
α	Angle of incidence
β	Full width half maximum
ϵ	Dielectric constant
η	Efficiency
θ	Grazing incidence λ Wavelength
κ	Boltzman constant
μ	Effective mass
ν	Frequency
ρ	Density
σ	Standard deviation, Surface tension
ϕ	Built in potential
χ	Electron affinity
Φ	Work function

Chapter 1

Introduction

1.1 Summary and Motivation

A brief definition of energy is the capacity of doing work. Energy is required in everyday life not only for human beings but for all living beings. For human beings, energy is required to move their bodies, to cook, to heat and light houses, to drive their vehicles and so on. Hence humans are great consumers of energy. Fossil fuels and nuclear power are the main source of energy in today's energy system. In 2012, about 87% of global primary energy consumption in the world was derived from fossil fuels. Fossil fuels are limited and the world's increasing energy demand is exhausting fossil fuel supply at a very high rate. [1] About 600 quads (1 quad = 1 quadrillion Btu = 1.055×10^9 GJ) of energy is currently needed to sustain the lifestyle of ~7 billion people worldwide per year. By the end of 2040, world energy consumption is expected to increase by 56% to maintain the current lifestyle.[2]

Massive consumption of fossil fuels has negative impact on the environment. During the combustion of fossil fuels, harmful gases such as CO_2 , CO, SO_x and NO_x and

hydrocarbon are emitted as a byproduct, which are the sources of environmental problems including the greenhouse effect and acid rain. Scientists have recognized that global warming is due to the massive use of fossil fuels. The concentration of CO₂ has increased significantly in the atmosphere and if this trend continues, the temperature of the Earth will have increased by as much as 3 °C to 5 °C by 2050.[3]

The world's population is continuously growing and will reach approximately 10 billion in 2050.[4] In order to improve average living standards of the growing population, the essential expansion of economic development will drive continued increases in annual energy consumption. Earth's future energy needs will be increasingly provided by sources other than traditional fossil fuels. For sustainable development, the additional energy sources are expected from environmentally friendly sources, known as renewable or sustainable energy sources.

Energy sources which are naturally replenished on a human timescale are called renewable energy sources. Most renewable energy comes directly or indirectly from the sun -- for example solar energy, wind, hydroelectricity, and bioenergy. There are some other renewable energy sources with no direct effects of sun such as geothermal energy, and ocean energy. Solar energy is a vast and inexhaustible energy source which represents a cleaner alternative to the fossil fuels that currently pollute our air and water, threaten our public health and contribute to global warming. There are various ways of capturing and using the SUN's energy such as solar thermal, concentrated solar power and solar photovoltaic (PV). Solar thermal technologies can be used for water heating, space heating, space cooling and process heat generation.[5] Solar concentrators are being used to convert sunlight indirectly into electricity using lenses or mirrors and

tracking system to focus a large area of sunlight to deliver the thermal energy needed to drive steam turbines in a conventional electric power generator.

The direct conversion of solar radiation into electricity is described as a photovoltaic (PV) energy conversion. The PV energy conversion takes place in a semiconductor device that is called a solar cell. By the end of 2013, the worldwide installed solar PV increased by 38% with respect to previous year to 139 GW as shown in Figure 1-1. The total power output of the world's PV capacity at the end of 2013 is therefore 160 TWh of electricity, which represents 0.85% of worldwide electricity demand. By 2016, China is predicted to take the lead of PV production and by 2018 the worldwide installed PV capacity is projected to have doubled or even tripled from 2013 capacity. [6, 7]

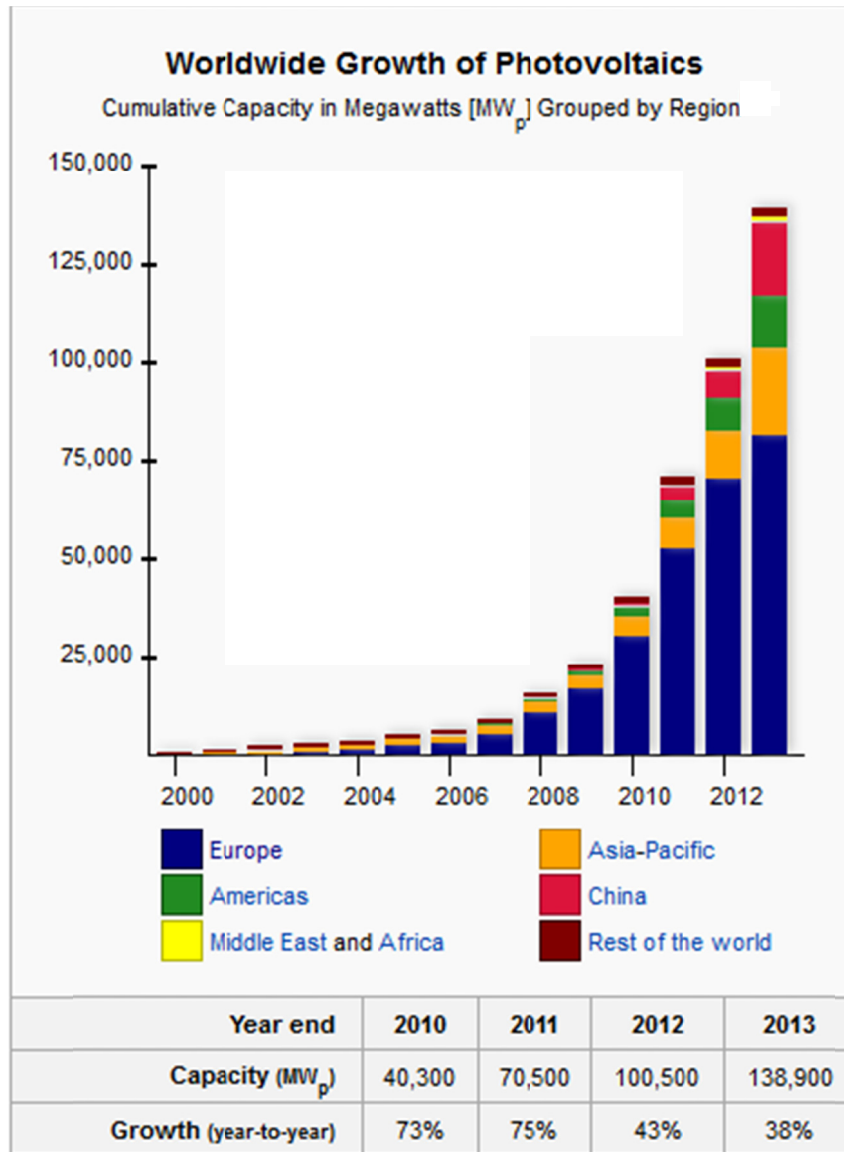


Figure 1-1. Growth of the photovoltaic in the world. [6]

1.2 Quantum dots for solar cells

Solar PV is a sustainable energy source[8] which uses semiconductor materials that exhibit the photovoltaic effect to convert sun light into usable electricity. Conventional materials presently being used for PV application include the crystalline

silicon (monocrystalline and polycrystalline) [9, 10], thin film [11], and QD/NC solar cells. [12-16]

Silicon photovoltaics may not ultimately be the least expensive route to the fulfillment of an unavoidable energy demand of the world due to its high manufacturing costs and technologically limitations associated with low light absorption. In addition, much of the energy from sunlight hitting a silicon solar cell converts directly to heat (thermal energy) rather than to electricity. Crystalline silicon absorbs photons of energy ≥ 1.1 eV (~ 1127 nm). That means photons with energies higher than 1.1 eV are absorbed but the photogenerated electrons and holes rapidly cool, or relax, to their respective band edges. Crystalline silicon solar cells possess power conversion efficiency values of approximately 22.4 % commercially [17], and 24.7% - 25% experimentally in the lab respectively.[18] For now, crystalline silicon solar cells are the highest efficiency solar cells for terrestrial applications. At the time this thesis was written photovoltaic record efficiencies provided by the NREL certified chart are given in Figure 1-2.

Best Research-Cell Efficiencies

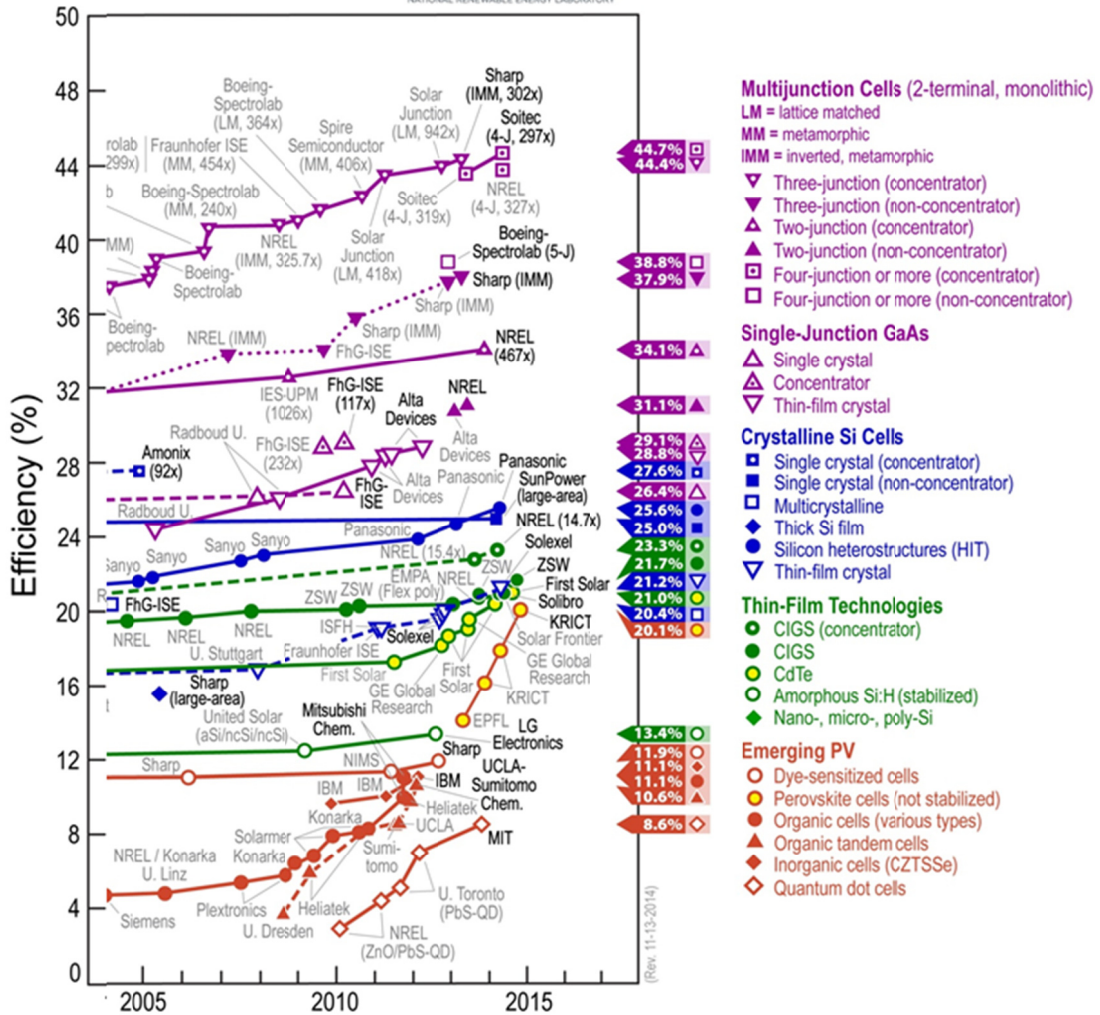


Figure 1-2. Research cell efficiency records prepared by NREL.[19]

Thin film polycrystalline and amorphous semiconductor materials such as a-Si, CdS/CdTe (CdTe), and CdS/CuIn_xGa_{1-x}Se₂ (CIGS), and also some nascent technologies such as those based on perovskite absorbers, have been developed in order to tackle the need for cheaper solar cells. Some of these thin film solar cells have improved substantially in efficiency, even though they lag behind the crystalline silicon technology.

For example, CIGS solar cells allow lab scale efficiencies up to 21.7 %. [19, 20] This value, however, drops when integrating into larger panels with reported efficiencies of 15.7% [18]. Similarly, CdTe, another successful thin film solar cell, has reached cell efficiency of 21.5% [19, 21] and panel conversion efficiencies of 16.1%. [22] Recently, the perovskite family has shown great promise for use in photovoltaic devices. Lab scale power conversion efficiency of lead halide perovskite based thin film photovoltaic devices has reached as high as 20.1%. [19] So, some of these thin film solar cells have shown promise in terms of increased efficiencies and lower material usage, but improvements are only incremental. The full benefit of solar energy perhaps may be realized when very different type of photovoltaic technology is developed.

It may be that colloidal quantum dot (CQD) based solar cells will eventually provide both low cost and high efficiency. The emerging field of CQD solar cell research has been based primarily on QDs such as PbSe, PbS, CdSe, and CdS as the light absorbers. In contrast to bulk materials, where the bandgap is fixed by the choice of material composition, QDs have adjustable bandgaps that are tunable across a wide range of energy levels by changing the QD size, without a need for adjusting material compositions. Because of size tunable properties, QDs can absorb and convert light to electricity even in the infrared energy region, a range of frequencies that includes half of the solar energy reaching the Earth. [23-25] PbS (bulk band gap at 0.41 eV) and PbSe (bulk band gap at 0.28 eV) QDs have the ability to absorb in the infrared region of the solar spectrum, which from a silicon solar cells is impossible due to its band gap at 1.1 eV. [26]

In QDs, quantum confinement effects originate from the spatial confinement of intrinsic carriers (electrons and holes) to the physical dimensions of the material smaller than to the bulk exciton length scale (Bohr radius). One of the better known confinement effects is the increase in semiconductor band gap energy with decreasing particle size. The charge carrier confinement property of QDs leads to additional desirable properties for the solar cells such as extended hot carrier lifetimes and multiple exciton generation (MEG).[27, 28] Unlike in bulk semiconductors, where hot electrons undergo rapid thermal relaxation to the band edges thus converting extra energy above the bandgap energy to heat, in QDs hot electron lifetimes can be extended by coupling a QD to either a hole or electron accepting materials. [29, 30] If these hot electrons can be collected and converted before thermalization loss, solar-to-electric power conversion efficiency can be increased to as high as 66% (theoretically). Similarly, generation of multiple $e^- - h^+$ pairs becomes efficient for semiconductor QDs as they require lower energy incident photon than in bulk materials. For example, to generate two $e^- - h^+$ pairs per absorbed photon in QDs, the energy required is as low as two times the threshold energy.[27] Thus, one of the potential uses of MEG is to improve the efficiency of solar cells.[24, 28]

Quantum dot photovoltaic (QDPV) modules may have advantages in terms of price. This is possible for following reasons. The first, an adaptable manufacturing process is applicable to roll-to-roll processing. This enables continuous and high-output production of PV modules and diversifies the number of applications due to their flexibility.[31] The second, reduced module area, for the same energy production due to higher efficiencies, reduces the amount of encapsulation materials, and third, reduced mass per power reduces transportation costs.

Optical losses (reflection from interfaces at the surface of a PV module) and carrier losses (recombination of carriers due to the poor interface or material quality) are two important sources of loss in solar to electricity conversion. Additional significant energy loss occurs from the sub-bandgap light (low photon energy infrared light which is not absorbed) and hot-electron or thermalization loss (relaxation of carriers photogenerated by photons with energy exceeding the bandgap energy). The concept of QD solar cells seeks to minimize these losses.[32]

1.3 Life cycle analysis of PV systems

For the systematic study of a product's complete life cycle and impact on water consumption, net energy production, and byproduct waste or pollution -- from raw materials extraction to final disposal -- life cycle analysis is considered a very important approach. [33, 34] Life-cycle analysis has been popular to evaluate environmental aspects of various products including solar cells. The operation of fossil-fuel based power plants has caused health effects and increased atmospheric CO₂ concentrations. Although operating photovoltaic systems do not generate any toxic- or greenhouse gases in the environment, such gases are emitted during the extraction, production, transportation and disposal phases of the materials used for solar PV systems. Crystalline silicon PV manufacturing process is very labor and energy intensive. The capital costs of manufacturing plant of crystalline silicon PV are high, limiting the scale-up potential. Life cycle greenhouse (GHG) emission and life cycle energy payback time (EPBT) from crystalline silicon PV are comparatively very high with respect to the other PV

technologies.[35] Thin film PV (a:Si, CdTe and CIGS) are typically made by depositing a thin layer of photo-active material onto glass or a flexible substrate. The most recent analysis found that CdTe PV generated the least amount of GHG emissions, and that the initial energy investment to produce these systems is paid back in shortest time period. [36] The QD based solar PV has been estimated to achieve higher efficiencies and lower costs than the previous two PV technologies. It is also estimated that the GHG emissions and EPBT from third generation solar PV systems will be least compared to all other types of PV systems mainly because of the least embodied energy required throughout its life time. [37]

So far I have discussed the application of nanocrystalline materials as the absorber layer in solar cells. The absorber layer plays a central role in the device performance, since it is in this layer that the photogenerated electron-hole pairs must survive until charge separation. However, the absorber layer itself cannot ensure good conversion efficiency without high performance from other layers such as the window layer, and front contact and back contacts. Nothing in this world behaves as ideal but people focus their efforts to make something close to ideal. If they cannot reach even close to ideal, they must seek alternatives. The back contact in CdTe thin film solar cells has presented significant challenges since the beginnings of CdTe PV technology. The most commonly used back contact for CdTe solar cells at laboratory scale is Cu/Au. People want to replace Cu by some other material as this is creating problem in the performance of the device in the long run.[38, 39] My work also addresses these challenges, and offers a new material pathway forward. The detailed work on the back contact of CdTe solar cells is explained in chapter 6 but here I would like to provide general overview of the back

contact to the CdTe solar cells and introduce nanocrystalline FeS₂ as a back contact buffer layer which may enable the omission of Cu.

1.4 Back contact for CdTe solar cells

In forming a contact to the CdTe layer at the back of a CdS/CdTe solar cell, one faces challenges based on CdTe's high work function and low inherent p-type doping density. The electron affinity and band gap of CdTe are 4.5 eV and 1.45 eV respectively and as the Fermi level is close to the valence band, the value of work function is ~5.7 eV. This is higher than typical metal work function, resulting in a Schottky barrier forming at the CdTe/metal interface. Thus in contrast with the desired barrier-less ohmic contact to CdTe, this barrier inhibits hole transport to the back contact.

The p-type doping level achievable for CdTe is typically assumed to be of the order of 10^{14} cm^{-3} which makes the film relatively resistive in the dark. Very low carrier concentrations limit mainly the device open circuit voltage and fill factor. CdTe is considered as a defect semiconductor such that the carrier density in CdTe is controlled by the native defect states. For at least the pseudo ohmic contact with a high work function metal, one would prefer that the carrier density of CdTe be raised to $\geq 10^{16} \text{ cm}^{-3}$. External doping of CdTe with various dopants is only partially successful. It is thought that the spontaneously generated point defects (vacancies, interstitials) are the main cause of experimentally observed doping problems.[40] These defects are assumed to neutralize dopants electrically by trapping their free carriers. Although attempts have been made to dope CdTe during growth with various impurities such as phosphorus, arsenic, and antimony, net free carrier concentrations have been limited to 10^{15} - 10^{16} cm^{-3} . [41, 42]

From the above discussion, the author finds three main problems in CdTe films for high efficient solar cells: (1) CdTe's high work function, (2) low intrinsic carrier concentrations, and (3) difficulty in achieving extrinsic doping to produce the desired free hole concentration. Because of these properties of CdTe, the barrier height at the back contact metal reduces the open circuit voltage and the conversion efficiency. One way to get overcome these problems is to find a contact material with proper work function to produce as a low- or negligible-barrier height at the contact. A layer of suitable semiconductor may be interposed at the contact before depositing the back contact metal. To accomplish this task, one should find a semiconductor material with the following properties: its work function lies between those of the back contact metal and CdTe, its electron affinity matches with the electron affinity of the CdTe, it has low resistance, good reproducibility and high stability, and shows a small lattice mismatch with CdTe. Although the lattice mismatch between iron pyrite (FeS_2) and CdTe is comparatively large ($a_{\text{CdTe}} = 6.48\text{\AA}$ and $a_{\text{FeS}_2} = 5.4\text{\AA}$), a thin nanocrystalline film of FeS_2 does satisfy the majority of the above-mentioned properties and in fact does function relatively well as a back contact for CdTe solar cells. A detailed analysis of the FeS_2 back contact for CdTe thin film solar cells is provided in chapter 6.

As described earlier, the absorber layer is an important constituent of a solar cell device. In making heterojunction solar cells, a window layer (heteropartner) is chosen so as to facilitate efficient charge separation across the interface between the absorber and window layers. Efficient charge separation is possible if the heterojunction between two semiconductors is type-II where the electron affinity of the absorber layer is smaller than that of the window layer, and the valence band edge of the absorber layer is within the

band gap of window layer. Even in this condition, magnitudes of the valence and conduction band offsets between two semiconductors determine the efficiency of charge transfer. The higher the band offset between the two semiconductors, the better is the charge transfer from the absorber to the window layer. Therefore, the choice of absorber and window layers matters in making high performance device. The author identified a good opportunity to study valence and conduction band offsets between CdS bulk and PbS QD films using photoelectron spectroscopy. The detail of this study is described in chapter 7 but here general information is outlined in the following section.

1.5 Electronic energy alignment between two semiconductors

Semiconductor lead salts, and in particular PbS quantum dots, have attracted particular attention as viable candidates for applications in photovoltaics.[43, 44] They can be size tuned to absorb light strongly in the IR to near-IR wavelength regions of solar spectrum. One of the well-known architectures for fabrication of QD based photovoltaic devices is the heterojunction solar cell. In the fabrication of QD films, ligand molecules (e.g. oleic acid) which are necessary for the colloidal QD synthesis and suspension in solution, present electronic potential barriers which inhibit inter-QD charge transport. However, conductivity of QD films can be increased by treating the films during film formation with several organic or inorganic molecules such as hydrazine, 1,2-ethanedithiol and so on. During this treatment process, long molecules are replaced by shorter molecules so that QDs can communicate easily and proficiently through electronic coupling.

In the heterojunction architecture, efficient electron injection from a photo-excited QD to the wide bandgap semiconductor window layer requires favorable alignment of the conduction and valence band levels of the absorber layer and window layer. The most favorable heterojunction for efficient charge transport is type-II band alignment in which the excited electrons in the QD lie above the conduction band edge of the window layer. Because of the size dependent band gap of QDs, this situation can be achieved by choosing the QD diameter. Size dependent charge transfer from CdSe and PbS QDs to TiO₂ nanoparticles has been studied by several authors. [45-47] There are only limited techniques available to explore the energy level alignment between two semiconductors. Cyclic voltammetry, ultraviolet photoelectron spectroscopy (UPS) and x-ray photoelectron spectroscopy (XPS) have been used by several authors.[47-49] Cyclic voltammetry is a quantitative technique, which measures the highest occupied molecular orbital (HOMO) and lowest unoccupied molecular orbital (LUMO) in the presence of counter ions from the electrolyte solution. In this thesis, the author reports on results of the KPFM and UPS methods to explore work functions and valence band maxima of CdS and PbS-QD films. The author also used XPS to determine valence and conduction bands offsets generated at the interface between CdS and PbS-QD films. The detail analysis is provided in chapter 7.

So far general information about each chapter is provided. Now I would like to present content on each chapter in the following section.

1.6 Dissertation Overview

This thesis presents experimental investigations of (a) optical and electronic properties of colloidal PbS quantum dots synthesized in Schlenk line technique using different organic solvents and non-solvents; (b) heterojunction formed between CdS thin film and PbS-QD; (c) Schottky and heterojunction PbS-QD solar cells with different window layers; (d) optical and electronic properties of FeS₂ and SnS₂ NCs; and (e) applications of FeS₂ NCs as a successful back contact for thin film solar cells.

Chapter 2 explains theory and experimental procedures as well as literature studies for PbS-QDs, FeS₂ NCs and SnS₂ NCs. Chapter 2 begins with the general information of direct and indirect semiconductors. Crystal and band structures of both PbS and FeS₂ are explained thereafter. Density of states, quantum confinement of quantum dots, general synthesis scheme of quantum dots and nanocrystals, surface passivation and charge recombination are explained in this chapter. At the end the chapter is finalized with the basic operational principles of solar cells.

Chapter 3 deals with the synthesis, characterizations and applications of PbS-QDs in solar photovoltaic. Chapter begins with the introduction and continues to PbS-QD synthesis. The product obtained from the synthesis is characterized both in solution and in films in a way to apply them in solar cells fabrication. As QDs show size dependent properties, performance of the solar cells is seen with respect to the size along with the thickness of the window layer. At the end chapter is wrapped up with the demonstration of light soaking effects of these solar cells in detail.

Chapter 4 provides new concept of utilizing CdS thin films as window layer for PbS-QD thin film solar cells. As is chapter begins with the introduction and is followed by synthesis of QDs. Quantum dots device fabrication process is described starting with the sputtered CdS film deposition, CdS film characterization, PbS-QD film deposition and back contact deposition in chronological order. Performance of the devices is seen with respect to the size of QDs, thickness of CdS films and at the end chapter is closed with the device stability test.

In chapter 5, syntheses and characterizations of iron pyrite and tin disulfide nanocrystals are described. Experimental is described after the introduction of this chapter. Fabrication of FeS₂ NCs is done using completely new iron precursor along with few different surfactants. Then layer by layer film fabrication process is described where hydrazine is used for the ligand exchange. Characterizations of both the films and NCs are performed using large number of standard instruments. Main focus is given in dealing with the electrical properties of these NCs with the help of hot probe, four point probe and Hall measurements. At the end proof has been given to show that FeS₂ NCs are not good for absorbing materials for thin film solar cells.

For the SnS₂ NCs, only the synthesis and characterization parts are studied. The purpose of doing this work was to utilize NC film as n-type window layer in FeS₂ solar cell. However, no any useful results were collected as FeS₂ hesitated to work as absorbing material in thin film solar cells.

In chapter 6, a very good application of iron pyrite NCs is shown. These earth abundant nanoparticles are designed to utilize as copper free back contacts for polycrystalline CdTe solar cells. Chapter begins with the introduction where very short

background of FeS₂ is followed by very short description of back contact of CdTe. I also address the problems with using gold as a back contact to CdTe, and why a thin elemental Cu layer is incorporated before Au deposition. Then results related to the FeS₂ back contact are presented, for both sputtered CdTe and close spaced sublimation (CSS) CdTe devices. Back contact thickness dependent study, intensity dependent study and benefit of FeS₂ to Cu/Au back contact devices; temperature dependent J-V measurements are all included.

Chapter 7 is for interface study between CdS and PbS-QD. For this various techniques Kelvin probe force measurement (KPFM), ultraviolet photoelectron spectroscopy (UPS), and Xray photoelectron spectroscopy (XPS) measurements have been used. From KPFM and UPS, material work function information is gathered. Again from UPS and XPS, valence band maxima, valence and conduction band offsets are calculated.

Chapter 8 addresses life cycle assessment analysis of major photovoltaic systems available commercially in the market. The goal of this chapter is to do a systematic review and meta-analysis of the embedded energy, energy payback time (EPBT) and energy return on energy invested (EROI) metrics for the crystalline silicon and thin film PV technologies published in 2000 to 2013. To accomplish this work, a rigorous screening is applied for 232 papers initially collected ending up with 11 papers for EPBT/EROI and 23 for embedded energy analysis respectively. Data were analyzed by harmonizing several parameters used in the study.

Finally, chapter 9 demonstrates summaries of all research results and discussions presented in this thesis and the overall conclusions drawn from it. Future directions for

the optimization of quantum dots solar cells from different perspectives, future direction for the optimization of nanocrystals back contacts and some other future works are mentioned.

Chapter 2

Colloidal synthesis and characterization of PbS and FeS₂ semiconductor nanocrystals, and the basics of solar cells

2.1 Introduction

Chapter 2 begins with the general information of direct and indirect semiconductors. Crystal and band structure properties of PbS and FeS₂ materials are provided thereafter. When a crystalline particle size reduces to nanoscale length, it exhibits exceptional properties which differentiate it from the bulk form of the material. The size dependent band gap and quantum confinement properties of nanocrystalline materials are explained starting with density of states, particle in box model, and the natural exciton wave-function size. Whereas in bulk semiconductors the exciton does not intimately encounter the potential barrier of the crystal surface, sufficiently small nanocrystals (so-called quantum dots) confine the exciton to a volume smaller than that corresponding to the natural exciton size, yielding so-called quantum confinement and size-dependent properties. A very general synthesis scheme of both quantum dots and nanocrystal materials is provided along with the importance of surfactant molecules for

surface passivation. At the end, a short description of basic operational principles of solar cells is provided where formation of PN junctions of semiconductors and solar cells external parameters are explained.

2.2. Direct and indirect semiconductors

All semiconductors can be classified either as direct band gap semiconductors (GaAs, PbS, ZnO) with valence band (VB) maximum and a conduction band (CB) minimum occurring at the same \vec{k} values in the Brillouin zone, or as indirect band gap semiconductors (Si) where the VB maximum and CB minimum occur at different \vec{k} values. [50] Figure 2-1 shows plots of the kinetic energy vs. wave vector or momentum vector for the direct band gap material (left) and an indirect band gap material (right) for the electron or hole. The kinetic energy of an electron or a hole in momentum space is represented by $E = \frac{k^2 \hbar^2}{2m^*}$ where $\hbar = h/2\pi$, h is Plank's constant and m^* is effective mass of electron or hole.

When a photon of energy ($h\omega_{\text{exc}}$) higher than the band gap energy of a semiconductor is absorbed, an electron-hole pair is created; following thermalization of the charge carriers with the crystal lattice, the electron and hole energy distributions follow the product of the Fermi function with the density of states. The condition to be satisfied in the photon absorption process is to satisfy the conservation of both energy and momentum. In Figure 2-1, the electrons and holes created due to the absorption of photons ($h\omega_{\text{exc}} > E_g$) are represented by the shaded regions at the bottom of the

conduction band and empty regions at the top of the valence band respectively. In direct band gap semiconductors, photon absorption at the band gap energy proceeds such that momentum is conserved, without the creation or annihilation of a phonon. That is because the momentum of the absorbed or emitted photon is negligible compared to the momentum of electron. Therefore, the absorption and emission processes are represented by vertical arrows on the $E-\vec{k}$ diagram. In indirect band gap semiconductors, the conduction band minimum and the valence band maximum are at different \vec{k} points. Therefore, during photon absorption or emission, assistance of phonon absorption or emission is considered. In Figure 2-1, absorption and emission of phonons are represented by “+” and “-” sign respectively.

The excited electron and hole do not remain in their excited states for a long time. They minimize energy rapidly through carrier-phonon scattering; the electron reaches to the bottom of the conduction band and hole reaches to the top of the valence band. Ultimately, the electron and hole recombine radiatively, with the emission of photon, or nonradiatively, with the generation of thermal energy (phonons). The radiative emission of a photon from a semiconducting material is called photoluminescence (PL). The PL occurs in both direct and indirect semiconductors but for the indirect semiconductor a change in both energy and momentum of the excited electron is required. Hence PL in indirect semiconductor is a second order process with a longer radiative lifetime. The PL in a direct gap semiconductor is a first order process with a relatively short radiative lifetime.

Here, the author has conducted photoluminescence studies mainly for PbS-QD solution and films, but also for other NC-based thin films. The detail is provided in chapter 3 but here I explain some electrical properties of PbS QDs and FeS₂ NCs. Before diving into their electrical and optical properties, however, it is a good place to define QD and NC and their difference. Quantum dots are zero dimensional aggregates of atoms of semiconductor materials having diameter smaller than the bulk Bohr exciton radius. They constitute a class of materials intermediate between molecules and the bulk form of matter. The size of NCs on the other hand is, in general, greater than exciton Bohr radius. The implication of this is that carriers exhibit strongly size-dependent properties (confinement) QDs but not in NCs. The size (diameter) of QDs can in general be of the order of 2-10 nm whereas the size of NCs can go up to a few hundred nm. The diameter of PbS QDs synthesized here are of the order of 2-5 nm whereas the size of our synthesized FeS₂ NCs ranges from 50 – 150 nm which is very large compared to their exciton Bohr radius, $r_B = \frac{\epsilon \hbar^2}{e^2} \left(\frac{1}{m_e^*} + \frac{1}{m_h^*} \right) = m_e \epsilon a_B \left(\frac{1}{m_e^*} + \frac{1}{m_h^*} \right) \approx 2.6 \text{ nm}$ (For FeS₂, $\epsilon = 10.9$, $m_e^* = 0.25m_e$ and $m_h^* = 2.2m_e$; a_B is exciton Bohr radius of hydrogen).

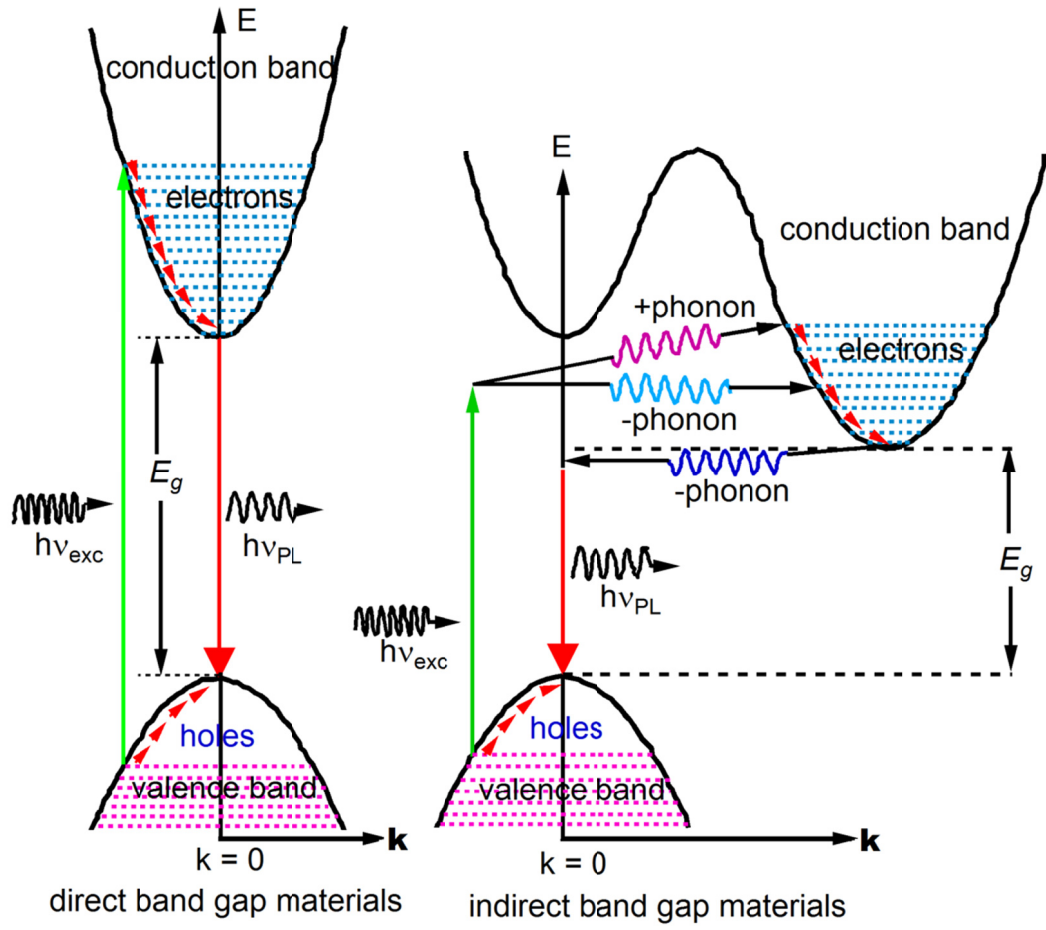


Figure 2-1. Direct and indirect bandgap semiconductors: absorption and emission of light adapted from Aigen Li. [50]

2.3 Crystal and band structure properties of bulk and quantum dot PbS

Lead chalcogenides, PbS, PbSe and PbTe have been applied in long-wavelength imaging, [51] diodes lasers,[52, 53] and in photovoltaic energy converters [54]for many years. These semiconductors possess some peculiar electronic and structural properties

relative to the more conventional II-VI and III-V compounds and alloys. Lead is one of the post-transition metals with high atomic number. The electrons configuration of ^{82}Pb is $[\text{Xe}] 4f^{14}, 5f^{10}, 6s^2 6p^2$.

Lead in PbS belongs to the group 4 element in periodic table, for which the group valency is four. The electronegativity of these elements has risen quite high, with the Pb atom having an electronegativity of 2.33. The high electronegativity of these elements leads to a strong inert pair effect in Pb. Electrons in the outermost s atomic orbital of post transition metals tend to remain unionized or unshared in the compound they make. This phenomenon is known as inert pair effect. The oxidation state of the heavier elements such as Pb(II) is 2 less than the group valency of 4. This means the increasing stability of oxidation state of these elements is due to the inert pair effects.

The reason for the “inert pair effect” lies in the theory of relativity. With heavier elements such as lead there is a relativistic contraction of the electrons which tends to draw the electrons closer to the nucleus. So, because of the high atomic number of the Pb in PbS, relativistic effects localize its valence $6s$ orbital making this orbital chemically inactive and transforming this $s^2 p^2$ orbital into a pseudo-divalent p^2 orbital corresponding to II-VI compounds, i.e. cadmium selenide (CdSe) and cadmium sulfide (CdS).[55] Both the valence-band maximum (VBM) and the conduction band minimum (CBM) states occur at the L point in the Brillouin zone, whereas these two parameters in the direct band gap II-VI semiconductors occurs at the Γ point.[56, 57] There are several ways of calculating band structure for lead salts such as an augmented plane wave (APW), pseudo-potential calculations, density functional theory (DFT) and so on. The electronic band structure of PbS by pseudo-potential treatment, suggested by Lin and Kleinman,[58]

is shown in Figure 2-2, where the band gap energy is defined between L_1^6 and L_2^6 region. In Figure 2-2, the energy $E(\vec{k})$ of an electron is plotted as a function of wave vector \vec{k} for two direction in \vec{k} space. Right hand side of the zone center (Γ) shows $E(\vec{k})$ as a function of \vec{k} in an [001] direction whereas in the left hand side of Γ , $E(\vec{k})$ is plotted in [111] direction. In energy scale, an arbitrary zero is chosen on the top. In PbS, the occupied s -state in the valence band plays a significant role in forming the band gap. Although there are several bands as candidates for the VBM, L_1^6 is the only one that has symmetry identical to that of the s -level. Because of the anticrossing repulsion, the L_1^6 state is pushed upward to form the VBM. Similarly, because of the relativistic effect represented by the spin-orbit coupling only the L_2^6 state is pushed downwards by the equal symmetry thus becoming the CBM. [59]

The bandgap type for PbS, PbSe and PbTe is direct and located at the L point. The lead chalcogenide system (PbX) shows the anomaly that bandgap energy does not decrease monotonically with the anion's atomic number ($E_g^{PbS} > E_g^{PbTe} > E_g^{PbSe}$) whereas it does in II-VI semiconductors. All three PbX semiconductors have a very similar band structure. [57] The NaCl lattice of the lead salts has inversion symmetry in addition to the symmetry elements of the zinc-blende lattice of the III-V compounds, so that band extrema occur strictly at the Γ , L and X symmetry points of the Brillouin zone and the twofold degeneracy is preserved at all points in the Brillouin zone. The lead salts have twofold degenerate valence-band maxima and twofold degenerate conduction-band

minima at the L point in contrast to the III-V compounds, which all have fourfold degenerate valence bands at Γ with maxima nearby.[60]

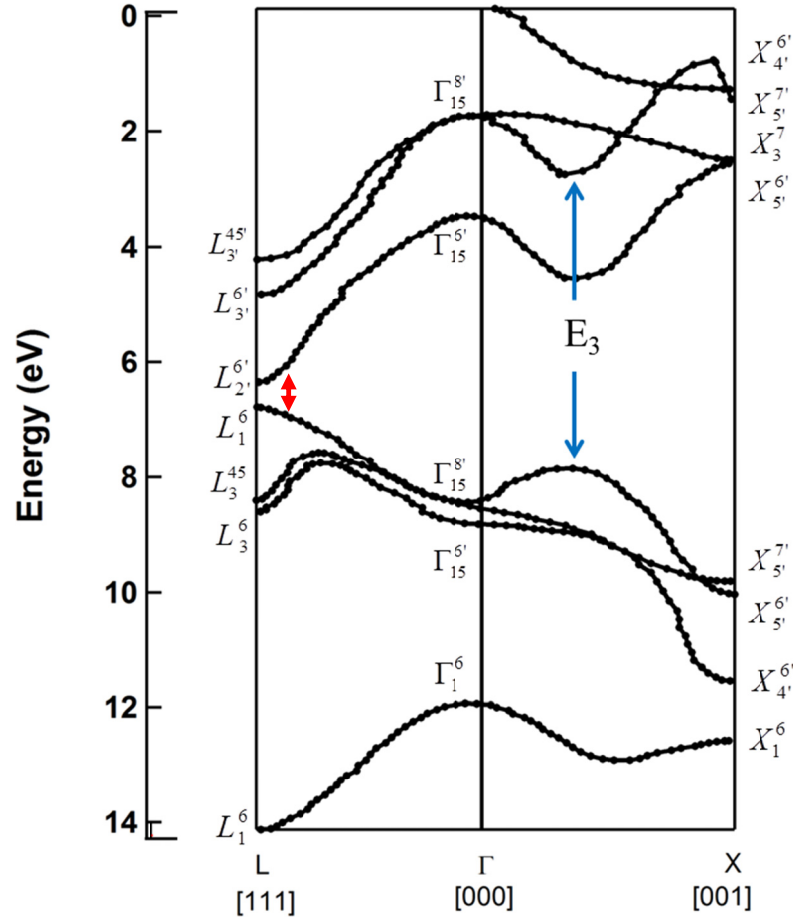


Figure 2-2. Electronic band structure of PbS adapted from Richard Dalven. [61] The minimum energy direct band gap is situated at L: $L_1^6 \rightarrow L_2^6$. The higher energy transition E3 can also be seen.

Lead chalcogenides are polar semiconductors in which the bonding is mostly due to the electrostatic forces between the ions forming the crystal. An estimate of the effective charge present on the lead and sulfur ions in PbS is $e^* = 0.71e$ (highest in lead salts) indicating more ionic and less covalent nature.[61] The ionic nature of these

materials is also reflected by the fact that they have NaCl or rock salt crystal structure. Lead chalcogenides are narrow bandgap semiconductors: at 300 K, the bandgap energies for PbS, PbSe and PbTe are 0.41, 0.27 and 0.31 eV respectively.[60] The author in this thesis focuses on PbS QDs instead of bulk PbS. Both bulk and QD PbS possess rock salt crystal structure (Figure 2-3a) with a lattice constant of $a = 5.936 \text{ \AA}$ at room temperature.[62, 63] In the rock-salt structure, the space lattice is face-centered cubic, with a basis of one Pb^{2+} ion and one S^{2-} ion associated with each lattice point.[61] The coordination number of each Pb and S atom in this structure is 6: each Pb cation coordinates to 6 anions at the vertices of an octahedron; similarly each S coordinates to 6 cations at the vertices of an octahedron. Figure 2-3b represents the Brillouin zone of rock salt crystal structure where there are eight hexagonal faces each centered around the L point and six equivalent square faces each centered around the X point. The Γ point is at the center zone, and the crystal structure possesses mirror symmetry. The 3D band structure is made by plotting the energy levels in k-space along x, y and z directions. PbS has large dielectric constant of $\epsilon_r(\infty) = 17.2$; the electron and hole masses are comparable and relatively small ($m_{e(h)}^* \approx 0.08m_0$), where m_0 is the mass of electron in vacuum.[64] This leads to a large exciton Bohr radius ($R = 18 \text{ nm}$) and strong quantum confinement for both electron and hole in PbS QDs.

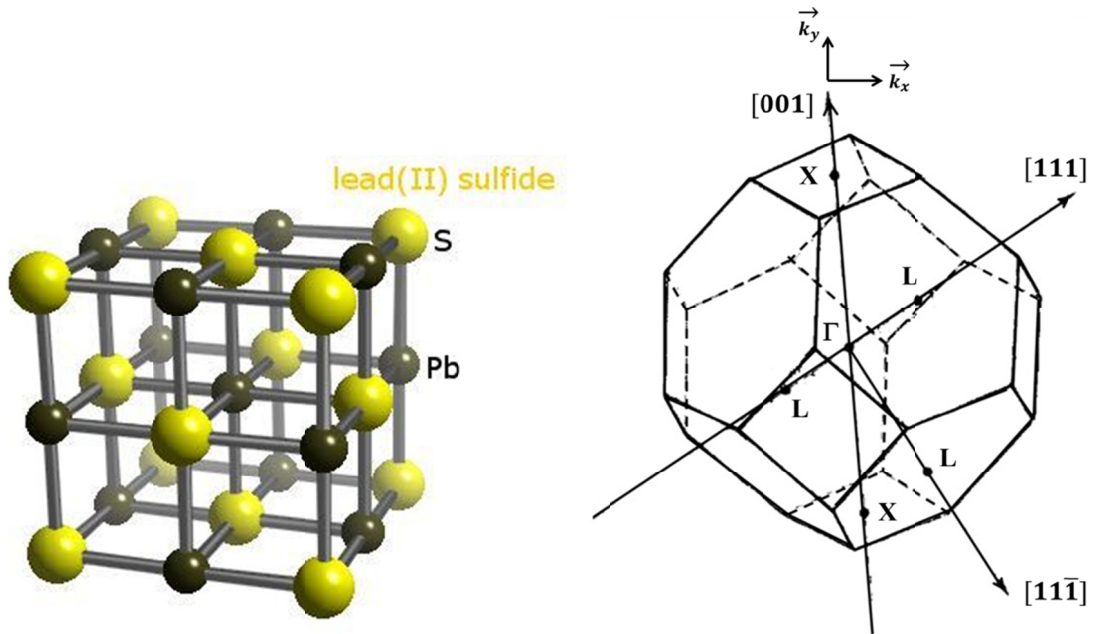


Figure 2-3. (a) Rocksalt crystal structure of PbS. (b) Brillouin zone for rocksalt crystal with space group $Fm\bar{3}m$. There are four equivalent L points at the center of the faces on the surface of the Brillouin zone. The growth direction is along $[111]$ and is chosen to point along the z-axis. [61, 63]

2.4 Crystal and band structure of iron pyrite

Iron pyrite is one of the most important sources of iron and sulfur, and is the most abundant sulfur mineral found in the earth. Iron pyrite possesses rock salt crystal structure (face centered cubic) with the arrangement of Fe^{2+} and S_2^{2-} ions. As shown in Figure 2-4, each Fe atom is octahedrally surrounded by six sulfur atoms while each S atom is tetrahedrally coordinated with one neighboring S atom and three neighboring Fe atoms.[65] Because of this coordination, it is assumed that the anions (S_2^{2-}) use hybridized sp^3 orbitals. The interatomic distance between two nearest S atoms is 2.18 Å, between nearest Fe and S atoms 2.26 Å and between two nearest Fe atoms is 3.81 Å

respectively.[66] Since the metal ions are too far apart for sufficient overlap of electron, a band of available electron states due to the metal-metal interaction does not appear as an important consideration for iron pyrite. Because of the trigonal distortion of the lattice, the t_{2g} orbitals of Fe^{2+} are not degenerate and the orbitals used by Fe^{2+} can be considered to be $(e_g)^2 sp^3$ hybridized.[67] As the σ -orbital overlap is greater than π -orbital overlap, σ -type bonding (utilizing e_g orbitals) is considered stronger than any π -type. Of the orbitals involved in bonding between the cation and anion sublattices, bonding electrons belong primarily to the anions and the antibonding electrons belong primarily to the cations.

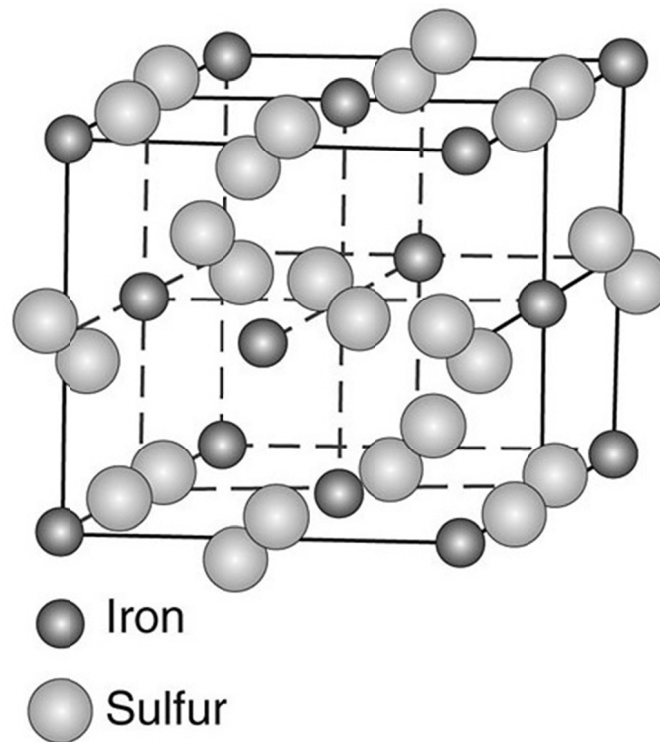


Figure 2-4. Iron pyrite crystal structure.[65] Smaller dark spheres represent Fe and larger white spheres represent S atoms.

Due to this, bonding electrons are stabilized whereas antibonding electrons are destabilized by covalent mixing as shown in Figure 2-5.[67] Anions have higher electronegativity than cations and hence they lie lower on an energy level diagram than cations. As shown in Figure 2-5 for the transition metal pyrites, the bonding bands will always be filled and the highest antibonding band are always be empty. Therefore, only those states which originate from the transition metal d levels need to be considered and only these will be examined in the individual compounds.

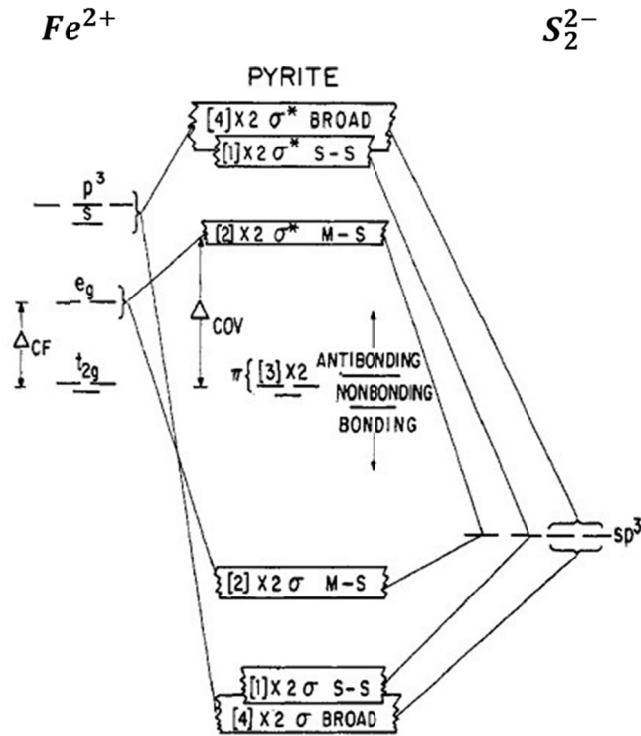


Figure 2-5. Energy bands of FeS₂ are drawn for the pyrite structure.[67] The orbital degeneracy of each level is represented in brackets and because of spin degeneracy is multiplied by 2.

The PbS and FeS₂ studied here are nanocrystalline materials, and for sufficiently small crystallites, the optical and electronic properties of these materials will differ from those

of their bulk counterparts. It is therefore desirable to understand the size dependent behavior of PbS and FeS₂. The size dependent band gap energy and quantum confinement effect of these particles are described in the following sections.

2.5 Size dependent band gap and quantum confinement of NCs

2.5.1 Density of states

Semiconductors are the foundation of the modern electronics industry. They have long been used extensively in communication, information and computer industries. In order to decrease size, enhance functionality, and/or reduce energy consumption, miniaturization of semiconductor devices has been a major focus.[68, 69]

Due to the advanced semiconductor growth techniques like molecular beam epitaxy (MBE) and chemical vapor deposition (CVD), fabrication of various semiconductor nanostructures such as quantum wells, (charge carriers and their wave functions are confined perpendicular to the thin film but are free to move in the other two directions), quantum wires (charge carriers are confined in two directions and only allow one dimensional motion) and quantum dots (QDs) (charge carriers are confined in all three directions) are possible. The small physical dimensions of quantum dots act to restrict the wave function of electrons and holes located inside the quantum dot. The boundary conditions associated with the spatial confinement of the wave functions, instead, modifies the density of states. The resulting change in density of states in QDs is discrete and is analogous to the particle in a box in quantum mechanics. Strong interband transitions are possible in these nanostructures because of the possibility of strong overlap between the wave functions of the electrons and holes.

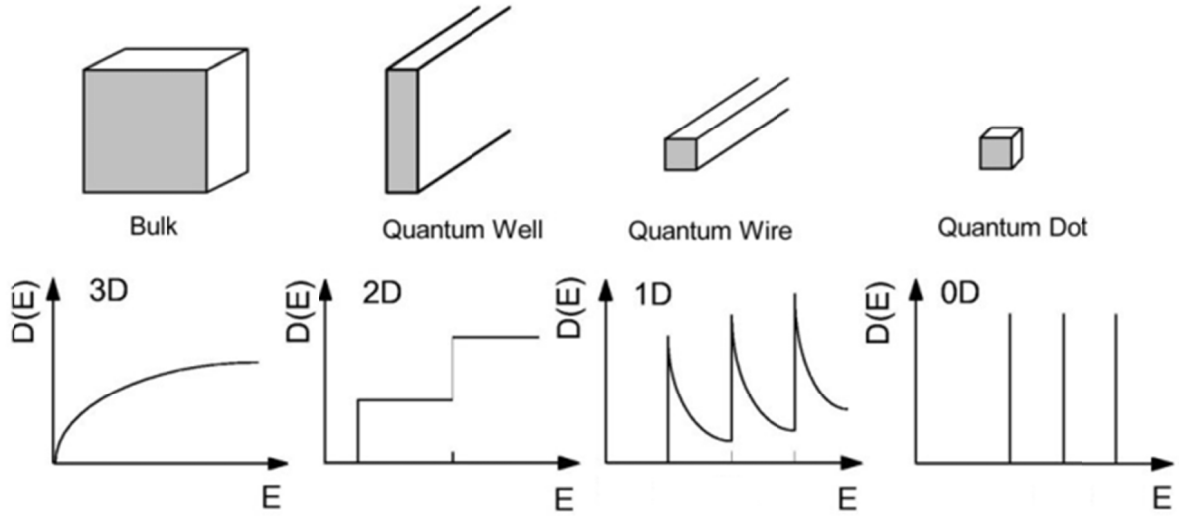


Figure 2-6. Density of states in semiconductor structures in different dimensions.[70, 71]

Density of states in semiconductor structures of different dimensionality is provided in Figure 2-6. The density of states refers to the number of quantum states per unit energy. [72, 73] The electronic density of states for bulk semiconductors is, $D(E) \propto E^{1/2}$ so that the electron can occupy a continuum of energy levels. For quantum wells and quantum wires, quantum confinement effects result in discrete subbands in both the conduction and the valence bands and an increase of bandgap energy. The density of states can be written as $D(E) \propto E^0$ for 2 dimensional quantum wells and $D(E) \propto E^{-1/2}$ for 1 dimensional quantum wires respectively. In a zero dimensional quantum dot system, the carriers are confined in three dimensions and hence the density of states is described by a delta function $D(E) \propto \delta(E)$ as shown in Figure 2-6. In PbS QDs the density of states in the valence band has a similar distribution to that in the conduction band.

2.5.2 Particle in infinite potential well

The one dimensional (1D) infinite square potential well, as shown in Figure 2.7, is the simplest case of particle confinement in quantum mechanics. By solving the time-independent Schrodinger equation in all boundary conditions, the wave function and the energy of a confined particle can be obtained.[74]

$$\psi(x) = \sqrt{\frac{2}{a}} \sin\left(\frac{n\pi x}{a}\right) \quad (2.1)$$

$$E_{n,l} = \frac{\hbar^2 \pi^2 n^2}{2ma^2} \quad (2.2)$$

where, a is the size of the potential well, m is the mass of an electron

In 3D, y - and z -axis terms are to be added in above equations. If QDs are spherical in shape rather than a box, the 3D-confined particle's wave function and energy can be written using Bessel functions and spherical harmonic functions.

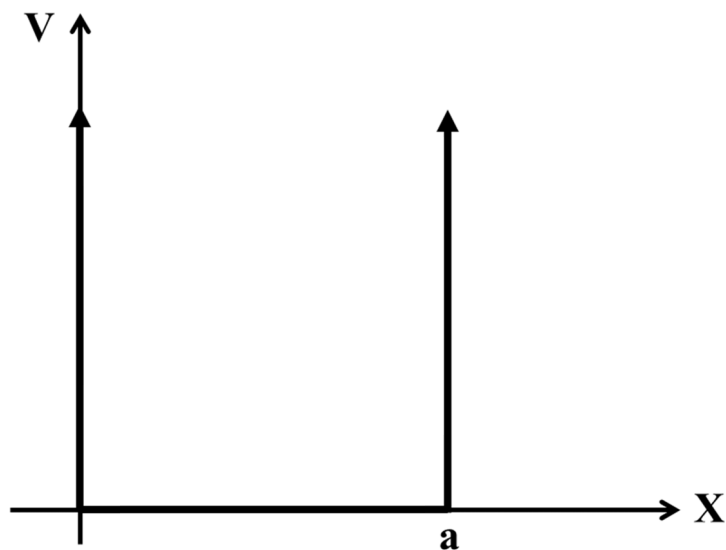


Figure 2-7. Infinite square potential well

2.5.3 Excitons in a bulk semiconductor

An exciton is a coulombically bound electron-hole pair. The energy required for the creation of an exciton is slightly lower than the material band gap energy due to the strong Coulomb interaction between the electron and hole. The separation between the electron and hole is known as the exciton Bohr radius. The exciton Bohr radius depends on the dielectric constant of the semiconductor material and the reduced mass of electron and hole as given in equations (2.3) and (2.4). [74]

$$r_{ex} = \frac{4\pi\epsilon\epsilon_0\hbar^2}{\mu e^2} \quad (2.3)$$

$$\frac{1}{\mu} = \frac{1}{m_e^*} + \frac{1}{m_h^*} \quad (2.4)$$

where m_e^* and m_h^* are the electron and hole effective masses respectively. Due to thermal motion, the exciton also has a de Broglie wavelength. Quantum size effects arise when the size of a NC is comparable to the de Broglie wavelength, λ given by

$$\lambda = \frac{h}{p} = \frac{h}{\sqrt{2m_{e(h)}^*k_B T}} \quad (2.5)$$

At room temperature the de Broglie wavelength of exciton in PbS is 8.2 nm, exciton Bohr radius is 18 nm and Bohr radii of the electron and hole are identical at 9 nm each.[75]

2.5.4 Quantum confinement in quantum dots

When a semiconductor NC is embedded in an insulating material (e.g., an organic ligand or surfactant), as shown in Figure 2.8, the photoexcited carriers exist in a potential

well in all three dimensions and the conduction and valence bands are quantized due to the finite size of the NC.[76, 77] Quantum dots exhibit a series of discrete energy levels of electron and hole as opposed to bulk, energy levels of electron and hole in bulk is continuous. The optical absorption spectra of QDs are strongly dependent on the size of the crystallite. Based on the size of the dot and exciton Bohr radius, the following four confinement regimes are considered. [74]

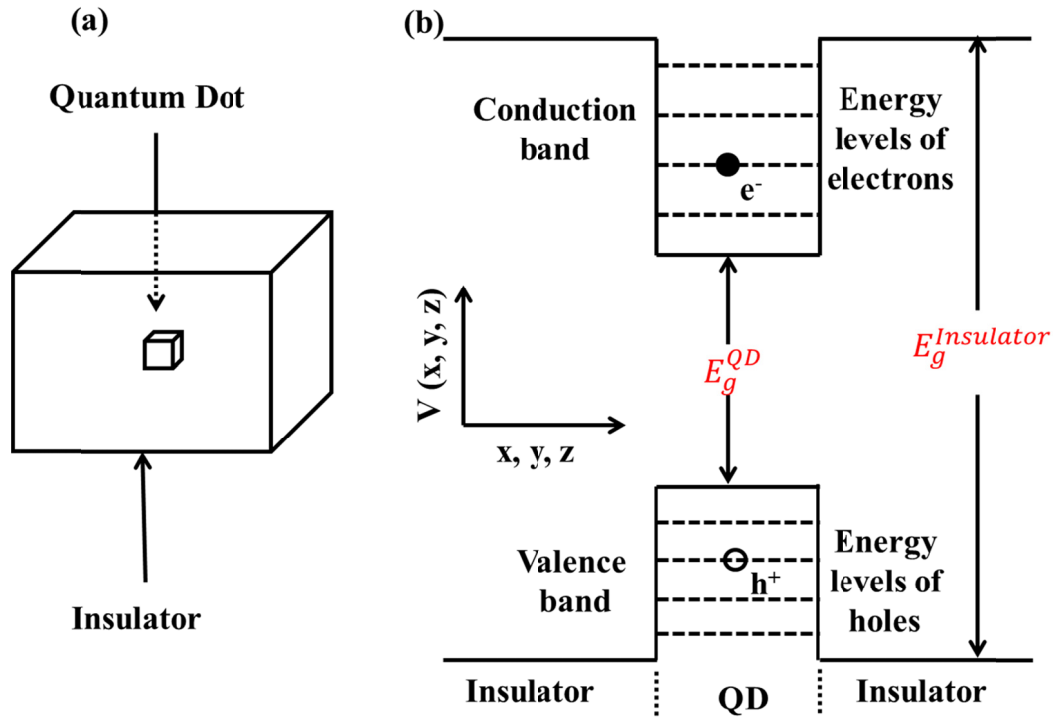


Figure 2-8. (a) Schematic of a single QD with its surrounding matrix (capping ligand); the diagram (b) represents the potential well for each of the three spatial dimensions, and the quantized energy levels of electrons and holes in a QD.

- i. When $r_{NC} \gg r_{ex}$

When the size of a NC is very large compared with the exciton Bohr radius, there is no evident confinement effect. In this case the material shows bulk-like properties.

ii. When $r_{ex} < r_{QD} \sim \lambda$

When the size of a NC is larger than exciton Bohr radius but similar to de Broglie wavelength, there is a weak confinement; we refer to NCs of this size or smaller as a QD.

iii. When $r_{QD} \sim r_{ex}$

When the QD size is comparable to the radius of the exciton, this confinement regime is known as intermediate confinement. In this case, classical mechanics does not work to describe the motion of the electron and hole, and one must solve the Schrodinger equation for electron and hole.

iv. When $r_{QD} \ll r_{ex}$

This condition corresponds to the strong confinement regime where the radius of the QD is much smaller than the exciton Bohr radius. It is said that in strong confinement regime, the individual motions of the electrons and the hole are quantized.[78] In this situation, the kinetic energy of the electron and hole is higher than exciton binding-energy. Electron and hole cannot remain in bound state but they have to be separated. Therefore, in strong confinement, electrons and holes are confined separately in QD (see below equation 2.7).

When a photon of energy higher than the band gap energy impinges on a semiconductor, it excites an electron from the VB to the CB, creating an exciton. The

excess energy (above the effective band gap energy) of the exciton is thermally dissipated in the system as the exciton relaxes through exciton-phonon and/or surface-mediated interactions. Finally, the exciton undergoes annihilation, yielding either thermal energy or a photon (fluorescence) with energy slightly less than the effective band gap. The energy of the emitted photon is represented by $E_g^* = E_g - |E_n|$. A representing exciton in bulk is shown in Figure 2.9.

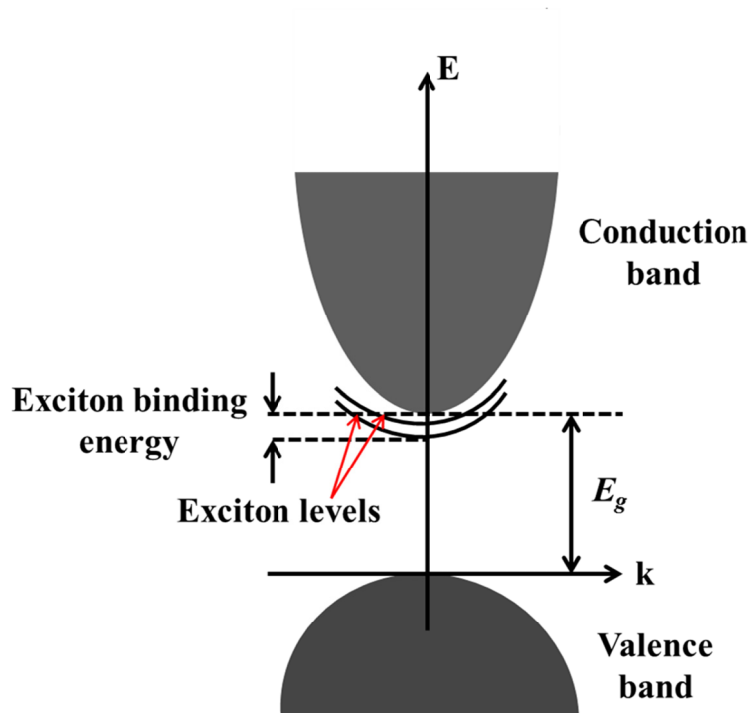


Figure 2-9. Energy levels of an exciton in a direct band gap semiconductor with conduction and valence bands at $k = 0$. [72]

In case of QD for strong confinement regime, the exciton energy is the sum of the band gap energy in bulk plus the lowest energies of quantization for the electron and the hole [78, 79] and is given by.

$$E_{QD} = E_{bulk} + \frac{\hbar^2 \pi^2}{2\mu r^2} \quad (2.6)$$

Here the second term describes the energy levels of a particle (exciton) of mass μ in a spherically symmetric potential box. This equation explains the quantum size effect in QDs -- i.e. the increase of band gap (energy separation between the lowest-energy CB and VB levels) with the decrease of QD size.

A more accurate representation of the calculation of exciton energy in a semiconductor QD (using CdS and CdSe as examples) is provided by Kayanuma in equation (2.7).[80, 81]

$$E_{QD} = E_{bulk} + \frac{\hbar^2 \pi^2}{2\mu r^2} - \frac{1.78e^2}{\epsilon_r \epsilon_o r} - 0.248 \frac{\mu e^4}{2\hbar^2 \epsilon_r^2 \epsilon_o^2} \quad (2.7)$$

The second term on the right of Eqn. (2.7) is the kinetic energy which is due to confinement of the electron and hole and indicates a blue-shift with respect to the bulk band gap. The third term is due to the Coulomb attraction between electron and hole (red-shifting effect) and the last term is the bulk exciton binding energy in terms of the Rydberg energy (again, a red-shifting modification). The third and fourth terms are significant only in case of semiconductor materials having low dielectric constants. The exciton in bulk material is solely due to the Coulomb attraction between electron and hole. In QD, coulombic attraction still exists but its strength depends on the confinement regime. In strong confinement, the confinement energy of each carrier depends as $1/r^2$ and the Coulomb interaction depends as $1/r$ (equation 2.7). Therefore, in sufficiently small quantum dots, the quadratic confinement term dominates. In the strong quantum

confinement regime, the electron and hole can be treated independently and each is described as a particle in a sphere.[82]

2.6 General synthesis scheme of colloidal NCs (or QDs)

It is possible to prepare semiconductor NCs colloiddally using a chemical synthesis process. These NCs consist of a nanoscale semiconductor inorganic core surrounded by shell of organic ligand molecules. [83-86] These organic ligand molecules act as surfactants which mediate their growth, confer solubility, and prevent agglomeration. Ligands influence NCs' solubility and chemical reactivity, and organic surfactant molecules in the growth medium are chosen for their affinity to the surface of a growing crystal. Examples of organic surfactant molecules include trioctylphosphine oxide (TOPO), alkyl phosphine oxides, alkyl phosphonic acids, alkyl phosphines, fatty acids and amines. [87]

Surfactant molecules not only bind to the growing NCs surface, but also form a complex with the reactive monomer species. [87] The stability of these complexes and the binding strength of the surfactant molecules depend strongly on the temperature. As temperature increases, decreases are observed for the stability of the intermediate complexes formed in the solution as well as for the binding of the surfactants to the NC surface. This increases the diffusion rates of these complexes favoring the nucleation and growth of the NCs. Uncontrolled growth is expected if very high temperature is used. [88, 89]

The formation of NCs involves two steps: nucleation and growth. For nucleation to occur, the monomer solution (monomer: at sufficiently high temperature precursors chemically transform into monomers) must be supersaturated either by directly dissolving the solute at higher temperature and then cooling to lower temperatures, or by adding the necessary reactants to produce a supersaturated solution during the reaction. Once the monomer reaches a sufficiently supersaturated level, nucleation initiates NC growth. For nucleation to occur, an energy barrier must be overcome. The nucleation of NC growth in the monomer solution is determined by the difference in the free energy between two phases: the crystalline phase, in which the atoms are bound to a crystal and the solution phase, in which the atoms are dispersed freely in the solution. When a spherical nucleus consisting of n atoms is formed, there is a change in free energy of the system given by [90]

$$\Delta G = \frac{4\pi\rho}{3} r^3 (\mu_c - \mu_s) + 4\pi r^2 \sigma \quad (2.8)$$

Where μ_c and μ_s are the chemical potentials of the crystalline phase and the solution phase respectively, r is the radius of the nucleus, ρ the density of atoms and σ the surface tension. In equation (2.8), the surface term provides the main difference between NC and bulk. For the bulk, the surface energy term does not contribute anything whereas in the case of a NC, a significant portion of atoms are often situated on the surface and thus the surface term plays an important role. For stable NCs to be formed, the chemical potential for the solution must exceed that of the NCs, and so the first term in equation is negative. In this case, the free energy becomes maximum for a certain radius r_c at which a nucleation barrier is imposed as shown in Figure 2-10 (left).

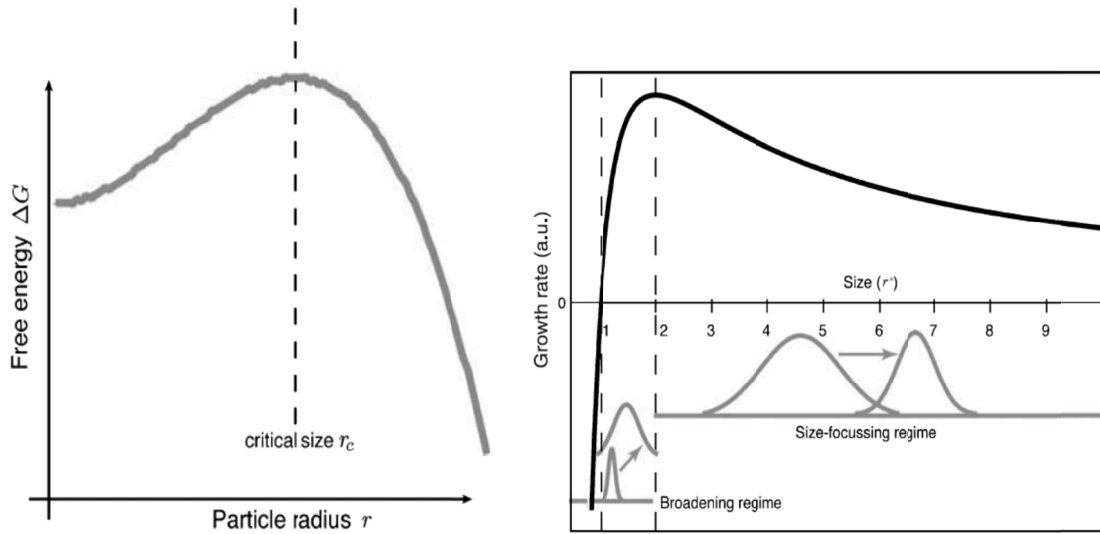


Figure 2-10. (left) Change in free energy with respect to the NC size, (right) growth rate with respect to the critical radius r^* . [90]

For the growth of the NC, monomers have to be added to the growing NCs by transporting the monomers toward the growing NCs and by reacting monomers with the surface of the NCs. In the beginning of the reaction, the concentration of the monomers is very large and uniform throughout the solution. In this case reaction-controlled growth dominates. When the concentration of the monomers is partially depleted, the NC growth is determined by the diffusion of the monomers. The growth rate of the NC is given in equation (2.9). [90]

$$\frac{dr}{dt} = \frac{2\sigma DC_\infty}{\rho^2 k_B T} \frac{1}{r} \left(\frac{1}{r^*} - \frac{1}{r} \right) \quad (2.9)$$

where D is the diffusion constant, C_∞ is the vapor pressure at the flat surface, k_B is Boltzmann constant, T is temperature and r^* is critical size corresponding to the zero growth rate and is equal to the critical radius r_c .

Figure 2-10 (right) provides the growth rate with respect to the critical size (r^*). From Figure 2-10 (right) and equation (2.9), it is clear that crystal with size r^* ($=r_c$) never grows because a crystal of this size is in equilibrium in solution. For r smaller than r^* , growth rate is negative. If the radius of the NC is 2 times the critical radius, the growth rate is maximum. When the radius of all the NCs are greater than $2r^*$ the smaller crystals grow faster than larger ones and monodisperse NCs are possible. If the radius of all the NCs are smaller than $2r^*$ then growth is due to Ostwald ripening.

Since for QDs or NCs the surface to volume ratio is high, their surfaces play a larger role in determining their properties and behavior. In this regard, the author will discuss passivation of the surface against recombination of charge carriers.

2.6.1 Surface passivation and charge recombination

A broken covalent bond is known as a dangling bond. An atom in the interior of a piece of crystalline semiconductor material forms covalent bonds with neighboring atoms. An atom on the surface, however, will have one or more valence electrons not bonded to other atoms. If these valence electrons do not take part in a covalent bond with another material (for example hydrogen, oxygen etc.), then dangling bonds are formed. Dangling bonds give rise to localized defect states, providing sites for non-radiative recombination of an exciton, thus destroying the photoluminescent efficiency of the material and decreasing the photogenerated carrier lifetime. [91] In such a case, the material is said to be “unpassivated”. Therefore, it is important to find a method that is well suited for passivation of the NCs.

Electronic passivation of the NCs is provided by the ligands by terminating dangling bonds on the surface. Nanocrystal surfaces with dangling bonds can affect the emission efficiency as they support recombination of electron-hole pairs before the emission of the photon. Surface passivation with various organic ligands or epitaxial overcoating with a wide band-gap semiconductor [92] can be used to enable efficient radiative recombination of the intrinsic charge carriers within the NC. As an example, the passivating materials considered for Si NCs are SiO₂ and hydrogen, and the techniques to evaluate the passivation are x-ray photoelectron spectroscopy (XPS) and photoluminescence (PL).

Nanocrystals passivated with organic molecules often display low fluorescence quantum yield due to surface related trap states. To address this issue, surface passivation by epitaxial overcoating of a core NC with a large band-gap semiconductor has been developed for a number of NCs. In core/shell NCs, the shell passivates the surface trap states and also provides protection against any environmental changes. In core/shell structures, the band gap of the core is smaller than that of the shell so that the conduction and valence band edges of the core lie within the band gap of the shell which confines both electron and hole within the shell. For example, surface passivation of CdSe NCs by epitaxial overcoating with ZnS [93, 94], CdS [95] or ZnSe [96] gives strong band-edge fluorescence with a pronounced improvement in the fluorescence quantum yield. However, large band gap semiconductor with compatible lattice constants and crystal structure is required for good epitaxial overcoating of the NCs.

Recent studies show that both the type and quality of surface passivation are very important for the optical gain and light absorption. [97] In CdSe NC synthesis,

Kalyuzhny et al. used two surfactants (TOP and TOPO) to understand their interaction with the surface of the NCs. They found that TOP made a very good coordination to Se atoms on the surface of the NCs whereas TOPO did not. [98] This indicates that different ligands have different effects on the same NCs. Therefore, one has to choose some ligands with care. As indicated above, NCs surfaces promote recombination of charge carriers due to the high surface to volume ratio. Some of the recombination mechanisms can be controlled by passivating the NCs surfaces.

In solid state of semiconductor, recombination of electrons and holes is a process by which both carriers annihilate each other. Trap-assisted recombination occurs when an electron falls into the trap. If a trap presents a large target to the carrier, the recombination rate will be high. When the velocity of the carrier is high, it has more opportunity within a given time period to encounter a trap, and carrier lifetime is low. Also as trap site concentration increases, the probability of trapping increases; carrier life time is therefore inversely proportional to the trap concentration.[99]

Radiative recombination, in which the energy is emitted in the form of a photon, is much more efficient in direct band gap semiconductors than indirect band gap semiconductors since in the latter case phonon participation reduces the event probability. Experimental evidence shows that Auger recombination (AR) is the dominant mechanism of electron relaxation in semiconductor NCs photoexcited with two or more photons. For Auger recombination to happen, three carriers are required; for example, two electrons in conduction band and a hole in valence band. When the electron in the conduction band and the hole in valence band recombine, the emitted energy does not come out as heat or photon but is provided to the second electron in the conduction band. Auger

recombination therefore, depends on the preexistence of electrons in the conduction band, and hence is dependent on excitation and doping levels. [100] Because of the restrictions imposed by energy and momentum conservation, AR is inefficient in bulk semiconductors. However, due to enhanced Coulomb interactions and relaxation of momentum conservation, AR becomes efficient in NCs. [100] Because of their bandgap tunable properties, NCs have emerged as the new building blocks in solar cell devices. In NCs, charge carrier recombination can often be controlled, thus increasing the potential efficiency of the photovoltaics devices. The basic principles of photovoltaic devices are explained as following.

2.7 Basic operational principles of solar cells

The basic principle of a solar cell is based on the photovoltaic effect which is the creation of voltage or electric current in a material upon exposure to light. To understand a solar cell, it is necessary to understand the PN junction which is explained in following paragraph.

2.7.1 The PN junction

When an n-type and a p-type semiconductor materials are brought together, a very large difference in free electron and free hole concentration between these semiconductors causes a diffusion of electrons from the n-type material across the junction into p-type material and holes from the p-type material across the junction into n-type material. Due to this diffusion process, the region close to the junction becomes depleted of mobile charge carriers. This depleted region is called the space-charge region,

or depletion region, and the regions outside the depletion region are called the quasi-neutral regions. The opposite charge on the free carriers at the two sides of the junction yields an internal electric field. This depleted region is called a PN junction.

A PN junction has rectifying (diode) current-voltage characteristics as shown in Figure 2-11. The PN junction is the basic structure of a solar cell, a light emitting diode, and diode laser.

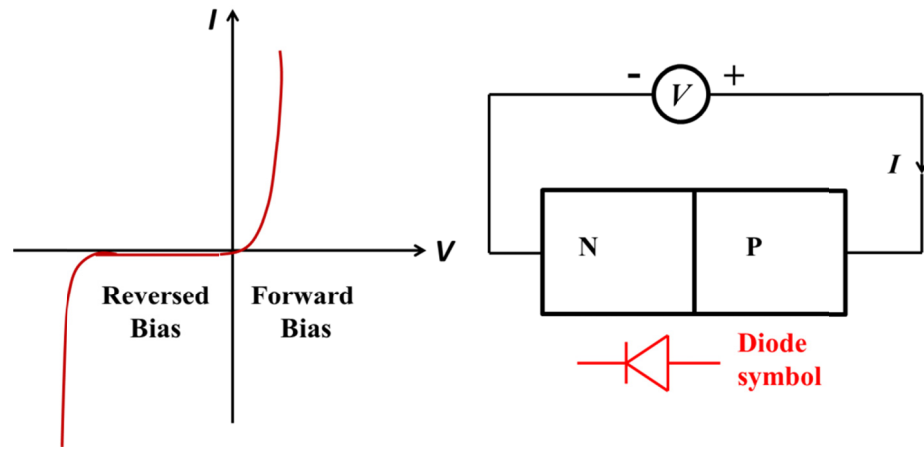


Figure 2-11. (a) The IV characteristics of a PN junction, and (b) representation of a diode.

The presence of the internal electric field in the PN junction indicates that there is an electrostatic potential difference across the space-charge region. This voltage difference is known as the built-in potential and is denoted by ϕ_{bi} . The study of a PN junction provides information of various parameters such as built in potential, depletion width, and capacitance.[101] The built in potential depends on the donor (N_d) and acceptor (N_a) concentrations and intrinsic carrier concentration n_i as given in equation (2.10).

$$\phi_{bi} = \frac{k_B T}{q} \ln \frac{N_d N_a}{n_i^2} \quad (2.10)$$

The depletion width depends on the built in potential and is given in equation (2.11)

$$W_{dep} = \sqrt{\frac{2\epsilon_s (\phi_{bi} + V_r)}{q} \left(\frac{1}{N_a} + \frac{1}{N_d} \right)} \quad (2.11)$$

where ϵ_s is the dielectric constant of the semiconductor, V_r is the reverse bias

A PN junction can be considered as a parallel-plate capacitor with capacitance

$$C_{dep} = A \frac{\epsilon_s}{W_{dep}} \quad (2.12)$$

When light impinges on a solar cell, most of the photons are absorbed within the depletion region and within the neutral p-side and generate electron hole pairs in those regions. The electron-hole pairs photogenerated within the depletion region are separated by the built in electric field. The electron drifts and reaches to the other end of n-type layer and hole drifts and reaches to the other end of p-type layer. When electrons and holes are collected at the end of n-type and p-type semiconductors, an open circuit voltage is developed between the end of the device with p-side positive and n-side negative. When external load is connected, the excess electrons travel from the n-type side through the external circuit and recombine with excess holes in the p-type layer. Electron-hole pairs photogenerated in the neutral p-side of the semiconductor diffuse around as they do not experience electric field effect. If these carriers diffuse to the depletion region before recombining, the internal electric field separates them. Under illumination, when the two ends of the device are short circuited, the photo-generated current is called “short circuit current” (I_{sc}). Similarly, under illumination, when the two

ends of a solar cell are not connected to the external circuit, no current flows inside the PN junction but the voltage across the two end is maximum and is known as open circuit voltage (V_{OC}).

2.7.2 Solar cell external parameters

The main parameters that are used to characterize the performance of a solar cell are the short circuit current density, the open circuit voltage, fill-factor and peak power. Using these parameters, the photo-conversion efficiency can be calculated. Figure 2-12 shows the current density as a function of voltage for a solar cell in the dark and under illumination.

Open circuit voltage (V_{OC})

The open circuit voltage (V_{OC}) gives the maximum voltage that a solar cell can generate (at open circuit). It is defined in an ideal solar cell as the difference between the quasi Fermi levels of electrons in the n-type material and holes in the p-type material. In the case of a non0-ideal diode model, the V_{OC} is given by[101],

$$V_{OC} = \frac{nk_B T}{q} \ln\left(\frac{J_{ph}}{J_o} + 1\right) \quad (2.13)$$

Where n is the ideality factor with values typically between 1 and 2, J_{ph} and J_o are the photo-generated current density and reverse saturation current density respectively

Short circuit current density (J_{SC})

The short circuit current density (J_{SC}) represents the maximum number of photogenerated carriers per unit area extracted from a solar cell, at short circuit condition, and depends on the intensity and spectrum of illumination, the spectral absorbance of the

solar cell's active layers, and on recombination losses in the solar cell. The current density in the conventional solar cell can be expressed as [101]

$$J = J_o \left(\exp\left(\frac{qV}{nk_B T}\right) - 1 \right) - J_{ph} \quad (2.14)$$

At short-circuit current condition, $V = 0$, and $J = J_{SC} = -J_{ph}$

Fill factor

In Figure 2-12, the dark current shows rectification characteristic of the diode nature of a solar cell. Under illumination photo generated carriers shift the J-V curve downward into the fourth quadrant (the J-V curve can also be plotted with the sign of the current inverted, such that the power generation under illumination occurs in the first quadrant). The fill factor (FF) is given by

$$FF = \frac{P_{max}}{J_{sc} V_{oc}} \quad (2.15)$$

where, P_{max} is the maximum power point (operating point of the solar cell), J_{SC} is the short circuit current and V_{OC} is the open circuit voltage. FF, in conjunction with V_{OC} and J_{SC} , determines the maximum power from a solar cell. It is a measure of the squareness of the solar cell's J-V response and depends on many qualities of the device being correct.

Efficiency

The power conversion efficiency of a solar cell is given by

$$PCE = \frac{V_{max} J_{max}}{P_{inc}} = \frac{V_{oc} J_{sc} FF}{P_{inc}} \quad (2.16)$$

In real solar cells, series (R_S) and shunt (R_{Sh}) resistances also need to be considered.

Series resistance reduces J_{SC} but has little effect on V_{OC} while shunt resistance has little

effect on J_{SC} but reduces V_{OC} . R_{Sh} is mainly due to the pinholes or defect states in the absorbing layer and R_S is the sum of film resistance, electrode resistance and contact resistance.

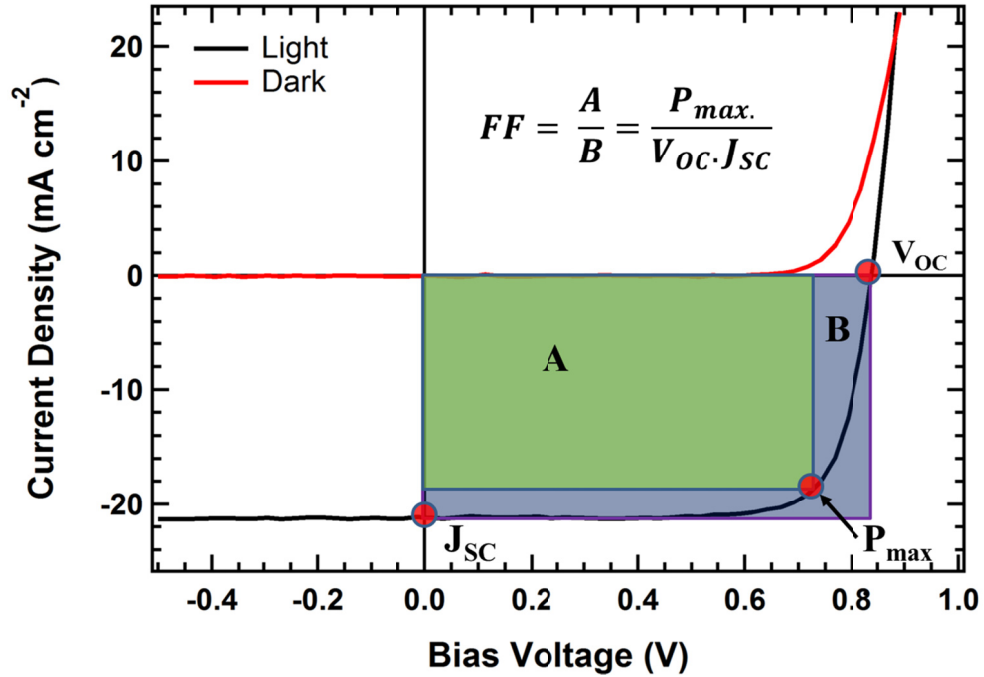


Figure 2-12. J-V characteristic of a solar cell in the dark and under 1-Sun illumination. The area of the green rectangle represents the maximum power output, the product of the optimally chosen operating current and voltage.

2.8 Conclusions

Relative positions of the top of the valence band and bottom of the conduction band in k space determine the type of semiconductor. In a direct band gap semiconductor such as CdTe, the absorption coefficient reveals a sudden increase as the photon energy exceeds the band gap energy, E_g . In an indirect band gap semiconductor such as Si, since photon absorption must be accompanied by phonon emission or absorption, the

absorption coefficient rises only slowly as the photon energy exceeds the indirect band gap energy. Lead chalcogenides are direct band gap semiconductors and possess some unusual electronic and structural properties relative to the more conventional II-VI and III-V compounds and alloys. Because of the high atomic number of the Pb, in lead chalcogenides, relativistic effects make valence orbital chemically inactive and transform this $s^2 p^2$ orbital into p^2 orbital. Both the valence band maximum and conduction band minimum states occur at the L point in Brillouin zone, contrary to the case in II-VI and III-V materials. Their band gap does not decrease monotonically with anion's atomic number unlike in II-VI semiconductors. They have rock salt crystal structure and have twofold degenerate valence band maxima and twofold degenerate conduction band minima at the L point in contrast to the a III-V compounds. Rock salt structured materials possess more ionic and less covalent band structure.

Iron pyrite is the most abundant sulfur mineral and also belongs to rock salt crystal structure with the arrangement of Fe^{2+} and S_2^{2-} ions. In FeS_2 , each Fe atom is surrounded by 6 S atoms while each S atom is coordinated with one S atom and 3 Fe atoms. The σ -orbital overlap is greater than π -orbital in FeS_2 , bonding of σ type is stronger than any π type. The implication of this structure is that FeS_2 remains stable for a long time. Since the lead salt PbS and sulphur mineral FeS_2 studied here are nanocrystalline, their optical and electronic properties are somewhat different than their bulk counterpart. The density of states of these NCs is discrete. Since charge particles are confined in small volume, their analysis is possible by particle in box model. In PbS QDs, the size of the dot is smaller than exciton's Bohr radius, and quantum confinement is very

strong. These nanoparticles are synthesized colloiddally in solution based methods where some particular organic molecules are used as capping ligands and help to determine the size and shape of the nanoparticles. These nanoparticles are utilized in the fabrication of solar cells based on the concept of P-N junction, built in potential, depletion width and so on. Photovoltaic solar cells convert sun light into electricity and the efficiency of a cell, or device, depends on several parameters such as open circuit voltage, short circuit current density, and fill factor.

Chapter 3

Synthesis, characterization and photovoltaic application of PbS quantum dots

3.1 Introduction

Lead chalcogenide quantum dots (QDs) have been extensively explored for applications in photovoltaic devices [12, 14, 43, 102-106], photo-detectors [107-109], telecommunications [110], light emitting diodes [111], and thermoelectric devices.[112] In particular, PbS QDs are considered as prime candidates for the photo-active materials in photovoltaics and photo-detectors. As light absorbers, PbS colloidal QDs possess size-tunable band gaps, and strong oscillator strength near the band edge. [62, 113] Because of their size-dependent electronic structure, one can design PV devices with QD energy levels ideally-positioned relative to the bandedge states of wide bandgap semiconductors such as ZnO or TiO₂. [102, 114-116] When photons are absorbed in these PbS-QD solar cells, electron-hole pairs photo-generated in the QD layer charge-separate such that electrons transfer to the wide band gap semiconductor and holes transfer through the QD layer to the back contact. A number of solar energy conversion strategies are being explored for PbS-QDs, [14, 104, 117] and the field of PbS-QD solar cells has

demonstrated a bright pathway to the future with the present record power conversion efficiency of 8.55%. [118]

In this chapter, the author reports on (a) synthesis and film fabrication of PbS-QDs (b) characterization of QD solutions and thin films, (c) fabrication of QD Schottky junction and heterojunction solar cells, including results of the dependence of performance on QD size and window layer thickness for ZnO/PbS-QD heterojunction solar cells, and (d) measurements and observations showing that continuous illumination improved the performance of heterojunction solar cells based on CdS/PbS-QD or ZnO/PbS-QD junctions, and of Schottky junction solar cells. The maximum power conversion efficiency obtained here from these devices exceeds 4%.

3.2 Experimental

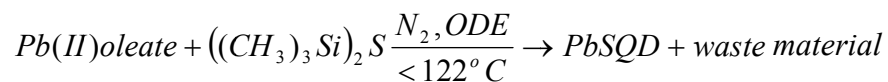
3.2.1 Materials

Oleic acid (OA), octadecene (ODE, >95%), hexamethyldisilal-thiane ((TMS)₂S), lead(II) oxide (PbO, 99.9+%), ethyl alcohol (EtOH, absolute, anhydrous), acetonitrile (99.8% anhydrous), hexane (C₆H₁₄, anhydrous, 95.0%), 1,2 ethanedithiol (98.0%). All chemicals were purchased from Sigma Aldrich except EtOH and OA. EtOH was obtained from chemistry supply store, at the University of Toledo and OA from Fisher Scientific.

3.2.2 PbS QD synthesis

PbS QDs were synthesized according to a previously published method [15, 119] under an inert atmosphere using standard Schlenk line techniques as shown in Figure 3-1. The reaction is carried out in a three neck flask, the middle neck of which is connected to the Schlenk line. The remaining two necks are sealed with rubber septa where one neck

serves for the measurement of the temperature inside the flask and the other for the injection of reactants. In general, the PbS QD synthesis is summarized as follows:



where lead (II) oleate is also written as LEAD OLEATE and is $C_{36}H_{66}O_4Pb$. In a typical synthesis, 2 mmol of PbO (0.446 g), 39 mmol of octadecene (ODE, 12.7 mL), and 4 mmol of oleic acid (OA, 1.27 mL) are heated to 120 – 122 °C under N_2 in a 100 mL round bottom three neck flask. The mixture is continuously stirred with a magnetic stirrer bar. The mixture is heated until all the PbO is dissolved and Pb(II) oleate is formed typically within 45 minutes.

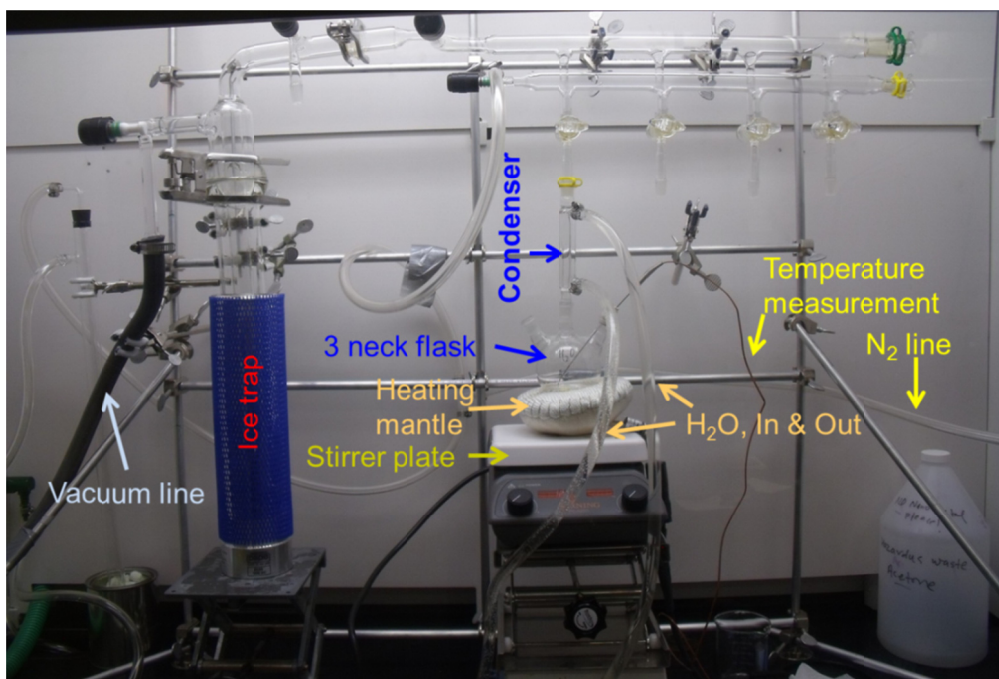


Figure 3-1. Photograph of a Schlenk line showing its various parts. Syntheses of QDs or NCs are performed in a nitrogen environment.

In a nitrogen atmosphere glove box, 1 mmol of Bis(trimethylsilyl) sulfide [hexamethyldisilathiane, TMS_2S (210 μL)] is dissolved in 12.4 mmol (4 mL) of nitrogen purged ODE. The mixture is loaded in a syringe with a needle and carefully transferred to the Schlenk line with the help of zip lock bag. The heating mantle is removed and the mixture is injected immediately at $\sim 110^\circ\text{C}$ into a three neck flask. A rapid nucleation event takes place after the injection of the S precursor into the Pb-oleate mixture which is evidenced by an immediate brown color change in the reaction vessel. After nucleation, growth of the NC begins by consuming remaining monomer species into the nucleated seeds. Purification of the NC so obtained is done in air using hexane and ethanol, once the temperature of the mixture drops down to room temperature. The purpose of purification is to separate QDs from other products (waste product in second equation) that are formed during the reaction. After purification, QDs are dried under nitrogen and utilized for experimental purposes.

3.3 Experimental results and discussion

3.3.1 Quantum dots synthesis

Absorbance spectra (optical density, OD) were measured using a Perkin Elmer model Lambda 1050, UV/VIS/NIR spectrophotometer. Due to the quantum confinement effect decreasing the particle size results in a hypsochromic shift of the absorption onset. A relatively sharp absorption feature near the absorption onset corresponds to the excitonic peak and gives the band gap of the QDs. The first exciton peak's form and width enable one to deduce the size distribution of the QDs. Room temperature

absorbance spectra of some selected PbS QD samples dispersed in hexane are shown in Figure 3-2(a). The path length of the quartz sample cuvette used to measure absorbance was 2 mm. These QDs were capped with oleic acid, and the QD average diameters were calculated using empirical relations derived elsewhere [62, 120]. The first exciton energy (band gap energy) was found to decrease when the diameter of the QDs was increased as shown in Figure 3-3(a). The size of the QDs depends on several parameters mainly the amount of oleic acid, and the injection temperature of S precursor. It also depends on the amount of lead precursor, and the amount of ODE. In general, to synthesize QDs of various sizes only one parameter is varied. For PbS QDs with ≥ 900 nm first exciton peak, amount of oleic acid is varied and all the other parameters are kept constant. The average QD diameter depends directly on the amount of OA, i.e. larger the concentration of OA, the larger the diameter of the product QDs. Similarly, to synthesize QDs with < 900 nm first exciton peak wavelength, only the S-source injection temperature is varied. When S-source is injected at lower temperature (lower than 220 °C), smaller size dots are obtained. In Figure 3-2(a), sizes of bottom two spectra were controlled by injection temperature whereas the sizes of top two were controlled by amount of OA respectively.

The organic surfactant molecules play very important roles in the synthesis of the NCs. Surfactant helps to solubilize and disperse the NCs in organic solvents. They control the speed of the reaction during synthesis especially influence the reactivity of the monomer species. Surfactant molecules bind and unbind dynamically on the surface of the growing crystals. When the molecule breaks the bond with NCs, new atomic species can be incorporated into the NCs and crystal growth takes place. When the concentration of oleic acid is high, the monomer reactivity decreases which decreases the number of

discrete nucleation events. This finally increases the size of the NCs. When the concentration of oleic acid is reduced, (sufficient to provide ligand stabilization) the reactivity of Pb monomers increases. In this case, the number of nucleation events increases which ultimately provides smaller size NCs. For size-monodisperse NCs, the nucleation of all the particles must occur rapidly and instantaneously at the same time. Another criterion for monodisperse particles is that the nucleation and growth process should not occur at the same time. In other words, nucleation should stop before significant growth begins.

At higher temperatures, growth of nucleated particles is higher because reaction rates are faster. This also increases crystallinity of the NCs. At higher temperatures, the thermal energy of each atom is high. In this case, each atom rapidly finds energetically favorable bonding positions in the crystal lattice. Growth of NCs at higher temperature for the same time duration is always higher than the growth of same NC at lower temperature at the same time.

Fourier Transform Photoluminescence Excitation Spectroscopy (FT-PLE) was used to take steady state photoluminescence (PL) spectra of QD solution dispersed in hexane. The instrumental set up of FT-PLE is very similar to the one explained by McDonald *et al.* [121]. The room temperature steady state PL and absorbance spectra (OD) of PbS QDs with the first exciton peak at 792 nm are shown in Figure 3-2(b). The PL peak is normalized to the same excitonic peak height to compare the spectral bandwidth. The PL peak has Gaussian shape with a full width at half maximum (FWHM) comparable to the energy width of the first exciton absorption peak, indicating that the emission comes from well-defined single quantum states rather than an ensemble of trap

states (trapped state emission from a QD solution typically has FWHM significantly larger than the FWHM of first exciton absorption peak).[122] The energy of any photon emitted via photoluminescence is less than the energy of the originally absorbed photon due to the energy loss to internal conversion. The energy difference between the first exciton absorption peak and the PL peak is called the Stokes shift. The Stokes shift is fundamental to the sensitivity of PL technique because it allows emitted photons to be detected against a low background, isolated from the excitation photons. The Stokes shift for this particular QD solution is ~ 147 nm (0.244 eV). The Stokes shift for various sizes of QDs were calculated by a similar method and found to follow a linear relationship with the first exciton peaks as shown in Figure 3-3(b). [123]

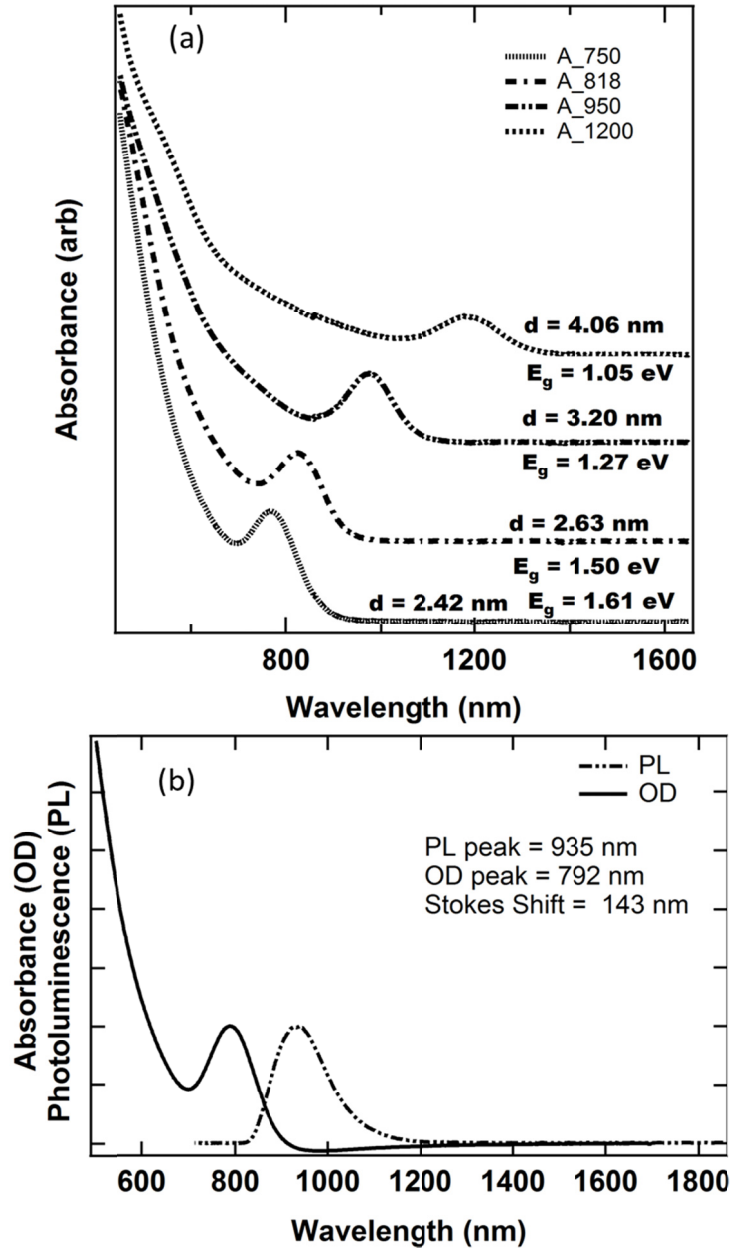


Figure 3-2. (a) Absorbance with respect to wavelength (nm) for PbS QD samples dispersed in hexane; (b) Absorbance (OD) and photoluminescence (PL) spectra of a PbS-QD solution in hexane.

It is clear from Figure 3-3(a) that in PbS-QDs the absorption band edge depends on QD size, with the band edge shifting to higher energies as the size of the QD

decreases. Figure 3-3(b) shows variation of the Stokes shift as a function of the absorption band edge peak. In Figure 3-3(b), it is seen that the Stokes shift increases linearly as the band edge increases in energy. This implies that as the size of the PbS QD increases, the Stokes shift decreases. The large Stokes shift observed in PbS QDs was explained by the presence of a trap state.[124] In oleic acid capped PbS QDs, oxygen atoms bind only to the lead atoms at the surface leaving sulfur atoms unpassivated, which acts as shallow hole traps.[125] The surface state is comprised of unpassivated sulfur atoms and lies more than 370 meV below the bulk semiconductor valence band-edge. [124]Zhang and Jiang demonstrate that the large Stokes shift in PbS QD films is due to the confinement dependent below-gap state (BGS). [126] This BGS belongs to certain trap state (vacancies, impurities or adsorbates at the surface cause the formation of trap states) and is responsible for the Stokes shift. In such trap states, photoexcited electron can drop or the photoexcited hole can ‘float’.[127] An et al. reported band-edge energy levels splitting due to the high quantum confinement in PbSe QDs. [128]As the calculated Stokes shift here is large, this phenomenon cannot be ruled out for PbS QDs as well. This also explains why Stokes shifts increases as the size of the QDs decreases. For smaller dots, the separation between energy states is greater than the thermal carrier energies, which increases the life time of the excited electron. Therefore, by reducing the size of the QDs, one can increase the life time of the exciton. For all these QDs, relatively large Stokes shifts were present which increased for decreased dot size.

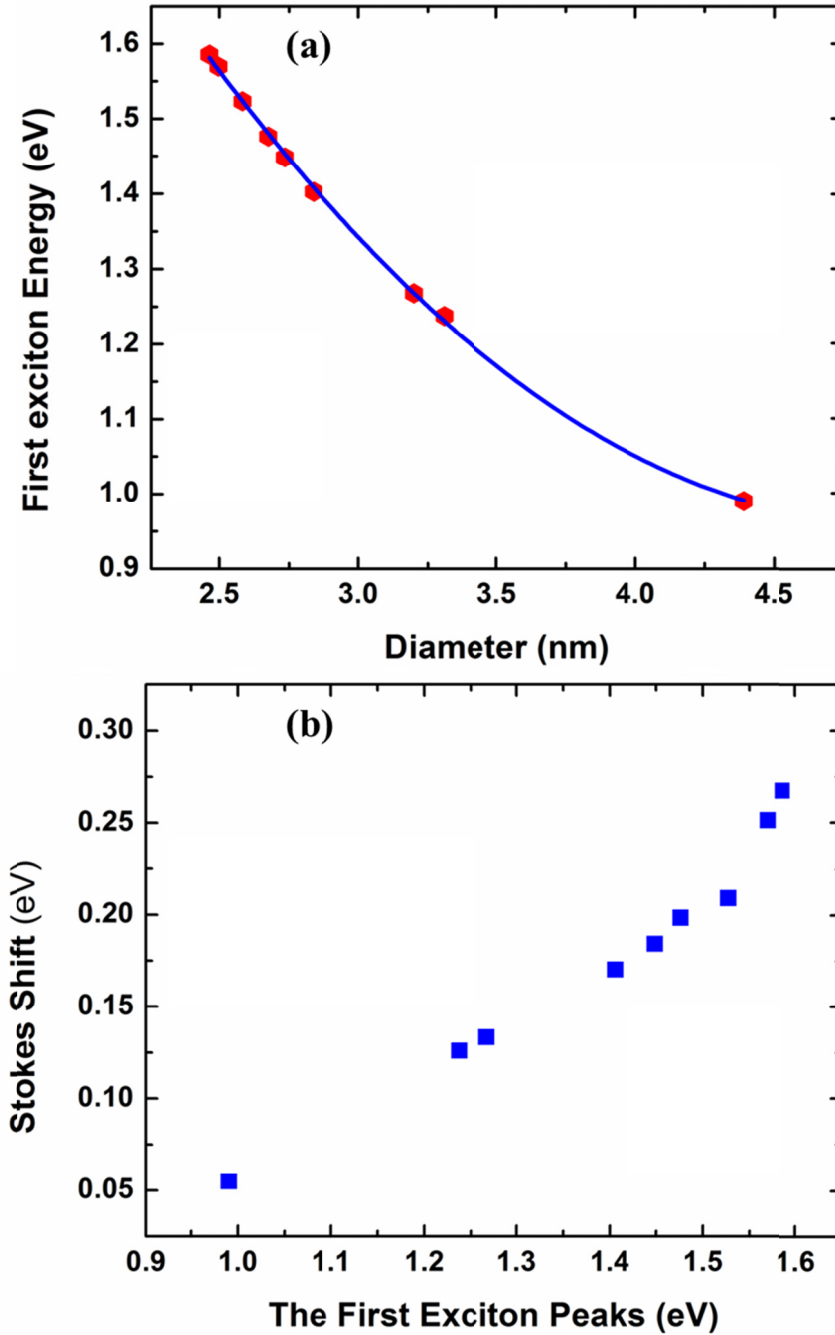


Figure 3-3. (a) Dependence of first exciton energy of QDs with size of the dots (b) Stokes shifts of various size QDs relative to the first exciton peaks (both in terms of energy in eV).

3.3.2 PbS QDs film fabrication

PbS QD film preparation utilized the layer-by-layer (LbL) deposition method reported elsewhere,[129] relying on 1,2-ethanedithiol (EDT) to achieve thin films of electronically coupled QDs. During this process, long chain hydrocarbon molecules (OA) are replaced by shorter ones (EDT), in a process called ligand exchange. Possible ligand exchange chemistry while making LbL QD films is provided in Figure 3-4.[129] For the preparation of QD films, two beakers are required; one contains the QD solution dispersed in an organic solvent such as hexane, and another contains 1 mmol EDT solution in acetonitrile. The substrate is first dipped into the QD solution with the help of tweezers such that a layer of QD film is adhered on the substrate. The substrate is removed from the QD solution slowly and uniformly, and allowed to dry. It is then dipped into EDT solution to effect a ligand exchange between OA and EDT as shown in Figure 3-4. This two-step process completes one cycle. A certain number of cycles are repeated depending on the thickness of the QD film needed. Rotation of the substrate by 90° after each cycle improves the uniformity of the final film. Hand dipping is a tedious job, with some risk of inhalation exposure to the solvents. In addition, the speed of the substrate going in and out of the QD solution is not constant, so that particle adhesion varies. This variation will ultimately bring thickness non-uniformity and surface roughness. For the better quality of the film, a computer-controlled dip coater (Figure 3-5) is used. The dip-coater offers quantitative control of the substrate dipping speed, though it does not allow for substrate rotation after every cycle; therefore automated dip-

coating yields thickness variation because of surface tension and the gravitational force on the drying solution.

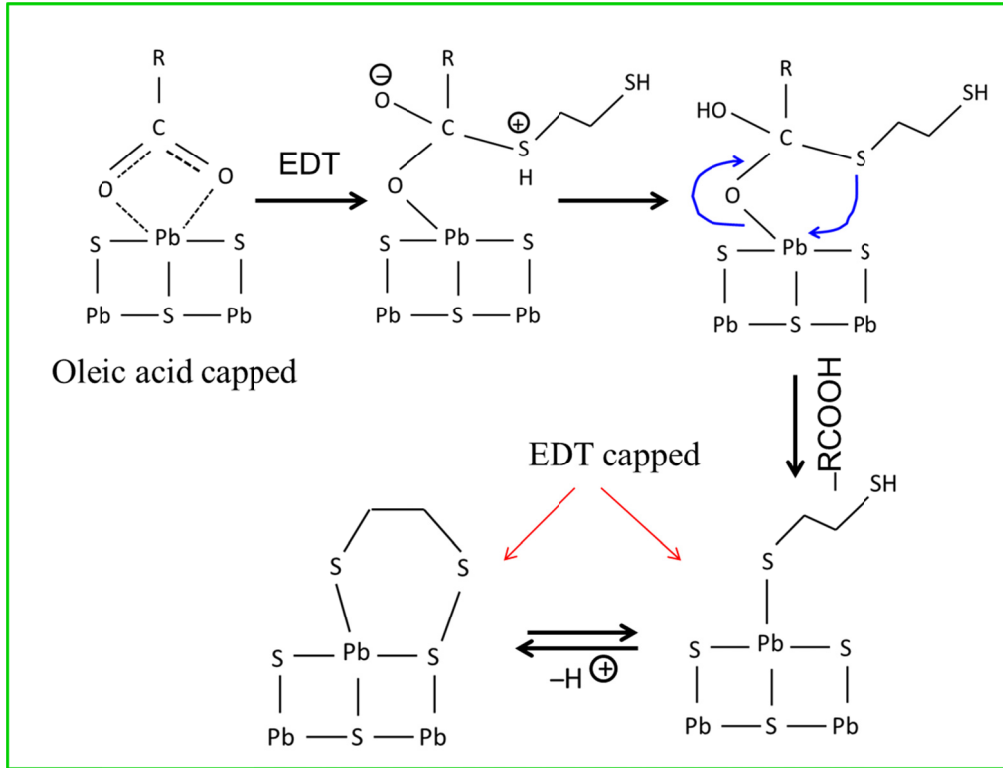


Figure 3-4. Possible ligand exchange procedure between oleic acid and 1,2-ethanedithiol (EDT) when making PbS QD film.

The dip coater that has been using here is from NIMA Technology and is shown in Figure 3-5(b). Dip coating technique is used for solution based method to fabricate thin films on substrates. In the coating process, the substrate is partially dipped into a beaker containing the solution to be coated and the film is withdrawn in air to dry. This process is repeated several times as necessary to prepare a film of the desired thickness. The machine is controlled by LabVIEW programming software where different dipping

parameters can be chosen such as dipping time, speed of substrate moving up and down, number of cycles and some other.

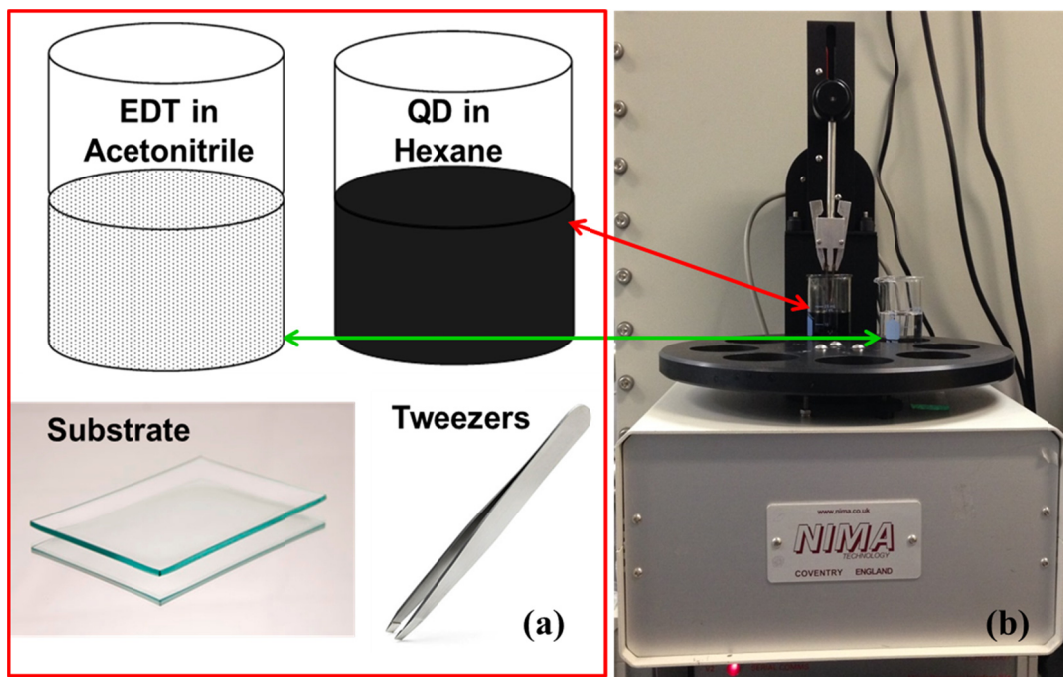


Figure 3-5. Layer by layer dip coating process using (a) hand dipping (b) dip coater

Due to the surfactant assisted stabilization of QDs in solution, dip coating has been considered one of the best techniques to form a uniform layer on a substrate. Convective assembly in the meniscus and direct adsorption on the substrate from the solution are considered two pathways for the QD-layer formation during the dip coating process.[130] Due to the solvent evaporation, there is a constant upward flow of QDs toward the liquid meniscus. When the substrate is pulled outward with a controlled withdrawing speed, QDs at the meniscus adhere to form an order layer by lateral capillary action. [131] Evaporation rate of solvent, substrate withdrawing speed, and concentration of the solution are the critical factors determining the order layer of film on

the substrate. Quantum dot layer formation can also take place due to the interaction between the particles and substrate in the bulk suspension of QDs. EDT capped QD film adhesion is found stronger in some substrates such as ITO coated glass or ZnO coated glass than bare glass substrates. Adsorption of QDs on the substrate is also determined by the type and amount of surfactants that cap the QDs. Films of oleic acid capped QDs do not adhere as strongly to the substrate than do EDT-treated QD films. This is caused by the adsorption to the substrate of these long chain molecules prior to the particles which reduce the interaction energy for QDs adsorption. Due to the strong interaction between the substrate and the organic molecules, thin films so prepared do not dry efficiently.

Fourier transform infrared (FTIR) spectra of a drop cast film before and after the ligand exchange are shown in Figure 3-6(a). The C-H intensity of treated films (dipped in 1 minute in EDT) is 12 - 14% of the C-H intensity of untreated films. Quantitative exchange of OA by EDT is expected, which would correlate with an ~88% decrease in the concentration of C-H bonds (33 C-H bonds in OA vs. 4 C-H bonds in EDT); the C-H bond density can be measured by infrared (vibrational mode) absorption spectroscopy. Also, following substitution of OA by EDT, the adsorbed EDT exists as ethanedithiolate bound in a bidentate fashion either on single QDs or between QDs; therefore, S-H vibrational peaks are no longer seen in the spectrum.[129] Bidentate ligand is one that can make two bonds to a metal ion. The first exciton absorption peak of the QD film is red shifted relative to QDs in solution (see Figure 3-6(b)) due to the increased dielectric constant and substantial electronic coupling in EDT-treated films.[129, 132] The QDs move closer together, as a result of replacing OA by EDT due to the substantial volume reduction and produces cracking in the film. Cause of volume reduction is due to the very

short length of EDT molecule, ~12.5% of OA(1.97 nm vs. 0.25 nm). [133] These cracks are filled by successive deposition layers as required to prepare 150 to 200 nm thick QD films for photovoltaic application.

To calculate the absorbance spectra for the films of QDs, first transmission and reflection percentages were measured using UV/VIS/NIR spectrophotometer. Then absorbance spectra were calculated using equations (3.1) or (3.2).

$$A = \frac{1}{2.3} \left(-\ln \frac{T}{1-R} \right) \quad (3.1)$$

$$A = 2 - \log_{10}(T\% + R\%) \quad (3.2)$$

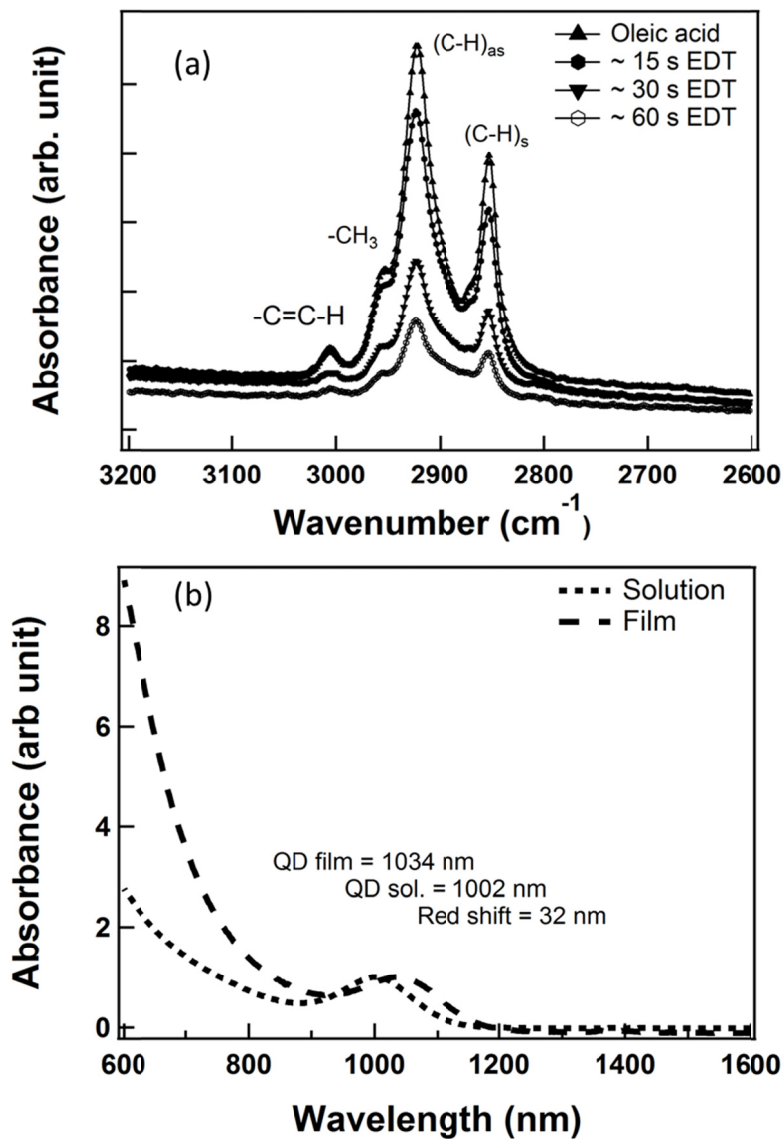


Figure 3-6. (a) C-H vibrational modes of molecule in OA and EDT treated films. It is seen in figure that soaking of QD film in 1 mmol EDT solution in acetonitrile for one minute leaves only ~14% of its original C-H intensity. (b) Red shift in the first exciton peak of the absorbance spectra from the QD film vs. solution.

3.3.3 Photovoltaic device fabrication

For heterojunction solar cells, either unintentionally doped ZnO, or CdS, was deposited by sputtering method to serve as the n-type window layer. Top contacts were deposited by electron beam/ thermal evaporation method through the shadow mask. For Schottky junction devices, aluminum (Al) was used as a back contact and for the heterojunction devices gold (Au) was used as a back contact. Current voltage characteristics were measured using a Keithley 2440 source meter and Newport 91195A-1000 solar simulator. The EQE spectrum was obtained using a PV Measurements model IVQE8-C system for measuring spectral response.

3.3.3.1 Schottky junction solar cells

Figure 3-7 shows the device structure of Schottky solar cells and the corresponding equilibrium band diagram. In the device architecture, a ~150 nm thick QD film is deposited onto soda-lime glass coated with a transparent conducting layer of pattern indium-doped tin oxide (ITO), in a superstrate configuration; light is incident through the glass and ITO. The shape of pattern ITO and the corresponding mask to get six cells each with an effective area of 0.0975 cm^2 are given in Figure 3-8. Only the six cells (labeled as cell 1, cell 2 ...) available at the center of the substrate are used and remaining six cells at the edge of substrate are neglected. The mask is positioned exactly the same shape (Figure 3-8b) onto the substrate positioned exactly the same shape (Figure 3-8a) to define the cell area. As a back contact, metals with very low work function such as aluminum are chosen.[12, 43] Other groups have utilized Ca, Mg or a

thin layer of LiF before depositing Al, which reduces the effective work function of Al. [134, 135] Luther et al. in reference [43] established an empirical relationship between a Schottky device open circuit voltage and the PbS QD bandgap as

$$V_{OC} \approx 0.49 \left(\frac{E_g}{e} \right) - 0.253V, \text{ where } e \text{ is the electron's charge.}$$

The V_{OC} of a Schottky solar cell depends linearly on the barrier height, where the barrier height is expressed by the relation $e\Phi_B = E_g - e(\Phi_m - \chi)$. Here Φ_m denotes the work function of metal, and χ is the electron affinity of the QD thin film. The barrier height tends to increase for smaller QDs.[116] From these relations, it can be seen that V_{OC} of a Schottky solar cell is less than half of bandgap of the QD. The V_{OC} also depends on the work function of a metal back contact; smaller the metal work function, higher will be barrier height and higher will be the V_{OC} .

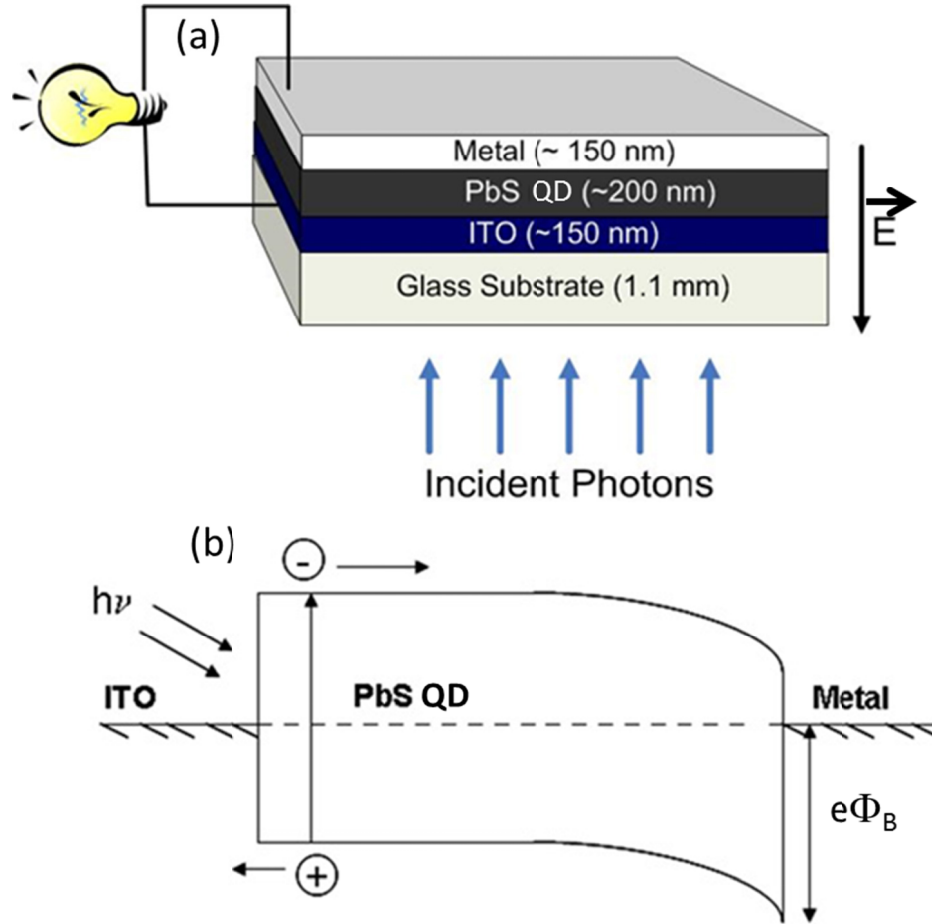


Figure 3-7. (a) Device structure of a PbS-QD thin film Schottky junction solar cell (b) Band diagram in equilibrium with metal work function

Band bending occurs at the interface between the QDs and the evaporated metal contact as shown in figure 3-7(b) due to the difference between the metal work function and the electron affinity of the semiconductor. At the interface of metal/semiconductor, a Schottky junction (potential barrier) is developed due to the diffusion of free electrons from the metal to the p-type semiconductor. The resulting electric field drives the free carriers photogenerated in the PbS-QD layer (e-h pairs emitted at or near the depletion width where internal electric field's effect is realized) to their respective electrodes:

electrons are extracted through the back contact, and holes are extracted through the transparent conducting ITO contact. The e-h pairs generated away from the depletion width where no electric field is present may be collected through diffusion. There are two disadvantages of Schottky junction PbS-QD solar cells: (1) the V_{OC} depends on the QD bandgap energy and (2) electrons generated near the front contact must travel diffusively across the absorber region to reach the space charge region near the metal contact. In the latter case, there is a chance of recombination of carriers, which does not favor thick PbS-QD absorber layers.

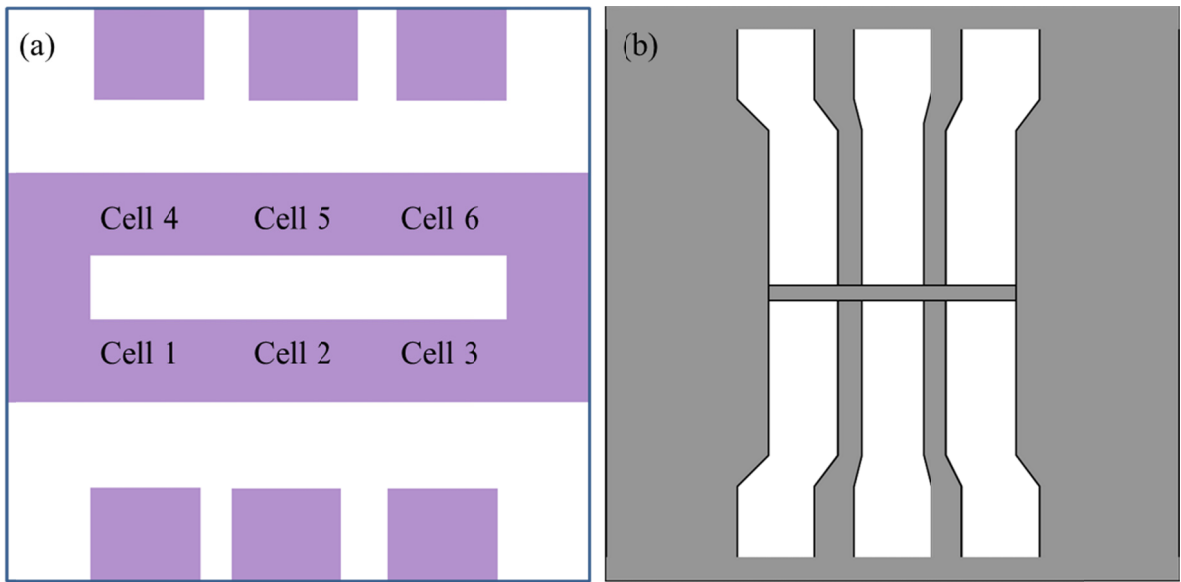


Figure 3-8. (a) Pattern ITO coated glass substrate, (b) metal mask to deposit back contact

The current voltage characteristics of a typical Schottky junction device, in the dark and under 100 mW cm^{-2} simulated AM1.5G sunlight, are reported in Figure 3-9. This PbS QD sample with solution first exciton peak at 890 nm, was used as the absorbing layer, ITO was the front contact, and aluminum ($\sim 100 \text{ nm}$) as the back contact.

Under standard AM1.5G illumination, this device showed a V_{OC} of 347 mV, J_{SC} of 11.0 mA cm^{-2} , and a FF of 39.4 %, yielding an overall device conversion efficiency (η) of 1.5%. In Figure 3-10, external quantum efficiency (EQE) of the cell, shown in Figure 3-9, is displayed. At short wavelength (~ 500 nm), the EQE reaches to $\sim 40\%$. At longer wavelengths, the distinctive excitonic feature is resolved and at the first exciton peak the EQE is $\sim 14\%$.

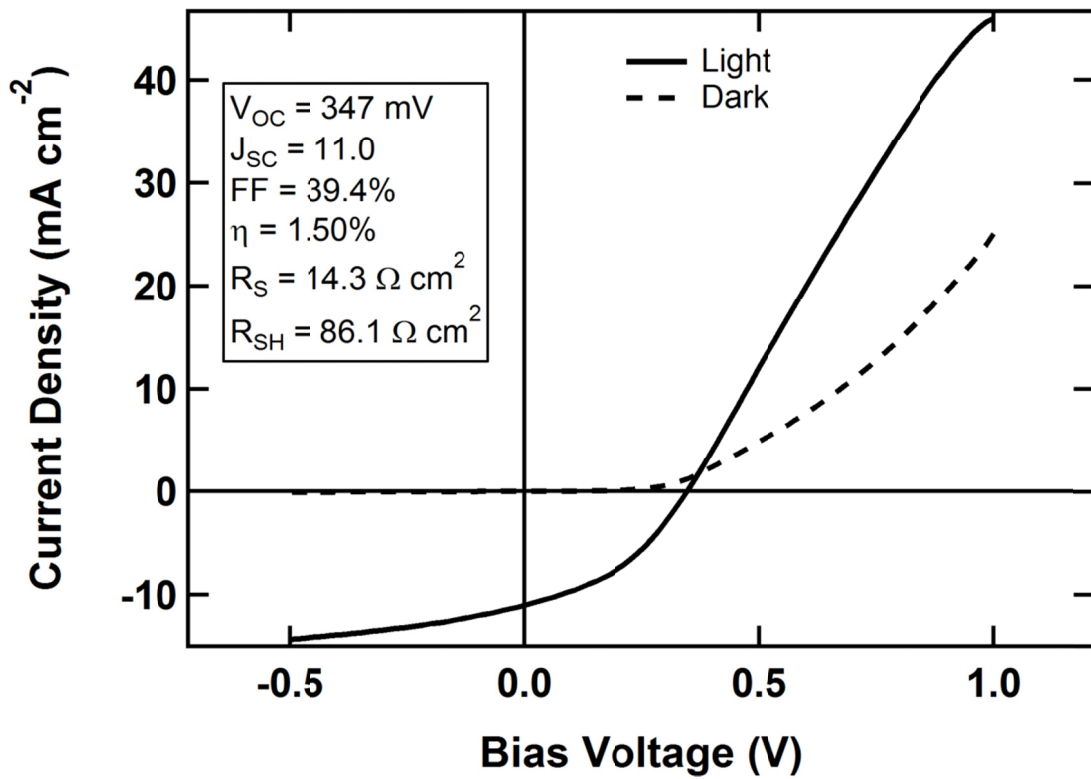


Figure 3-9. Current voltage characteristics of Schottky junction solar cells. PbS-QD with the first exciton peak at 890 nm has been used to make these devices. Solid line represents light measurement and dash line represents dark measurement. R_S and R_{SH} are series and shunt resistances of the device.

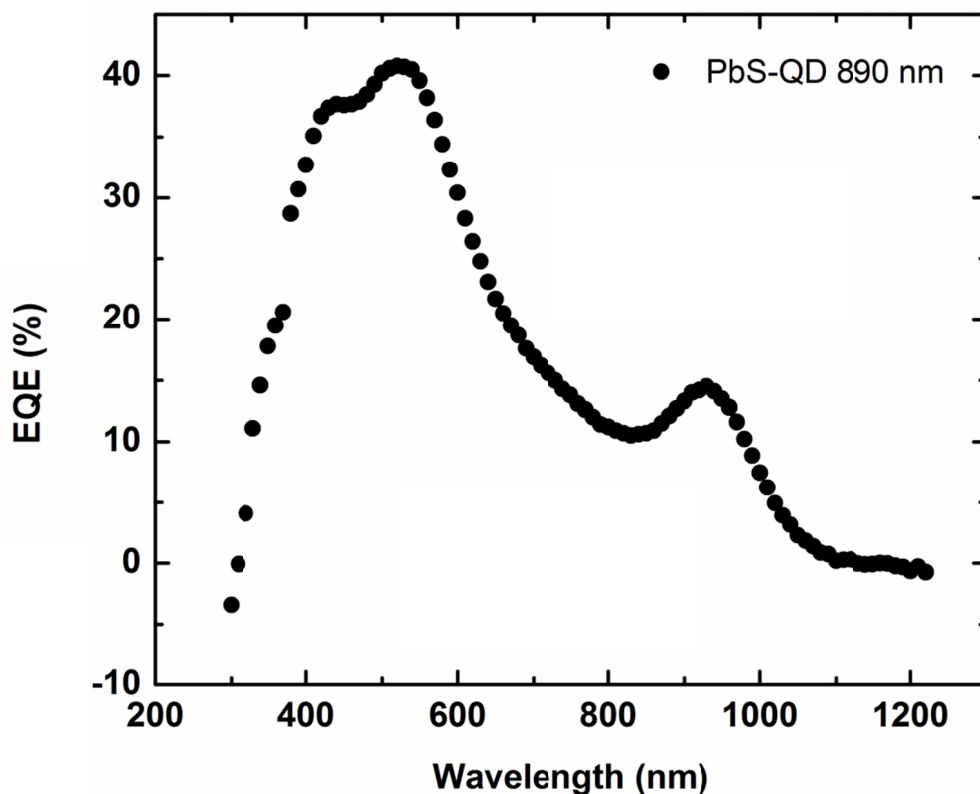


Figure 3-10. External quantum efficiency of Schottky junction solar cells is shown. For this device, PbS QDs of ~ 3 nm diameter, corresponding to the first exciton absorption peak at 890 nm, were used. The 6 cells in the device showed nearly uniform performance.

Performance parameters of three different Schottky devices are summarized in Table 3.1, and their corresponding J-V curves are given in Figure 3-11. For this, PbS QDs of band gaps 1.61 eV, 1.40 eV and 1.25 eV were tested as absorber layers and Schottky junction devices were completed using the same procedure as mentioned above. Best and average values (average was taken from 6 cells) of V_{OC} , J_{SC} , FF, η , R_S and R_{Sh} are summarized in the table. The thickness of QD layer in each device was ~ 150 nm. As shown by Figure 3-11, as the QD size decreases, V_{OC} increases and J_{SC} decreases. Ratios

of V_{OC} and E_g in three different cases (table 3.1) are given by 0.27, 0.27 and 0.2 for best cells and 0.26, 0.24 and 0.20 for average values respectively.

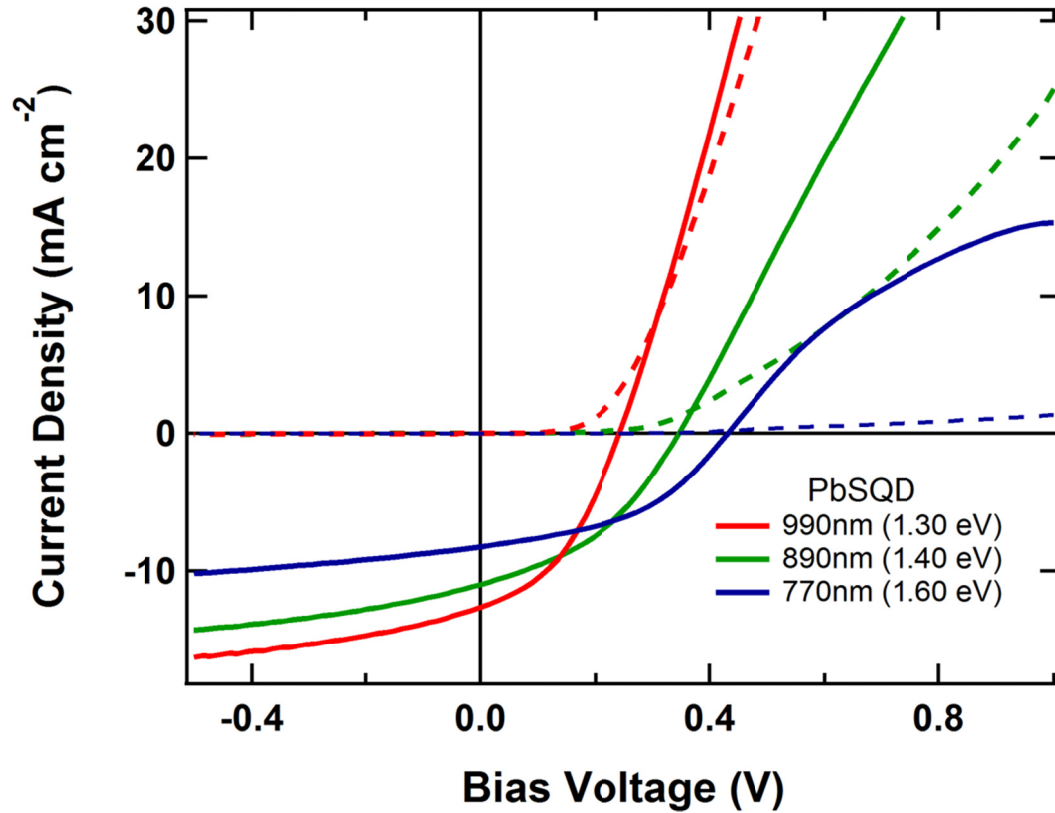


Figure 3-11. Current voltage characteristics of Schottky junction solar cells when PbS QDs of three different sizes were used as absorber layers. Solid lines represent light measurements and dash lines represent dark measurements.

Table 3.1: Performance parameters of Schottky junction solar cells when PbS-QDs of three different band gaps were used as absorber layers

PbS-QD Band gap	Result	V_{oc} (volt)	J_{sc} (mA cm⁻²)	FF (%)	η (%)	R_s (Ω.cm²)	R_{sh} (Ω.cm²)
770 nm (1.61 eV)	Best	0.432	8.94	44.1	1.7	20.3	183.3
	Average	0.418	8.78	42.6	1.6	19.2	175.5
890 nm (1.40 eV)	Best	0.347	11.01	39.4	1.5	14.3	86.1
	Average	0.331	10.36	37.6	1.3	16.3	80.5
990 nm (1.25 eV)	Best	0.247	12.74	40.9	1.3	8.9	69.6
	Average	0.242	11.94	36.3	1.1	11.6	58.1

3.3.3.2 ZnO/PbS-QD heterojunction solar cells

Figure 3-12 depicts the device structure of our ZnO/PbS-QD heterojunction solar cells and shows relevant energy level positions relative to vacuum; these findings concur with literature reports.[136, 137] A typically ~100 nm thick n-type window layer (ZnO) film is deposited at room temperature by DC sputtering method onto patterned ITO coated glass substrate. Subsequently, a ~200 nm PbS-QD film is deposited by a (LbL) dip coating method, and a thermally evaporated Au back contact completes the device. As shown in Figure 3-12(b), for a 2.5 nm diameter QD-based thin film, the conduction band edge lies well above the ZnO conduction band level and injection of photoexcited electrons into the ZnO would be energetically favorable. There is a large discontinuity between the top of valence bands of PbS and ZnO, providing a ~2.5 eV barrier to the undesired passage of majority holes from the QD film into the ZnO layer.[123]

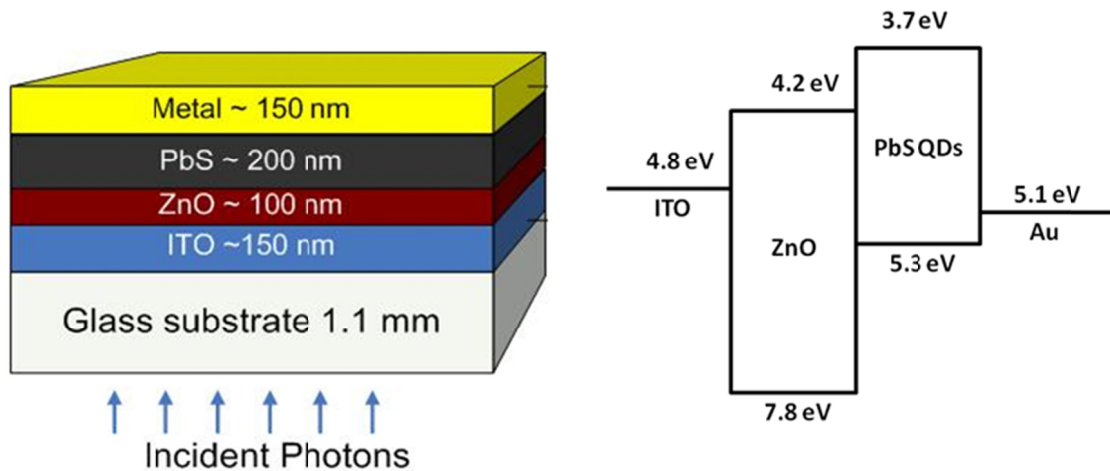


Figure 3-12. (a) PbS-QD photovoltaic device architecture (b) non-equilibrium energy level alignment of ITO, ZnO, PbS-QD (2.5 nm diameter) and Au.

Two complete devices having device structure of ITO/ZnO/PbS QD/Au are shown in Figure 3-13. The only difference in these devices is the thickness of the PbS QD layer. Figure 3-13(a) shows a device with PbS QD film of 30 cycles whereas Figure 3-13(b) shows device with QD film of 40 cycles.

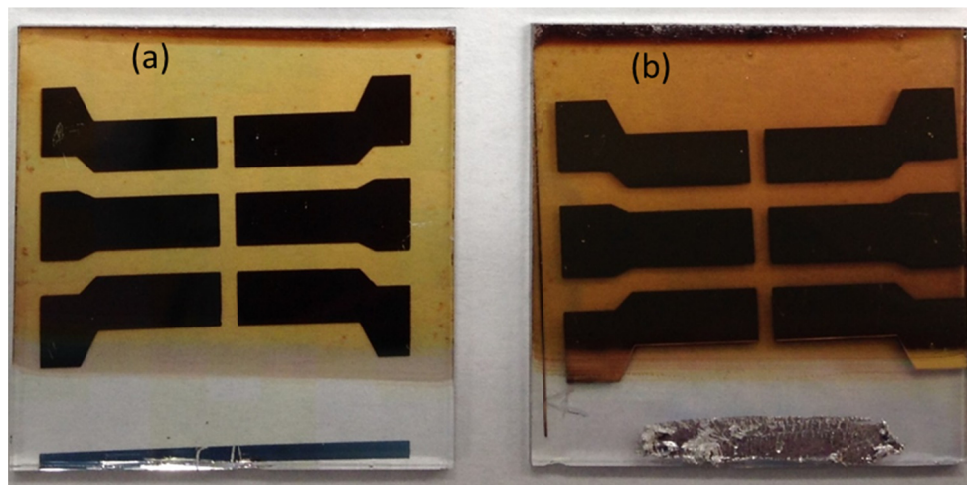


Figure 3-13. Complete heterojunction devices prepared from PbS QD film as absorber layer.

The photovoltaic responses as well as the diode response of our best ZnO/PbS-QD device are reported in Figure 3-14. This device showed a V_{OC} of 595 mV, J_{SC} of 15.6 mA cm^{-2} and FF of 44.2 %. The AM1.5G power conversion efficiency was 4.1%. In Figure 3-15, external quantum efficiency (EQE) is reported and shows a maximum value of $\sim 70\%$. At longer wavelengths, the distinctive excitonic feature is resolved and at the first exciton peak the EQE is about 14%. For comparison, the absorbance spectrum in solution of this QD sample is included in the same Figure. The performance of these devices are similar to [138] in the similar device structure. In Ref [138], the authors fabricated 4.40% efficient solar cells with J_{SC} of 18.145 mA cm^{-2} , V_{OC} of 524 mV and FF 46.2% with the introduction of MoO_x as a hole extraction layer before the deposition of back contact.

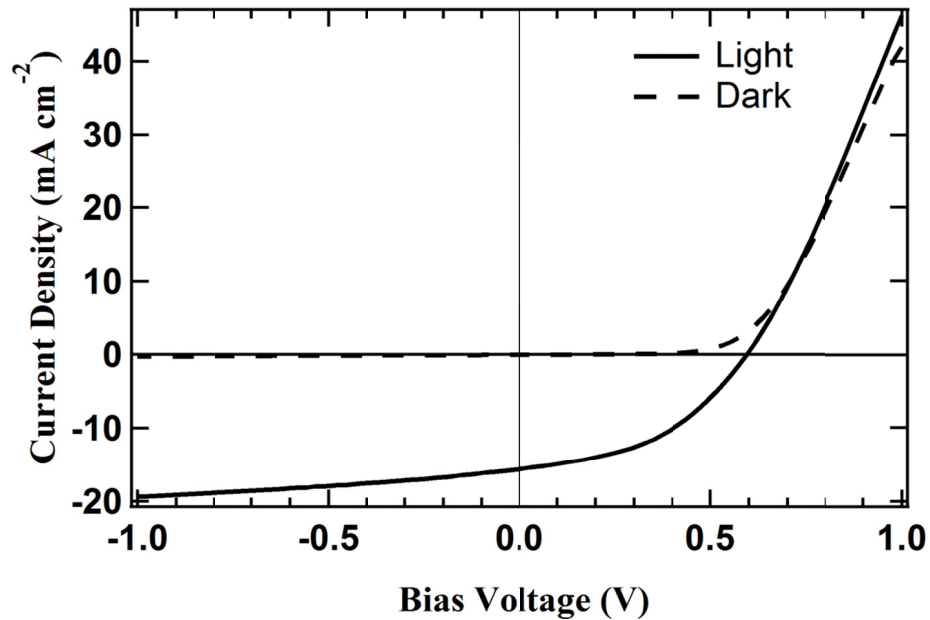


Figure 3-14. Measured current voltage characteristics under AM1.5G simulated solar illumination for a representative device. V_{OC} , J_{SC} , FF and PCE of this device were 595 mV, 15.6 mA cm^{-2} , 44.2% and 4.1% respectively.

The J-V characteristics, in both light and dark measurements, of devices based on films made from various QD sizes, are shown in Figure 3-16. Here, the band gap of the QD varies from 1.25 eV to 1.6 eV and the J-V data show that the open circuit voltage is maximized for smaller QDs, in accord with the QD size-dependent bandgap energy. The V_{OC} was >600 mV for QDs with band gap of 1.6 eV and <500 mV for QDs with band gap of 1.25 eV. Similarly, J_{SC} was minimum for QDs with band gap 1.6 eV (12.9 mA cm^{-2}) and maximum for QDs with band gap of 1.45 eV (15.3 mA cm^{-2}) respectively. May be because of the slightly smaller electron driving force, devices made from QDs with band gap of 1.25 eV could not provide as much current density as was expected. As the QD size decreases, range of solar spectrum to be used for absorption decreases and ultimately J_{SC} decreases. For the QDs of band gap 1.63eV, 1.45 eV and 1.25 eV, the theoretically obtained J_{SC} , provided that light incident on the device is all absorbed and electron-hole pairs generated are all collected, are given by 22.4 mA/cm^2 , 28.2 mA/cm^2 and 34.4 mA/cm^2 respectively. Average and best values of solar cells parameters in QD size dependent study when using ZnO as window layer are provided in table 3.2. The average is the average of 6 cells. Series and shunt resistances are expressed in $\Omega \text{ cm}^2$ by multiplying resistances in ohms by effective area of each cell in cm^2 .

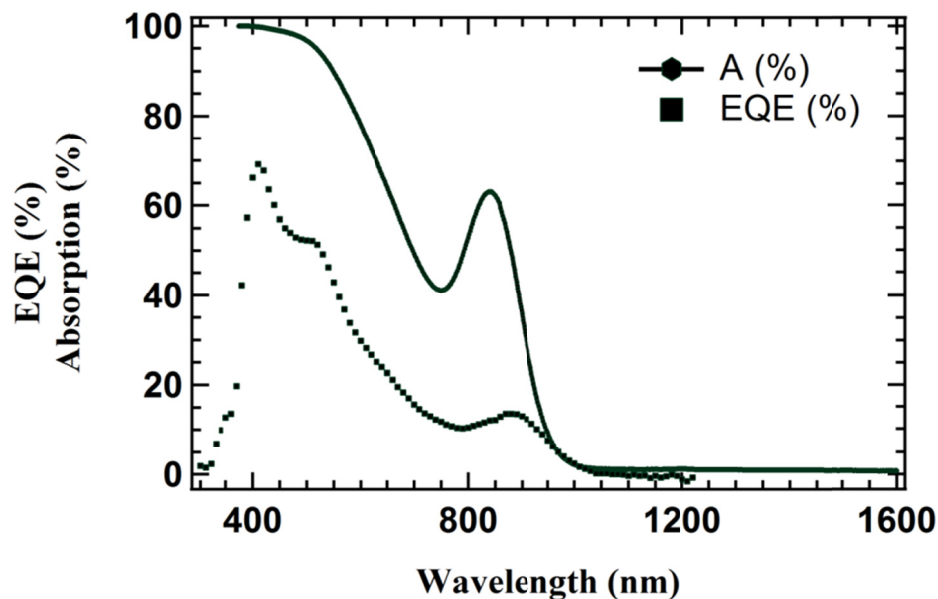


Figure 3-15. External quantum efficiency of the representative ZnO/PbS-QD device; for comparison, the absorption spectrum of the QDs in solution are also shown.

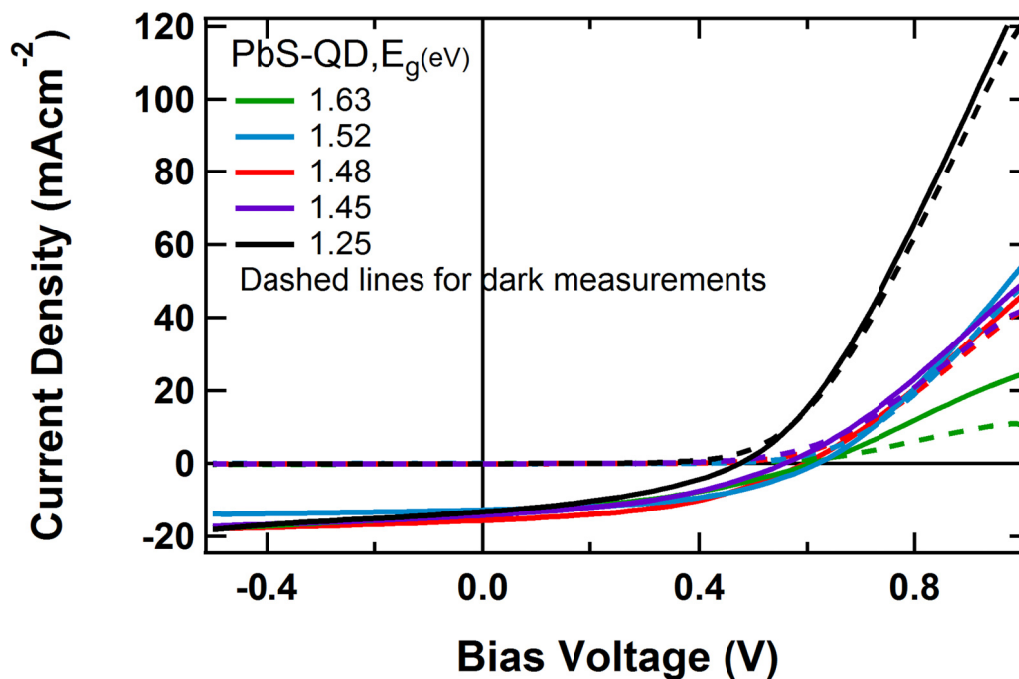


Figure 3-16. J-V curves for five devices made from PbS-QDs with various diameters. V_{OC} was obtained high from smaller dots and low from larger dots whereas J_{SC} followed opposite trend.

Table 3.2: Performance parameters of ZnO/PbS QD solar cells when PbS-QDs of five different band gaps were used as absorber layers.

PbS QD Band gap	Results	V_{OC} (V)	J_{SC} (mA/cm²)	FF (%)	η (%)	R_S (Ω cm²)	R_{Sh} (Ω cm²)
776 nm (1.60 eV)	Best	0.626	11.5	40.6	2.9	21.5	191.1
	Average	0.623	10.5	39.1	2.6	23.8	190.1
816 nm (1.52 eV)	Best	0.619	12.8	47.6	3.8	14.5	252.5
	Average	0.617	13.1	43.9	3.5	17.9	241.1
840 nm (1.48 eV)	Best	0.595	15.6	44.0	4.1	14.0	164.8
	Average	0.587	15.1	41.4	3.7	16.7	153.0
860 nm (1.44 eV)	Best	0.558	15.4	40.2	3.5	16.5	122.9
	Average	0.555	15.3	39.4	3.4	17.6	126.4
990 nm (1.25eV)	Best	0.476	14.4	39.1	2.7	16.3	143.3
	Average	0.474	13.9	39.2	2.7	16.9	139.4

Figure 3-17 shows the J-V characteristics of solar cells prepared with different window layer thickness. The bandgap energy of ZnO is ~3.6 eV, and the V_{OC} depends on the bandgap energy of the absorbing layer which is constant at ~1.5 eV. So, as expected there is no appreciable change in V_{OC} and J_{SC}, when the thickness of the ZnO layer is varied. The average V_{OC} was found to be ~617 mV and average J_{SC} was ~13 mA cm⁻² respectively. Thicker ZnO might possess some defect states leading to the recombination of photogenerated carriers and thus reducing current density to some extent as shown in Figure 3-17. However, since the band gap of ZnO is very high, light absorption is independent of the thickness of the window layer. At this point it is worth showing the

trends observed for series and shunt resistances and is given in Figure 3-18. From Figure 3-18, it is evident that thicker ZnO layer increases series resistance, decrease shunt resistance and finally decreases fill factor and efficiency of the devices.

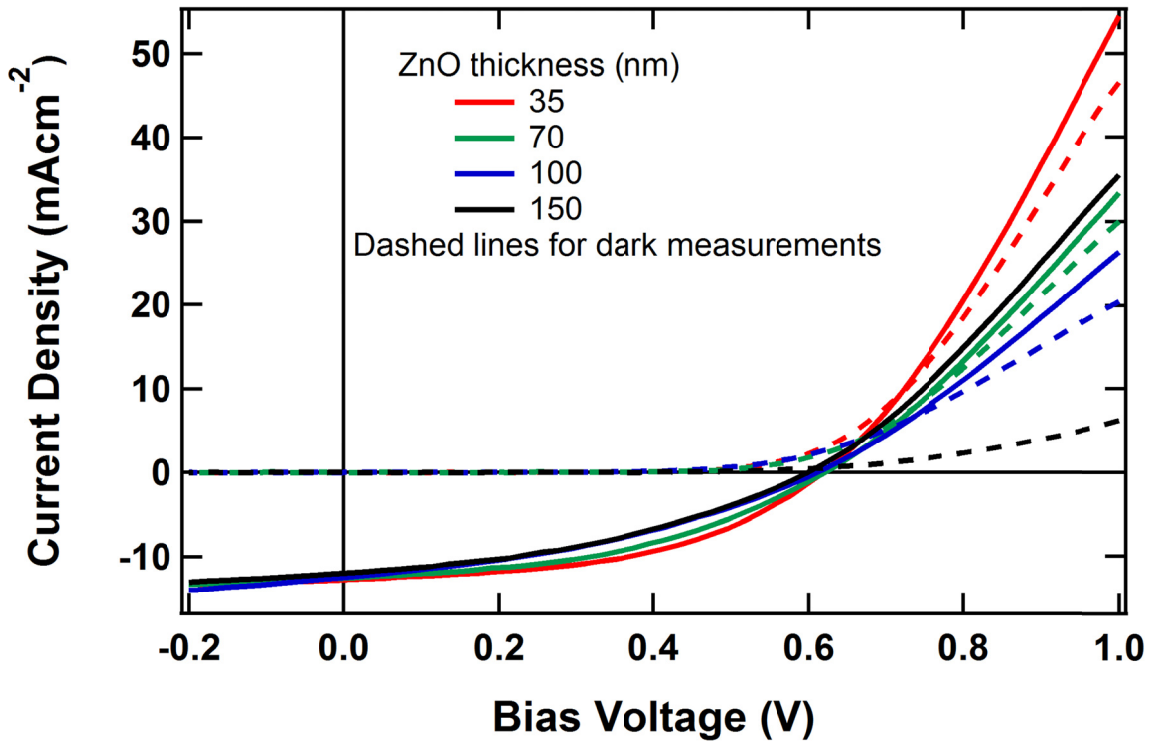


Figure 3-17. J-V characteristics of ZnO window layer thickness effects on ZnO/PbS-QD devices (QD diameter = 2.6 nm).

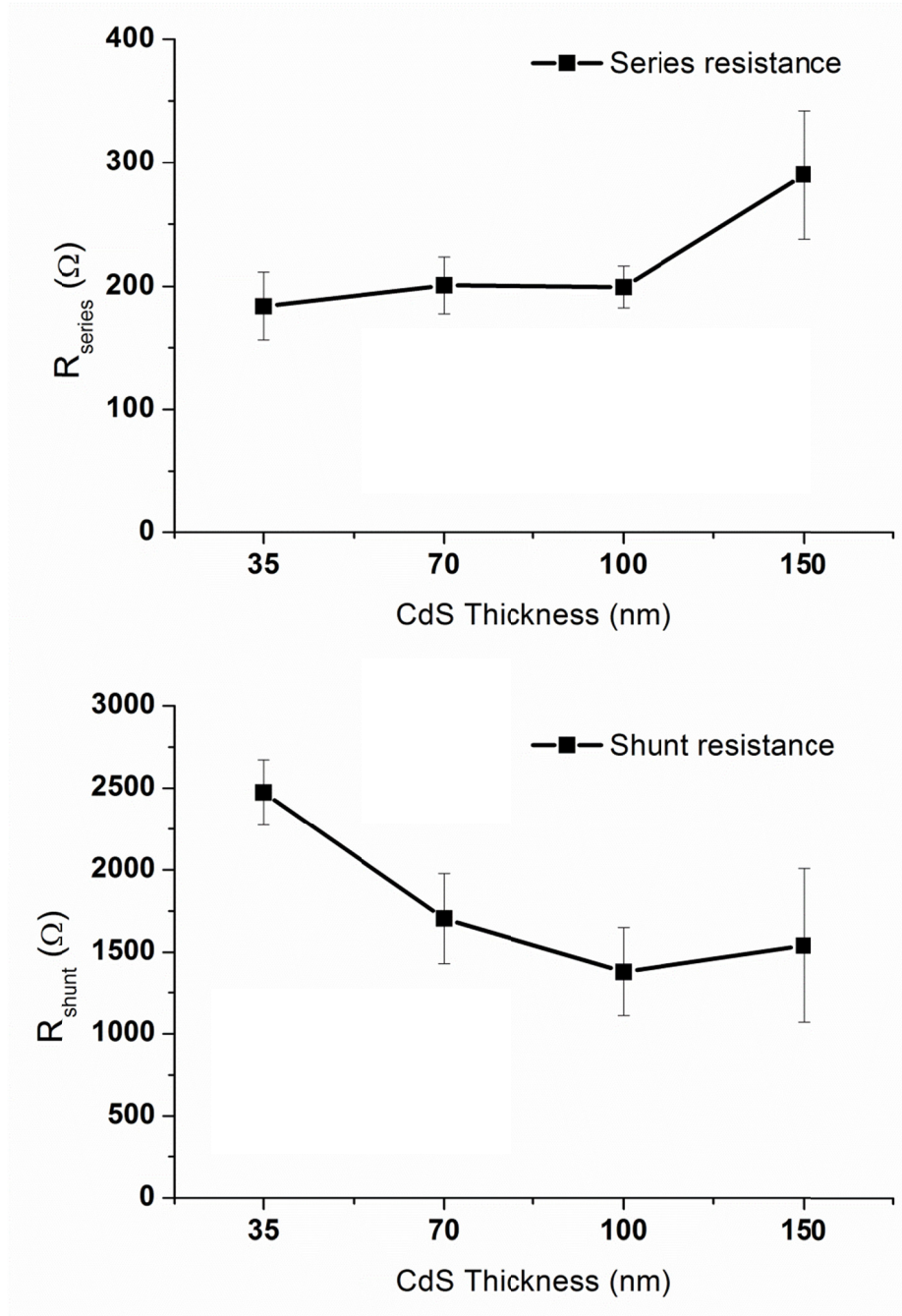


Figure 3-18. Series and shunt resistance of PbS QD solar cells when the size of the QD is fixed but the thickness of window layer is varied.

3.3.3.3 Light Soaking Effects

Solar cell conversion efficiency was found to increase during the continuous illumination of light. The solar simulator illuminates the cells under test with 100 mW cm^{-2} , AM1.5G to record the efficiency and other performance parameters. The performance of a typical solar cell remains essentially constant with repeated or continuous illumination. For the hetero- and Schottky-junction QD solar cells prepared here, performance was found to improve with integrated illumination. In other words J_{SC} , FF, and PCE of the solar cell all increased, while V_{OC} remained constant, and both series resistance (R_S) and shunt resistance (R_{SH}) improved. Light soaking effects and the proposed underlying physical mechanisms, as obtained in heterojunction and Schottky solar cells, are explained below in detail.[139] Group member Paul Roland assisted with these measurements.

3.3.3.3.1 Light soaking effects in ZnO/PbS-QDs heterojunction solar cells

Figure 3-19 presents J_{SC} and PCE for conducting J-V measurements over an extended period of time under illumination. The sample, which was fabricated according to the structure shown in Figure 3-12 where the first exciton peak of the QDs was 792 nm, was tested for four hours under the standard light source (AM1.5G). It has been proposed that light soaking photo-dopes the ZnO, increasing the n-type carrier density which in turn increases V_{OC} and J_{SC} .[140] When the free carrier density of the window layer increases, the depletion layer width increases as does the strength of internal electric field. Under this condition, charge separation and collection probability increases by increasing both the V_{OC} and J_{SC} of the device. However, in four hours long measurement

V_{OC} was found constant (Figure 3-20), suggesting that ZnO photo doping is not responsible for the observed enhancement.

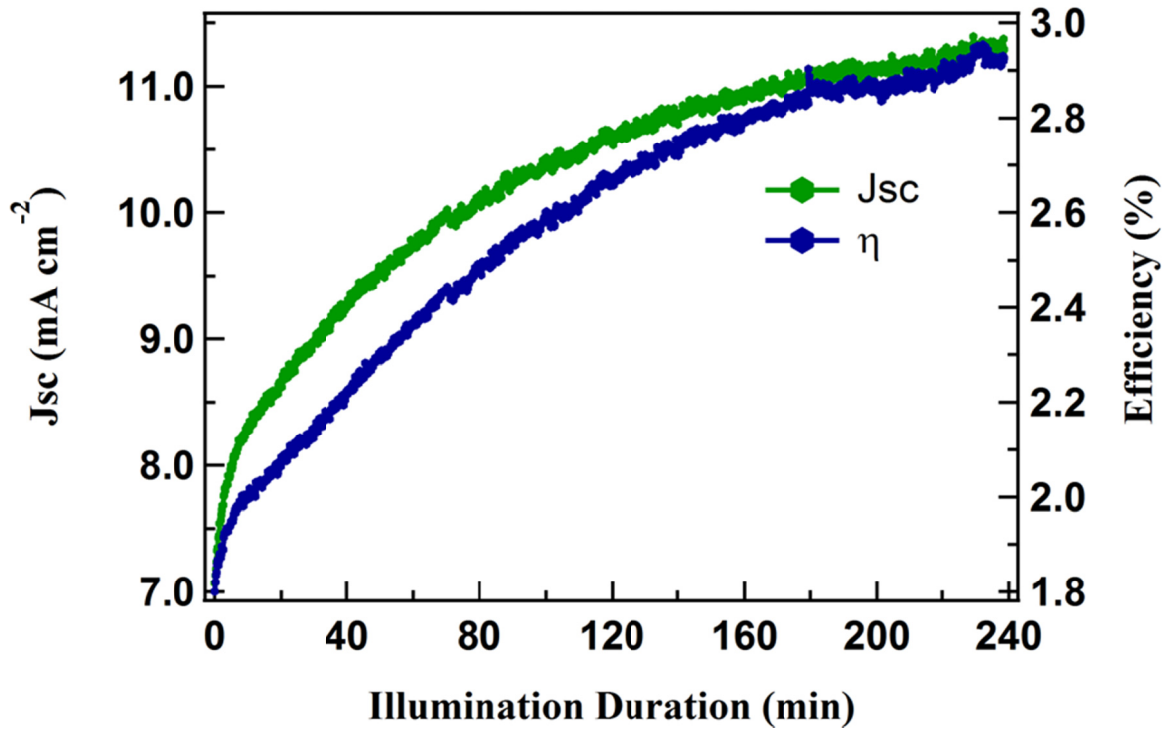


Figure 3-19. Increase in J_{SC} and PCE with respect to time. No saturation was observed after a scan of four hours consisting of two thousand J-V curves.

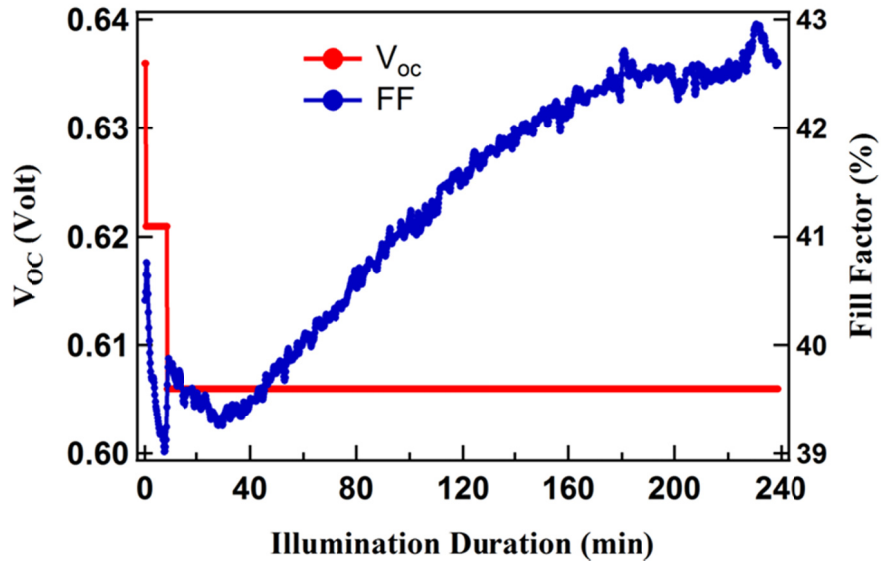


Figure 3-20. V_{OC} and FF with respect to time (min). V_{OC} appears nearly constant over this time period.

3.3.3.3.2 Light soaking effects in CdS/PbS-QDs heterojunction solar cells

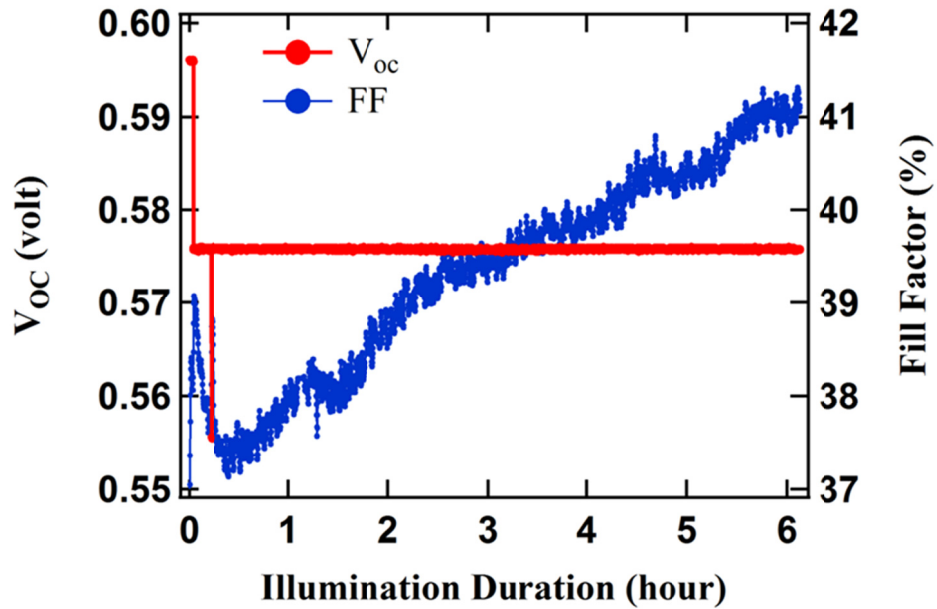


Figure 3-21. Open circuit voltage and fill factor of the solar cells with respect to time (hour).

Light soaking effects for CdS/PbS-QD solar cells were also studied. The device structure was glass/ITO/CdS/PbS-QD/Au. Light soaking effect was performed for 6 hours with 3000 J-V curves. There is no saturation of current. Figures 3-21 and 3-22 give V_{OC} and FF, and J_{SC} and PCE respectively.

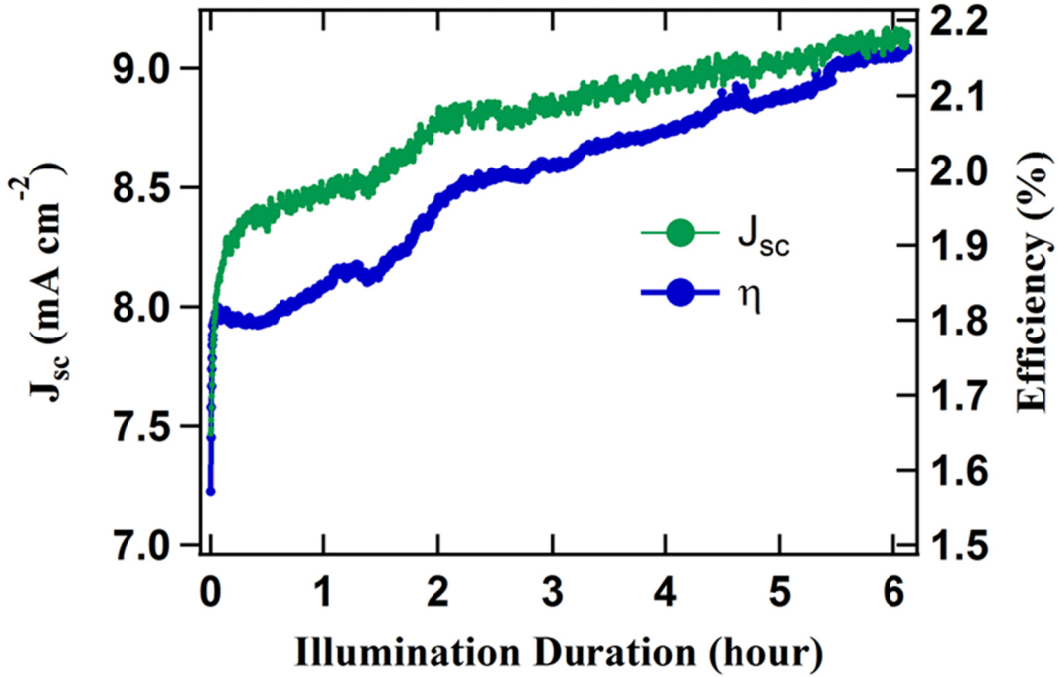


Figure 3-22. J_{SC} and PCE of the solar cells with respect to time (hour); there is no indication of saturation of these values.

During the measurement of light soaking effect, current voltage characteristics were also recorded. Figure 3-23 gives current voltage characteristics for the 1st, 1500th and 2999th scans of all 3000 measurements. Improvement in J_{SC} can be seen at 1500th and 2999th scan in comparison to 1st scan. Figure 3-23 also shows slight decrease in V_{OC} value in 1500th scan, keeping constant until 2999th scan, with respect to the 1st scan. This confirms the sharp decrease in V_{OC} in Figure 3-20 and Figure 3-21.

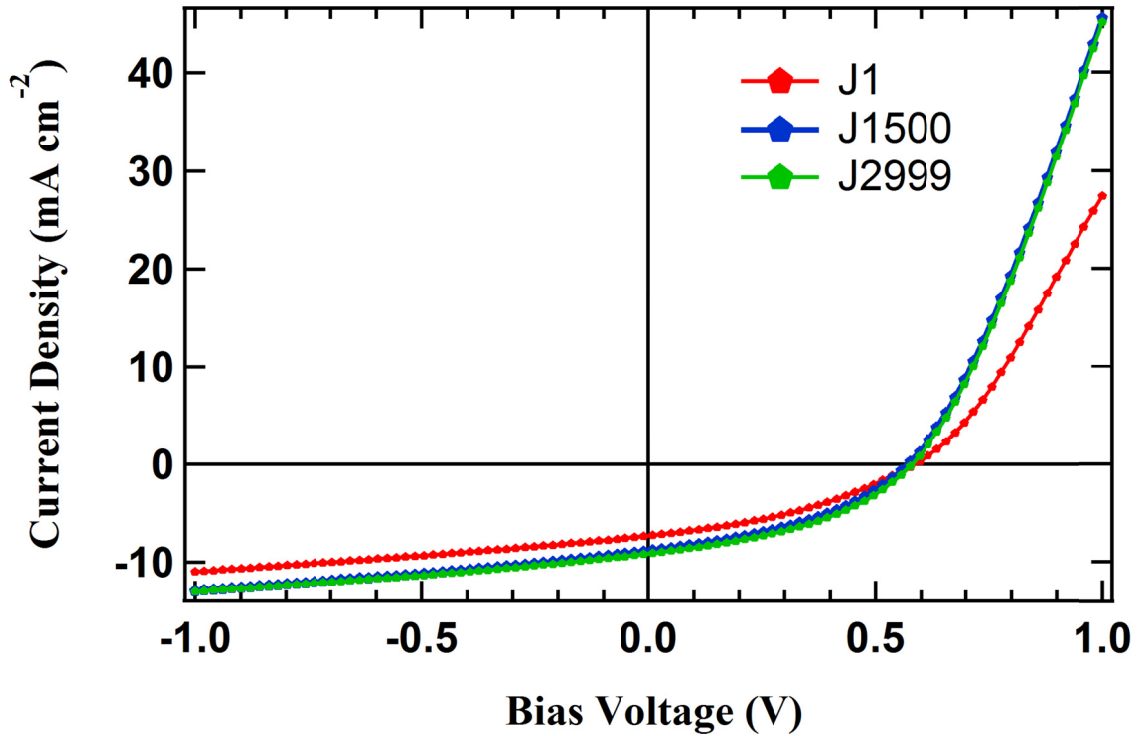


Figure 3-23. Current density in mA cm^{-2} is plotted with respect to open circuit voltage in Volts in the 1st, 1500th and 2999th scan of light measurement. While V_{OC} remained constant, J_{SC} improved over time.

3.3.3.3 Light soaking effects in Schottky junction solar cell

From these data we know that light soaking effect appears not only when window layer is ZnO but also when it is CdS. In case of CdS this effect is stronger than for ZnO. To independently understand the importance of window layer to light-soaking effects, a Schottky junction device was made from 2.5 nm diameter PbS QDs. The device structure was glass/ITO/PbS-QD/Al. For this device, the light soaking measurement was conducted for one hour. During this time of measurement, the effect of light soaking can be seen but not as strongly as seen in heterojunction devices. Figure 3-24(a) shows J_{SC} and PCE obtained from the measurement. In Figure, J_{SC} is decreasing but PCE is nearly

constant until one hour which is due to the improvement in FF as shown in Figure 3-24(b). V_{OC} increased for the first few minutes and remained constant in later part of the measurement.

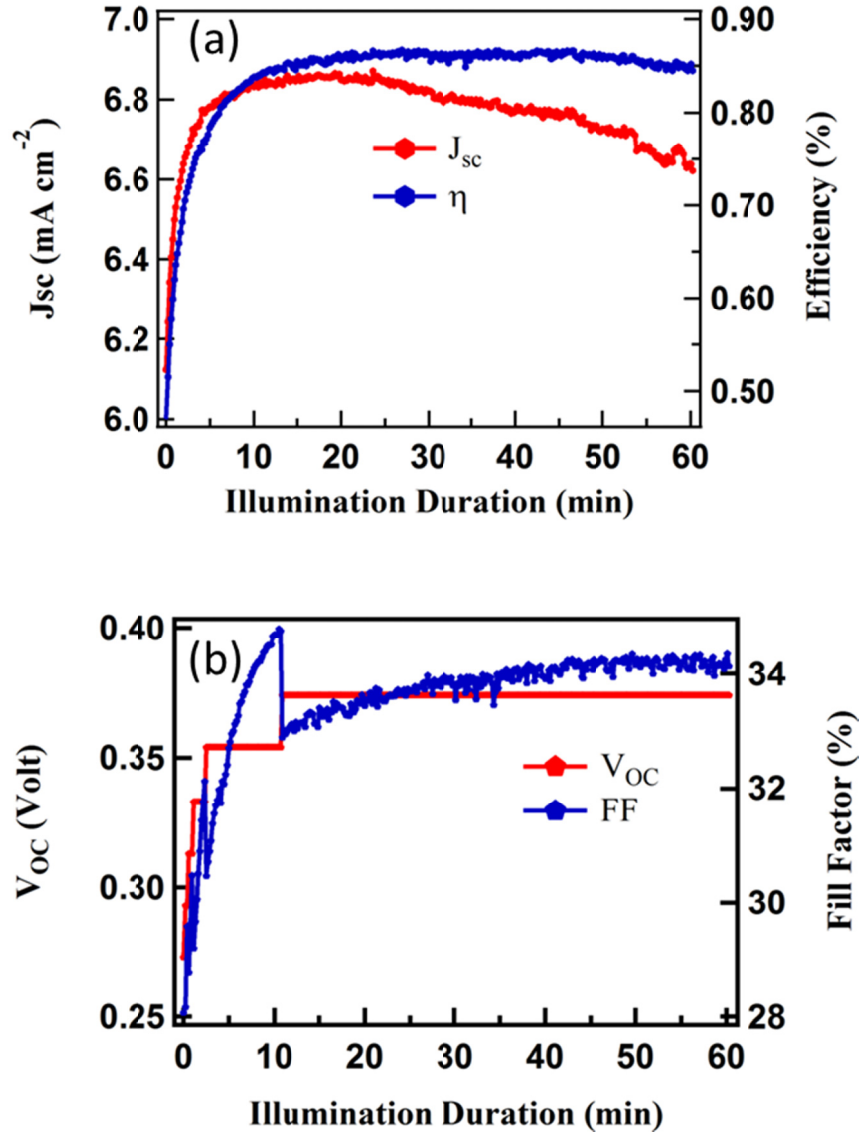


Figure 3-24. J_{sc} and PCE with respect to time in minutes; it is seen that PCE is increasing until around 45 minutes.

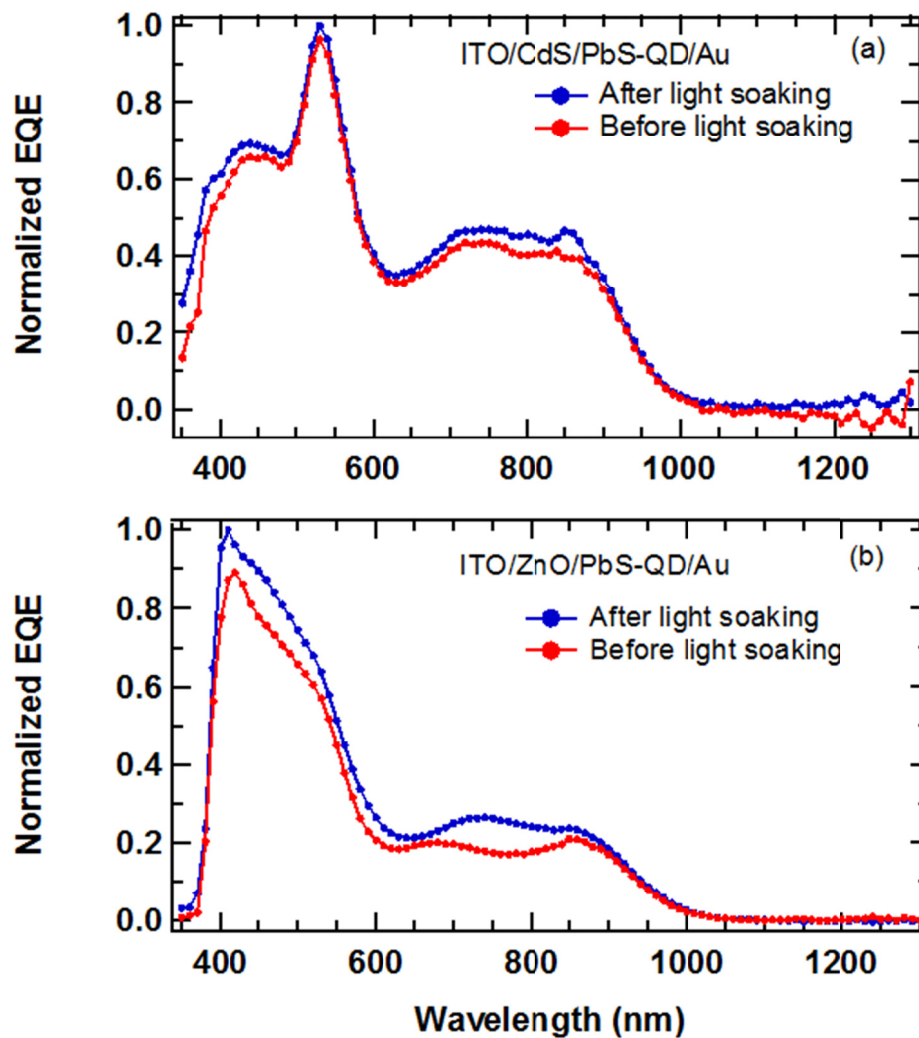


Figure 3-25. EQE before and after the light soaking performance; both were normalized with respect to after light soaking values. (a) EQE, when CdS is window layer and (b) EQE, when ZnO is the window layer. In the case of the CdS/PbS QD, a large spike in the EQE at around 450 nm can be seen. This behavior was observed repeatedly in other sets of devices and was thought to be the photocurrent contribution of CdS layer.

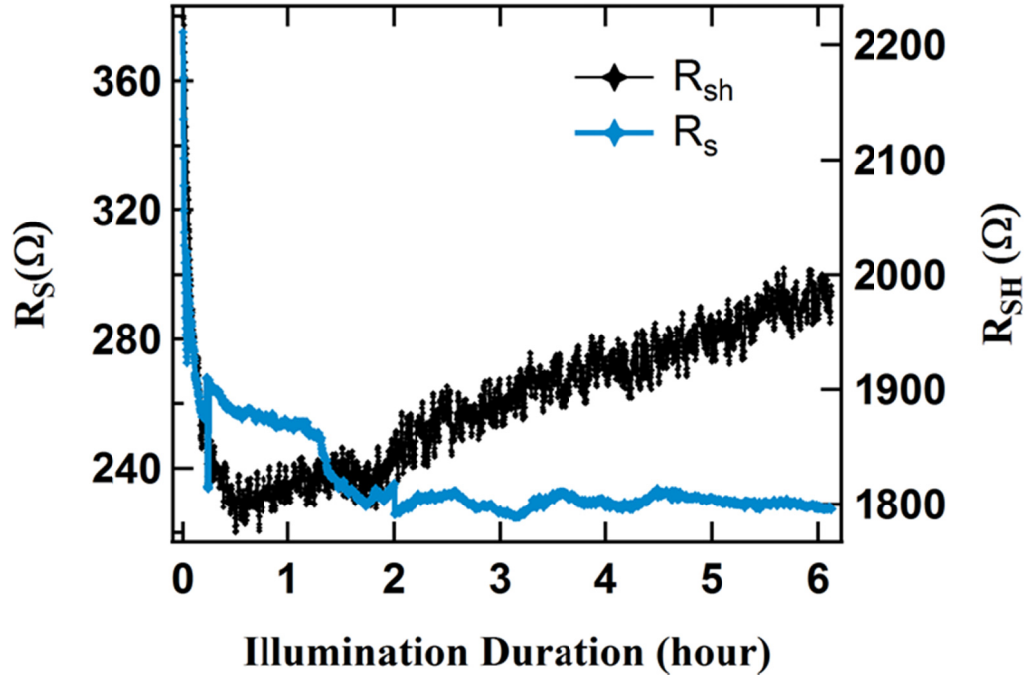


Figure 3-26. Decrease in series resistance and increase in shunt resistance with respect to time (min) when the window layer is CdS in heterojunction devices.

3.3.3.3.4 More discussion of light soaking effects

Preliminary assessment of light-soaking effects indicates that the behavior is intrinsic to the PbS-QD absorber layer, or to the interface between the QD thin film and the window layer or just the window layer. When comparing these results to published works, differing results were found where the present results show enhancement of J_{SC} and FF, stability in V_{OC} and enhancement in device efficiency. Luther et al [104] performed a 1000-hour long light soaking under constant illumination to the device with device structure ITO/ZnO/PbS-QD/Au. In their experiment, they found slight decay in the V_{OC} and FF which they say are due to the slight increase in J_{SC} and constant device efficiency. Their speculations to the increase in J_{SC} are "increase in the conductivity of

either the PbS-QD film upon oxygen exposure, increase in the ZnO NC film conductivity from continuous illumination, or a decrease in the device resistance due to the repetitive electrical measurement." [104] In the present work, the light soaking effect is not permanent and ZnO (and CdS) films are sputtered ZnO (and CdS) as opposed to colloidal NC-based ZnO (and CdS).

However, the photoinduced increase in ZnO conductivity is not expected to depend on the ZnO film fabrication method. When device illumination ceases, performance slowly reverts to what it was before the light-soaking and again goes up once illumination resumes. This explains why the light soaking is not permanent. In the process of light soaking, a decrease in the device series resistance (R_S) and increase in the device shunt resistances (R_{Sh}) were found, which are central signatures of improvement in the quality of devices. The author also found a largely wavelength-independent increase in the EQE (Figure 3-25) when tested immediately after the light soaking, contrary to what was seen in Ref. [104]. Neju *et al.* [141] studied light soaking and gas effect on nanocrystalline $TiO_2/Sb_2S_3/CuSCN$ photovoltaic cells. The authors obtained higher efficiency after the cells were held under light soaking at 1 sun intensity in ambient air and open circuit condition for ~20 - 200 min. Unlike the present work in heterojunction devices, they found a light-soaking-induced increase also occurred in V_{OC} . During such light soaking, their cell temperature increased from room temperature to 45 – 60 °C. They believed that oxygen, trapped during the cell fabrication, played an important role for improving cell performance by decreasing R_S and increasing J_{SC} and V_{OC} . Here, a constant V_{OC} was observed suggesting that the bandgap of the PbS-QD layer is not changing. In the present work, in light soaking, rapid evolution of J_{SC} and PCE can

be seen in Figures 3-19, 3-22, and 3-24 respectively. The initial decrease in FF in Figures 3-20 and 3-21 corresponds to the increase in J_{SC} . Upon initiating light soaking, the J_{SC} increased because R_S decreased (Figure 3-26). However, R_{Sh} is not high enough to maintain higher FF in the initial stage. After a while, the increase in R_{Sh} is accompanied by the increase in FF. The trend of performance of Schottky devices in an hour long light soaking test seems similar to the one obtained by Tang et al. [142] in their longer test. In 2010, these authors tested stability of Schottky devices with device structure of Glass/ITO/PbS-QD/LiF/AL/Ag under simultaneous and continuous AM1.5G illumination of 100 mW cm^{-2} . Even though the V_{OC} remained constant, their device lost 13% of the initial efficiency after 63 hours of illumination.

Based on the experimental results discussed above, the author found that light soaking effect resulted in an increase in J_{SC} , FF and PCE and a decrease in R_S . High R_S reduces J_{SC} but has no effect on V_{OC} , while low R_{Sh} has no effect on J_{SC} but reduces the V_{OC} . The R_S is the sum of film resistance, electrode resistance and the contact resistance between the film and the electrode. The R_{Sh} is mainly indicative of carrier recombination loss. FF is related to R_S and R_{Sh} ; large R_{Sh} and small R_S lead to good FF.

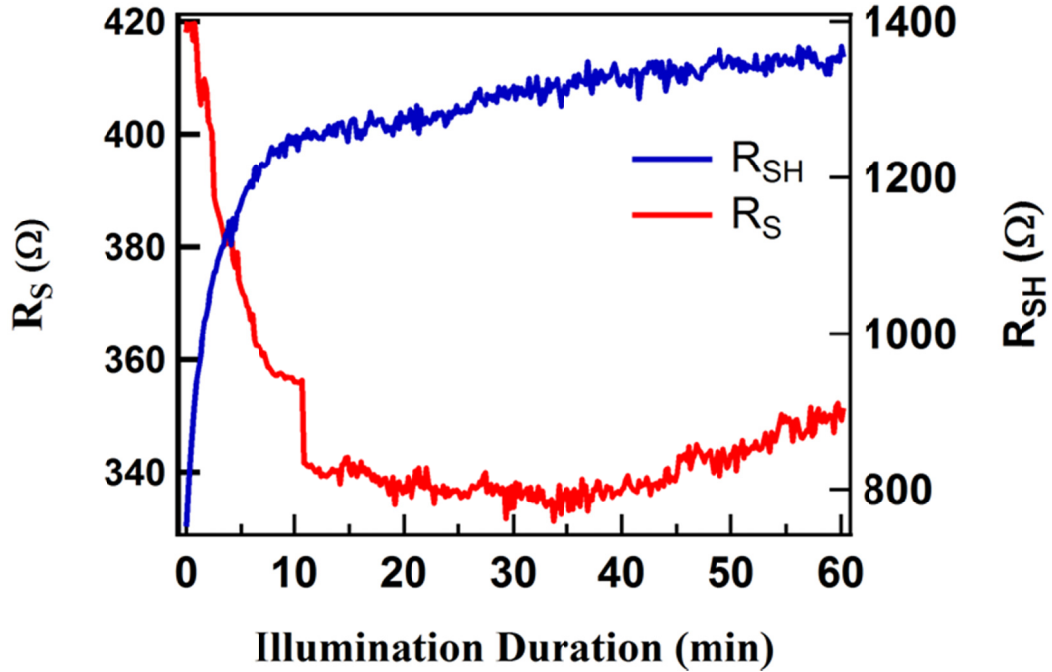


Figure 3-27. Decrease in series resistance and increase in shunt resistance with respect to time (min) for PbS-QD Schottky junction solar cells.

In the heterojunction devices presented here, the initial decrease in V_{OC} and FF is accompanied by the sharp decrease in R_{Sh} , which is due to the very large carrier recombination loss mainly caused by the window layer. Some recombination loss may also be due to the presence of dangling bonds on the surface of quantum dots. When the illumination is continued in air, the conductivity of the film is increased, in accord with decreasing recombination loss. This helps to increase the R_{Sh} slowly and continuously (Figure 3-26), improving the FF of the device. Since there is a sharp decrease in R_S in the beginning of illumination, which may be due to the repetitive electrical measurement, there is also a sharp increase in J_{SC} . Subsequent changes in R_S and R_{Sh} continue gradually, keeping V_{OC} constant but slowly increasing J_{SC} , FF and PCE.

In contrast, for Schottky solar cells there is no recombination loss due to the window layer – i.e. there is no decrease in R_{Sh} in the beginning of illumination (Figure 3-27). Instead, when the illumination was initiated, R_S is decreased and R_{Sh} is increased sharply increasing V_{OC} , J_{SC} , FF and PCE.

3.4 Conclusions

A synthetic route of PbS QDs was explained for the production of narrow size dispersions of PbS QDs. These size-tunable NIR emitting QDs were found to be ideal materials for device applications and subsequent device studies. The synthetic route used here is cost-effective for large scale production. From these QDs, uniform and conductive films fabrication method was developed with excellent control of film thickness. The best applications of these films were found in the production of QD solar cells. Their initial performance obtained from the fewer amounts of materials, and low cost of instrumentation at ambient environment indicates that these materials may offer an avenue for future solar cell technologies.

Chapter 4

PbS-QD based thin film heterojunction solar cells using CdS as an n-type window layer

4.1 Introduction

Researchers have been investigating suitable n-type heteropartners for PbS QD solar cells for several years. To date, only ZnO and TiO₂ in their various forms (nanoparticles, nanowires, and bulk thin film) have been widely used as n-type heteropartners with PbS-QD thin films. With these heteropartners, QD solar cells have shown promising efficiencies in the 4-7% range up to 7.4%.[138, 143] ZnO is a wide bandgap (3.37 eV) II-VI semiconductor, and typically shows n-type character even in the absence of intentional doping with low carrier concentration. The synthesis of nanocrystalline TiO₂ paste for industrial production involves a lengthy process which may be economically challenging,[144] and because of its relatively small electron affinity, TiO₂ cannot be utilized for all sized PbS QDs (efficient electron transfer from PbS QDs to TiO₂ occurs only for QD diameters below approximately 4.3 nm).[47] These facts, together with the desire to expand our knowledge of photovoltaic (PV) materials

science, suggest consideration of other possible heteropartners for the PbS QDs solar cells.

In this study the author has explored sputtered CdS as a new heteropartner for PbS QD solar cells, and has compared these cells' performance with cells utilizing either ZnO or nanostructured TiO₂. CdS is a non-stoichiometric n-type semiconductor with a direct band gap energy of 2.42 eV.[145] In this chapter, the author reports CdS/PbS-QD heterojunction solar cells that show an open circuit voltage (V_{OC}) as high as ~0.65 V. To the author's knowledge, no previous report has been made on photovoltaic devices based on sputtered CdS as a window layer for a PbS QD thin film absorber layer, and at the time of publication the 0.65 V value for V_{OC} represented a record high reported value for any cells using a PbS-QD thin film absorber layer. The current record V_{OC} for PbS-QD PV is 692 mV.[134]

Thin films of CdS have been studied extensively over the past four decades, owing in large part to the fact that CdS has been the most widely used and most successful n-type window layer for high efficiency thin film solar cells based on CdTe[146, 147] and Cu(InGa)Se₂ (CIGS).[148, 149] Various techniques such as chemical vapor deposition,[150] RF magnetron sputtering,[151] and chemical bath deposition[152] have been used to make uniform and transparent CdS films to produce high efficiency solar cells. For CdS, sputtered films have shown both larger crystalline grain size as well as smoother surface roughness as compared with films produced by chemical bath deposition;[153] in addition, the author finds excellent adhesion qualities onto glass substrate for the sputtered CdS films. In addition, sputtering offers potential benefits in terms of deposition rate, substrate throughput, and film thickness uniformity.

4.2 Experimental

4.2.1 PbS quantum dot (QD) synthesis

For the applications discussed in this chapter, PbS QD samples were synthesized in diameters ranging from ~ 2.3 nm to 3.3 nm, corresponding to first exciton peak positions in the range of 738 nm to 1000 nm. The author has demonstrated control over the synthesized QD diameter by varying surfactant concentrations and reaction conditions, as follows. The size of the QDs depends mainly on the amount of surfactant used and the injection temperature of sulfur precursor into the lead oleate. Therefore, to get above mentioned QDs, only these two parameters were varied keeping all other aspects constant (even though their variation also bring changes in the size of the dots). For example, to synthesize ~ 2.9 nm diameter QDs: 2 mmol of PbO, 10g of ODE, and 1.14 g of OA are heated to 120 – 122 °C under N₂ in a 100 mL round bottom three neck flask for about 45 minutes where all the PbO is dissolved. The mixture is continuously stirred with a magnetic stirrer bar. The mixture is heated until all the PbO is dissolved completely, typically within 45 minutes, forming lead oleate.

In the glove box, 1 mmol (TMS)₂S is dissolved in 3.16 g of nitrogen-purged ODE. The mixture is loaded in a syringe with a needle. The heating mantle is removed and the mixture is injected immediately at various temperatures below 220 °C into a three neck flask. When the temperature of the mixture reaches room temperature, purification is done in air by adding ~ 5 mL of hexane and ~ 30 mL of EtOH and centrifuging at 5000 rpm for about 20 minutes. The supernatant is removed and sediment is cleaned two more

times with hexane/ethanol. QDs so obtained are dried under nitrogen and utilized for the experimental purposes.

4.2.2 Photovoltaic device fabrication

PbS-QD film (absorbing layer) preparation was done via a layer-by-layer (LbL) deposition method reported elsewhere.[43, 142] Patterned indium tin oxide (ITO) coated glass substrates, obtained from Thin Film Devices, Inc., were cleaned by sonication at a temperature of ~ 180 °F using Micro-90[®] (concentrated cleaning solution) and deionized water. Cleaned glass substrates were then dipped into a beaker containing 15 to 20 mL of NC solution with the concentration of about 8 mg/mL prepared in hexane in a 30 mL beaker followed by a second beaker containing 1 mM EDT solution in acetonitrile. Approximately 20 to 40 dip cycles were used to make films for devices which are 150 to 200 nm thick. Dip-coating was performed using a dip coater from NIMA Technology, England. The added thickness of the QD film from each cycle depends on the concentration of the colloidal solution and the removal speed (typically ~ 0.7 mm/sec) of the substrate from the solution. For heterojunction solar cells, CdS was used as window layer (n-type semiconductor) which was deposited by RF magnetron sputtering method in an Ar atmosphere. Prior to deposition of CdS, the chamber was heated to 270 °C for thirty minutes. The transparent and conducting ITO layer shows a sheet resistance of ~ 32 Ω/\square and forms the top contact of the device. A 150 nm thick gold (Au) film is used as the back contact and was deposited either by electron beam evaporation or thermal evaporation methods. Au was selected as the back contact due to its high work function

so as to minimize back junction effects.[116, 138] Six cells were fabricated on a single substrate, each with an active area of 0.0975 cm^2 .

4.2.3 Device fabrication for Mott Schottky measurement

For one sample, a film of approximately 200 nm of PbS QDs (first exciton absorption peak at 834 nm) was LbL-deposited onto a sample of patterned ITO coated glass obtained from Thin Film Devices Inc. A back contact of 96 nm thick Al was deposited by thermal evaporation onto the PbS-QD layer such that the device area was approximately 0.0975 cm^2 . A second Schottky junction sample of 200 nm sputter deposited CdS onto TEC-15 coated glass was fabricated by depositing a layer of Ag paint of approximate thickness 80 μm onto the surface of the CdS forming a device area of 0.378 cm^2 . Electrical contact to the TCO layers in both samples was accomplished via indium solder joining lead wires to the TCO layer while contact to the metal (back contact) layer was made using a Au-plated spring probe. A Princeton Applied Research 263A potentiostat/galvanostat coupled with a Stanford Research Systems SR830 lock-in amplifier was used to acquire the capacitance-voltage characteristics of each device using Labview control software designed in-house. The potential of the semiconductor thin film was reported with respect to the metal back contact.

4.3 Results and Discussion

Figure 4-1 shows the complete solar cell device structure, its cross-sectional view, and equilibrium band diagram in the dark. Valence band maximum and work function of both CdS and PbS-QD films were obtained using UPS measurement (vide infra). Using their band gap information, approximate electron affinities were calculated. Using these

values and approximate valence and conduction band offsets obtained from UPS/XPS measurements, an approximate equilibrium energy band diagram was constructed. Depletion width is not calculated; it is just an approximation. Varying the thicknesses of the n- and p- type layers, best cell performance was found using 70 nm of CdS and 150 – 200 nm of PbS QDs. The completed device was processed for cross-sectional imaging using focused ion beam (FIB) milling, and imaged by scanning electron microscopy (SEM). A layer of platinum was deposited onto the Au layer to avoid Ga^+ ion implantation and milling of the Au surface during FIB processing.[154]

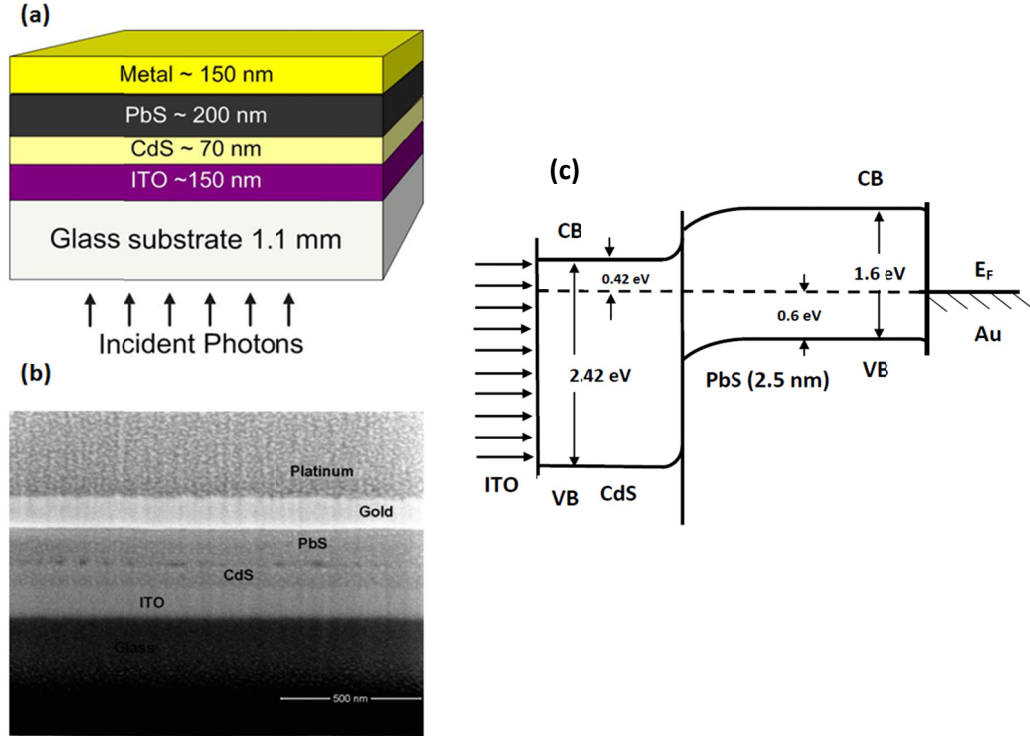


Figure 4-1. (a) Schematic of the PbS QD/CdS heterojunction solar cell; approximately thickness of each layer is labeled (b) Cross-sectional scanning electron microscopy (SEM) of the PbS QD/CdS junction solar cell illustrated in (a) taken with the help of focused ion beam. (c) Schematic of the energy band diagram of an ITO/CdS/PbS-QD/Au solar cell.

X-ray diffraction (XRD) was used to study the crystallinity and crystal orientation of the CdS films. X-ray diffraction pattern was measured in the 2θ range of $20 - 70^\circ$ using Cu $K\alpha$ radiation ($\lambda = 0.15406$ nm) operated at 40 kV, 40 mA and 1.65 W. The XRD pattern of the sputtered (50 W power) CdS thin films (Figure 4-2a) showed the hexagonal wurtzite crystalline phase with the most prominent diffraction peak at $2\theta = 26.48^\circ$, which corresponds to the (002) lattice plane of CdS.[155, 156] Additional peaks were identified for the lattice planes corresponding to (100), (002), (101), (110), (103), (200), (112), (201) and (004) lattice planes. The average grain size was calculated using Scherer analysis [157] as given in equation (4.1) for the primary diffraction peak.

$$D = \frac{k\lambda}{\beta \cos \theta}, \quad (4.1)$$

where k is a constant taken to be 0.9, λ is the wavelength of X-ray used ($\lambda = 1.5406 \text{ \AA}$), β is the full width at half maximum of primary peak (002) of XRD pattern, and 2θ is the Bragg's angle. The value β is expressed in radians.. The crystallite size (D) is revealed in the broadening of a particular peak in a diffraction pattern. In equation (1), D depends inversely on FWHM - the more narrow the peak, the larger the crystallite size. If a material possesses periodic grains in phase and crystals are defect free, the diffraction of the X-ray beam is constructively added, resulting in tall narrow peak. On the other hand, if crystals are more randomly arranged with low degree of periodicity, the resulting diffraction peaks will have broader peaks. In other words, if the material is less crystalline and tends to go to amorphous in nature, it will have broad diffraction peak. When it is completely in amorphous, it does not exhibit XRD peaks. Using all the parameters, it is found that the film consists of oriented grains with an average size of 33

nm. Using Brag's law (equation 2), inter-plane spacing d was calculated to be 3.36 Å. Using the Miller indices (hkl) of these planes, the lattice parameter $a = b$ and c of the unit cell were evaluated according to the relation (4.2) for hexagonal structure.

$$2d \sin \theta = n\lambda$$

$$\frac{1}{d^2} = \frac{4}{3} \left(\frac{h^2 + hk + k^2}{a^2} \right) + \frac{l^2}{c^2} \quad (4.2)$$

The calculated values of a and c were 4.47 Å and 6.73Å, respectively, which are close to the published results of 4.14 and 6.71 respectively. [158] The angle θ is half of the x-axis value in Figure 4-2a, which was converted to radians for use in equation 4.2.

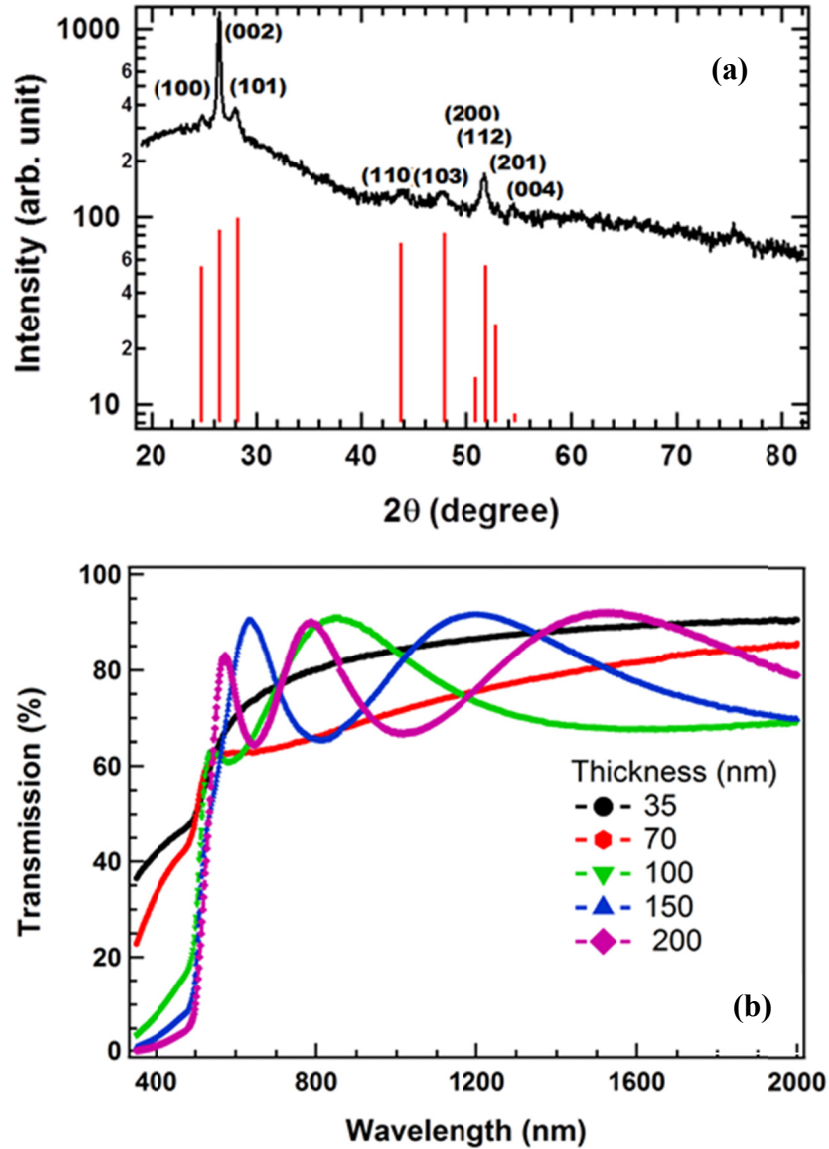


Figure 4-2. (a) X-ray diffraction (XRD) pattern for a CdS thin film on glass substrate deposited at 270 °C; Red vertical lines represent powdered diffraction lines as obtained from the characterization software jade 2010; (b) transmission spectra of CdS thin films , sputtered on soda lime glass substrates of thickness ~1 mm at 270 °C, of varying thicknesses.

The optical transmittance of the CdS film was measured for the wavelength range 350 - 2000 nm using a Perkin Elmer Lambda 1050 Spectrophotometer as shown in Figure 4-2(b). Transmittances of CdS film of five different thicknesses were taken. A 70 nm thick CdS film transmits more than 60% of incident light of wavelength > 515 nm. The sharp drop in the transmittance of the film below ~ 515 nm is due to the strong band edge absorption of CdS. In order to construct the solar cell's band diagram, the electronic and interface properties of sputtered CdS and LbL PbS-QD thin films were investigated. Work functions of CdS films and PbS-QDs were measured by ultraviolet photoelectron spectroscopy (UPS) and Kelvin probe force microscopy (KPFM) methods. Ultraviolet photoelectron spectroscopy was also used to calculate the valence band maximum (VBM) for both CdS and PbS-QD films. The VB edges were obtained with respect to the Fermi level which is considered as the zero binding energy in the UPS spectrum. The band offset at the interface is one of the most important properties for a semiconductor heterostructure device, and enables the design and optimization of different contacts to minimize the loss of photogenerated carriers resulting in a cell with higher conversion efficiency. X-ray photoelectron spectroscopy (XPS) and UPS were used to determine valence band offset ΔE_V and conduction band offset ΔE_C at the CdS/PbS-QD heterojunction. Details of all these measurements and interpretation of data are provided in chapter 7.

Under illumination, electron-hole pairs photo-generated within the depletion region are separated by the built-in electric field with electrons drifting to the CdS and holes drifting to the PbS-QD layer. When the device terminals are shorted, excess electrons in the CdS flow through the external circuit to recombine with the excess holes

in the PbS-QD layer – this represents the photocurrent. The current voltage (I-V) characteristics of one of our best solar cells are shown in Figure 4-3. To complete this device, a 200 nm thick PbS-QD film (QD diameter of 2.5 nm, first exciton peak at ~792 nm, or 1.57 eV) was deposited atop a ~70 nm thick CdS film. The device was completed by evaporating 150 nm of Au onto PbS-QD layer. The resulting solar cell exhibited an open circuit voltage, V_{OC} of 638 mV, short circuit current, J_{SC} of $12.0 \text{ mA}\cdot\text{cm}^{-2}$, and overall photo-conversion efficiency (PCE) of 3.3% when illuminated with $100 \text{ mW}\cdot\text{cm}^{-2}$ simulated AM1.5G solar spectrum. Direct comparison of these results with the past work is not possible because we have not seen heterojunction devices based on CdS/PbS-QD combination in previous literature.

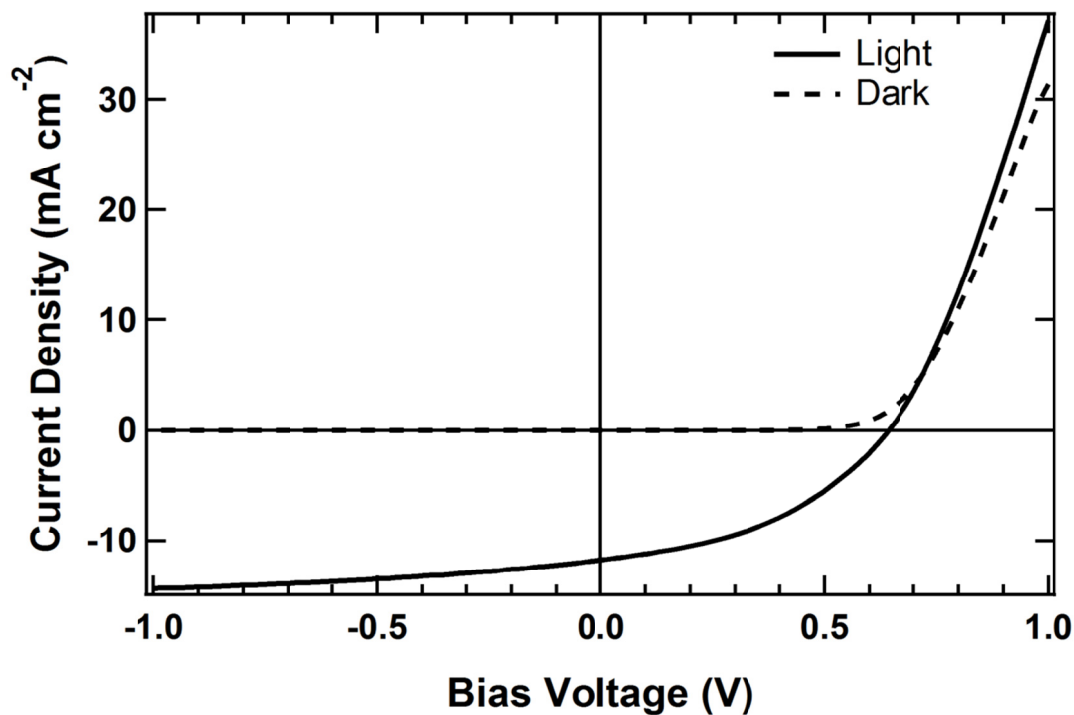


Figure 4-3. Current-voltage (I-V) characteristics of a CdS/PbS-QD heterojunction solar cell recorded in the dark and under $100 \text{ mW}\cdot\text{cm}^{-2}$ simulated AM1.5 illumination. The device was assembled using a $\sim 200 \text{ nm}$ thick EDT-treated PbS-QD film deposited from $\sim 2.5 \text{ nm}$ diameter QDs, a 70 nm thick CdS film, and a gold back-side contact. Values of V_{OC} , J_{SC} , FF and PCE of this device were 638 mV , $12.0 \text{ mA}\cdot\text{cm}^{-2}$, 43.5% and 3.3% respectively.

The Table 4.1 shows the device test performance data (V_{OC} , J_{SC} , FF, and PCE) for the three sets of devices which include the best device (3.3% efficiency). The PbS QD size and band gap energy for these devices are $\sim 2.5 \text{ nm}$ diameter and $\sim 1.56 \text{ eV}$. All these measurements were made under simulated AM1.5G illumination. All six cells are located at the center of a substrate of size $1''\times 1''$ as shown in Figure 4-4. This is one of the photographs of my champion devices of this kind. In the most of my work all 6 cells were found to be working equally.

Table 4.1: Parallel test results: CdS70/PbS792 solar cells

Substrate #	cell #	V_{oc} (V)	J_{sc} (mA-cm⁻²)	FF (%)	PCE (%)
1	1.1	0.642	11.3	41.5	3.01
	1.2	0.638	12.0	43.5	3.33
	1.3	0.630	11.5	42.1	3.05
	1.4	0.632	11.4	42.3	3.04
	1.5	0.637	11.5	43.0	3.15
	1.6	0.636	11.5	42.7	3.12
2	2.1	0.631	11.2	41.2	2.91
	2.2	0.633	11.8	41.8	3.12
	2.3	0.623	11.5	42.1	3.02
	2.4	0.632	11.2	41.9	2.97
	2.5	0.635	11.3	42.2	3.03
	2.6	0.631	11.4	41.8	3.0
3	3.1	0.639	11.8	40.3	3.04
	3.2	0.639	11.9	41.9	3.2
	3.3	0.630	11.7	40.1	2.96
	3.4	0.639	11.6	40.9	3.03
	3.5	0.643	11.8	41.8	3.17
	3.6	0.638	11.8	41.0	3.09

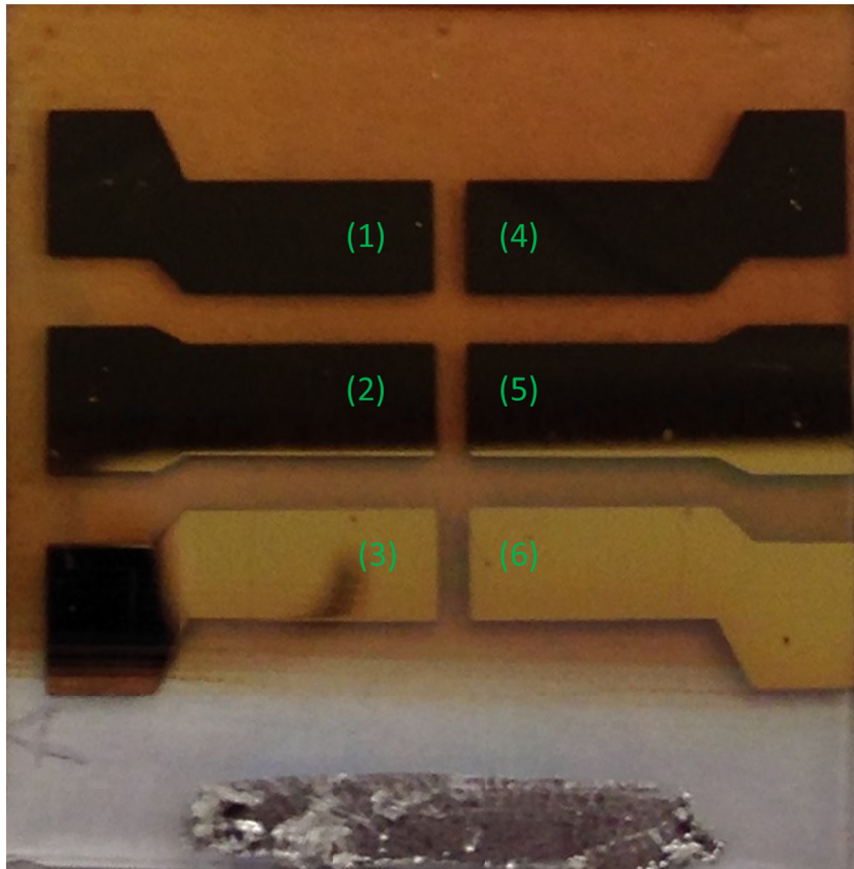


Figure 4-4. Real device with device structure of ITO/CdS/PbS QD/Au where PbS QD of size 2.5 nm was used to make ~200 nm thick layer of QD.

These results can be compared with heterojunction devices based on other partner materials such as ZnO, Bi₂S₃, and TiO₂. Solar cells utilizing 1.6 eV band gap QDs achieved V_{OC} , J_{SC} and PCE values of < 600 mV, < 5.0 mA·cm⁻² and $< 2.0\%$ respectively.[116] Choi *et al.* constructed a solution processed PbS-QD tandem solar cell with ZnO NC as a heteropartner.[140] The best PbS-QD tandem solar cell did attain a V_{OC} of 0.91 volts, but the J_{SC} , FF, and PCE were all lower than reported here. Luther *et al.* constructed a 3% bilayer PbS/ZnO QD heterojunction solar cell using air-stable 1.3 eV PbS QDs.[104] For a similar QD size, their FF is comparatively larger than the

present results, resulting in a larger PCE even though the J_{SC} and V_{OC} are similar. Recently, Brown *et al.* demonstrated improvements in PCE for ZnO/PbS QD heterojunction device through the incorporation of a MoO₃ interlayer between the PbS QD layer and the back contact.[159] They achieved highest efficiency of 3.5% from dots having an effective band gap of 1.3 eV and using gold as a back contact. For larger dots their devices show slightly better performance than what has been demonstrated here. Employing 3.5 nm diameter PbS QDs and an approach similar to that of Brown *et al.*, Gao *et al.* fabricated ZnO NC/PbS QD solar cells showing 4.4% PCE with a J_{SC} of 18 mA·cm⁻². [138] Rath *et al.* [160] employed Bi₂S₃ nanocrystals as an n-type semiconductor in their p-n junction based solar cell based on p-type PbS-QD. Their best device demonstrated V_{OC} 0.44 volts, with a power conversion efficiency of 1.6% for 860 nm (1.4 eV) PbS-QDs and over 1% for 1300 nm (0.95 eV) PbS-QDs. Several other reports of PbS QD solar cells exist with PCE results in the 3-5% range.[161, 162] Recently, a record QD thin film solar cell efficiency was reported by Ip *et al.* based on a hybrid passivated PbS QD layer deposited onto a ZnO/TiO₂-coated substrate.[143] Ip and co-workers achieved a remarkable PCE of 7%, suggesting that further improvements lie ahead for the field.

Experimental and theoretical (modeled) external quantum efficiency (EQE) for the solar cell from Figure 4-3 is shown in Figure 4-5. [15] First, the complex refractive indices, $\tilde{n}(\lambda) = n(\lambda) + ik(\lambda)$ for the materials used were obtained by spectroscopic ellipsometry (SE). Afterwards, the electric field strength and photo-induced carrier generation rates were calculated as functions of wavelength and position in the film stack following the method outlined by Petterson *et al.* [163] Specifically, an optical model

based on a 2×2 system transfer matrix [163] was applied by P. Roland in our group to model the QE and current losses of solar cell devices shown in Figure 4-1. Finally, the EQE curve shown in Figure 4-5 was calculated by summing the photons absorbed within the CdS and PbS-QD layers, assuming one electron-hole pair per absorbed photon. While including recombination can in principle yield more detailed performance modeling, specific recombination considerations are excluded as the QD film electronic properties are not yet fully understood. The result is a prediction of the maximum EQE curve attainable with the given solar cell structure.

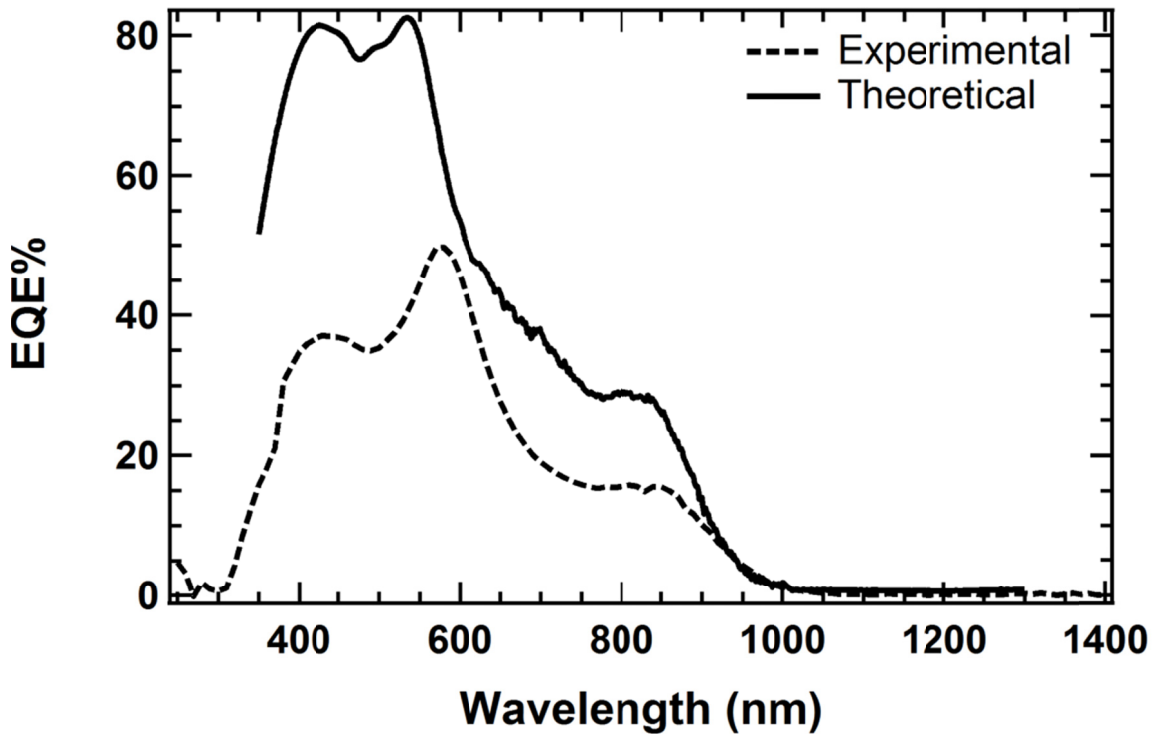


Figure 4-5. External quantum efficiency spectrum of the PbS-QD solar cell featured in Figure 4-1 from both theoretically and experimentally obtained data. In the theoretical EQE, charge collection contributions from both CdS and PbS-QD layers are included, and recombination losses are neglected.

The photocurrent generated between 515 and 900 nm is attributable to absorption in the PbS-QDs absorber layer followed by electron transfer to the CdS window layer. The small peak in EQE near 450 nm in Figure 4-5 may represent photocurrent contributed by the CdS film, which absorbs strongly for photon energies above the bandgap of ~ 2.4 eV (515 nm). Unlike CdTe/CdS thin film solar cells, these data show contributions from carriers photogenerated in the thin CdS window layer.

As mentioned above, an optical model, based on a 2x2 system transfer matrix for solar cell device with device structure as given in Figure 4-1, was constructed.[15] Figure 4-6 shows the calculated reflectance and transmittance curves for the thin film stack using this model. Figures 4-7(a) and 4-7(b) show the results of an optical model calculation of the electric field strength, $|E|^2$, and charge carrier generation rate, G , as functions of depth and wavelength. Figure 4-7(b) shows that the CdS absorbs light uniformly from 410 nm to 540 nm. At these wavelengths, however, significant absorption still takes place in the PbS-QD film within the first 120 nm.

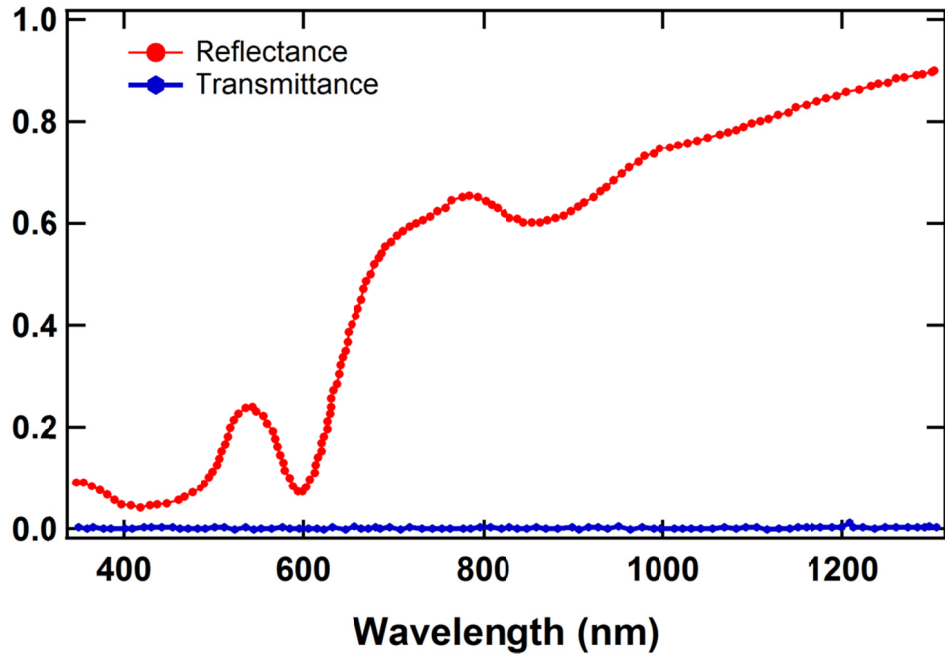


Figure 4-6. Reflectance and transmittance of a stack of solar cell device obtained by using an optical model based on 2x2 transfer matrix.

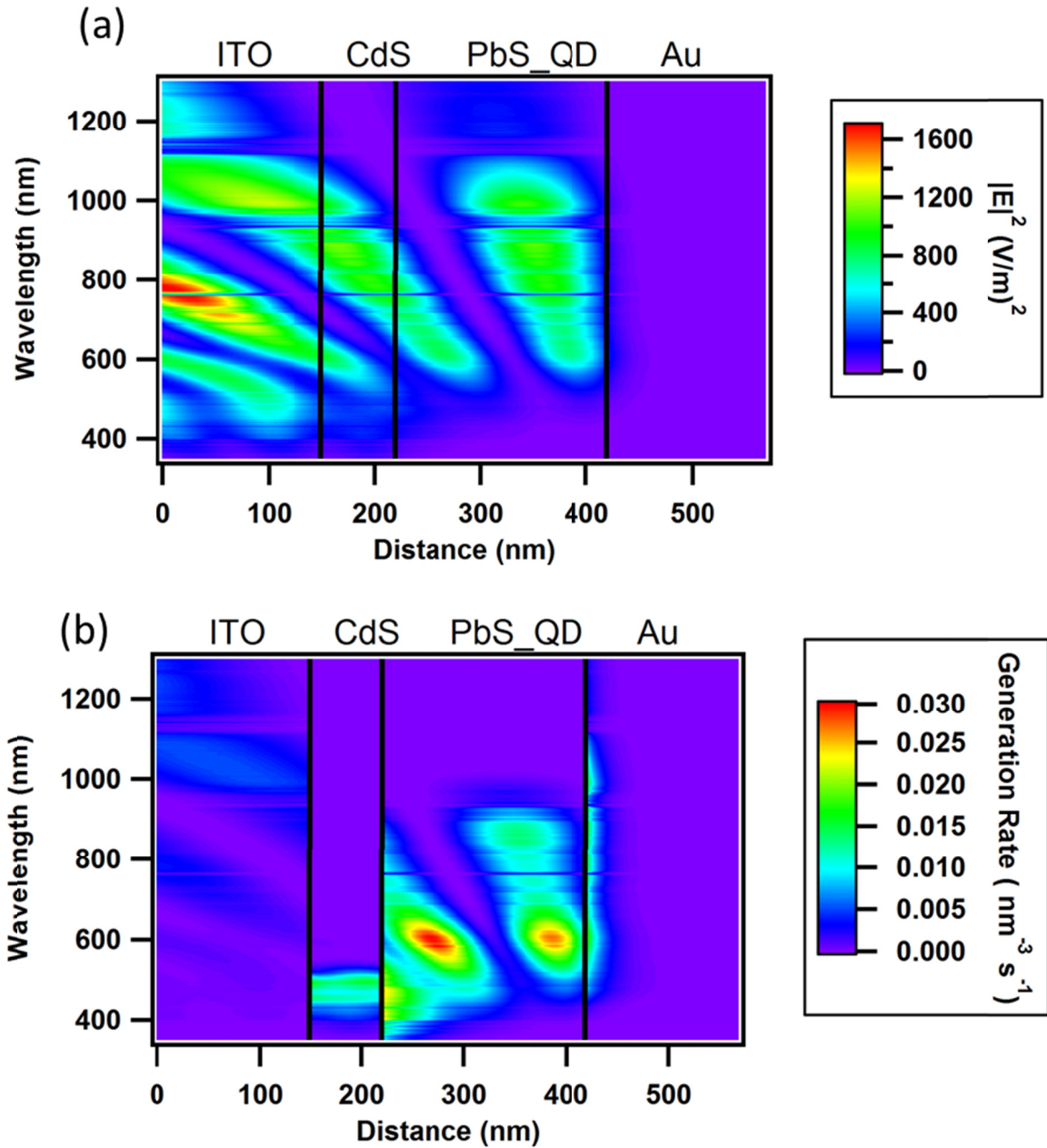


Figure 4-7. (a): Optical model calculation of the electric field strength with respect to film depth and wavelength, (b) Optical model calculation of the charge carrier generation rate with respect to film depth and wavelength

The optical model shows that collection could be improved by reducing reflectance at 550 nm and in the near infrared region (NIR) of the spectrum (Figure 4-6).

This model was also used to calculate the electric field strength and charge carrier generation rate as a function of the depth and wavelength.[164] The model shows that the CdS absorbs light relatively uniformly from 410 nm to 540 nm (Figure 4-7). A theoretical maximum of the QE was calculated by counting every absorbed photon as a contributor to the light-induced current in two cases: the first by considering the collection contribution only from PbS-QD layer and the second by considering the collection contribution from both CdS and PbS-QDs. By counting every absorbed photon as a contributor to the light induced current, a theoretical maximum for the QE curve can be calculated. Figure 4-8 shows the QE curve that would result from only the PbS-QD layer; loss contributions associated with reflection from each layer are shown with dotted lines. Figure 4-9 shows the QE curve “if” a collection contribution from the CdS layer is considered. By comparing Figures 4-8 and 4-9, it is seen that the QE curve in the 400 to 540 nm region can be represented as a contribution from both layers; and therefore one cannot conclude which layer is responsible for the photocurrent in this spectral region. However, consideration of the location of absorbed photons in the PbS-QD film, it is reasonable to conclude that the majority of this region’s photocurrent comes from the QD film.

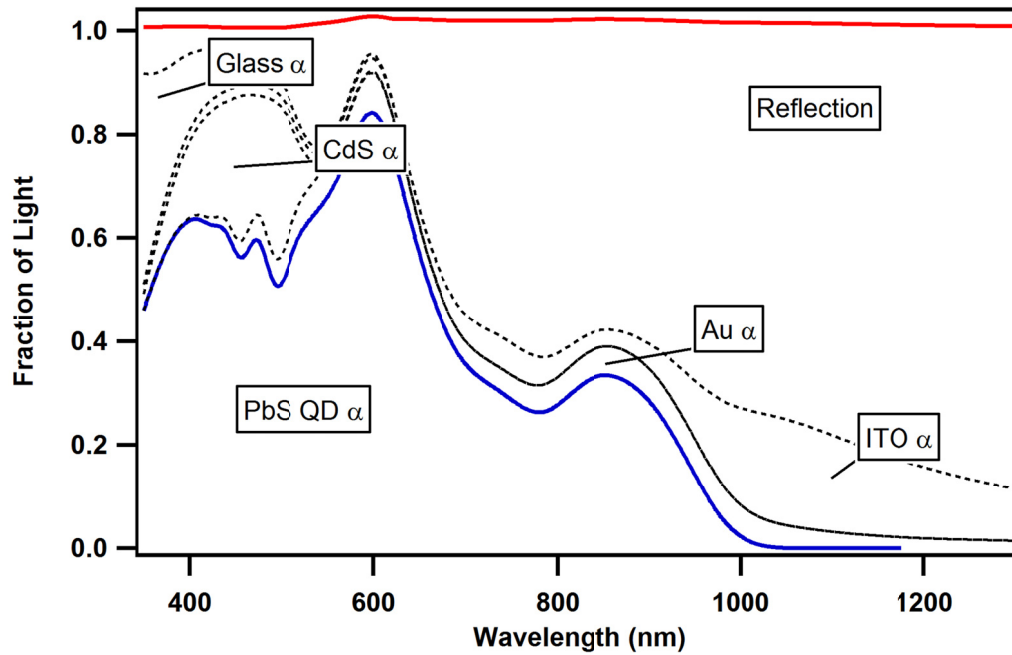


Figure 4-8. Theoretical study of the fraction of light absorbed within each layer. The red curve shows the sum of absorption in all layers, and the blue curve shows the fraction of light absorbed within the PbS-QD layer. Note that the absorption within the CdS layer is separated from that of the PbS-QD layer.

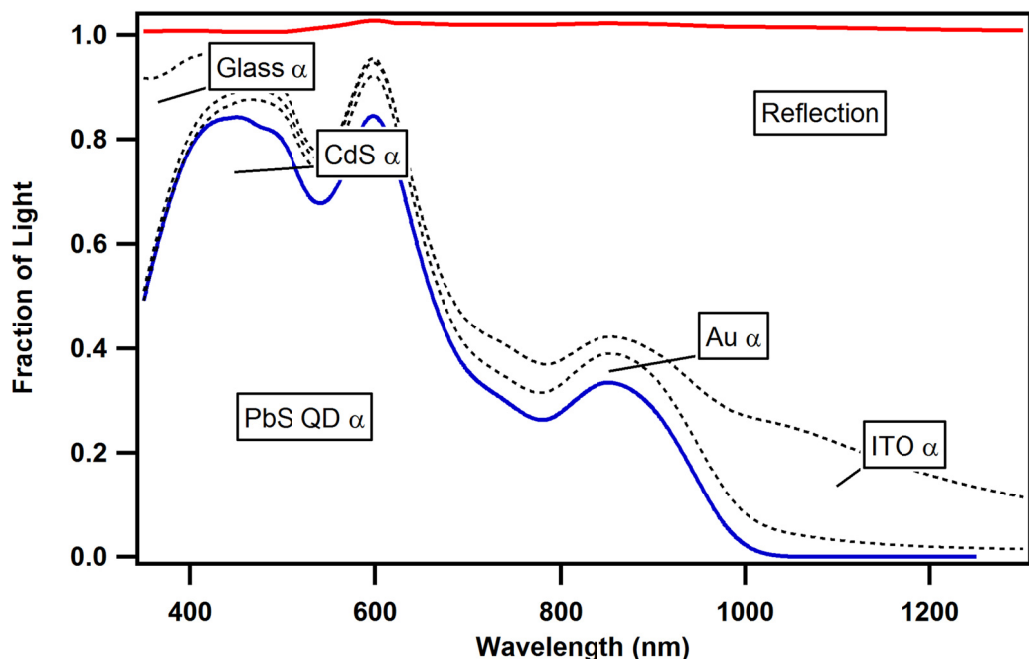


Figure 4-9. Theoretical study of the fraction of light absorbed within each layer. The red curve shows the sum of absorption in all layers, and the blue curve shows the fraction of light absorbed within the CdS and PbS-QD layers.

The performance of solar cells presented here can be tuned by changing the QD size and hence the electronic energy levels within the QDs. Figure 4-10 shows the variation of V_{OC} , J_{SC} , FF and PCE for solar cells assembled using different size QDs as a function of the first exciton peak (effective band gap energy, E_g) of the QDs in eV. Six devices were fabricated at a time and reproduced three times. As each prepared substrate consists of six cells, each column in Figure 4-10 is the average of 6 cells with the error bar representing the standard deviation. We see that V_{OC} decreases with decreasing bandgap (increasing QD size and decreasing quantum confinement). As expected, V_{OC} depends on the valence band and conduction band (HOMO and LUMO) levels of the QDs and is strongly correlated with the size of the QDs.

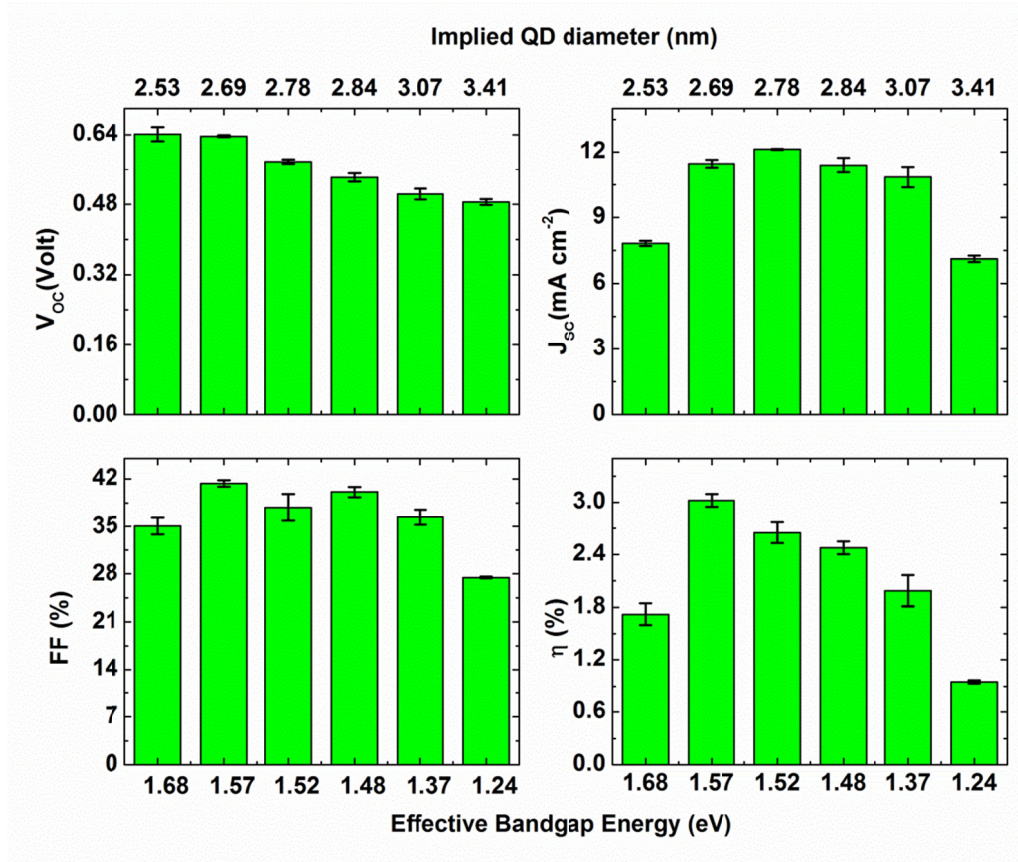


Figure 4-10. Dependence of V_{oc} , J_{sc} , FF and PCE on the diameter and effective band gap energy (the first exciton peak, E_g in eV) of PbS- QDs; All solar cell devices were prepared using ~ 200 nm thick EDT-capped PbS-QD film deposited onto ~ 70 nm thick CdS. Diameters of the QDs are based on the first exciton peak values as measured in solution.[62, 120]

Short circuit current density decreases for both smaller and larger size QDs. For smaller QD diameters (large bandgap), the long wavelength absorption cut-off moves to shorter wavelength, reducing the portion of the spectrum absorbed within the PbS-QD layer, resulting in a decrease in J_{sc} . Larger dots (smaller bandgap) allow larger portions of the solar spectrum to be absorbed by the PbS-QD layer but the driving force for electron transport to the CdS is reduced because of the resulting band alignment.

Therefore, judicious selection of the QD size is necessary to achieve optimal J_{SC} . The fill factor shows a similar trend as that of J_{SC} while photo-conversion efficiency demonstrates a maximum for PbS-QDs of diameter 2.5 nm corresponding to the first exciton peak at 792 nm.

The variation of V_{OC} , J_{SC} , FF and PCE for solar cells assembled using PbS-QDs of size 2.6 nm, corresponding to the first exciton peak at 816 nm, with respect to CdS film thickness is shown in Figure 4-11. Since the thin PbS-QD film (~200 nm) is deposited on top of CdS by a solution based method, surface roughness of the CdS film (Figure 4-12) may hinder uniform deposition of the QD film. It is found that surface roughness of the PbS-QD film (Figure 4-13) is larger when deposited onto thicker CdS films. This rough surface may yield a higher density of trap centers on the QD film surface, increasing the reverse saturation current density (J_0). One clear effect of defect-related recombination is a reduction in the open circuit voltage (V_{OC}), which depends not only on J_0 but also on the photo-generated current density (J_{ph}) of the solar cell by the relation

$$V_{OC} = \frac{nk_B T}{e} \ln \left(\frac{J_{ph}}{J_0} + 1 \right) \quad (4.3)$$

where n is the ideality factor, K is Boltzman constant, T is absolute temperature, and e the charge of an electron. J_0 depends on the recombination in the solar cell and may vary by orders of magnitude. Hence, V_{OC} is one measure of recombination in the device for the thicker CdS layers as shown in Figure 4-10. In our case, V_{OC} decreases as the CdS thickness increases from 35 nm to 150 nm. However, for CdS/CdTe solar cells the V_{OC} dependence on CdS thickness follows an opposite trend. Plotnikov *et al.*[165] studied

the V_{oc} dependence on CdS thickness for CdTe cells prepared on bare TEC-15 and HRT-coated TEC-15 substrates and found higher V_{oc} for higher CdS film thickness until it became maximum for about 130 nm CdS film. However, they found optimized CdS/CdTe device efficiency when the CdS film thickness was about 80 nm on bare TEC-15 and 30 - 130 nm on HRT TEC-15.

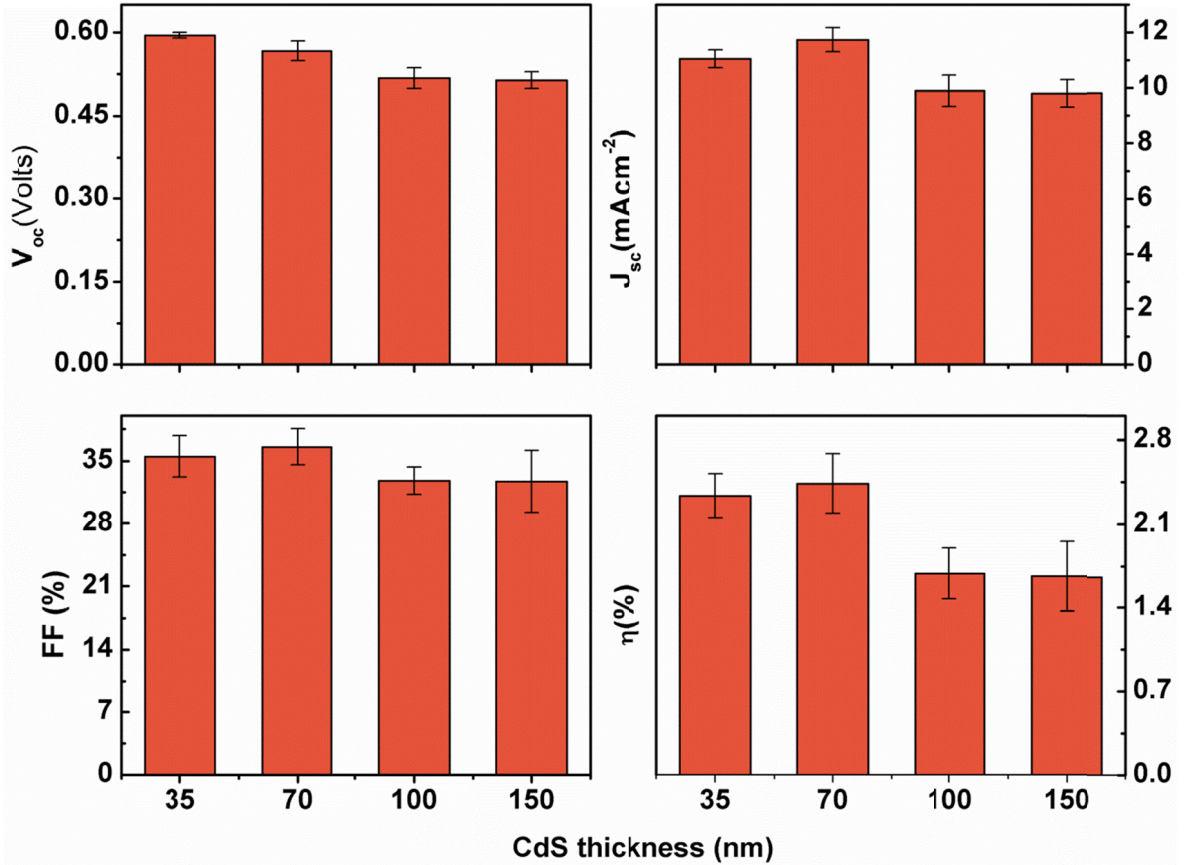


Figure 4-11. Dependence on window layer thickness of the performance of PbS-QDs solar cells; Six devices for each CdS thickness (35, 70, 100 and 150 nm) were fabricated on a single substrate by depositing a PbS-QD film of thickness ~ 200 nm. The PbS QD diameter was 2.6 nm, corresponding to the first exciton peak at 816 nm (1.52 eV).

The thickness dependence of the surface roughness of CdS films, deposited onto glass substrates by sputtering method, was studied using atomic force microscopy (AFM). Figure 4-12 (a, b, c) shows the height profile and 4-12 (d, e, f) shows the 3D image for CdS film of thickness 35, 70 and 100 nm respectively. Surface roughness of the CdS films of thickness 35, 70, 100, 150 and 250 nm are found to be 1.0, 0.8, 1.7, 1.4 and 4.4 nm respectively. Similarly, Figure 4-13 shows the AFM results (height profile and 3D images) based on PbS-QD films, deposited onto the CdS film of different thicknesses. These QD films were deposited by solution based method with a final film thickness of ~150 nm. As measured by AFM, the PbS-QD film surface roughness values are 0.9, 0.8 and 1.4 nm for LbL deposition on 35, 70 and 100 nm thick CdS films. This shows that the surface roughness of the PbS-QD films depends on the surface roughness of the window layer. In Figure 4-13, (a) and (b) represent height profile and (c) and (d) represent 3D image for PbS-QD films deposited onto 100 nm CdS films respectively. Please note that the surface roughness was measured in the region excluding the some anomalous feature as seen in Figure 4-13.

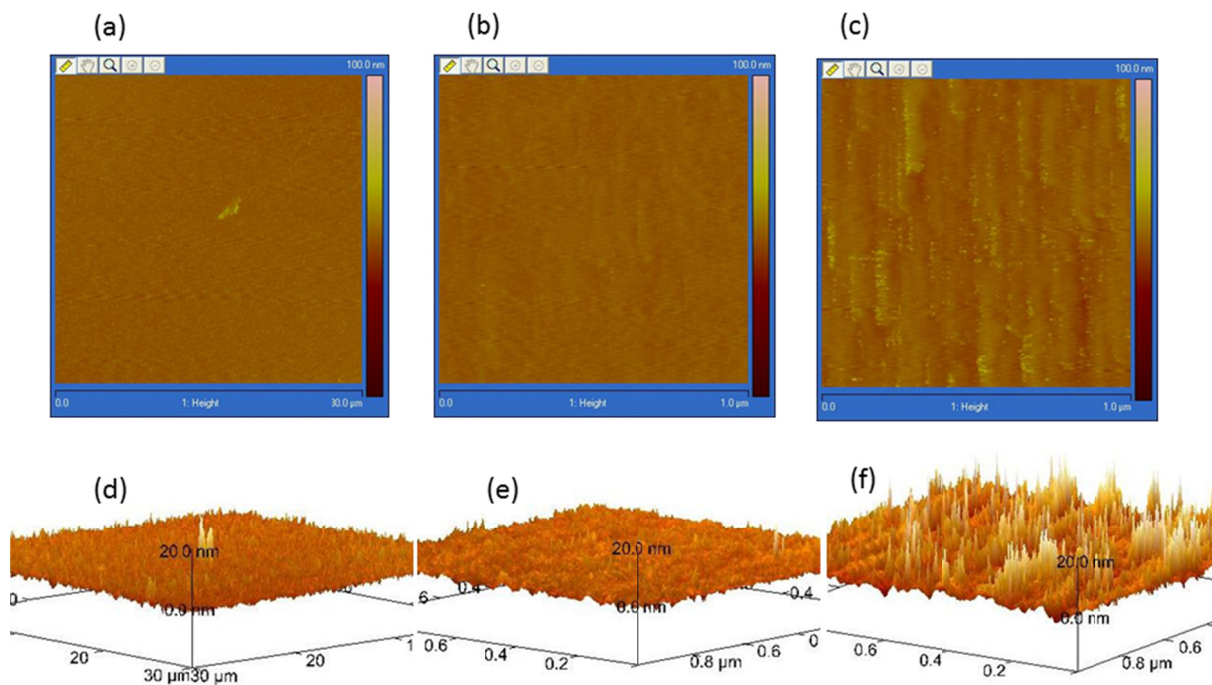


Figure 4-12. Surface roughness of CdS films with respect to CdS thickness in nm.

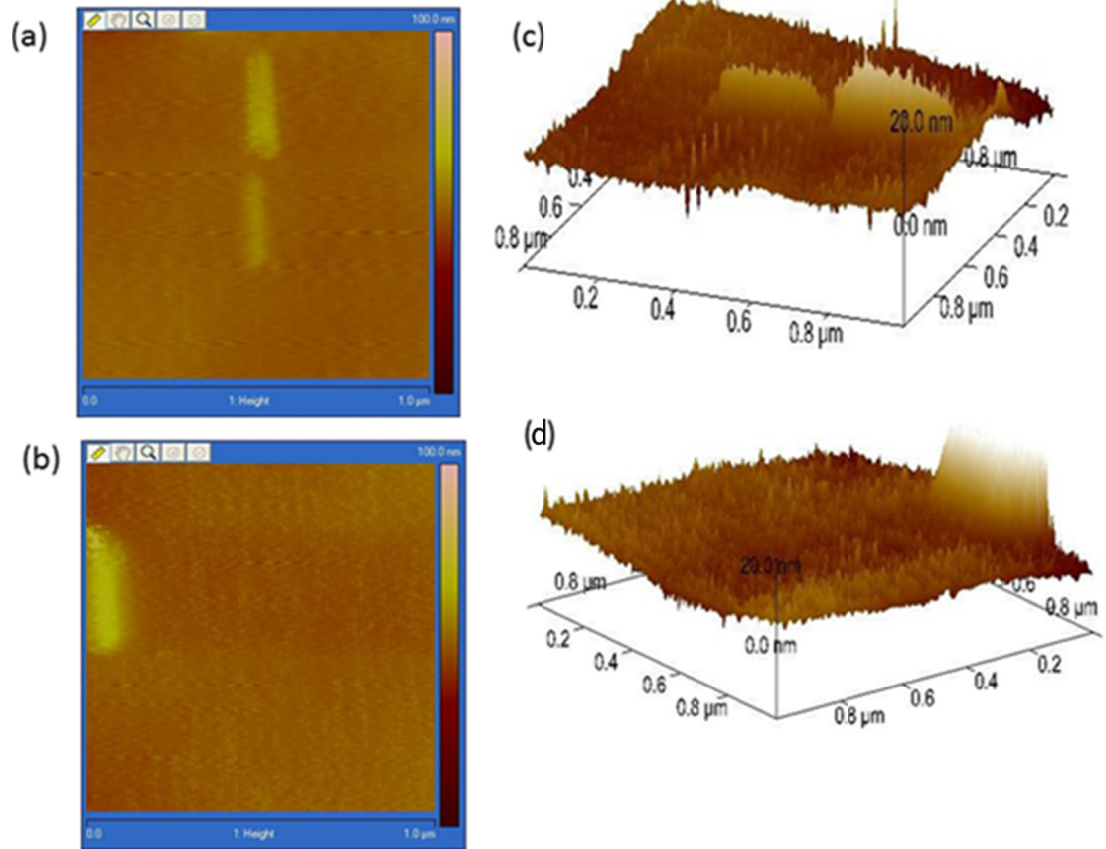


Figure 4-13. Surface roughness on PbS-QD films deposited onto CdS films of different thicknesses.

In most of the devices fabricated here with CdS thickness of 70 nm, higher J_{SC} and ultimately higher efficiencies were observed. The EQE (Figure 4-5) shows an apparent contribution of the CdS to the photocurrent, especially in the higher energy region. This contribution is found to be maximized when CdS thickness is 70 nm – indicating an optimum thickness of the window layer at 70 nm. With increasing photon energy above the band gap of 2.42 eV, CdS shows an increasing absorption coefficient. For a 100 nm thick CdS film, the penetration depth for 2.48 eV (500 nm) photons is ~62 nm. As the CdS layer thickness is increased, the absorption within CdS of higher energy

photons reduces the photon flux absorbed within the PbS-QD layer, and this may in part explain the observed drop in J_{SC} . The FF is lower for the two thickest CdS films, in accordance with higher series resistance and lower shunt resistance as shown in Figure 4-14. Figure 4-14 shows variation of the average values of series and shunt resistances, obtained from 6 cells in a device, with respect to CdS window layer thickness. A high series resistance reduces J_{SC} , and contributes to a reduced FF. A low shunt resistance reduces V_{OC} and also lowers the FF. Because of the organic molecules in QDs, mobility of the charge carriers is low[166], R_S values are higher, and R_{Sh} values are smaller than they appear in commercial thin film solar cells. The area-normalized series and shunt resistances of our best device are $21 \Omega\text{cm}^2$ and $204 \Omega\text{cm}^2$ respectively. Series and shunt resistances of CdS/CdTe solar cells of device area of 0.08 cm^2 obtained by Vigil *et al.*[167] were $2.9 \Omega \text{ cm}^2$ and $787 \Omega\text{cm}^2$. The highest efficiency they achieved from this device is 12.3%. Similarly, from a device area of 0.25 cm^2 , Pena *et al.*[168] obtained series and shunt resistances $8.0 \Omega\text{cm}^2$ and $631 \Omega\text{cm}^2$ from CdS/CdTe solar cells of efficiency 6.3% with Cu/Mo back contact. Figure 4-14 shows that the series resistance for 70 nm CdS layer thickness is small ($21 \Omega \text{ cm}^2$), and that it increases with increasing CdS thickness. Shunt resistance is large for smaller thickness films, which indicates that as the thickness of the window layer is increased, it provides shunting pathways due to the presence of defect states or recombination centers.

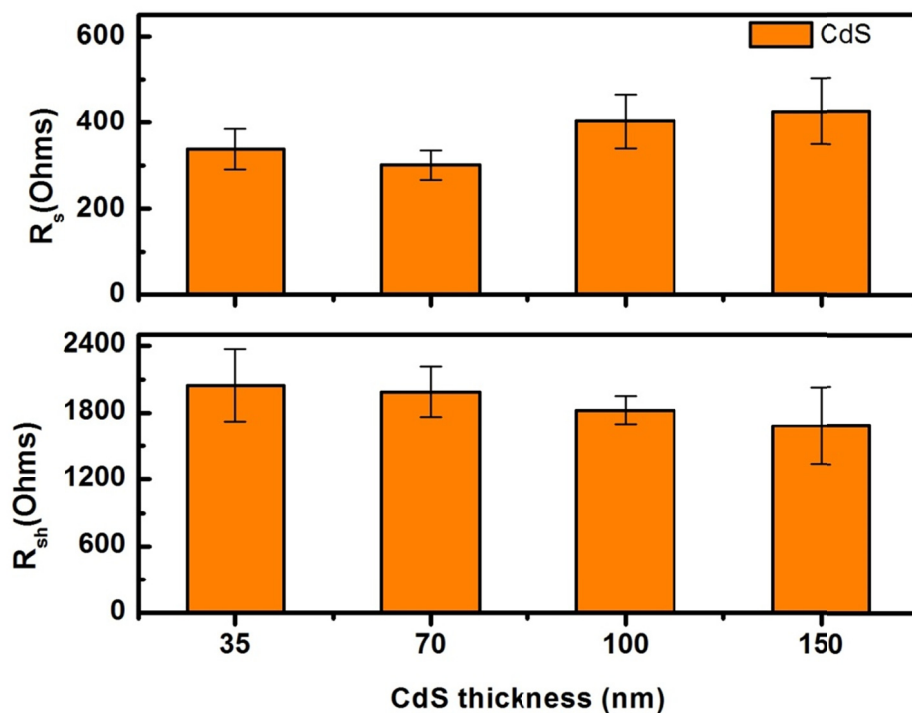


Figure 4-14. Series and shunt resistances with respect to CdS thickness in nm; The PbS QD diameter was 2.6 nm.

The stability of the devices was studied by measuring their J-V characteristics with respect to time following a procedure similar to that of Tang *et al.*[14]. For the stability test, two identical devices were made simultaneously in air. One of the devices was kept in laboratory air and the other in an inert N₂ atmosphere; both were kept in the absence of illumination. For the first 8 days, J-V curves were measured daily. After 8 days, they were measured in the intervals of few days over a period of more than two months for a total of 33 measurements. In Figure 4-15, the relative change in V_{OC} , J_{SC} , FF and PCE are plotted with respect to time in days. The relative change is obtained by dividing each day's results by the first day's results. The purification of the QDs after

synthesis and the fabrication of the devices were all done in ambient air. All of these devices fabricated here show better performance a few days after their first measurement as shown in Figure. This may be due to the better surface passivation due to air and drying of the QD films resulting in improved performance in the second day and thereafter compared to the first day. This indicates that the performance of these devices does not degrade significantly in air on the timescale of months, though longer time studies are required to determine the extent of the air-stability of these devices.

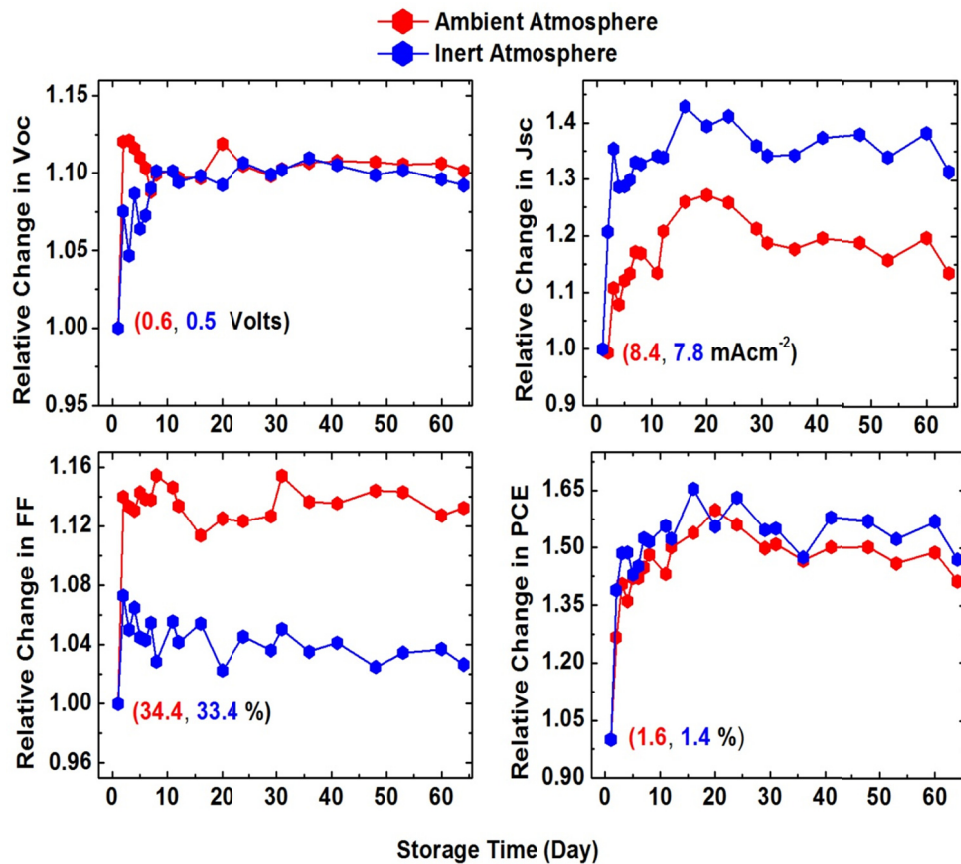


Figure 4-15. Representative device performance evolution after more than sixty days; each datum point represents the average relative value change of six cells. All values are relative to the initial values of the cells. In the brackets, the magnitudes of the first day measurement are shown. Both devices were stored in the absence of light.

In order to determine the approximate carrier concentrations of the PbS QD (size ~2.8 nm) and bulk CdS films used in the heterostructure device discussed earlier, Schottky junction devices were fabricated from each film separately for use in capacitance-voltage testing methods and Mott-Schottky analysis. [15] For the PbS QD device fabrication, LbL deposition method was used in which case oleic acid ligands were replaced by EDT and aluminum was used as a back contact to complete the device. The device area used for these devices was 0.0975 cm². The data analyzed demonstrated that the PbS QD layer was in full depletion mode at potentials near open circuit, which was demonstrated by a flat (unchanging) C-V curve in the region near open circuit. Only when the device is placed in forward bias (i.e. positive potential applied to the PbS QD layer) does the capacitance change (increases with increasing positive potential). Using the relation for a parallel plate capacitor

$$C = \frac{A\epsilon\epsilon_0}{d} \quad (4.4)$$

where C is the capacitance, A is the area, ϵ is the dielectric constant of the material (thin-film semiconductor in this instance), ϵ_0 is the permittivity of free space and d is the distance between the conductive surfaces taken as the thickness of the fully-depleted PbS layer (~ 58 nm). In some cases, the built in potential (V_{bi}) and carrier density (N) are found larger than expected values. The high values of these two parameters can be explained by including a constant capacitance generated due to the charge injection barriers at the electrodes. This constant capacitance can be removed from the observed capacitance values by knowing the thickness of the fully depleted film.[169] The

corrected data is shown in Figure 4-16 and the carrier concentration can be extracted from the slope of the linear region via the equation (4.5) [170, 171]

$$\frac{A^2}{C^2} = \frac{2(V_{bi} - V)}{q\epsilon\epsilon_0 N} = \left(\frac{-2}{q\epsilon\epsilon_0 N} \right) V + \frac{2V_{bi}}{q\epsilon\epsilon_0 N} \quad (4.5)$$

where V is the applied bias, N is the carrier concentration and q is the charge of the carrier. For forward bias, V is positive and for reverse bias, V is negative. The built in potential (V_{bi}) and doping density (N) can be calculated using equation (4.5) and the experimental data plot. For large values of injection barrier capacitance, the $(A/C)^2$ vs. bias voltage curve appears more flattened as shown in Figure 4-16. In this case, the Mott Schottky fits indicated larger V_{bi} (x-axis crossing) and carrier density N values (inversely proportional to the slope), than the true values. The large increase in capacitance in PbS is due to the effect of hole injection into the PbS QD which increases the amount of charge. These holes on PbS can only be extracted when a sufficient external bias is provided and thus decreasing the capacitance of the device. PbS QD was found to be p-type in nature and the carrier concentration for this material was estimated as $5.7 \times 10^{16} \text{ cm}^{-3}$, which is similar to the values reported elsewhere for PbS QD films. [172-174]

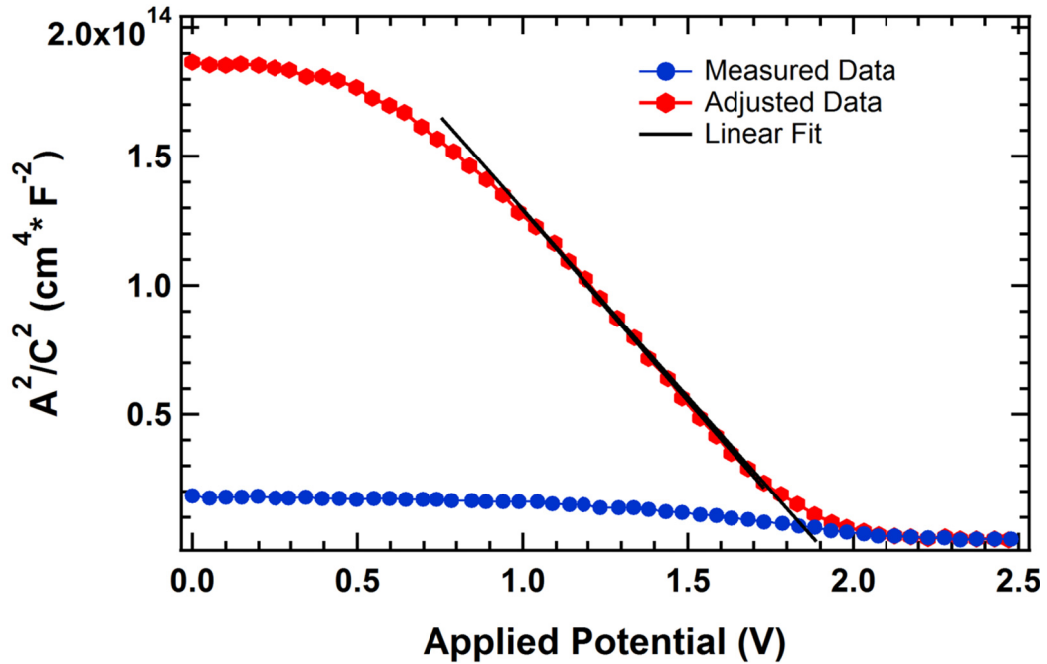


Figure 4-16. Mott-Schottky plot for PbS QD/Al Schottky junction showing the measured area²/capacitance² data and the data adjusted to eliminate constant capacitance due to charge injection barriers per the method of Willis et al.[169]

For the CdS sample, the measured data also indicated that the device was in a full depletion condition near open-circuit voltages. However, the calculated depletion width was approximately equal to the film thickness of 200 nm, so no adjustment was made to the measured capacitance data. The data used for the Mott-Schottky analysis is shown in Figure 4-17, from which the carrier concentration was estimated as approximately $9.95 \times 10^{15} \text{ cm}^{-3}$, which is close to some of the values reported in literature for CdS films prepared using various deposition methods.[175-177]

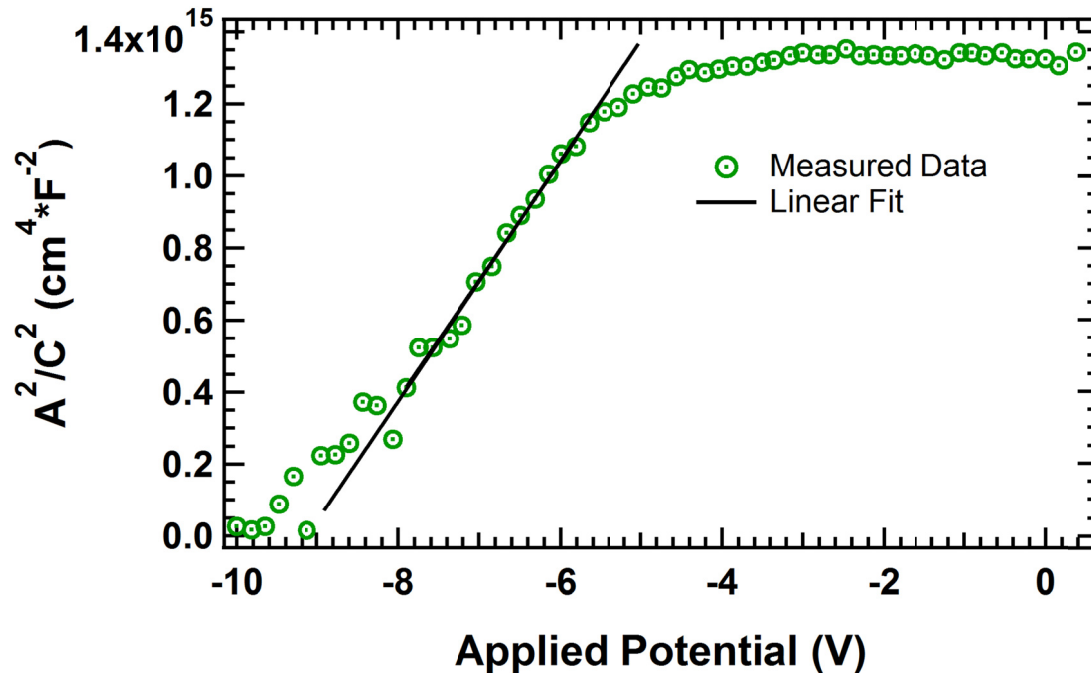


Figure 4-17. Mott-Schottky plot for CdS/Ag Schottky junction showing the measured area²/capacitance² data.

4.4 Conclusions

Synthesis of various sizes of colloidal PbS-QDs was made for the application of thin film heterojunction solar cells. Before the application, bulk CdS and PbS-QD films were characterized using optical absorption spectroscopy, KPFM, UPS/XPS, AFM, and capacitance-voltage measurements. From these measurements information regarding the optoelectronic properties of the materials, their work functions (and electron affinity), valence and conduction band positions, film surface roughness, and net carrier concentrations were gathered. With these fundamental data in hand, these semiconductor materials were then fabricated into solar cells. The first heterojunction solar cells based on PbS-QDs and RF magnetron sputtered CdS thin films, was demonstrated achieving efficiency greater than 3%. The devices exhibited higher V_{OC} values compared to

Schottky junction solar cells and other heterojunction solar cells based on PbS-QDs. It is found that PbS-QDs with the first exciton peak near 800 nm yield the best devices because in this case both V_{OC} and J_{SC} are higher. Similarly, CdS thin films with thicknesses of near 70 nm are considered as an optimized window layer thickness for the CdS/PbS-QD combination. From this study, it is concluded that understanding and optimizing the quality of the coupled QD film, as well as the properties of the interface between the CdS and the PbS-QD film, are both essential to enhancing the performance of heterojunction QD thin film solar cells in the future.

Chapter 5

Synthesis and Characterization of Iron Pyrite and Tin Disulfide Nanocrystals

5.1 Introduction

Iron pyrite (persulfide, FeS_2) has attracted considerable attention as a potential absorption layer in thin film photovoltaics (PV) because of its abundance, low toxicity, high absorption coefficient in the near-infrared and visible spectral regions,[178-180] suitable band gap energy,[181, 182] and low material cost.[183-185] Although the ~ 0.95 eV bandgap energy of bulk FeS_2 corresponds to a thermodynamically attainable photo-conversion efficiency of $> 20\%$, [186] the record device efficiency stands at just $\sim 2.8\%$ as achieved by the Tributsch group in the 1980s.[183] In recent years, FeS_2 nanocrystals (NCs) have been investigated as a potential route to efficient solution-based PV technologies.[184, 187] Despite considerable additional effort, no improvement in FeS_2 -absorber-based PV performance has yet been demonstrated.

Previous thermal injection syntheses of colloidal iron pyrite NCs have utilized chlorine-halogenated iron precursors such as $\text{FeCl}_2 \cdot 4\text{H}_2\text{O}$, FeCl_2 and FeCl_3 . [184, 185,

187-189] Similarly, iron pyrite NCs have been prepared via hydrothermal synthesis using a single source precursor which is initially prepared using iron(III)chloride (FeCl_3).[179, 190] I discuss here the use of iron (II) bromide (FeBr_2), which has been reported recently by Bhandari et al. as a new iron precursor for FeS_2 NC synthesis in the hot solution injection process. [191] Anhydrous FeBr_2 has already been used in a number of syntheses of iron compounds due to its relatively high solubility in organic solvents, [192, 193] though to our knowledge, no previous report has been made on the synthesis of FeS_2 employing FeBr_2 as a precursor. Iron pyrite is an Earth-abundant and non-toxic material and, based on the globally harmonized system of classification and labeling of chemicals (GHS), using iron (II) bromide rather than iron (II) chloride reduces the toxicity of the synthetic route to FeS_2 NCs. Iron compounds halogenated with chlorine are corrosive, and represent acute and chronic hazards to human and aquatic environments; in contrast, FeBr_2 does not possess any of these labels.[194] In addition, iron (II) chloride exhibits greater sensitivity to air and moisture, whereas sensitivity of FeBr_2 to air and moisture is negligible. Moreover, it is found that the use of FeBr_2 , together with carefully-optimized colloidal synthetic procedures, facilitates the reproducible preparation of highly crystalline, phase pure and air stable FeS_2 NCs; the author reports here on the characterization of these FeS_2 NCs in solution and thin film form.

Sheet resistance, resistivity, majority carrier type, carrier density, and mobility of thin films are important properties of semiconductors and are critical parameters in materials research. These physical parameters explain the transport behaviors of semiconductor films which determine their potential utility for device applications. Significant studies of these properties for FeS_2 NC films remain relatively rare,[184]

although some reports exist for FeS₂ films prepared by spray pyrolysis, electrodeposition, sol gel and molecular ink methods respectively.[195-198] In this work, hot probe, four point probe, and Hall measurement techniques are employed to characterize the electronic properties of FeS₂ NC-based films, and to assess their applicability within electronic devices.[191]

Tin (IV) disulfide (SnS₂) is considered as a good buffer layer for a pyrite solar cell because it is expected to form a type-II heterojunction with FeS₂. [199] SnS₂ is an n-type and direct band gap semiconductor with a band gap between 2.07 to 2.44 eV.[200, 201] Nanocrystalline SnS₂ has been reported to be prepared using various non-vacuum methods.[202, 203] SnS₂ is two dimensional layered nanostructure and it is synthesized by thermal decomposition of the precursor, tetrakis(N,N-diethyldithiocarbamate) tin (IV) [Sn(C₅H₁₀NS₂)₄] in an organic solvent at elevated temperature.[204] Among the variety of layered materials, SnS₂ is of particular interest because of its unique structural properties.[205] SnS₂ is composed of tin atoms sandwiched between two layers of hexagonally arranged close-packed sulfur atoms. FeS₂ has a very deep conduction band level, and it forms a Type-I heterojunction with common window layer materials such as ZnO and CdS. SnS₂ represents one of the n-type semiconductors which can make type-II heterojunction with FeS₂.

In this chapter, synthesis of these two nanocrystals (FeS₂ and SnS₂) will be described in detail. For their complete identification, both the NC solutions and NC films are studied in detail using a variety of characterization methods and instrumentation. The author will also detail the sulfurization approach for fabrication of FeS₂ NC thin films.

The author will discuss properties and performance of thin FeS₂ films, before and after sulfurization, for photovoltaic application.

5.2 Experimental

5.2.1 Materials for synthesis of FeS₂ and SnS₂ nanocrystals

Iron (II) bromide (FeBr₂, 98.0%), trioctylphosphine oxide (TOPO, 99%), oleylamine (OLA, 70%), 1,2-hexanediol (98%), hydrazine (Hy., 98%), toluene (99.8%), chloroform (99%), tin tetrachloride pentahydrate (SnCl₄.H₂O), sodium N, N-diethyldithiocarbamate trihydrate were purchased from Sigma Aldrich and elemental sulfur (S, 99.999%), Methanol (99.8%) and absolute anhydrous ethanol were purchased from Fisher Scientific. All chemicals were used as obtained.

5.2.2 Synthesis of FeS₂ NCs

Solution-based synthesis and deposition offers a potentially low-cost and scalable photovoltaic manufacturing method for large glass substrate processes and roll-to-roll processing on flexible substrates. Numerous routes have been followed to synthesize FeS₂ NCs[184, 185, 187, 206] and here the author follows a solution-based approach based on thermal injection reaction of an iron salt solution with an elemental sulfur source. While others have utilized FeCl₂ as the iron source, the author has found that FeBr₂ yields improved results regarding crystal structure and infrared absorption. In a typical synthesis, which is performed in a Schlenk line under N₂ environment, about 1.49 mmol of FeBr₂ and 3 mmol of trioctylphosphine oxide (TOPO) are mixed in 30 mL of oleylamine (OLA) in a three neck flask under constant stirring (Figure 5-1). The FeBr₂

mixture is heated to 170 °C for ~2 hours and 30 minutes using a heating mantle; during this time, the sulfur precursor solution is prepared.

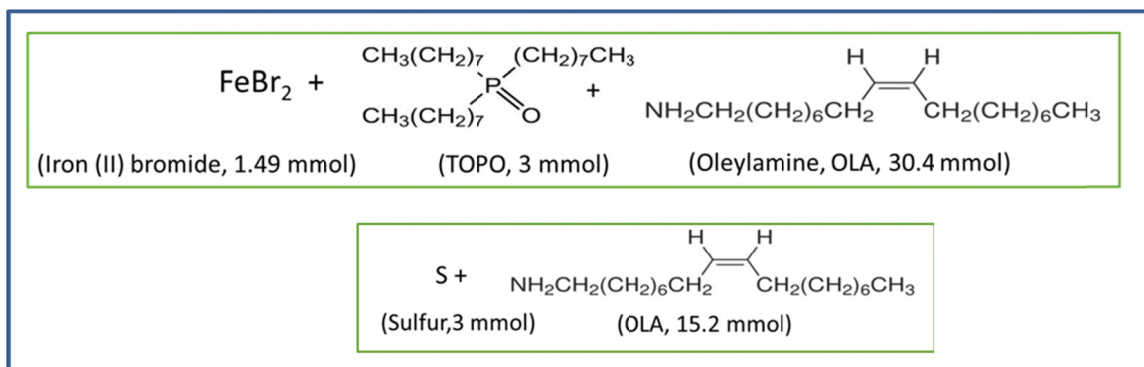


Figure 5-1. Chemical reaction for the synthesis of iron pyrite nanocrystals.

For this 8.98 mmol of elemental sulfur (~288 mg) is dissolved in 15 mL of OLA (Figure 5-1). For complete dissolution of sulfur in OLA, ~10 minutes of ultra-sonication is performed. The sulfur solution is kept in hot water bath at ~90 °C. Once the sulfur solution is ready, the temperature of the FeBr₂ solution is raised toward 220 °C, and once it exceeds 216 °C, the sulfur solution is rapidly injected. Nucleation of FeS₂ clusters initiates upon sulfur injection, and the growth of FeS₂ NCs proceeds at a temperature of 220 °C.

Following two hours at 220 °C, the NC solution is allowed to cool to room temperature, with continued stirring. Nanocrystals so obtained are washed a minimum of three times using methanol as a non-solvent and toluene or chloroform as solvent. For the first wash, methanol is added to the as-synthesized NC solution, followed by centrifugation for 10 minutes at 5000 rpm (2,400 x g). After decanting the supernatant, NCs were dispersed in toluene or chloroform with the assistance of sonication, and methanol is added to precipitate the NCs allowing for physical separation via

centrifugation. The wash procedure is repeated a minimum of three times. Finally NCs so obtained are dried under nitrogen gas flow.

During synthesis, TOPO is used as the surfactant and OLA as a non-coordinating solvent; in this method, FeS₂ NCs so obtained are understood to be capped by TOPO. However, the author found that FeS₂ NCs can be synthesized using OLA without the presence of TOPO. Likewise, high-quality FeS₂ NCs can also be synthesized using 1,2-hexanediol as the surfactant and OLA as a non-coordinating solvent. It is found that stability of the NCs capped with TOPO is improved compared with using only oleylamine. Hines and Guyot-Sionnest state that amines are weaker bases than phosphine oxide[207] and hence when TOPO/OLA mixture is used, TOPO binds more strongly to the NC than does OLA. The oxygen atom in TOPO forms a coordination bond with Fe, while the phosphorus atom coordinates with sulfur due to attractive charge interactions passivating both Fe and S sites as shown in Figure 5-2. However, when OLA is used both as coordinating and non-coordinating solvent, only the Fe atom is passivated with nitrogen (amine: R-NH₂) leaving S as dangling bond. When 1,2-hexanediol is used as coordinating solvent for FeS₂ NC synthesis, surface passivation is due to two oxygen atoms present in the molecules. One of the oxygen atoms makes covalent bond with Fe atom and another makes coordinating covalent bond with sulfur and thus passivating the NC surface.

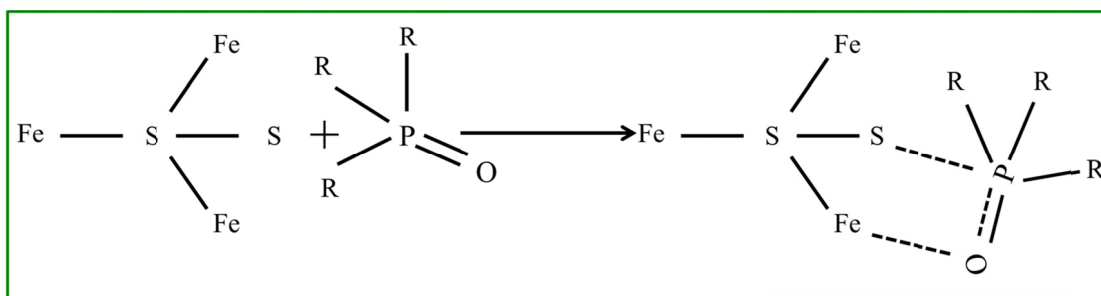


Figure 5-2. Surface passivation schematic of TOPO to FeS₂ NC.

5.2.3 Synthesis of SnS₂ Nanocrystals (NCs)

To accomplish SnS₂ NC synthesis, first the precursor, tetrakis(N, N-diethyldithiocarbamato) tin (IV) [Sn(C₅H₁₀NS₂)₄] was synthesized with the slightly modified version of Harreld and Schlemper. [204] For a typical reaction, 0.75 g of SnCl₄·5H₂O was dissolved in 20 mL of absolute ethanol. Similarly, 3.8 g of sodium N, N-diethyldithiocarbamate trihydrate was dissolved in 50 mL of absolute ethanol and filtered. The first solution was then added drop wise to stirred second solution. All these reactions were performed at room temperature at ambient environment. The reaction between the two solutions was instantaneous i.e. yellow solution was formed instantaneously when one solution was added drop wise. The bright yellow crystals were filtered, washed with DI water several times and dried in air. The purpose of washing with DI water is to dissolve NaCl, which is formed as a byproduct along with tetrakis-(N,N-diethyldithiocarbamato)tin(IV). The tetrakis-(N,N-diethyldithiocarbamato) tin (IV) dissolves in chloroform and hence to separate it from NaCl, the final product can also be dissolved in chloroform and filtered through the filter paper. The solvent is evaporated to get the pure final product.

SnS₂ NCs are synthesized with the slightly modified version of Seo et al. [208] For this 0.24 g of tetrakis-(N,N-diethyldithiocarbamate) tin (IV) was dissolved in 20 mL of OLA in three-neck flask and the flask is connected to the Schlenk line. The mixture was purged by nitrogen and evacuated, repeated three times at about one minute intervals, to get rid of the air trapped inside the powdery product. Simultaneously, 24 mL of toluene was added to the addition funnel. The solution was then heated at 280 °C for 10 minutes. After 10 minutes, the system was allowed to cool to ~105 °C. The reaction was then quenched by adding toluene and left to cool passively to room temperature. The mixture was centrifuged for 10 minutes at 5000 rpm (2,400 x g), the supernatant was decanted, and the solid was dissolved in excess acetone by sonicating for a few minutes and centrifuging for 10 minutes. This step was repeated two more times and the final product was dried with, and stored in, nitrogen.

5.2.4 Fabrication of Films from FeS₂ or SnS₂ NCs

Because of their large size (~70 nm – 150 nm), FeS₂ NCs do not remain in stable suspension for long periods of time and a well-dispersed but unstirred solution will effectively change in concentration as the NCs settle to the bottom of the container. FeS₂ NC films were prepared using drop-cast method in a layer-by-layer (LbL) process.[43, 142] To fabricate the FeS₂ NC films, FeS₂ NC solution in chloroform at a concentration of ~6 mg/ml, was prepared and preceded with film formation in an N₂ environment. A layer of drop-cast NCs is deposited onto the chosen substrate, and allowed to dry. At this point, the film can optionally be treated with hydrazine for ligand removal (*vide infra*). In the case of an untreated film, the film thickness may be increased by simply repeating

the drop-cast process followed by the drying process; preparation of a 1 μm film typically requires 3 cycles.

To make the FeS_2 NC films more conducting, long chain hydrocarbon molecules ($\text{C}_{24}\text{H}_{51}\text{OP}$, TOPO) were removed from the NC surface in an LbL process by cyclically depositing NCs and treating the film with 1 M hydrazine in ethanol. Subsequent to the first drop-cast layer deposition, the NC film is allowed to dry in the N_2 environment. The film is subsequently submerged in a 1 M hydrazine solution in ethanol for ~ 2 minutes. The film is withdrawn from the hydrazine solution and immediately submerged into a pure ethanol solution to remove any residual surfactant or hydrazine – i.e., as a rinse. The film is then allowed to dry. To attain a thicker film, the drop-cast/dry/hydrazine/rinse/dry process may be repeated as necessary for the desired film thickness. Removal of TOPO from the surface of the NCs by the application of hydrazine is depicted in Figure 5-3.

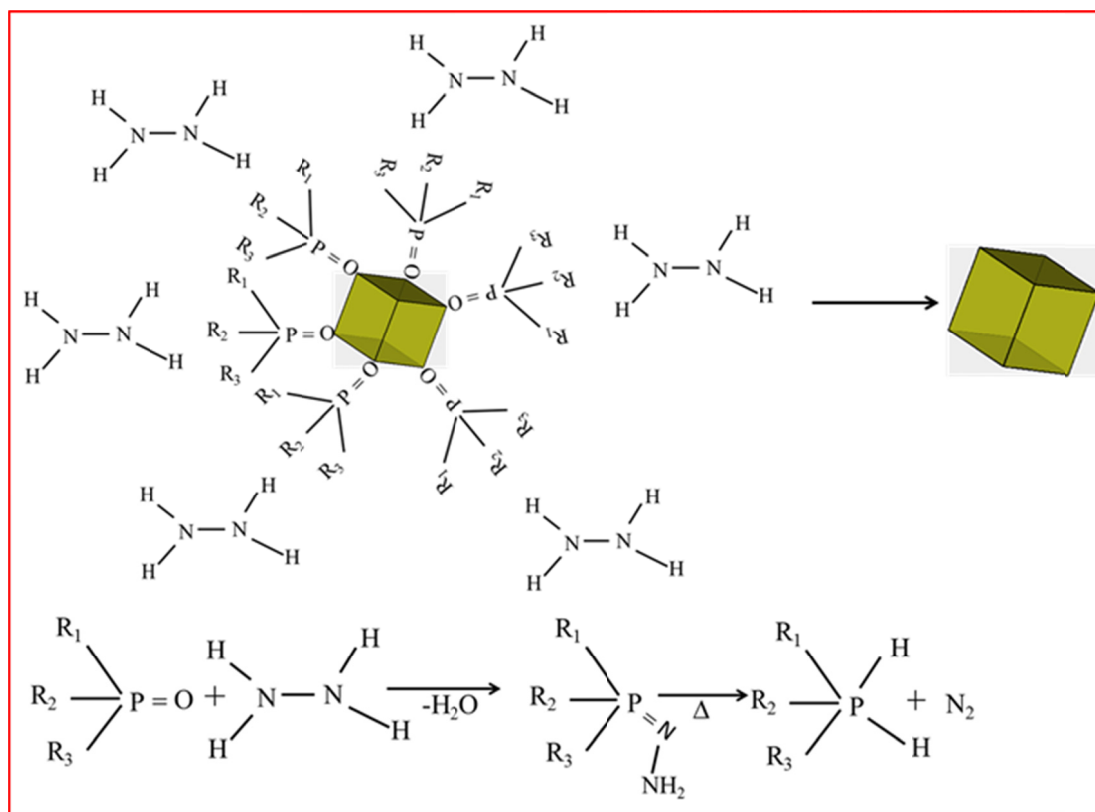


Figure 5-3. Schematic of the removal of TOPO from the surface of the NCs by hydrazine treatment.

FeS₂ NC films prepared by the LbL drop-casting method exhibit pin holes (microscopic areas of incomplete coverage by FeS₂) which occur independent of film thickness up to even 1 μm. In addition, one expects an improvement in charge carrier mobility and transport properties when neighboring NCs are brought into improved contact and/or surface defect states are removed. In an effort to ameliorate the presence of pinholes, and to investigate possible control over electronic properties, the NC films were sintered in the presence of sulfur vapor. Sintering may anneal the NCs together and/or promote grain growth, resulting in a film exhibiting more uniform coverage and/or improved electronic properties. Sintering of the films is conducted in a cylindrical quartz

tube furnace such that the film is heated uniformly. In the quartz tube, two coil heaters are arranged: one is being used for evaporating the elemental sulfur at $\sim 350^{\circ}\text{C}$ and the other is used to anneal the sample at various temperatures. Two ends of the quartz tube are sealed with flanges fitted with O-rings. Initially the tube is purged with a forming gas (95% argon, 5% hydrogen) for about 5-10 minutes and then low pressure argon gas (5, standard cubic centimeters per minute, SCCM) is introduced during the sintering process. The sintering process proceeds with the substrate and film held at a temperature of 500°C or 540°C , within a sulfur vapor, for 1-3 hours. Recently, photovoltaic devices have been made by sintering the layers of solution-deposited NCs to form an absorber layer. This technique has been applied on photovoltaic devices based on systems such as CdTe/ZnO[209], CuInSe₂[210] and CZTSSe.[211] Sintering FeS₂ NC films is non-trivial because of the phase change from FeS₂ to FeS at high temperature as indicated by XRD spectroscopy study. To protect pyrite FeS₂ from phase change at elevated temperature, one can sinter in a sulfur vapor, as Puthussery et al. demonstrated on FeS₂ NCs at $500 - 600^{\circ}\text{C}$. [185] Their purpose of sintering the NC films was to increase the average grain size, reduce possible sulfur deficiency, remove carbon and densify the films. No discussion was provided regarding the use of the sintered films within solar cells.

Film fabrication of SnS₂ NCs was conducted using spin-coating method. For this, SnS₂ NP solution was prepared in chloroform with a concentration of ~ 8 mg/mL and the substrate spinning rate was set at 2000 rpm. In this thesis, use of SnS₂ NC films were mostly limited to characterization purposes and occasionally as window layer for attempts at making functional FeS₂ NC thin film solar cells. The solar cells did not show

meaningful power conversion due the high free carrier concentration of the FeS₂ NC films.

5.2.5 Characterization of FeS₂ and SnS₂ NCs

FeS₂ and SnS₂ NCs are characterized both as solution and film. Table 5-1 provides a list of instrumentation and measurements for the study of FeS₂ NCs.

Table 5.1: Instrumentation used in the process of characterization of FeS₂ and SnS₂NCs.

	Name of tools	Used
1	Perkin Elmer 1050 Spectrophotometer	to measure absorbance, transmission and reflection in UV/VIS/NIR region
2	FTIR spectroscopy	to identify and study chemicals
3	Four point probe	to measure Sheet resistance
4	Hot Probe method	to find type of semiconductor (n or p-type)
5	X-ray Spectroscopy	to find crystal structure and purity of the FeS ₂ materials
6	Scanning Electron Microscopy (SEM)	to find topographical, morphological and compositional information
7	Electron Diffraction Spectroscopy (EDS)	to find elemental composition of a material
8	Raman Spectroscopy	to find individual chemical bond vibration of a compound
9	Hall measurement	to find resistivity, carrier density and mobility
10	Scanning Transmission Electron Microscopy (STEM)	to find crystal structure, size distribution of NCs
11	Atomic Force Microscopy (AFM)	Surface roughness (surface morphology) of a film
12	Sulfurization chamber	to anneal NC film in sulfur vapor

5.3 Results and Discussion

5.3.1 Iron pyrite NCs

Optical absorbance spectra of FeS₂ NC solution dispersed in chloroform as well as absorbance spectra of a FeS₂ film deposited onto soda lime glass substrate are shown in Figure 5-4. From these spectra, one notes that most of the light absorption takes place throughout the visible and near-infrared spectral regions. Light absorption is strong for wavelengths below ~1000 nm. Beyond about 1200 nm, the film is more (but incompletely) transmissive. The absorption of light in the infrared region below the indirect band gap energy (0.95 eV, 1305 nm) has been ascribed to S vacancies.[212] However, as reported recently by Yu et al.,[180] FeS₂ films (which show p-type defects and a high free carrier concentration) are prone to the formation of low-energy phases of Fe:S stoichiometry exceeding 0.5; such phases include troilite (FeS) and pyrrhotite (FeS_{1+x}, x = 0-1/7). Thus, the sub-bandgap infrared absorption may be ascribed to absorption caused by non-FeS₂ iron sulfide phases. In the inset, reflection spectra of ~150 nm thick NC films can be seen plotted with respect to wavelength in nm. The direct and indirect band gaps of FeS₂ NCs in films *via* absorbance spectroscopy were determined.[213, 214] Transmission and reflection percentages obtained from a film of thickness ~150 nm via Perkin Elmer Spectrophotometer were used to calculate optical absorbance spectra using the relation $A = 2 - \log_{10}(T\% + R\%)$. Optical absorbance or optical density of the film was then divided by the film thickness to convert optical absorbance to absorption coefficient (α). Then a graph of $(\alpha hv)^2$ vs. hv is used to extract the direct band gap of ~1.3 eV and a graph of $(\alpha h\nu)^{1/2}$ vs. $h\nu$ is used to extract the indirect

band gap of ~ 0.94 eV as shown in Figure 5-5. These data agree closely with literature values such as those reported by Bi et al. of 1.38 eV and 0.93 eV.[184] Various other groups have reported band gap energies in the range of 0.82 – 1.6 eV, with most results for the indirect gap near to 0.9 eV.[215-219] Figure 5-4 (red) shows the absorption coefficient of an untreated FeS₂ NC film of thickness ~ 150 nm. The absorption coefficient is very strong, $\geq 10^5$ cm⁻¹ in the visible and near-infrared region of the spectrum.

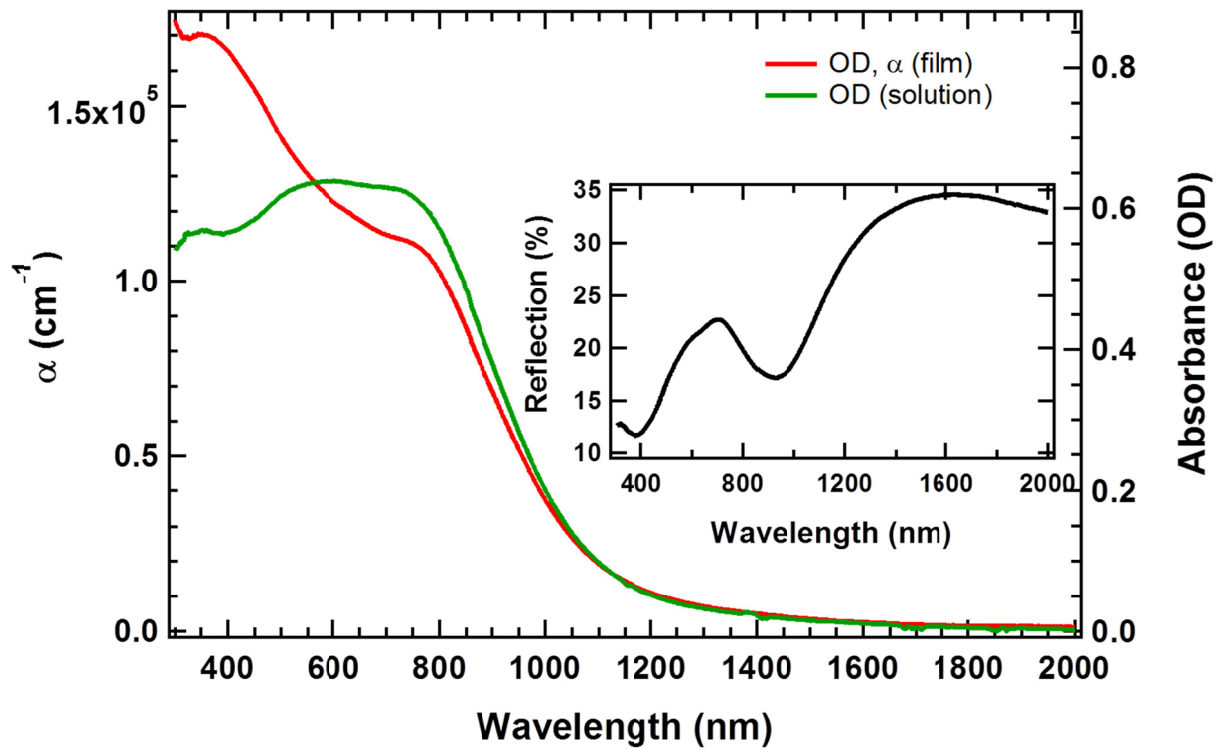


Figure 5-4. Optical absorbance spectra of as-obtained NC solution (green), optical absorbance and absorption coefficient obtained from as-synthesized NC film (red), and (inset) % reflection from as-synthesized NC film of thickness ~ 150 nm showing peaks at ~ 700 nm and 1600 nm.

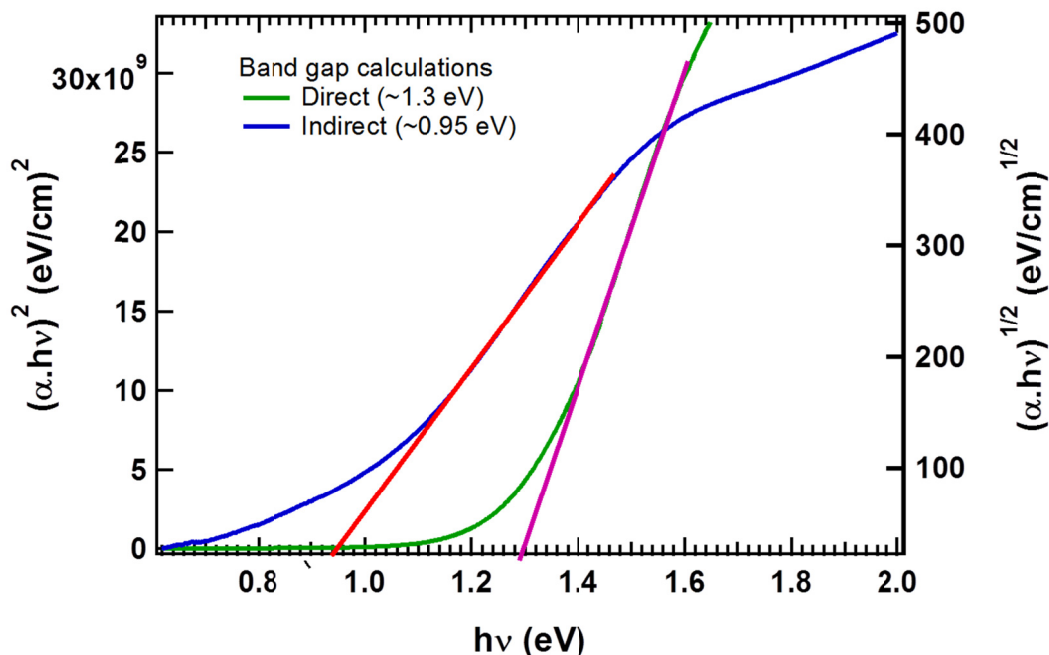


Figure 5-5. Direct and indirect band gap calculation of FeS₂ NC in film using optical absorbance spectra shown in Figure 5-4. Both direct and indirect values are plotted with respect to the energy in eV.

Iron persulfide NC films are prepared (*vide supra*) using LbL drop-cast method. Films used for structural and electrical characterization are deposited on soda-lime glass or onto a zero-background single-crystal Si substrate; films may be hydrazine-treated, untreated, and sintered or unsintered. Hydrazine treatment of the films is found to remove the capping ligands (Figure 5-3). In FTIR measurement as shown in Figure 5-6, red is the reference background spectrum obtained from the Si substrate, while the green and blue lines respectively show signals before and after ligand exchange. The C-H stretch signatures near 3000 cm⁻¹ and at 1500 cm⁻¹ show quantitative removal and/or replacement of TOPO (or 1,2 hexanediol) through hydrazine treatment. Hydrocarbon bond infrared absorption lines for the untreated film type are shown for narrowed spectral regions within the right side of Figure 5-6 (right). The majority of the peaks are based on

vibrations of bonds comprised of C and H and only few are from the combination of N-H and C-O. The nitrogen-hydrogen bond comes from amines whereas the others arise from phosphine oxide. Hydrazine has been widely used in solution process depositions of thin films, which is considered as one of the low cost routes for fabrication of electronic devices. CZTS and CZTSSe based solar cells using a hydrazine-based solution process have already reached energy conversion efficiency exceeding 10%. [220, 221]

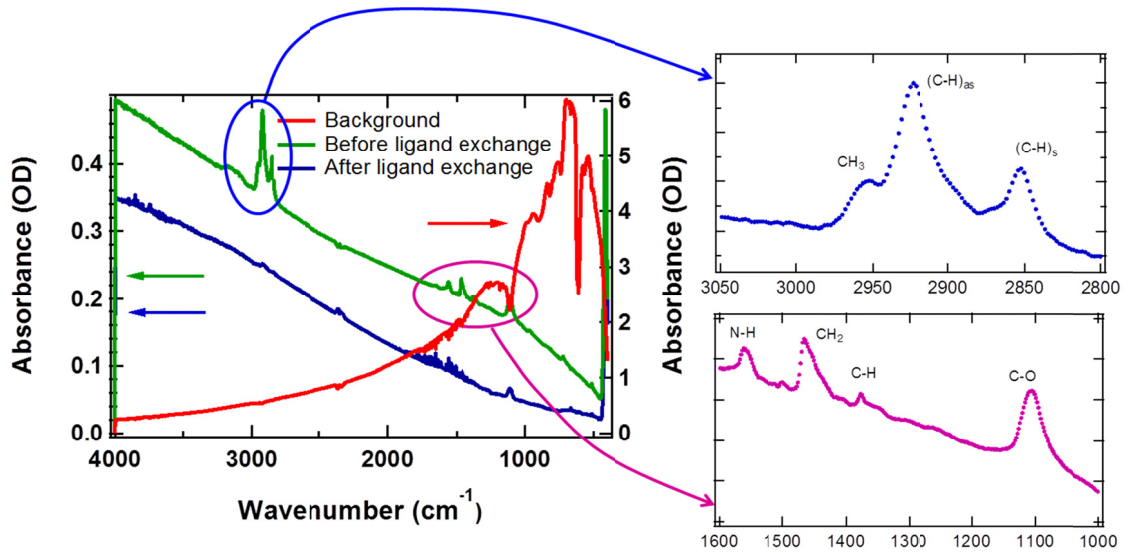


Figure 5-6. (left) Absorbance spectra of as synthesized and hydrazine treated FeS₂ NCs taken from FTIR measurement. Red spectrum shows background for single crystal silicon substrate. (Right) Zoom part of two spectral regions: 3000 cm⁻¹ and (1600-1000) cm⁻¹.

Iron persulfide NC-based thin film XRD data were collected with a Rigaku Ultima III diffractometer using Cu K α radiation using either focused or parallel beam geometry. Scanning electron microscopy (SEM) imaging was conducted at operating voltages 10 kV and 20 kV. Raman spectroscopy measurements were conducted using a 632.8 nm He-Ne laser beam. Figure 5-6 shows XRD spectrum of as-deposited FeS₂ NC

films. For XRD, the NC film was prepared on a zero-background Si substrate whereas for SEM and Raman the films were prepared on soda lime glass substrate. Energy-dispersive X-ray spectroscopy (EDX) was used to determine the stoichiometry of FeS₂ NC in films. The XRD image in Figure 5-7 shows pure FeS₂ cubic phase with no evidence of other crystal structures. The sharp peaks in the XRD pattern indicate excellent crystallinity of the as-synthesized FeS₂ NCs. Three digit numbers in the bracket represent the Miller indices for cubic crystal structure. XRD images for OLA capped and 1,2-hexanediol capped FeS₂ NCs are shown in Figure 5-8. Figure 5-8 shows that when OLA is used as a coordinating and non-coordinating solvent, NCs so obtained are mixed phase of pyrite and troillite but the phase of NCs is pure pyrite when 1,2-hexanediol is used as coordinating solvent.

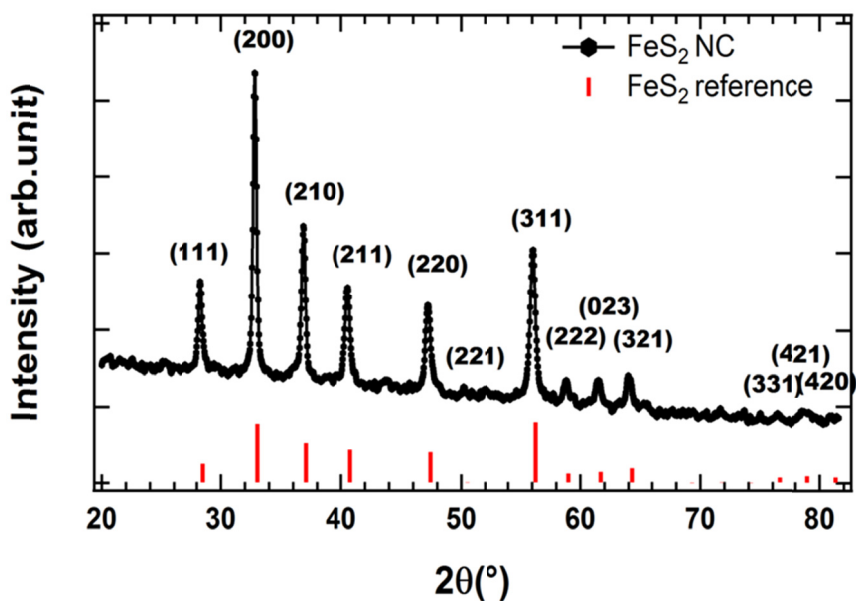


Figure 5-7. XRD spectrum (focused beam) of untreated and unsintered FeS₂ NC film deposited by drop-cast using NCs of size ~130 nm; Red vertical lines represent powdered XRD peak positions obtained in library of jade 10 software and are drawn for comparison.

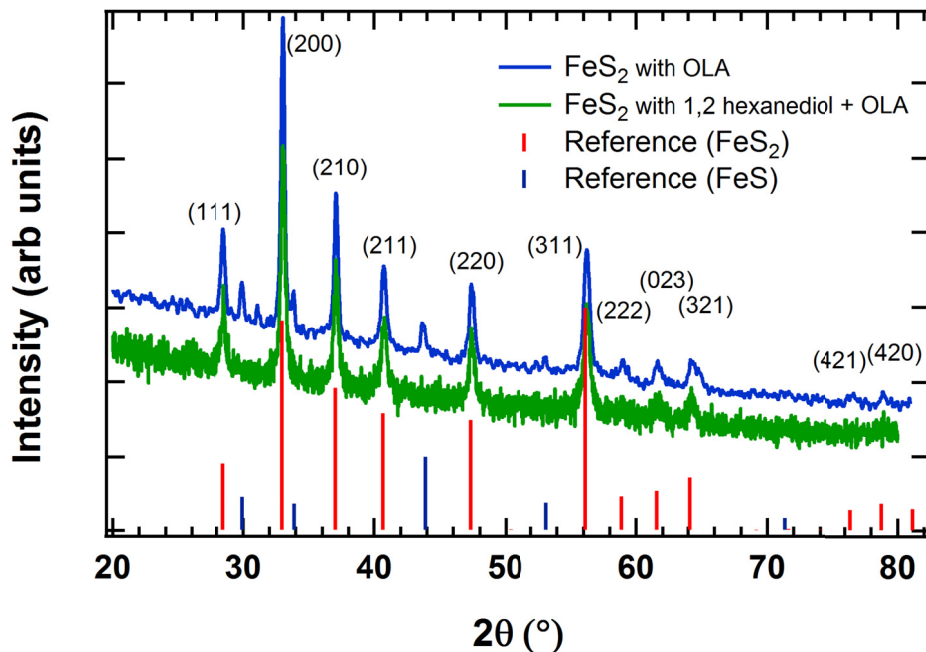


Figure 5-8. XRD spectra in cases when oleylamine works both as coordinating and non-coordinating solvents and when 1,2-hexanediol and oleylamine work as coordinating and non-coordinating solvents. Vertical lines represent powdered XRD peak positions obtained in library of jade 10 software and are drawn for comparison

Figure 5-9 shows the Raman spectrum of an as-synthesized drop-cast FeS₂ NC film, measured with 632.8 nm excitation. Raman peaks at 343.7 cm⁻¹, 380 cm⁻¹ and 431 cm⁻¹, corresponding to the A_g, E_g, and T_g(3) vibrational modes, are consistent with phonon vibrations previously observed for FeS₂. [184, 188, 222-224] There are actually five Raman-active modes of vibrations in pyrite (A_g, E_g, T_g(1), T_g(2), and T_g(3)) in which the Fe atoms stay at rest while the sulfur atoms move in opposite direction with equal amplitude. [225] The A_g mode of vibration is totally symmetric and corresponds to the in-phase stretching vibrations of the S₂²⁻. The E_g gives double degenerate librational mode of vibration in which S atoms are displaced perpendicular to the S₂²⁻ axis. Similarly, the triply degenerate T_g mode of vibration belongs to various librational and stretching

vibrations or their combinations. These previously-reported Raman results were based on 532 nm excitation of FeS₂ film, in contrast with the 632.8 nm excitation used in this study. The Raman peaks observed here are well separated from Raman peaks reported for troilite (FeS) which shows peaks at ~210 cm⁻¹ and ~280 cm⁻¹. [226, 227] Raman spectra of 1,2-hexanediol capped FeS₂ NCs are shown in Figure 5-10. Raman signals for iron pyrite from 1,2-hexanediol capped NCs are also in very close agreement with the literature results. Some variations in the positions of Raman Shift may be due to the use of different surfactant. Since NCs are capped with surfactant molecules, position of the Raman bands may change depending on which surfactant is used.

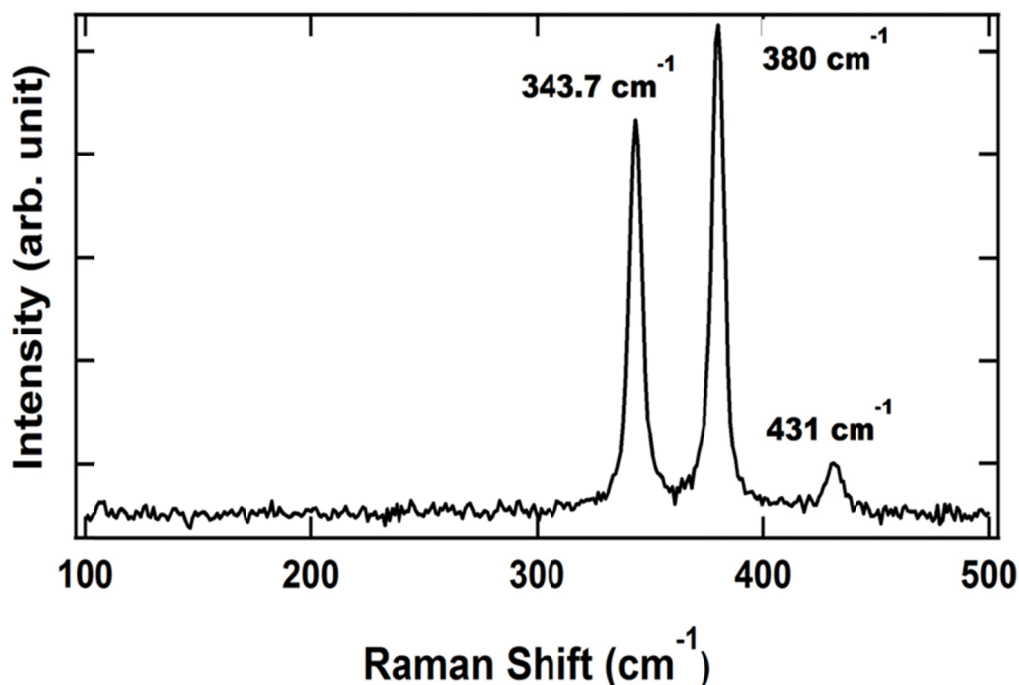


Figure 5-9. Raman scattering spectrum of untreated and unsintered FeS₂ NC in film deposited by drop-cast using NCs of size ~130 nm; NCs are capped with TOPO molecules.

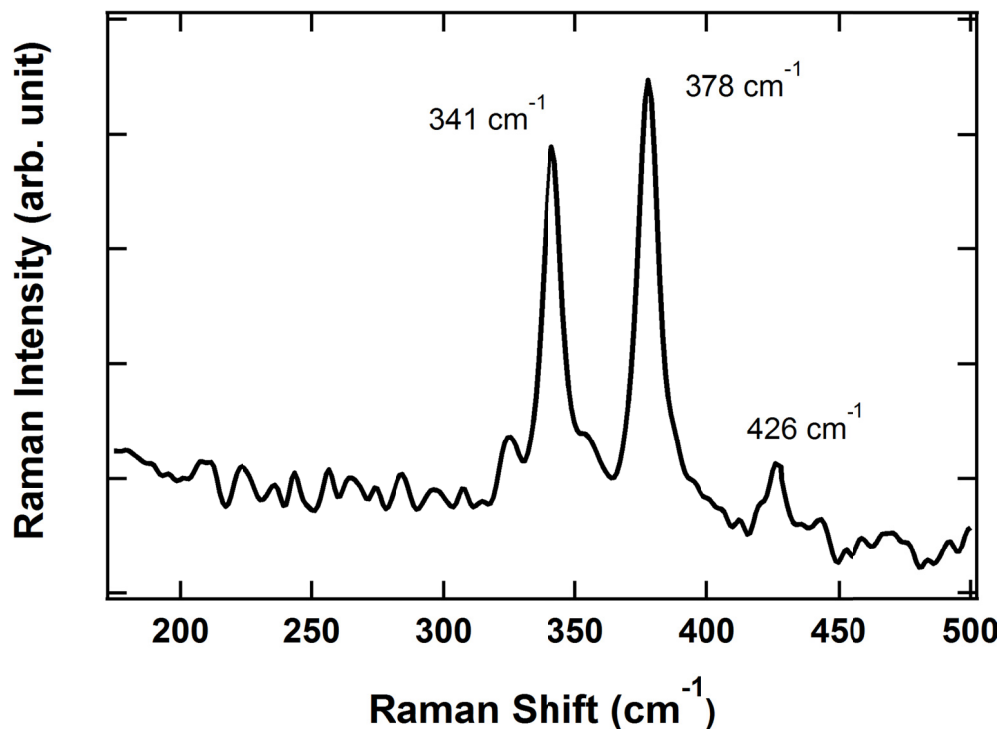


Figure 5-10. Raman spectrum when 1,2-hexanediol and oleylamine were used as surfactant and non-coordinating solvent respectively. The NC is apparently pure FeS₂ devoid of troillite.

Uniform cubically-shaped FeS₂ NCs synthesized with TOPO/OLA combinations are shown in Figure 5-11 in two different magnifications. Similarly, an SEM image of FeS₂ NCs synthesized with 1,2-hexanediol/OLA combination is shown in 5-12. Comparison of Figures 5-11 and 5-12 reveals the importance of surfactants in determining the NC average size. In both cases, the cubic crystal structure of iron pyrite remains the same. The average NC size also varies with the surfactant concentration, as shown in Figure 5-11 and 5-16. Growth of the NCs depends mainly on the amount and type of surfactants, and temperature. For all syntheses discussed here, the growth temperature remains constant. So, size is mainly governed by the type and concentration

of surfactants used during synthesis. In the case of 1,2-hexanediol, smaller size NCs are formed due to smaller surfactant concentration, and these NCs aggregate to form larger particles. On the other hand, in case of the longer TOPO molecules, the NCs so formed remain separated from others.

To calculate size distributions of TOPO capped NCs, TEM images similar to that shown in Figure 5-13(a) were analyzed using *image-J* software. The size distribution of these and similar FeS₂ particles were calculated as shown in Figure 5-13(b). The average edge length of NCs shown in Figure 5-13(a) is 133 ± 18 nm. By reducing the amount of TOPO, FeS₂ NCs with average edge length < 70 nm can be synthesized.

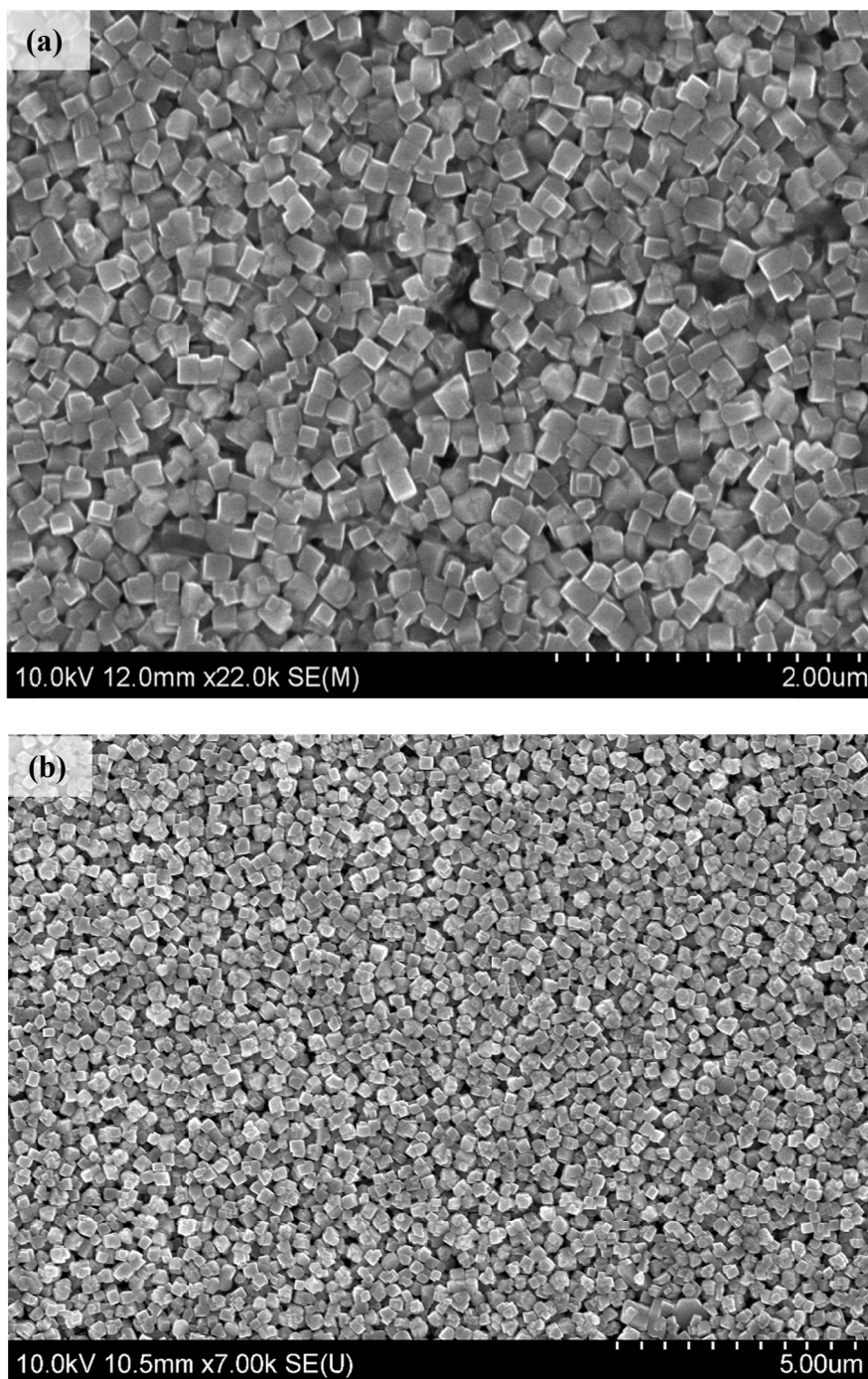


Figure 5-11. SEM image at 10 kV accelerating potential of untreated and unsintered FeS₂ NC film deposited by drop-cast using NCs of size ~130 nm with magnification (a) 22.0 k and (b) 7.0k. In both cases, TOPO was used as surfactant and OLA as solvent.

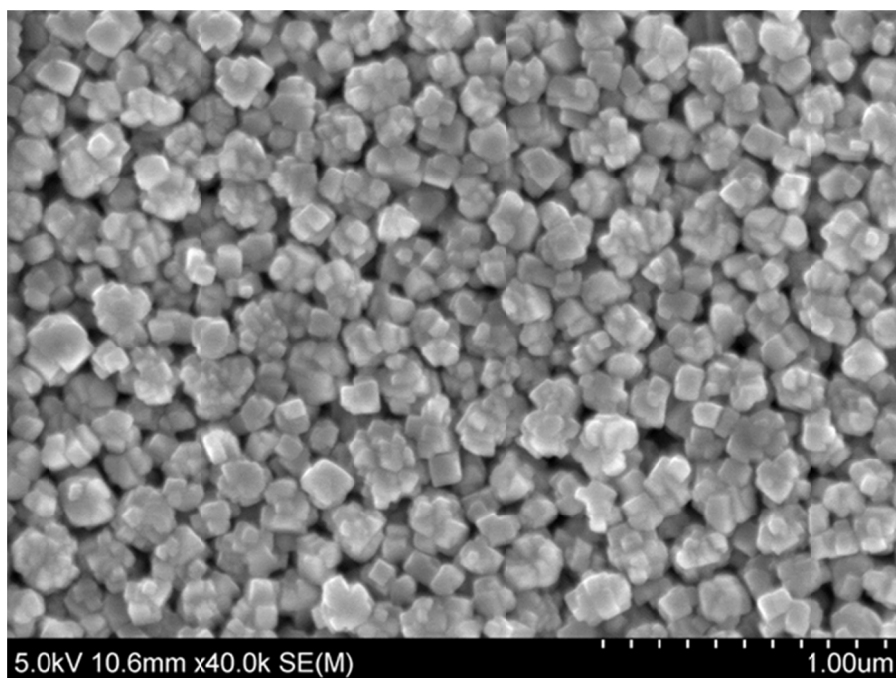


Figure 5-12. SEM image at 5 kV accelerating potential of untreated and unsintered FeS₂ NC films at magnification 40.0 k when using 1,2-hexanediol/OLA combination as surfactant and non-coordinating solvent.

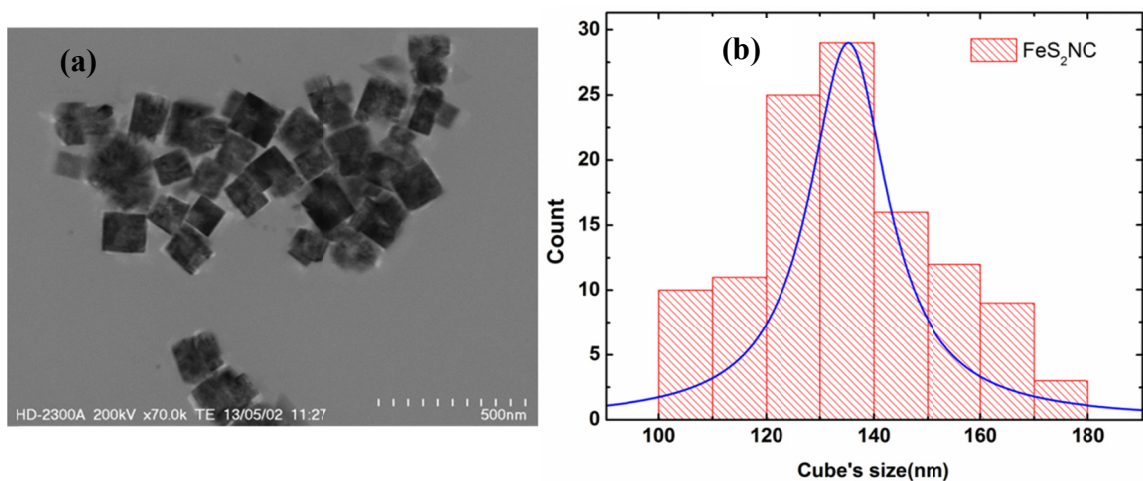


Figure 5-13. (a) TEM image for TOPO capped FeS₂ NCs. Each side of the cube has length ~133 nm; (b) Size distribution of the FeS₂ NCs synthesized with TOPO/OLA combination. Size distribution was calculated using TEM images and *image-j* software with the help of Origin software.

The observed limitation of V_{OC} in iron persulfide's first solar cells was thought to be due to the possible significant sulfur deficiency.[228] Significant changes in the crystalline structure and therefore the electronic properties of compound semiconductors can arise from the formation of phases that may correspond to relatively small deviations in stoichiometry. After earlier work on photo-electrochemical solar cells, which achieved 2.8% power conversion efficiency, efficient iron pyrite solar cells have been elusive. Many authors have found a significantly decreased S:Fe ratios in nominally FeS_2 samples, ranging from 2:1 to 1.74:1.[212, 229] Iron pyrite NCs synthesized at UT exhibit an essentially stoichiometric ratio (Figure 5-14). Energy Dispersive X-ray Spectroscopy (EDX) measurement for seven different batches of FeS_2 NCs, synthesized with varying amounts of surfactant yielded an average S:Fe ratio of 2.01:1 representing iron persulfide as a stoichiometry compound. The overall analytical accuracy of EDX is considered as $\pm 2\%$. Nonetheless, it merits noting that even small amounts of phase impurities, especially those near the 2:1 S:Fe ratio, may noticeably alter the aggregate optical and electronic properties.

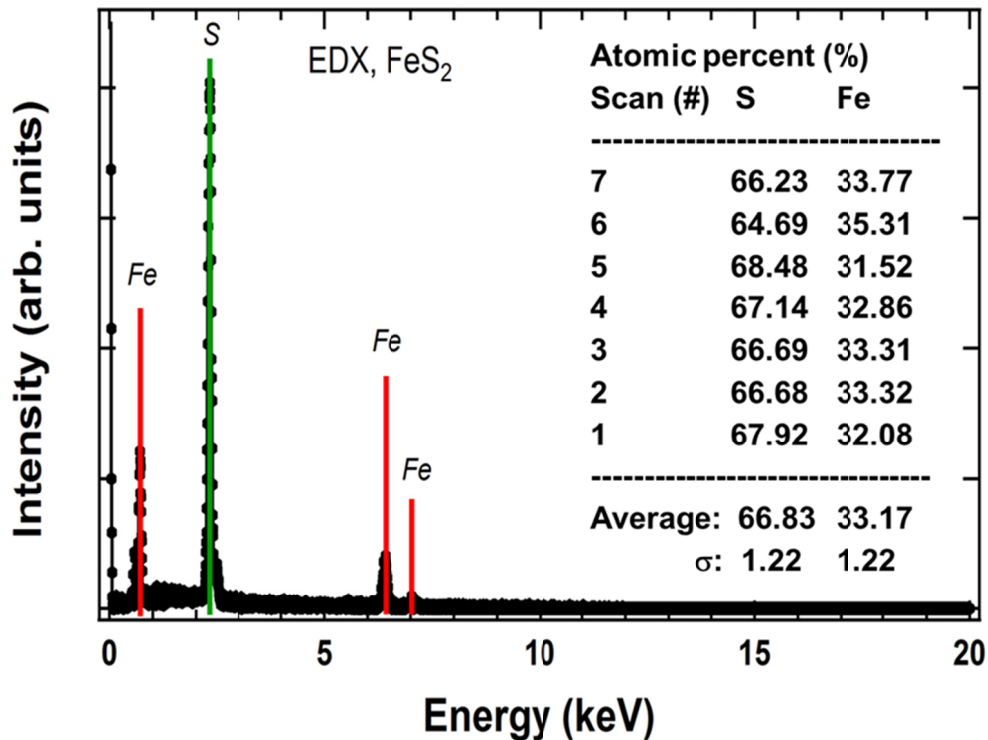


Figure 5-14. EDX measurement of seven FeS₂ NC films fabricated from distinct NC syntheses.

The poor performance of the FeS₂ NCs solar cells fabricated in our laboratory is thought to be due to the pinholes because they make the cells shunted. Pinholes in FeS₂ films have been previously noted and addressed; for example, Kment et al. used a novel sol-gel route to get pinhole-free FeS₂ thin films [230]. In addition, Smestad et al. described pinholes in their FeS₂ films formed by spray pyrolysis method[231]. They attributed pinholes to strain at the substrate-film interface, and to the cooling action of the spray droplets and the differences in thermal expansion between FeS₂ and the glass materials. The authors found fewer pinholes for films sprayed at a lower rate. Here I have followed different approach to remove pinholes in FeS₂ NC thin films which is the sintering of the films at high temperature. Iron pyrite is thermodynamically unstable

when heated above ~ 300 °C for long period of time, though it is observed here that heating for longer than ~ 15 minutes at ~ 400 °C, or heating at a higher temperature, resulted in conversion of pyrite to troilite (FeS) phase. Under such intense sintering conditions, the NC films were heated in sulfur vapor (in argon) to prevent sulfur evaporation and maintain the S:Fe ratio constant. Nanocrystal films are sintered at 500 °C and 540 °C from one to three hours in sulfur vapor. Figure 5-15(a) shows XRD spectra of FeS₂ NC films before and after annealing the films. Raman spectroscopy is more sensitive than conventional XRD to explain the purity of the NC films before and after sulfur annealing. Raman spectra in Figure 5-15(b) are sharper and intense because of the crystallinity of the film after annealing. Puthussery et al. sintered FeS₂ films at 540°C for 4 hours and found significant grain growth [185]. In this work, heating at 540°C from one to three hours did not increase appreciable grain growth of surface NCs on the films (as shown in Figure 5-16) but helped to some extent to block the pinholes. The XRD spectrum in Figure 5-15a, however, shows improvement in crystallinity after sintering the film. EDX measurement shows that atomic percentage of S/Fe before and after annealing the film remains unchanged, indicating that the films are thermodynamically stable in sulfurization. Considering the intense peak at (200) direction, full width at half maxima (FWHM) and grain size were calculated for all XRD spectra taken at different temperatures. Table 5-2 shows that with increased temperature and annealing time, the (200) peak FWHM decreases, corresponding to increasing average grain size. To calculate FWHM and grain size, following procedures were used.

Using Igor Pro software, a Gaussian fit was applied to the XRD peak corresponding to crystal plane of (200) direction. The equation used for this purpose was

$f(x) = y_0 + A \exp\left\{-\left(\frac{x - x_0}{width}\right)^2\right\}$, where $f(x)$ is Gaussian function, y_0 is a base line, x is

the variable quantity, A is the height of the curve's peak, and x_0 is the position of the center of the peak. After fitting the peak, the software provides magnitudes of fitting parameters y_0 , A , x_0 and width. The FWHM is calculated using a relation

$FWHM(\beta) = 2\sqrt{2 \ln 2} \sigma$, where σ is the standard deviation and is calculated by

$\sigma = \frac{width}{\sqrt{2}}$. Similarly, to calculate the average grain size we apply the Scherrer equation,

$\tau = \frac{K\lambda}{\beta \cos \theta}$. In this equation, τ is average grain size of the crystallites, K is a

dimensionless constant, shape factor, with a value ~ 0.9 , β is FWHM (radians) and θ is the Bragg angle. The Scherrer formula is limited to nanoscale particles and may not be used accurately if the grain size of the particle is larger than ~ 100 nm. [232] The peak width β due to crystallite size varies inversely with grain size and 2θ as $\cos \theta$. So, larger the angle 2θ , larger will be the size broadening. However, at large angle the peak intensity is usually weakest and instrumental profile width and microstrain (non-uniform lattice distortions, faulting, dislocations etc.) broadening are also largest at large angles.

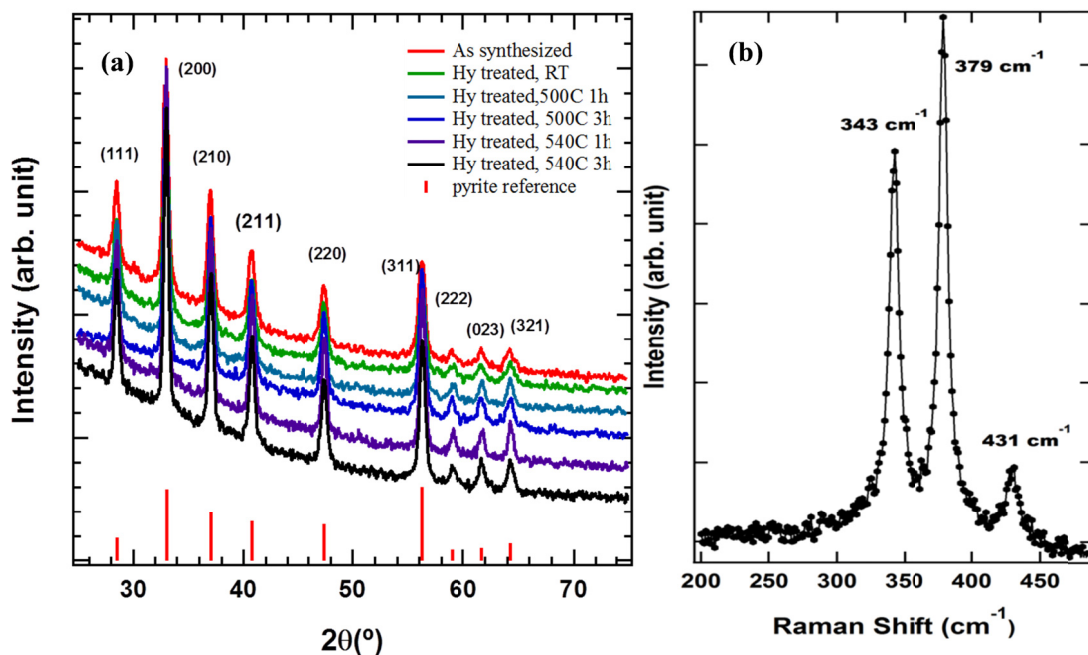


Figure 5-15. Characterization of FeS_2 NC films deposited by LbL drop-cast method using NC of size ~ 70 nm: (a) XRD spectra showing the effect of hydrazine and thermal annealing treatment, (b) Raman spectrum for a film annealed at 540°C for 1 hour.

Table 5.2. Effect of annealing temperature and time on the FWHM of the (200) XRD peak measured for FeS_2 NC films.

Hydrazine treatment	Temperature($^\circ\text{C}$), Time (hour)	2θ ($^\circ$)	FWHM (mrad)	Grain size (\AA)
No	Room temp	33.02	7.7	185.5
Yes	Room temp	33.02	7.9	180.3
Yes	500, 1	33.03	6.9	206.1
Yes	500, 3	33.04	6.8	211.9
No	500, 3	33.04	6.9	205.6
Yes	540, 1	33.03	6.3	227.6
Yes	540, 3	33.03	6.1	234.1

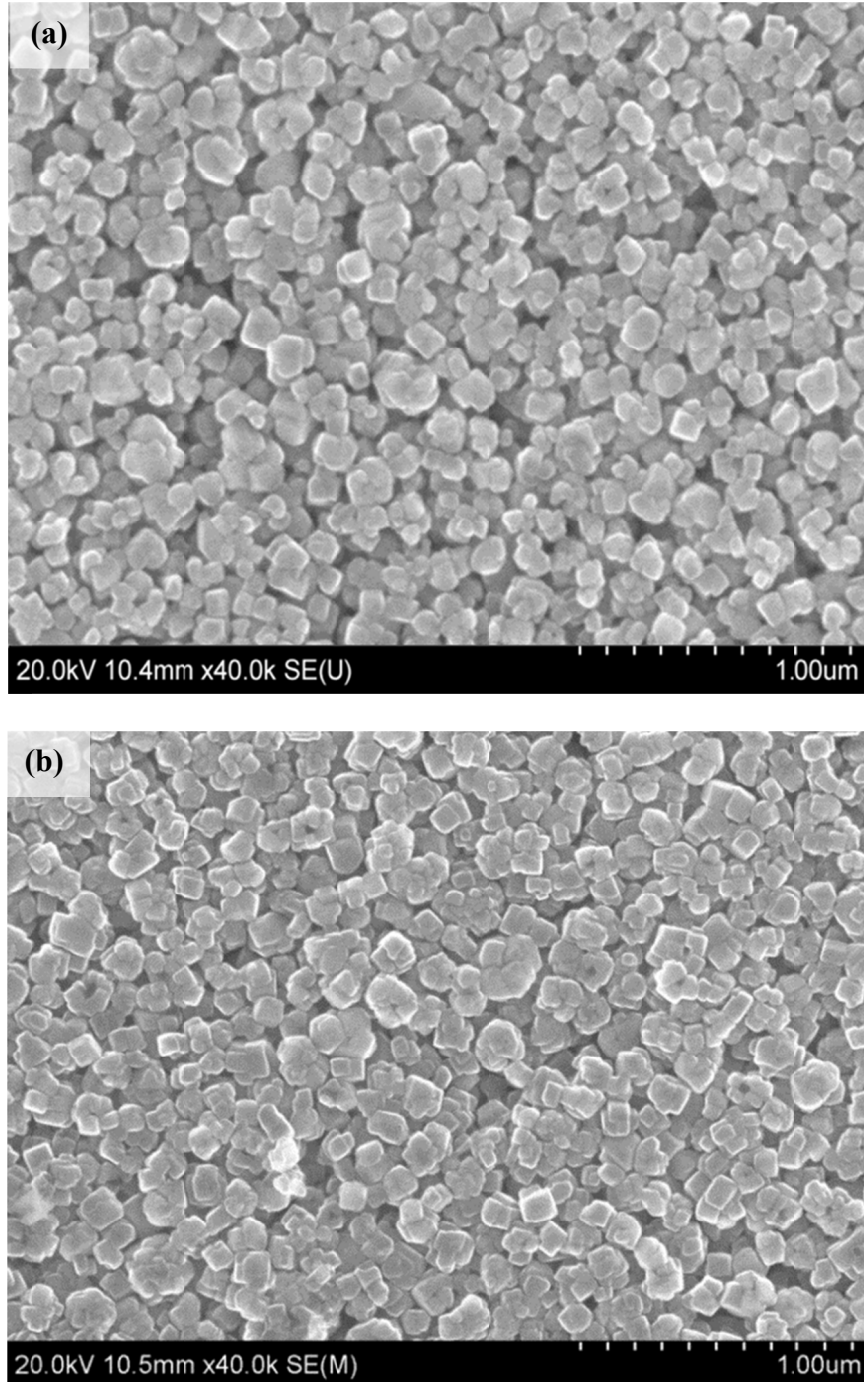


Figure 5-16. SEM micrographs of FeS₂ NC films deposited by layer by layer drop-cast method using NCs of size ~70 nm: (a) an as-deposited film and (b) a film hydrazine treated and annealed at 540 °C for 3 hours.

Iron persulfide films that were (1) as-synthesized, (2) hydrazine treated, and (3) hydrazine treated and annealed, were used for the fabrication of Schottky junction and heterojunction solar cells employing FeS₂ as the absorber layer. In all cases, results showed no improvement in PV performance resulting from hydrazine or thermal annealing treatments. PV devices yielded effectively zero open circuit voltage and zero short-circuit current density (the J-V curve passed through the origin). Detailed characteristics of Schottky and heterojunction solar cells are available in the appendix.

Electrical properties of FeS₂ NC films were studied using hot probe measurement, four point probe measurement, and Hall measurement methods, with results summarized in Tables 5-3 and 5-4. All hot probe measurements indicated clearly that the films were p-type, in agreement with reports from other polycrystalline and NC-based films,[184, 187, 233] and indicating that holes are the majority charge carriers in pyrite films prepared here.

Table 5.3: Four point probe measurements: average thickness of the film = 3.5 μm.

Synthesis of FeS ₂ Surfactant/solvent	Conditions		4-point probe measurement	
	Hydrazine treatment	Heat treatment	Sheet Resistance	Resistivity (Ω*cm)
1,2-hexanediol/OLA	No	No	3.4 x 10 ⁵	119
	Yes	No	3.5 x 10 ⁴	12.2
	Yes	Yes	6.3 x 10 ³	2.2
TOPO/OLA	No	No	3.8 X 10 ⁵	133
	No	Yes	7.4 x 10 ³	2.6
	Yes	No	3.4 x 10 ⁴	11.9
	Yes	Yes	1.5 x 10 ³	0.52

Table 5-3 shows the sheet resistance for two pairs of FeS₂ NCs on soda-lime glass, in three and four different conditions. For the first sample type, FeS₂ NCs were synthesized using 1,2-hexanediol/OLA and for the second case, FeS₂ NCs were synthesized using TOPO/OLA combinations. In the first case, three different films were prepared: the first as-synthesized NC film (No, No), the second NC film treated with hydrazine but at room temperature (Yes, No) and the third NC film treated with hydrazine and annealed in sulfur vapor for an hour at 500 °C (Yes, Yes). In the second case, one more condition, as-synthesized NC film annealed in sulfur vapor (No, Yes), is added. It is found that the films' sheet resistance decreases by a factor of ~10 when going from as-synthesized to hydrazine-treated, and by another factor of ~10 from just hydrazine-treated to hydrazine-treated and annealed. Sheet resistance of a sample that is annealed but not hydrazine treated is found lower than for a sample treated with hydrazine but not annealed and higher than for the sample which was hydrazine treated and annealed. Resistivity of the films in each case is obtained by multiplying sheet resistance by the average thickness of the films. These sheet resistance values are very close to those obtained from Hall measurement as given in Table 5-4. The decrease in sheet resistance of the hydrazine treated films correlates with the removal of the organic molecules from the surface of the NCs which insulate neighboring NCs against electrical conduction. When the films are annealed at high temperature, any residual organic molecules are evaporated; in addition, the increased NC grain size reduces the density of grain boundaries within the film by a factor of ~2.

Free carrier concentrations of the FeS₂ NC films also decrease by a factor of ~ 2 following hydrazine treatments, and by another factor of ~2 to ~5 following sulfur

annealing. The maximum carrier concentrations of treated and annealed film were of the order of 10^{19} cm^{-3} or higher in some cases. I did not find significant studies in the electrical properties of iron pyrite NCs, even though some studies were done in bulk pyrite thin film[234, 235] and iron pyrite nanowires.[236] Carrier concentrations obtained by Huang et al.[234] for bulk FeS_2 thin film are reported as $\sim 10^{18} \text{ cm}^{-3}$ and carrier concentration obtained by Caban-Acevedo et al.[236] for iron pyrite nanowires are of the order of 10^{21} cm^{-3} , bracketing the values obtained here from annealed films. It is found that these NCs even in their apparent pure phase possess very high carrier concentrations. Interestingly, when the films are annealed at high temperature ($>500^\circ \text{C}$), carrier concentrations are found to increase. As obtained by Hall measurement, in all different conditions, the mobility of the carriers in the NC film is found to be $\ll 1 \text{ cm}^2 \text{ V}^{-1} \text{ s}^{-1}$. Conductivity is proportional to the product of carrier concentration and mobility. Very low mobility strongly affects the workings of solar cells because poor transport under an electric field (drift) leads to substantial charge at interfaces under solar illumination. In addition, high carrier concentration leads to very short depletion widths, and one would have to rely on relatively long diffusion lengths.

Table 5.4: Hall Measurements; average thickness of the films = 3.5 μm .

Synthesis		Conditions		Hall Measurements		
Surfactant/ Solvent	Hydrazine treatment	Heat treatment	Sheet Resistance (Ω/\square)	Carrier conc. (cm^{-3})	Resistivity ($\Omega*\text{cm}$)	Mobility (cm^2/Vs)
TOPO/OLA	No	Room temp	1.1×10^5	4.3×10^{18}	139	0.04
	Yes	Room temp	3.8×10^4	9.7×10^{18}	13.3	0.22
	Yes	500C, 1h	4.3×10^3	1.5×10^{19}	1.5	0.32
	Yes	500C, 3h	1.8×10^3	3.5×10^{19}	0.6	0.37
	No	500C, 3h	4.9×10^3	1.6×10^{19}	1.7	0.22
	Yes	540C, 1h	3.0×10^3	3.4×10^{19}	1.1	0.17
	Yes	540C, 3h	1.8×10^3	5.7×10^{20}	0.6	0.42

The built-in electric field in the depletion region of a heterojunction solar cell serves to separate the photogenerated charge carriers across the interface. If the carrier concentration in the p-region is significantly higher than for the n-region, the width of window layer is depleted by the majority charge carriers of p-type region as shown in Figure 5-17. However, the built-in electric field in the n-type material does not contribute to the collection of photogenerated charge carriers as most of the incident photons pass through this region because of its wide band gap. In our efforts to create FeS_2 absorber layer solar cells, the window layer transmitted most of the solar spectrum, and those photons absorbed within the n-type window layer did not generate meaningful photocurrent. In addition, the photogenerated e-h pairs within the FeS_2 primarily recombine prior to diffusing to the (small) depletion region where they could be separated.

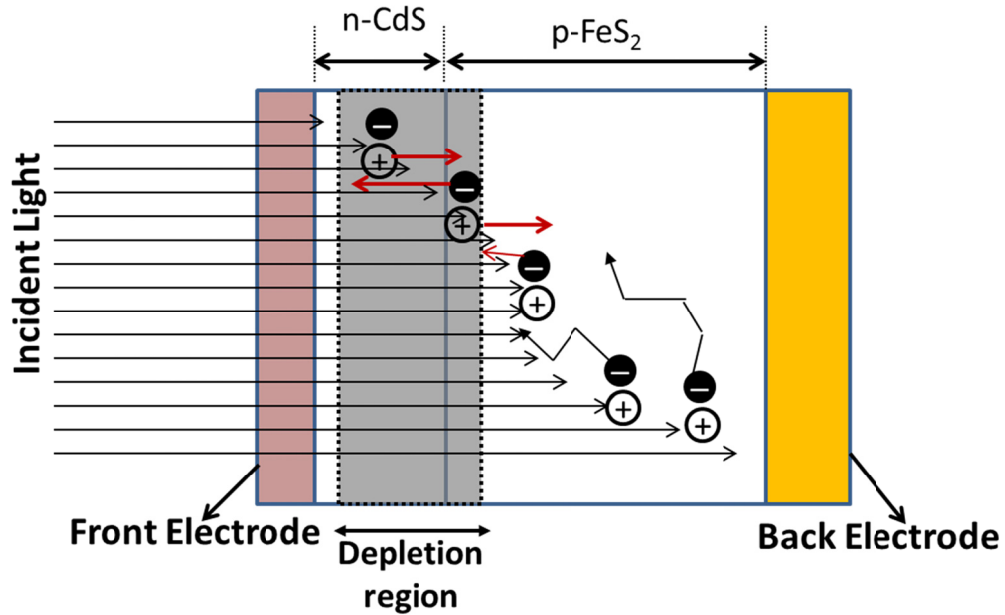


Figure 5-17. Solar cell schematic showing the problem of photo-generation when considering low free electron density CdS (n-type) and very high free hole density FeS₂ NC (p-type) heterointerfaced semiconducting films.

At sufficiently high free hole concentrations, the Fermi level moves into the valence band and the p-type semiconductor layer begins to show conductivity consistent with metallic conduction. Characterizing the temperature-dependent resistivity enables investigation of degeneracy and of the dominant transport mechanisms. Figure 5-18 shows the results of the temperature dependent resistivity measurements of the FeS₂ NC films of thickness 486 nm and 850 nm respectively in the temperature range of 80 K to 300 K. The films showed characteristic semiconducting behavior wherein the resistivity decreased with increasing temperature – i.e., the FeS₂ NC films have a negative temperature coefficient of resistivity over the range of ~100 to 300 K. This is as-expected for a semiconducting film because the number of ionized defect states (and the concentration of free carriers) increases strongly with temperature. It can also be seen that

the resistivity depends on the thickness of the film, with the thicker film showing a lower resistance.

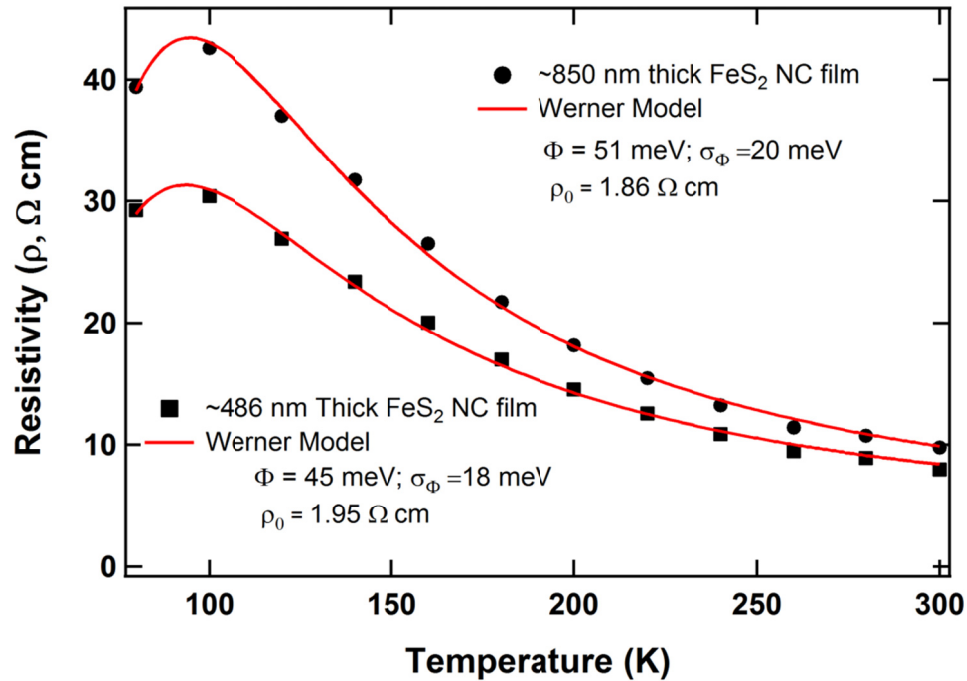


Figure 5-18. Temperature dependent resistivity of the hydrazine-treated treated FeS₂ NC film of thickness ~486 nm and 850 nm prepared on soda lime glass. The temperature dependent resistivity data were obtained by Paul J. Roland. [191]

Carrier concentration exceeding 10^{19} cm^{-3} indicates near-degenerate doping.[237, 238] Typically, degenerately-doped semiconductor films show conductivity that is nearly independent of temperature. In our case, a temperature-dependent conductivity indicates a significant role is played by the high density of grain boundaries. The classical grain boundary model, as first introduced by Seto,[239] omits accounting for the inherent variability in potential barrier height at the grain boundaries. Werner showed that a distribution of barrier heights results in a curved Arrhenius plot of conductivity vs.

temperature.[240] Indeed, such a temperature dependence is observed, and found as did Seefeld et al.[198] that the NC FeS₂ films behave according to the Werner model based on a Gaussian distribution of barrier heights as follows.[240]

$$P(\Phi) = \frac{1}{\sigma_{\Phi} \sqrt{2\pi}} \exp\left(-\frac{(\bar{\Phi} - \Phi)^2}{2\sigma_{\Phi}^2}\right) \quad (5.1)$$

where $\bar{\Phi}$ is the mean barrier height and σ is the standard deviation. According to the Werner model, the transport of carriers in polycrystalline films is limited by thermionic emission across inhomogeneous grain boundaries. In this case, the temperature dependent resistivity is given by

$$\rho = \rho_0 \exp\left[q\left(\frac{\Phi}{kT} - \frac{q\sigma_{\Phi}^2}{2k^2T^2}\right)\right] \quad (5.2)$$

Our temperature dependent resistivity data for two different thicknesses were fitted with this model (Figure 5-18) yielding barrier height $\Phi = 45 \pm 18$ meV for the FeS₂ film of thickness 486 nm and $\Phi = 51 \pm 20$ meV for the FeS₂ film of thickness 850 nm respectively. From this analysis, it can be seen that there is a good agreement between the Werner theory and the experimental results in the temperature range of 300 K to 95 K. Due to the inhomogeneity of the films, the standard deviation is relatively large.[241] The barrier height obtained in this work is higher than nanocrystalline FeS₂ film obtained by Seefeld et al.[198] and smaller than bulk polycrystalline film obtained by Ares et al.[242] In the Seefeld et al. study, pyrite films were prepared from the solution phase deposition of an iron (III) acetylacetonate ink and the temperature dependent study was performed in the temperature range of 80 – 350 K. In Ares et al. study, pyrite films were

prepared by thermal evaporation of iron powder on soda lime glasses at room temperature and the temperature dependent study was performed at higher than room temperature.

5.3.2 Tin disulfide (SnS₂) Nanocrystals (NCs)

Figures 5-19 and 5-20 provide absorbance spectrum of the NC solution dispersed in chloroform and transmission spectrum of a thin film of ~100 nm made in soda lime glass substrate respectively. Absorbance spectrum shows bulk like behavior as there are no discrete features evident within the spectrum. As can be seen from Figure 5-19, SnS₂ NC displays optical absorption over nearly the entire visible range of spectrum. A long wavelength tail of absorption seen by Zang et al.[243] can be seen in this work as well and may be due to the impurities present in the materials. From the spectrum in Figure 5-20, transmission percentage of light of wavelength higher than 1100 nm is more than 80%. Similarly, transmission percentage of light of wavelength 500 nm is more than 60%. The transmission spectrum of SnS₂ NC is very important as optical absorption will play a key role in determining whether the material is appropriate for use as a window layer in a heterojunction design. The transmission spectrum of SnS₂ NC is similar to the spectrum of CdS which has been used as one and only one window layer for CdTe device.[15] The direct band gap of nanocrystalline SnS₂ NC has been calculated using Figure 5-19 (as shown in Figure 5-21) and is found to be 2.7 eV, higher than published results. [244] Wider band gap is beneficial for the solar cell fabrication as the window layer allow all incident radiation to pass through to the absorber layer.

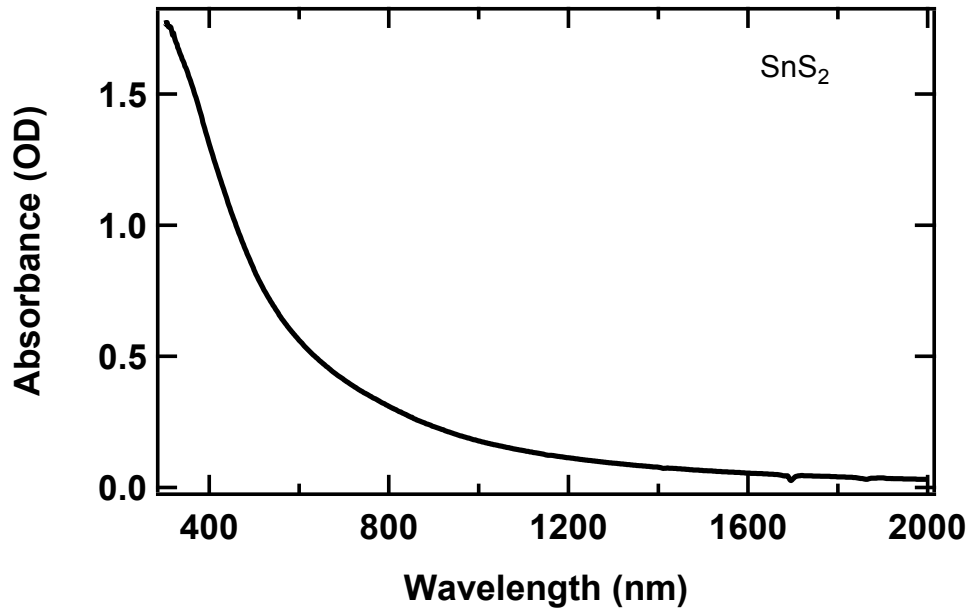


Figure 5-19. Absorbance spectrum taken from spectrophotometer; SnS₂ NC solution was prepared in chloroform. The path length of the cuvette was 2 mm. SnS₂ was very well dispersed in chloroform. The color of the solution was yellow-orange.

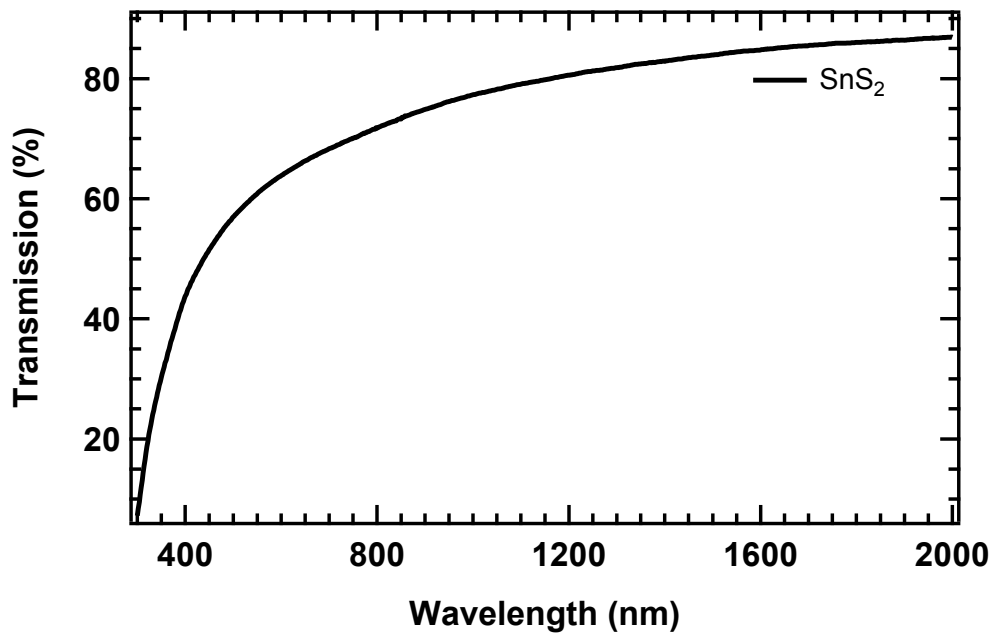


Figure 5-20. SnS₂ spin coated film was prepared in soda lime glass. The thickness of the film was about 77 nm measured from Dektak profilometer. The film looks light orange and adheres well in the substrate. This does not account for reflection losses.

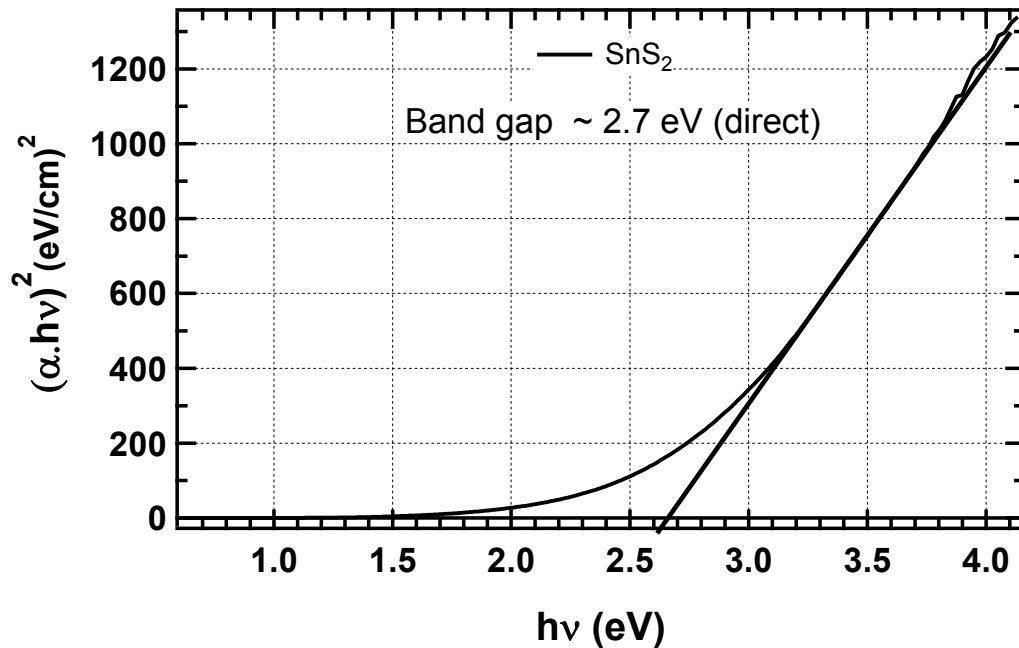


Figure 5-21. Band gap calculation using Figure 5-19; the direct band gap of the material is found to be ~2.7 eV. The NCs were dispersed in chloroform and the path length of cuvette is 2 mm.

Figure 5-22 shows the powder XRD spectrum of SnS₂ NPs. Powder XRD was required for apple-to-apple comparison, since many peaks were found missing when XRD was taken from the NC film deposited on a glass substrate. The intensity of each peak depends on the orientation of the lattice plane. Therefore, the intensity of each peak may be different obtained from powder XRD and that of the film. Vertical red lines represent standard diffraction peaks and from the spectrum, it is clear that most of the lattice planes are orientated along (001) direction. All these results are comparable to the one obtained by Jung-wook Seo et al. [208]

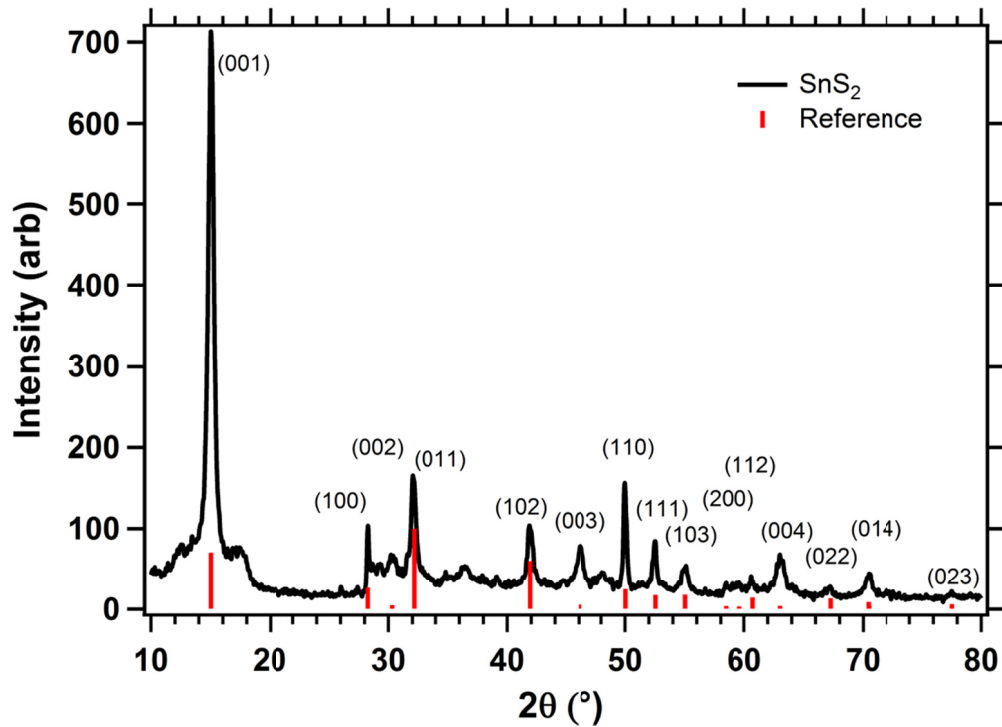


Figure 5-22. XRD pattern of SnS₂ product prepared by heating the tetrakis (N, N-diethyldithiocarbamate) tin (IV) at 280 °C for 10 min.. The intensity of some of the peaks is very low, possibly because of the differently orientation of crystal planes are oriented in other directions.

Figure 5-23 shows the Raman spectrum of SnS₂ NPs at room temperature, measured using a 632.8 nm laser source. The Raman spectrum showed a strong peak at 313 cm⁻¹ which is consistent with the A_{1g} vibrational mode of SnS₂. [245] Two weaker Raman peaks were observed at 160 cm⁻¹ and at 218 cm⁻¹; the assignment of the 160 cm⁻¹ peak is uncertain, but the peak at 218 cm⁻¹ belongs to E_u mode of vibration.[245]

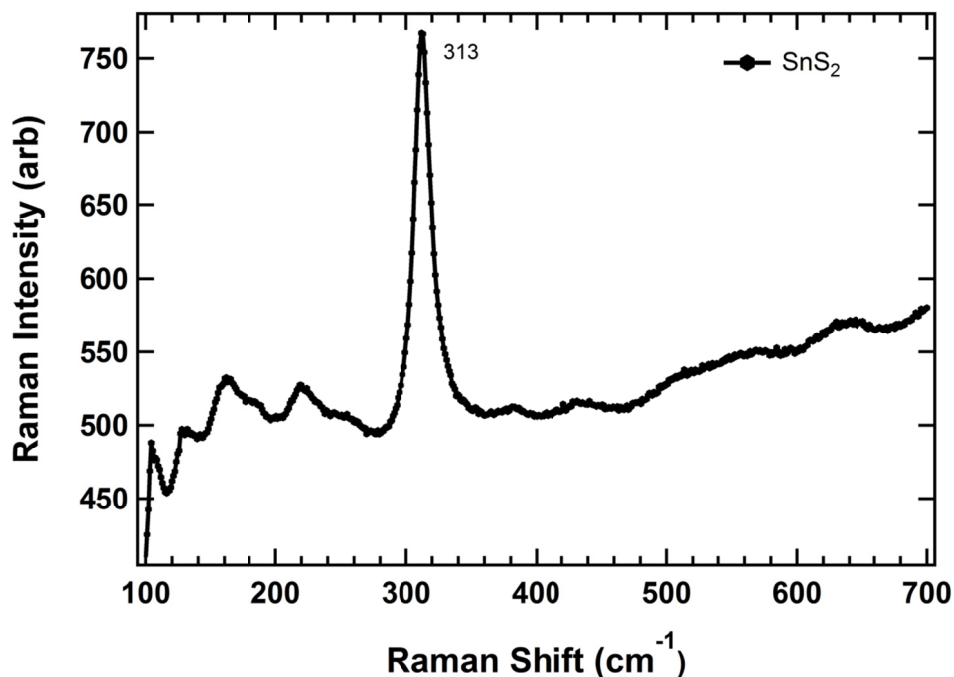


Figure 5-23. Raman spectra of SnS₂ prepared by heating tetrakis (N, N-diethyldithiocarbamate) tin (IV) at 280 °C for 10 minutes.

The electron micrographs in Figure 5-24 show hexagonal structure of SnS₂. Figure 5-24 clearly show that SnS₂ NCs are two dimensional hexagonal nanoplates with a lateral size of ~165 nm. Transmission electron microscopy (TEM) and scanning electron microscopy (SEM) images clearly showed that the SnS₂ NCs obtained by this procedure are 2D hexagonal nanoplates with a lateral size of >150nm and definitely some size distributions (Figure 5-24a and b). These results are comparable to the work done by Seo et al. [208] EDS Measurement was done to find out the stoichiometry of the material and EDS spectrum is shown in Figure 5-25 along with the table representing atomic percentage of S and Sn atoms. From the measurement, an average atomic % ratio of S/Sn was found to be ~2/1.

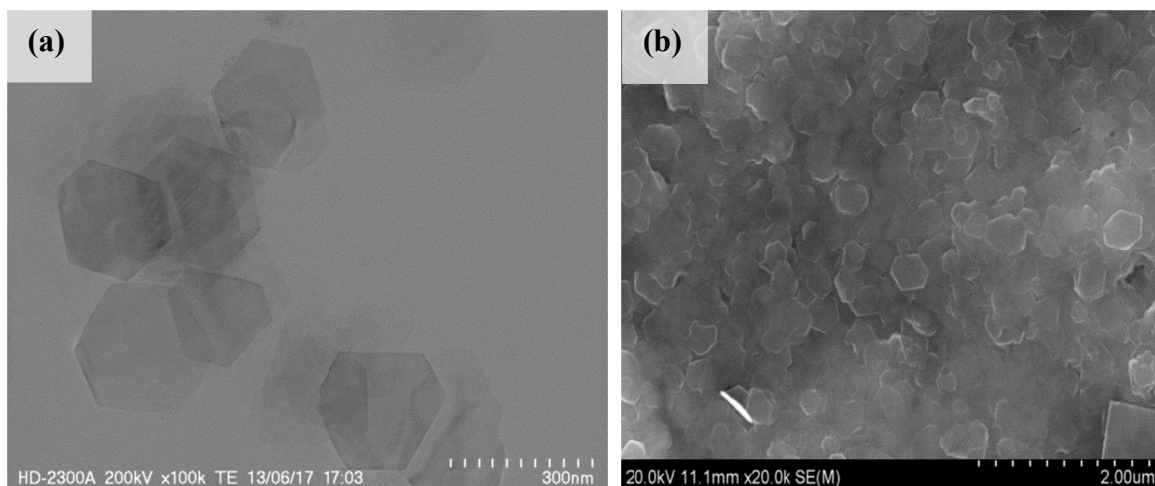


Figure 5-24. (a) TEM and (b) SEM images of SnS₂ NPs; For TEM image, graphene enhanced Cu grids were used and for SEM image, SnS₂ film was prepared on glass. Most of the particles are hexagonal in structure, with each side of length ~165 nm.

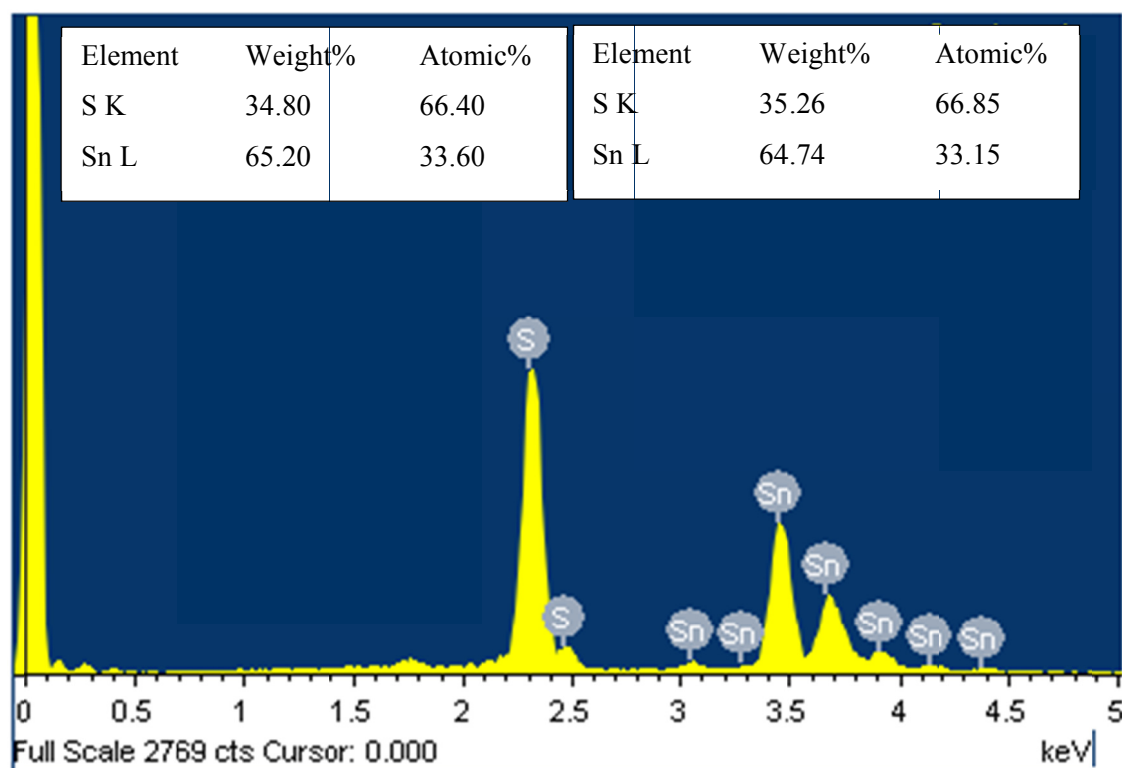


Figure 5-25. EDS measurement of SnS₂ NC film. Atomic and weight percentage of Sn and S are provided in tables.

5.4 Conclusions

Iron persulfide NCs were synthesized using hot injection method in an inert atmosphere. Phase pure and highly crystalline FeS₂ NCs were identified using iron (II) bromide (FeBr₂) as the iron precursor coordinating with TOPO or 1,2-hexanediol. From the detailed study of their electrical properties, FeS₂ semiconductor NC-based films were found to be p-type with very high carrier concentration up to $\sim 1 \times 10^{19} \text{ cm}^{-3}$, and very low mobility of $< 1 \text{ cm}^2 \text{ V}^{-1} \text{ s}^{-1}$. The high free carrier density and very low mobility limit the application of our FeS₂ NC-based films as the absorber layer in thin film solar cells. Temperature dependent conductivity studies revealed that even though they have high carrier concentration, these FeS₂ NC films behave as non-degenerate semiconductors. Temperature dependent conductivity studies indicated that the conductivity depends mainly on the density of grain boundaries in accord with the Werner model.

Tin disulfide nanoparticles were synthesized mainly to use as heteropartner for SnS₂/FeS₂ heterojunction solar cells. Unfortunately, their application did not improve the performance of the devices. Carrier concentration of SnS₂ NC should be of the order of 10^{16} cm^{-3} , very less than FeS₂ to make depletion region in the absorber layer side. Their applications in solar cell fabrication may be possible if window layer is prepared from a material with carrier concentrations higher than the carrier concentrations of FeS₂ which are of the order of 10^{20} cm^{-3} . SnS₂ NCs are hexagonal nanoplates with lateral size of more than 150 nm.

Chapter 6

Application of earth abundant iron pyrite nanocrystal as a copper-free back contact for polycrystalline CdTe thin film solar cells

6.1 Introduction

Iron pyrite (iron persulfide, FeS_2) exhibits an indirect band gap of 0.95 eV[181, 182] and an absorption coefficient exceeding 10^5 cm^{-1} for photon energies above 1.3 eV.[178-180] Following significant focus on FeS_2 solar cells in the early years of thin film photovoltaics,[182, 183, 246-250], FeS_2 has in recent years attracted renewed attention as a potential light-absorbing layer in thin film PV cells based on its suitable band gap energy, high absorption coefficient, low toxicity, and elemental abundance.[184, 185, 187-189, 251-255] However, FeS_2 -based PV devices have thus far performed poorly compared with devices based on other recently-developed absorber materials (e.g. CZTS, perovskites such as methylammonium lead iodide, and PbS QDs).[15, 143, 256-258] Tributsch et al.'s extensive efforts initiated in the 1980s led ultimately to a 2.8% efficient photo-electrochemical cell based on single crystal FeS_2

electrodes using an iodide/tri-iodide (I/I_3^-) redox couple.[182, 183, 246, 247] This result stands as the efficiency record for FeS_2 -based solar cells, owing in part to the well-recognized challenges presented by high defect densities resulting from poor phase and stoichiometry control.[180, 181] Specifically, phase purity has been an identified concern for effective FeS_2 photovoltaic devices because the different iron sulfide phases of Fe_xS_y exhibit a wide range of optoelectronic properties.[259]

Here, the author reports on the discovery that the properties of FeS_2 nanocrystal-based thin films yield excellent performance as a low barrier back contact to CdTe solar cells. [260] Cadmium telluride thin film modules represent ~7% of the 32 GW of PV modules produced in 2012, and CdTe manufacturing yields the lowest cost on a per-Watt basis ($\$0.49/W_p$).[261] Creating a low-barrier, ohmic back contact to CdTe requires addressing both the high work function and the low resistivity of the CdTe thin film. An ohmic contact represents an electrical junction between metal and semiconductor which follows Ohm's law with no rectifying behavior. Standard back contact preparation involves the introduction of copper, as a thin evaporated layer or as a $CuCl_2$ solution deposition, followed by thermally-assisted diffusion to create a low-resistivity Cu_xTe phase.[262] The detailed roles of copper in CdTe thin film are described in next paragraph. Several studies have shown that Cu diffuses readily, and over time reaches the CdS/CdTe interface, reducing the operating voltage of the device.[263, 264] Copper diffusion therefore serves as a critical pathway to degradation, influencing device performance over the life of a PV system and ultimately degrading the economic performance of the technology.[147] Alleviating the degradation associated with Cu

diffusion would yield significant economic benefits for CdTe-based photovoltaic systems.[38]

The low p-type doping in as-grown polycrystalline CdTe thin films is due to the presence of Cd vacancy (shallow acceptor).[265] When very small amount of Cu is deposited, the low conductivity of the CdTe thin film further decreases due to the inclusion of Cu impurities in the form of interstitial Cu_i . In this case, Cu_i sites act as shallow donors and compensate the conductivity due to Cd vacancies. In this case, the free hole density decreases and hence the conductivity of CdTe film also decreases. Slowly, Cu atoms not only fill the interstitial site, but also fill the Cd vacancies. In this case, two copper atoms are required to fill one Cd vacancy. These two diffusion processes are not considered energy favorable because of their higher formation energies (2.19 eV and 2.67 eV). Copper atoms also diffuse into the CdTe by replacing Cd as a substitutional acceptor, Cu_{Cd} . Diffusion of Cu in this fashion is more favorable because of low formation energy (1.31 eV. [266]According to Chin et al. the optimized Cu treatment temperature for substitutional doping of CdTe is 280 – 300 °C.[265] . When more Cu is introduced into CdTe, more Cu_xTe is formed increasing the hole concentration in the system and increasing the conductivity of the CdTe films. Beyond this temperature range, other two diffusion processes will be more favorable and thus decrease the conductivity of the film.

For CdS/CdTe solar cells, therefore, conventional back contacts are commonly made with Cu/Au or Cu/graphite.[267] Graphene has been employed as a back contact for thin film CdTe solar cells, but to narrow the barrier at the CdTe/graphene interface, either Cu or B was incorporated. [268, 269] Phillips et al. recently reported that thin films of single wall carbon nanotubes (SWNTs) make stable, high-performance back

contacts to CdTe without introduction of Cu. [38] Their analysis suggests that semiconducting SWNTs make ohmic contacts with p-CdTe while metallic SWNTs make rectifying contacts to p-CdTe. Our results applying FeS₂ NCs as the back contact to CdTe solar cells show substantial promise for this Cu-free and potentially low-cost approach.

6.2 Experimental

6.2.1 Synthesis and film preparation of FeS₂ NC

Solution-based synthesis and deposition offers a potentially low-cost and scalable photovoltaic manufacturing method for large glass substrate processes and roll-to-roll processing on flexible substrates. Numerous routes have been followed to synthesize FeS₂ NCs, [184, 185, 187, 251] and here a solution-based approach is initiated based on thermal injection reaction of an iron salt solution with an elemental sulfur source. While others have utilized FeCl₂ as the iron source, it is found that FeBr₂ yields improved results regarding crystal structure and infrared absorption.

To fabricate the FeS₂ NC films, a drop-cast layer-by-layer (LbL) method [15, 43, 142] was utilized. To make the NC films more conducting, long chain hydrocarbon molecules (TOPO or 1,2-hexanediol) introduced during the synthesis process were removed from the NC surface in the LbL process by cyclically treating films with 1 M hydrazine in ethanol. In the case of an untreated film, the film thickness was increased by simply repeating the drop-cast process followed by the drying process; preparation of a ~1 μm film typically requires 2 cycles. The detailed film fabrication process is explained in Chapter 5.

6.2.2 CdS/CdTe device fabrication

CdS/CdTe layers were grown by RF magnetron sputtering and closed spaced sublimation (CSS) methods on fluorine doped SnO₂ transparent conducting layer deposited on soda lime glass substrate. Magnetron sputtering techniques provide films with better adhesion, smaller grain size and relatively smooth surface due to its slow deposition rate at low temperature (200 – 300 °C).[270] Close spaced sublimation has been the most productive method due to the very high deposition rate, low material consumption and low cost of operation. As compared with sputtered CdS/CdTe films, CSS yields films with larger initial grain size (~2 – 5 μm vs. ~200 – 300 nm) due to the high deposition temperature (~600 °C substrate temperature for CSS vs. ~275 °C for sputtered films).[271] Independent of the deposition method, following the CdTe deposition a CdCl₂ treatment was carried out at room temperature. For the CdCl₂ activation a saturated solution is prepared by dissolving CdCl₂ white powder into methanol. Then a few drops of this solution were applied to the CdTe film, the film was shaken horizontally to spread the solution over the entire film, and the solution was allowed to dry in air at room temperature. The film was subsequently annealed at 378 °C in dry air to advance grain growth, release interfacial strain, and facilitate sulfur and tellurium mixing at the CdS/CdTe interface.[272] The thickness of CdS films in both methods was ~80 nm whereas the sputtered CdTe was ~2.0 μm and of the CSS CdTe was ~4 μm. Sputtered CdS/CdTe films enabling typical conversion efficiency of ~12%, and CSS CdS/CdTe films enabling typical devices of ~14.0% efficiency have been used; all device efficiency measurements are made under AM1.5G simulated solar spectrum at

ambient laboratory temperature. Standard devices were prepared on TEC15 TCO-coated glass (Pilkington N.A.) with a high-resistivity layer as part of the normal coating process. Following CdS/CdTe deposition, the standard back contact consists of a Cu/Au sequential deposition in which ~3 nm of Cu followed by ~30 nm of Au is evaporated onto the CdTe, and the film is then heated to 150 °C for 45 minutes in air to drive Cu diffusion.

6.3 Results and Discussions

6.3.1 Characterization of thin films: FeS₂, CdS, CdTe and Au

Iron pyrite exhibits a yellowish metallic luster reminiscent of gold, from whence it derives the nickname Fool's Gold. As-deposited FeS₂ NC films, with the initial surfactant (e.g. TOPO) intact, studied at room-temperature using four-point probe and Hall measurements showed low resistivity of ~100 Ω-cm, high free carrier concentrations of ~10¹⁹ cm⁻³, and low mobility of ~10⁻¹ cm²V⁻¹s⁻¹. In addition, FeS₂ NCs show strong sub-bandgap optical absorption, indicating the presence of electronic states in the gap arising from core and/or surface defects. Strong photovoltaic performance would not be expected when using these FeS₂ films as an absorber layer, based on the combination of high free carrier density, low mobility, and mid-gap absorption leading to reduced photovoltage. Indeed, the author notes here that within Tributsch's work, the highest open circuit voltage (V_{OC}) attained was ~0.28 V, much lower than the theoretically attainable value of ~0.5 to 0.6 V; [273] Tributsch et al. attributed the low photovoltage to both strong Fermi level pinning associated with surface states and to bulk defects caused by sulfur deficiency. [229] For purposes of comparison, note that CdTe, which has

achieved a conversion efficiency of >20% under standard test conditions,[18] typically exhibits resistivity of $\sim 10^4 \Omega\text{-cm}$, a free carrier concentration of $\sim 10^{14} \text{ cm}^{-3}$, and hole mobility of $\sim 10^2 \text{ cm}^2/\text{V}\cdot\text{s}$. [274, 275]

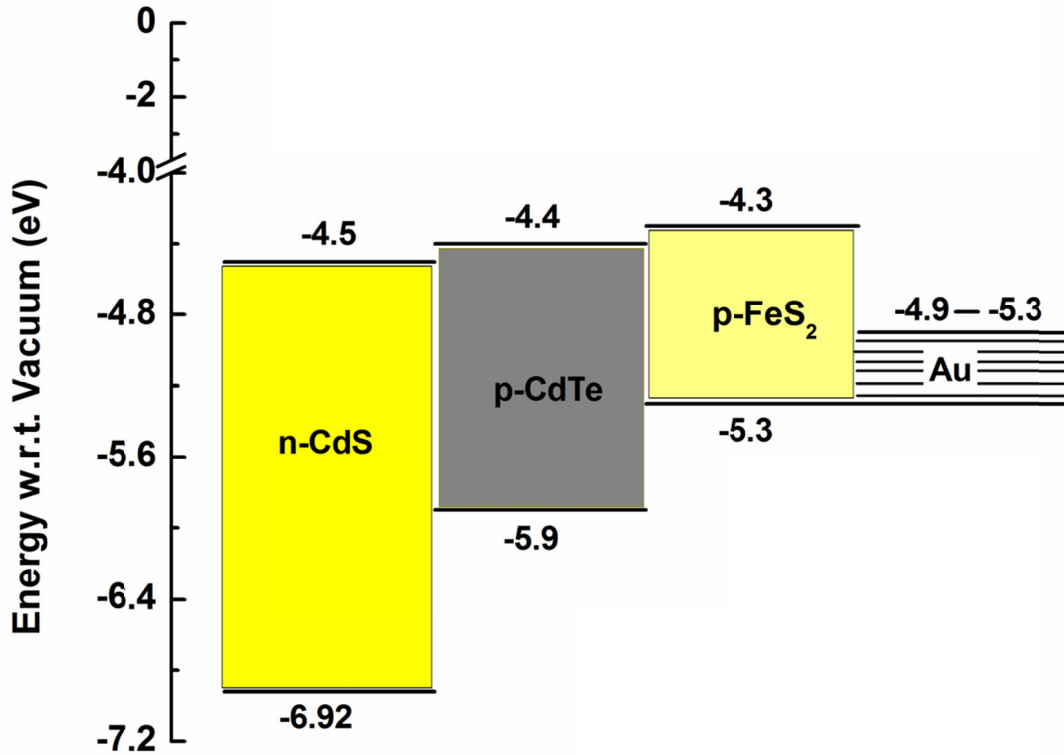


Figure 6-1. Non-equilibrium band diagram showing conduction and valence band positions relative to the vacuum level; the estimated carrier density of each semiconductor layer is also included.

The reported work function of FeS₂ ($\phi \approx 5.45 \text{ eV}$ [276], $\phi \approx 5.0 \text{ eV}$ [183]) compares favorably with that of Au ($\phi \approx 5.1 \text{ eV}$). As shown in Figure 6-1, the non-interacting band diagram indicates the possibility of a barrier-less interface, though charge polarization associated with Fermi level equilibration typically introduces band bending. The carrier densities of n-CdS and p-CdTe were measured using capacitance

voltage (Mott Schottky) measurement, and the carrier density of p-FeS₂ NC film was measured using a Hall measurement system. The observed high free carrier concentration and low resistivity suggest promise for FeS₂ as a conductive layer. Therefore, although FeS₂ has not served well as a solar cell absorber layer, the properties point to its potential as an ohmic contact to CdTe. For CdS/CdTe solar cells, conventional back contacts are commonly made with Cu/Au or Cu/graphite. Copper introduced at the back diffuses atomically to the CdS/CdTe junction, resulting in shunting at the n-p junction.[264, 277] As described below, our results from applying FeS₂ as the back contact to CdTe show substantial promise for this Earth-abundant and low-cost interface layer.

6.3.2 Application of iron pyrite as a back contact

Photocurrent contribution from the iron pyrite NC is not expected, but use of an FeS₂ NC film as an interface or buffer layer at the back contact improves the performance of CdTe solar cells. Since the work function of Au is not sufficient to form an ohmic contact to CdTe, the back barrier effect present in CdTe solar cell can be minimized to some extent by depositing a thin layer of Cu before the Au deposition. The Cu/Au back contact improves the performance, compared with that of Au-only, by increasing V_{OC} and FF. Nanocrystalline FeS₂ can be used as a replacement for Cu to achieve similar performance to that of Cu/Au. By inserting an FeS₂ NC layer between the deposition of Cu and Au, performance of CdTe solar cells can be further increased. The concept of utilizing a semiconductor interlayer at the back contact originated about 22 years back when Rioux et al. utilized ZnTe as an interface layer to minimize the barrier effect. [278] At present, the CdTe thin film PV technology leader, First Solar, has

implemented ZnTe as an interface layer to improve the performance of their CdTe solar cells. [279] Preliminary results show here that FeS₂ NC layer is a potential candidate for such an interface layer which can be used to increase the V_{OC} of a device by ~5% in comparison to standard Cu/Au back contact cells.

6.3.2.1 Performance of CdS/CdTe devices with different back contacts

Figure 6-2a displays CdTe solar cell device structure with FeS₂/Au as back contacts. For a standard device, a thin layer of Cu is deposited before depositing Au -- i.e. Cu/Au is used as a back contact for CdTe solar cells. Cross-sectional SEM images, shown in Figure 6-2b, were obtained for CdS/CdTe devices prepared in a stepwise process on TECTM15 glass using RF magnetron sputtering deposition of CdS (~80 nm) and CdTe (~2 μm), standard CdCl₂ treatment, LbL drop-cast deposition of NC FeS₂, and evaporation of ~30 nm Au for improved electrical contact for J-V and QE characterization. Because of relatively low magnification, the thinnest layers such as CdS are not clearly seen in cross-sectional images. Representative current density/voltage (J-V) characteristics for sputtered CdTe devices prepared with different back contacts are shown in Figure 6-3, and average device parameters are presented in Table 6-1. These solar cells were prepared on 1" x 1" TECTM15-coated glass substrates.

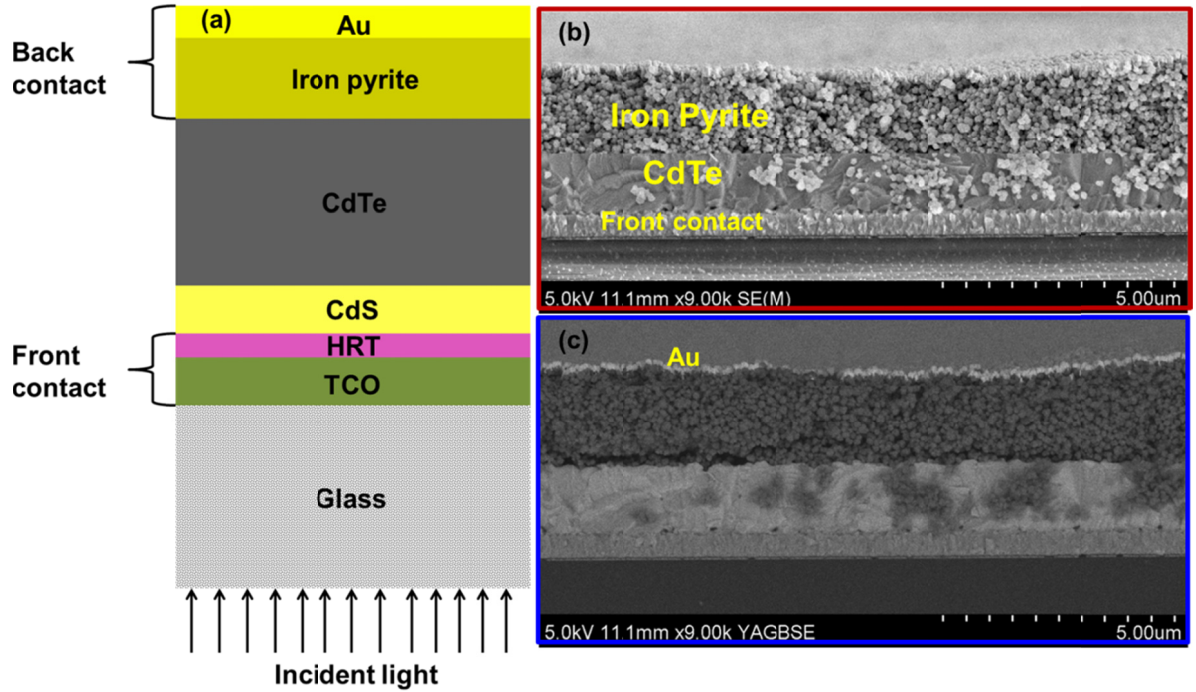


Figure 6-2. (a) Standard device structure of CdTe thin film solar cells with FeS₂/Au as a back contact and (b) Cross-sectional SEM images, obtained by SE detector and (c) cross-sectional SEM images obtained by back scattered detector, of drop-cast FeS₂ nanocrystalline thin film contacts formed by layer-by-layer drop casting onto sputtered CdS/CdTe thin films.

Table 6-1 demonstrates average and standard deviations of 15 cells of each type prepared on a substrate. Each J-V curve in Figure 6-3 shows best cell of these 15 cells. In Figure 6-3, solid lines represent light response and broken lines represent dark response of the devices. The red line represents the J-V curve when 30 nm Au was evaporated as a back contact, without any Cu diffusion layer, and shows a short circuit current density of 20.3 mA cm⁻². Although J_{SC} does not drop significantly compared to the other back contact types, V_{OC} and efficiency (η) are poor when Au is used alone as a back contact. Because of CdTe's high electron affinity, -4.5 eV from the vacuum level,[280] a high

work function material is required to form a zero barrier height (ohmic contact) with p-type CdTe. To form an ideal ohmic contact to CdTe, a metal should have a WF of least 5.9 eV.[281] In available metals, a Schottky barrier is always formed with CdTe at its typical free hole concentration; the barrier results in a significant limitation to hole transport from the CdTe to the metal. The Schottky junction acts as a diode, the direction of which opposes the main diode formed between CdS/CdTe interfaces (Figure 6-4). The diode at the back contact causes the current-voltage curve to roll over at forward bias, decreasing both FF and V_{OC} .[282, 283]

Table 6.1: Average parameters for 15 CdTe solar cells in three different back contacts

Back	V_{OC}	J_{SC}	Fill factor	Efficiency	Series resistance
Au	0.645±0.04	20.2 ± 0.9	59.3 ± 2.5	7.7 ± 0.9	7.7 ± 0.6
Cu/Au	0.789 ± 0.02	21.8 ± 0.7	65.4 ± 1.9	11.3 ± 0.9	5.4 ± 1.0
FeS₂/Au	0.766±0.01	22.4 ± 1.0	61.5 ± 1.0	10.6 ± 0.4	6.9 ± 0.4

The problem associated with using a metal-only (e.g. Au) back contact is minimized by depositing, by sequential thermal evaporation, ~3 nm Cu and ~30 nm of Au, onto CdTe and annealing the film at 150⁰C for ~45 minutes. If the CdTe surface is chemically etched after CdCl₂ treatment, the interdiffused Cu can form a distinct Cu_{2-x}Te layer and increase the effective doping level of a thin layer of the CdTe through interdiffusion.[262] The Cu_{2-x}Te layer increases the conductivity and narrows the barrier which allows pseudo-ohmic tunneling behavior at this interface.[284] Even in the absence of chemical etching, the Cu-rich layer reduces the height and width of the space

charge region (barrier), thus narrowing the barrier width sufficiently to allow efficient carrier tunneling to the Au; the result is a pseudo-ohmic contact.

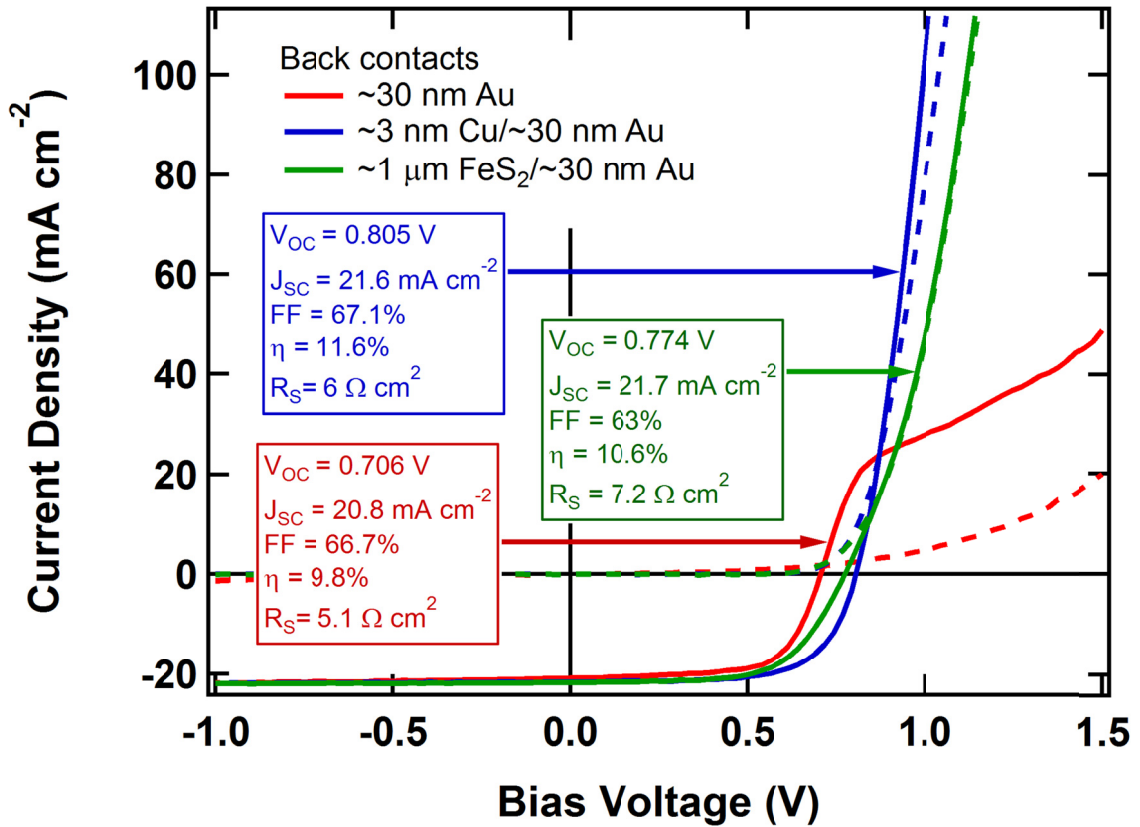


Figure 6-3. Current density vs. bias voltage measurements of sputtered CdTe device with Au, Cu/Au, and FeS₂/Au back contacts obtained under simulated AM1.5G solar spectrum.

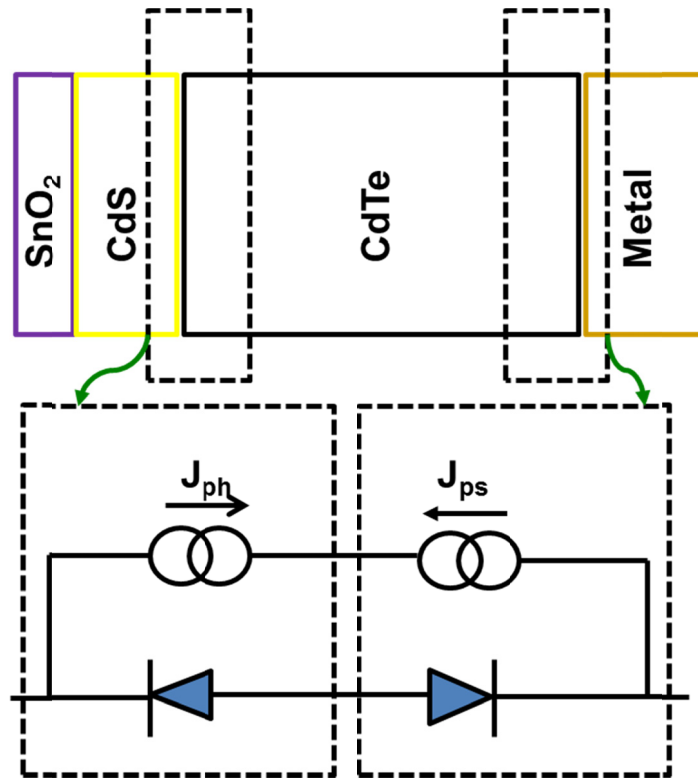


Figure 6-4. Two diode model equivalent circuit including a heterojunction diode between the CdS and CdTe films and Schottky junction diode between CdTe film and back contact metal; J_{ph} represents photocurrent density due to heterojunction and J_{ps} represents photocurrent density due to Schottky junction.

When a 3 nm thick layer of Cu was deposited before Au (blue curve, Figure 6-3), the V_{OC} improved from 679 mV to 794 mV and efficiency improved from 8.7% to 11.4%. When 3 nm Cu was replaced by a $\sim 1.0 \mu\text{m}$ thick FeS_2 NC layer at room temperature and 30 nm thick Au atop of it (green curve, Figure 6-3), performance of the device was similar to the Cu/Au standard back contact. The FeS_2 NC back contact, which consisted of an unheated hydrazine-treated film, showed a $V_{OC} = 774 \text{ mV}$, $J_{SC} = 21.7 \text{ mA}\cdot\text{cm}^{-2}$, and a 10.6% efficiency. The fill factor for the CdTe/ FeS_2 /Au contacted devices did decrease (Figure 6-3) due to a residual barrier and slight increase in the series

resistance. The increase in the J_{SC} is typically present for the sputtered CdTe cells, and tests are ongoing to confirm and understand the effect. Possible sources of the increased J_{SC} are (a) reabsorption of transmitted light by back-reflection, (b) a reduced interfacial recombination velocity at the back contact, and (c) a systematic error in the device area. Option (c) has been addressed by QE measurements which do not depend on the device area. As discussed below, the QE measurements shown in Figure 6-4 indicate that the FeS_2 back contact improves carrier collection in the CdTe and reduces the collection efficiency for photons absorbed in the CdS.

Carrier collection efficiency of the devices used for Figure 6-3 were examined by comparing their measured external quantum efficiency (EQE) spectra as shown in Figure 6-5. In the lower wavelength region (below ~ 600 nm), carrier collection when Au and Cu/Au were used as back contacts was slightly less than when the back contact was FeS_2/Au . Collection loss at the longer wavelength region when Au is used as back contact arises due to the interface problem between CdTe and Au which is improved when FeS_2 NC layer is deposited as an interface layer between CdTe and Au. The Cu/Au contacted cells show an EQE spectrum nearly identical to that of the FeS_2/Au contacted devices. Due to the application of FeS_2 NC as a back contact, EQE cutoff point at the CdTe band gap region decreased by ~ 10 nm (inset Figure 6-5) which may be due to the reduced reflection of photons with energies near the CdTe band gap energy, where CdTe is weakly absorbing. The decrease in EQE in the low wavelength region from 375 to 500 nm is not expected to depend on the back contact; the EQE in this region solely depends on the absorption of light due to CdS and TCO layers. Some variation in thickness occurs not only on CdS layer but also for the CdTe layer because of the geometry of the

sputtered deposition chamber – these thickness variations ultimately lead to variation in device performance.

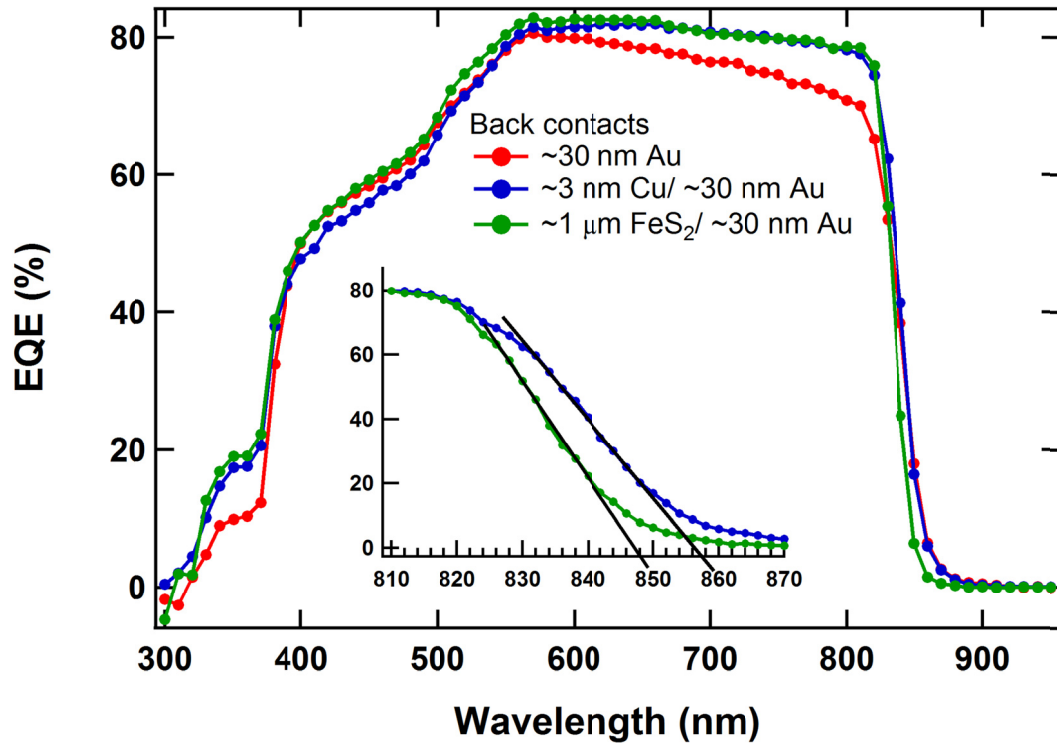


Figure 6-5. External quantum efficiency for sputtered CdTe devices with Au, Cu/Au and FeS₂/Au back contacts. The inset provides a zoomed view of EQE in the long wavelength cutoff region.

In contrast with the Cu/Au contact, which requires thermal treatment to drive diffusion of the Cu, preparation of the FeS₂/Au contact did not entail heating the device. A relatively thick layer ($> 1.0 \mu\text{m}$) of FeS₂ NCs was deposited onto the CdTe layer to prevent the evaporated Au layer from reaching the CdTe layer through pin holes within the FeS₂ NC layer. One possible disadvantage of this thick layer of FeS₂ NCs is that it may decrease the fill factor of the solar cells because of a series resistance increase at the back contact.

The author investigated the dependence of device performance on the FeS₂ NC layer thickness, using UT high-efficiency CSS-deposited CdS/CdTe device structures; an optimized CSS CdTe device fabricated at UT using the standard Cu/Au back contact has reached 15.5% under AM1.5G simulated solar radiation.[285] In our application, a CdTe film stack, using Cu/Au as the back contact and producing a maximum device efficiency of 14.3% under STC, was used. We proceeded to replace the Cu evaporation/diffusion step with varying thicknesses of FeS₂ NC layers (from 0.35 μm to 1.5 μm), while fixing the other device architecture and processing parameters. A ~30 nm Au layer was deposited following fabrication of the hydrazine-treated FeS₂ NC film. The performance parameters of these devices were compared with devices using a Cu/Au back contact. Current density vs. voltage curves for all four different back contact cases are shown in Figure 6-6. Initial tests show that thin FeS₂ layers (~0.35μm) yield poor performance, perhaps due to an increased occurrence of pinholes through which Au may contact the CdTe directly and lower the V_{OC}. The thickest FeS₂ film (~1.5μm) showed an effectively increased series resistance and thus a decreased V_{OC}. Comparatively low photo-conversion efficiency of the device, when the back contact was 0.35 μm of FeS₂ and 30 nm of Au, is due to the low V_{OC} even though other parameters are considerably higher. When the FeS₂ thickness was maximum both J_{SC} and fill factor were lower, yielding a slightly decreased efficiency of the solar cells. Optimal performance was found when the FeS₂ NC layer thickness was ~0.7 μm; in this case, V_{OC}, J_{SC}, FF and η were 2.9%, 0.4%, 10% and 13% less than standard device. It is evident from Figure 6-6 that there is slight

S-kink like behavior in J-V curves when the thickness of FeS₂ is increased beyond ~350 nm. The detail of this behavior is described in the following section.

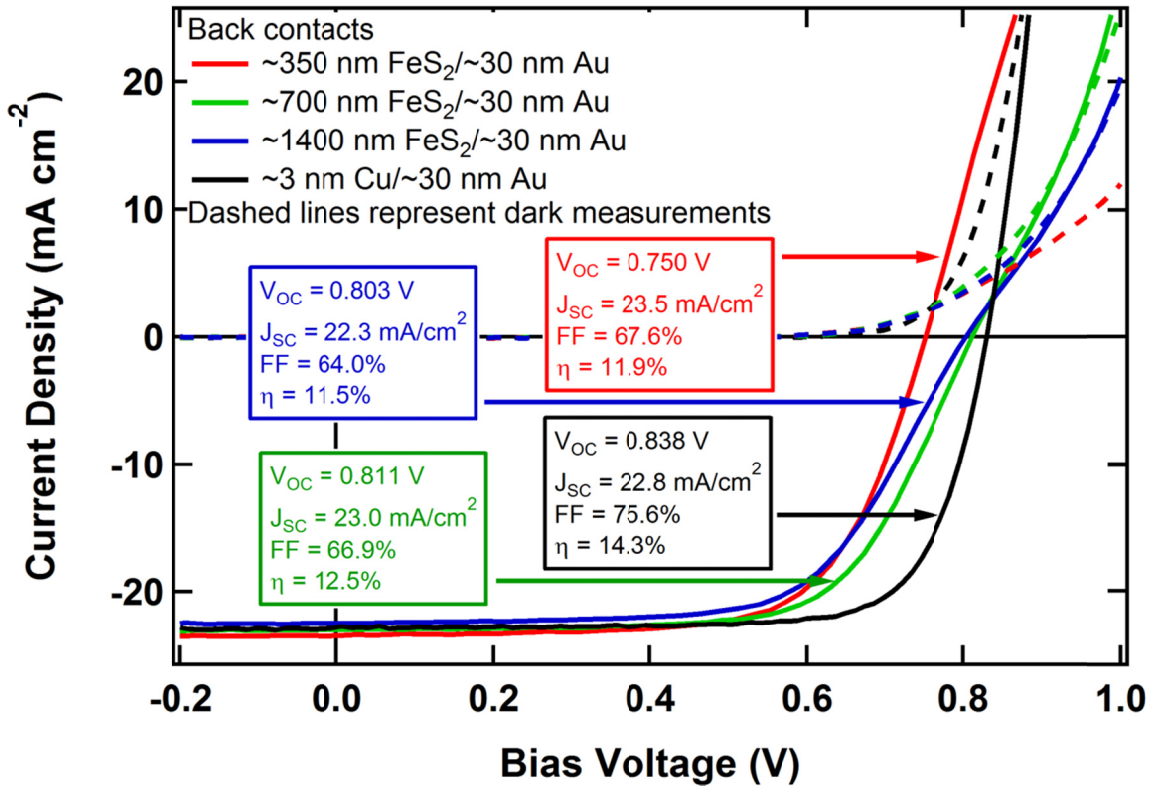


Figure 6-6. J-V curves when FeS₂ thickness was varied from 0.35 μm to 1.5 μm. Performance parameters for each device are shown in the boxes.

6.3.2.2 Thermal stability test of CdS/CdTe devices with different back contacts

The thermal stability of the sputtered CdS/CdTe devices having FeS₂/Au back contact was compared with that of the standard Cu/Au, and Au-only back contact devices. To test the stability of the FeS₂/Au back contact device, the completed device was tested at room temperature. The device was heated to 100 °C for an hour and tested for J-V characteristics when it comes to room temperature. This heating and testing procedure was repeated after 2, 6, and 23 hours. Finally the device was heated to 200 °C

for one more hour and tested for J-V measurement. This 24 hours long thermal stress treatment was conducted in N₂ environment (the thermal stress periods were carried out under ambient indoor lighting and not under solar intensity illumination). Figure 6-7 displays the performance of these devices before and after thermal treatment, and Table 6-2 displays the statistics of J-V parameters before and after the thermal stability test when FeS₂/Au was used as the back contact for sputtered CdTe device. Over a 24 hours time period, the efficiency of the device decreased from 10.7% to 10.3%. During this time period, V_{OC} decreased by 2.8% but the other parameters remained nearly unchanged. By the end of this stability test, the FF of the best cell increased by 1.6%. Figures 6-8 and 6-9 show J-V curves, before and after the thermal stability test, of sputtered CdTe devices when Cu/Au and Au were used as back contacts. The best cells' efficiencies for each back contact type, and at different times, are provided as well. These initial stability tests indicate that the devices with FeS₂/Au back contact show stability comparable with that of devices using the typical laboratory Cu/Au back contact.

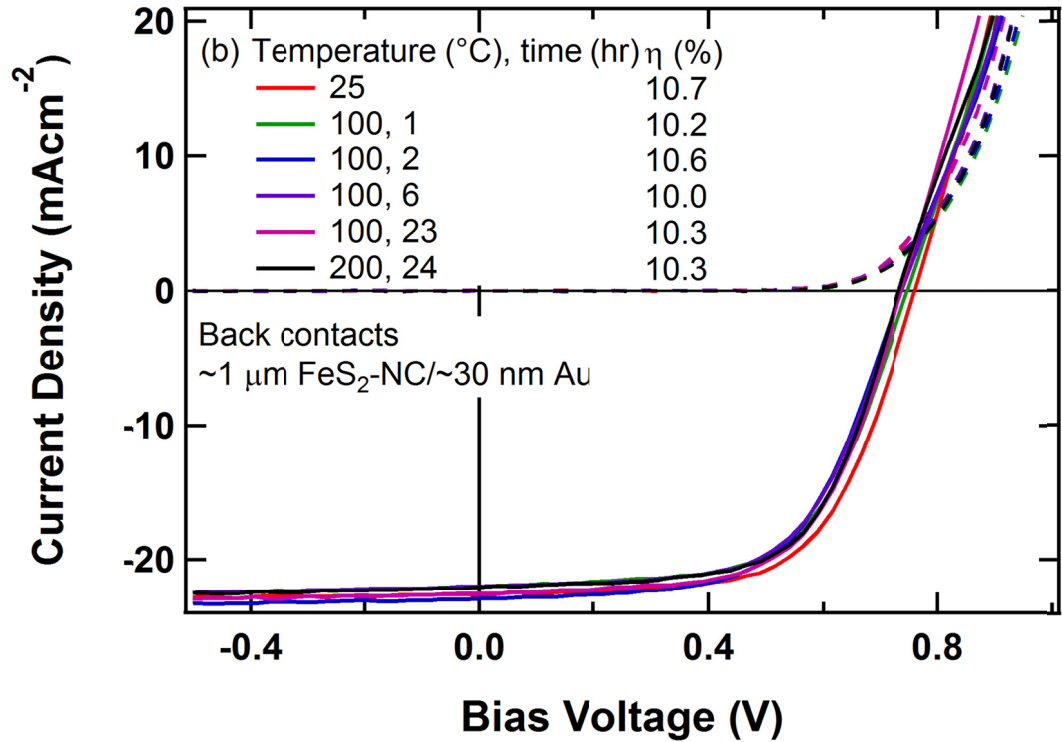


Figure 6-7. Thermal stability test for sputtered CdTe device when FeS₂/Au was used as a back contact. Best cells' efficiencies at different temperature and time are provided in the graph.

Table 6.2: Statistics of temperature dependent study of sputtered CdTe devices with FeS₂/Au as back contact; in each case, average and standard deviation of 15 cells were calculated.

Temp/Time	V _{OC} (volt)	J _{SC} (mA cm ⁻²)	FF(%)	η(%)	R _S (Ω cm ²)
Room	0.753±0.004	22.1±0.5	61.4±0.7	10.2±0.3	6.8±1.0
100 °C/1hr	0.741±0.005	21.6±1.0	60.4±1.1	9.7±0.5	8.4±0.8
100 °C/2 hrs	0.729±0.005	21.5±1.1	59.9±0.7	9.4±0.5	8.9±0.8
100 °C/6 hrs	0.732±0.005	21.78±0.9	60.3±0.7	9.6±0.5	8.8±1.0
100 °C/23 hrs	0.739±0.005	21.94±0.8	60.2±1.1	9.8±0.5	8.8±1.0

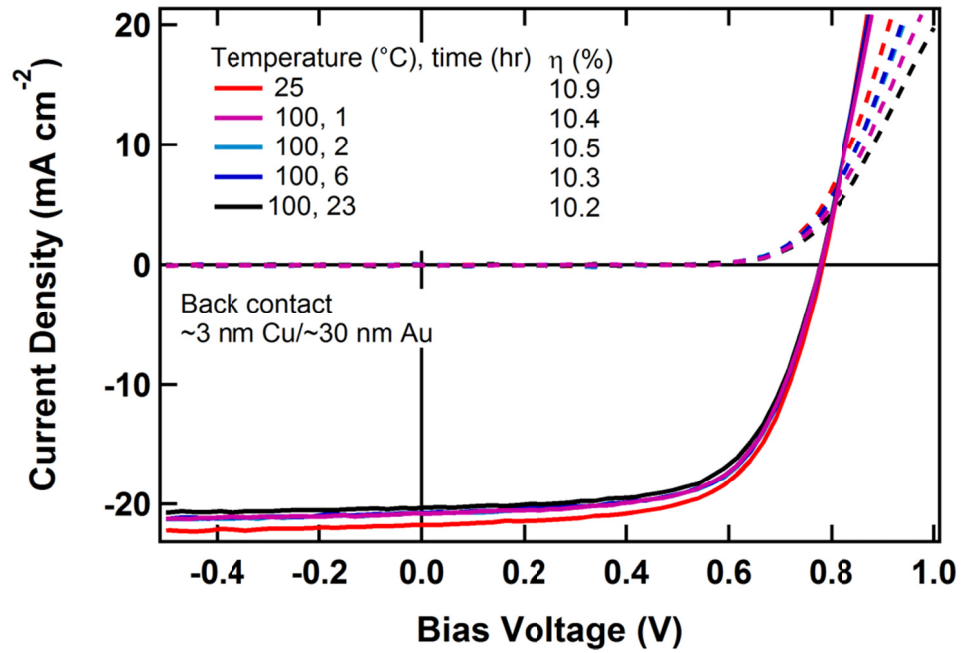


Figure 6-8. Thermal stability test for sputtered CdTe device when Cu/Au was used as a back contact; best cells' efficiencies at different time scales are provided.

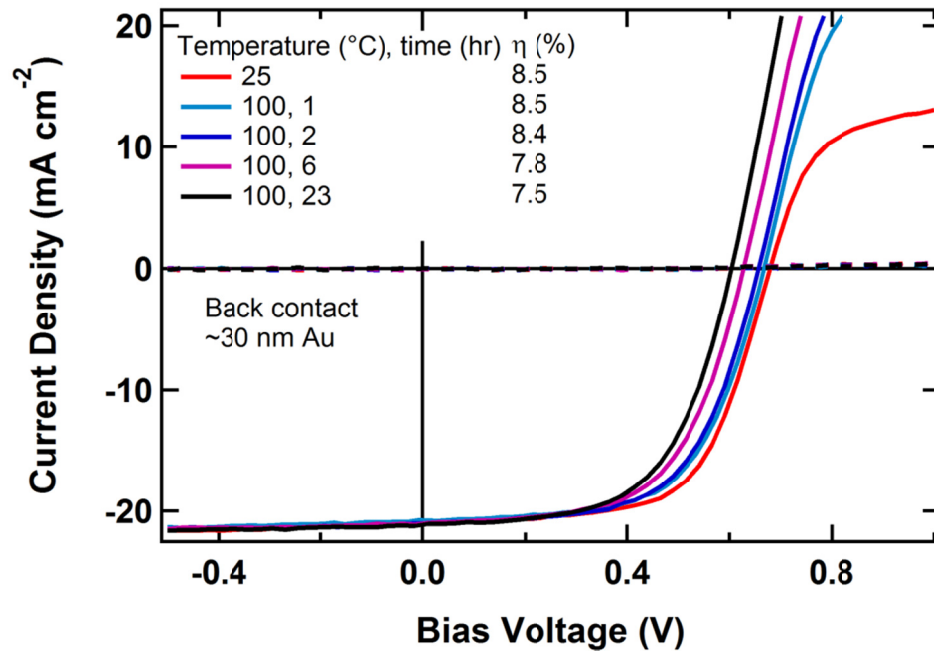


Figure 6-9. Thermal stability test for sputtered CdTe device when only Au was used as a back contact; best cells' efficiencies at different time scales are provided.

6.3.2.3 Effect of hydrazine on CdTe

To test whether the hydrazine does or does not favorably influence the CdTe material itself, two standard solar cell devices were prepared using sputtered CdS/CdTe. Before back contact deposition, one of the devices was dipped into 1 M hydrazine solution for about two minutes. Then the Cu/Au back contact deposition was completed using the normal procedure. Figure 6-10 displays J-V characterizations of complete devices in two cases. We see a very slight performance degradation when the CdTe film was treated with hydrazine before back contact deposition. This degradation may be due to the slight variations of CdS and CdTe thicknesses. In our 6" x 6" substrate, variation of thickness is expected as there is no rotation of substrate during the sputter deposition. In devices utilizing an FeS₂ NC back contact layer, the hydrazine treatment is performed after FeS₂ layer deposition, so direct contact of the hydrazine onto the CdTe is minimized, which helps to limit any deleterious effect on the CdTe.

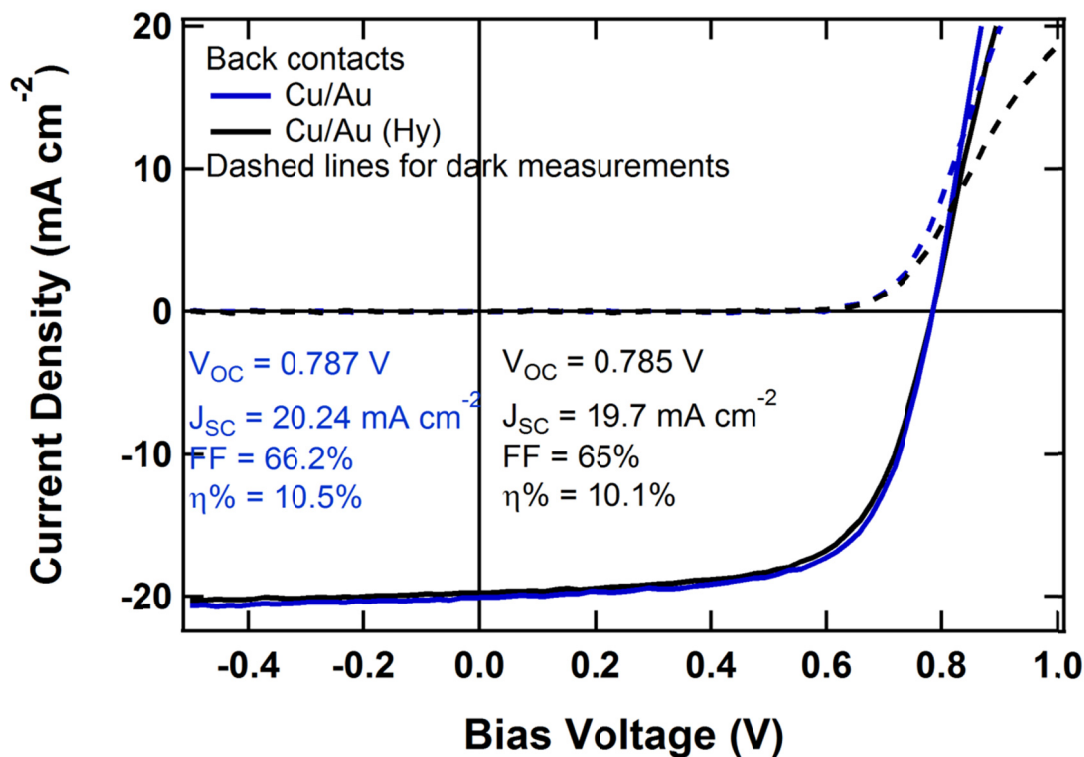


Figure 6-10. CdTe device was dipped into the hydrazine solution before depositing standard back contact to check the effect of hydrazine on CdTe.

6.3.2.4 Light intensity dependent JV curves

A light intensity dependence study was also performed on sputtered CdS/CdTe devices when FeS₂/Au and Cu/Au were used as back contacts as shown in Figures 6-11 and 6-12. Linear fits are applied to the short circuit current density points at different intensities. It is found that at room temperature, J_{SC} follows the linear trend up to intensities equivalent to 1 sun conditions. Linear behavior of J_{SC} vs. irradiance data up to one sun at room temperature can be attributed to two factors. First, photo-generation increases linearly with increasing irradiance intensity, and second, non-geminate recombination (recombination of charge carriers generated by two different photons) at short-circuit conditions is negligible at these intensities, and indicates that all separated

charges are extracted with a probability independent of photogenerated carrier concentration. [286] This fact is further supported by the intensity dependence of the fill factor. The fill factor increases toward lower excitation intensities, which is due to the increased parasitic power loss associated with the device series resistance. For the FeS₂/Au back contact, the fill factor increases from ~62% at 100 mW cm⁻² to ~69% at 20 mW cm⁻² as shown in Figure 6-12.

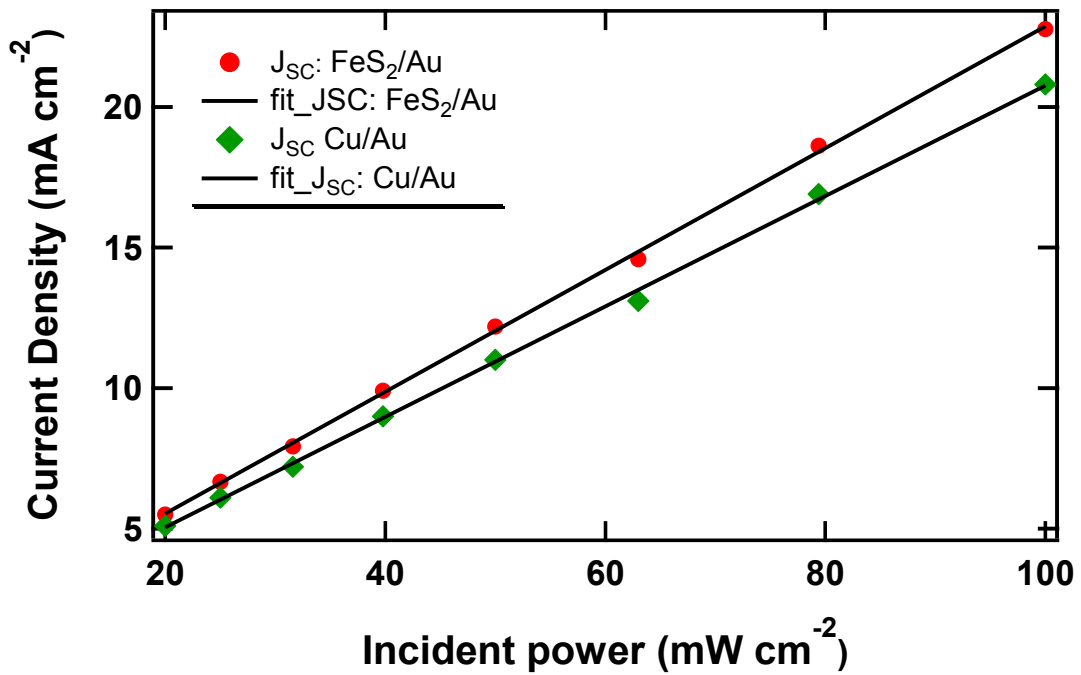


Figure 6-11. Light intensity dependent current density of sputtered CdTe devices when Cu/Au and FeS₂/Au were used as back contacts.

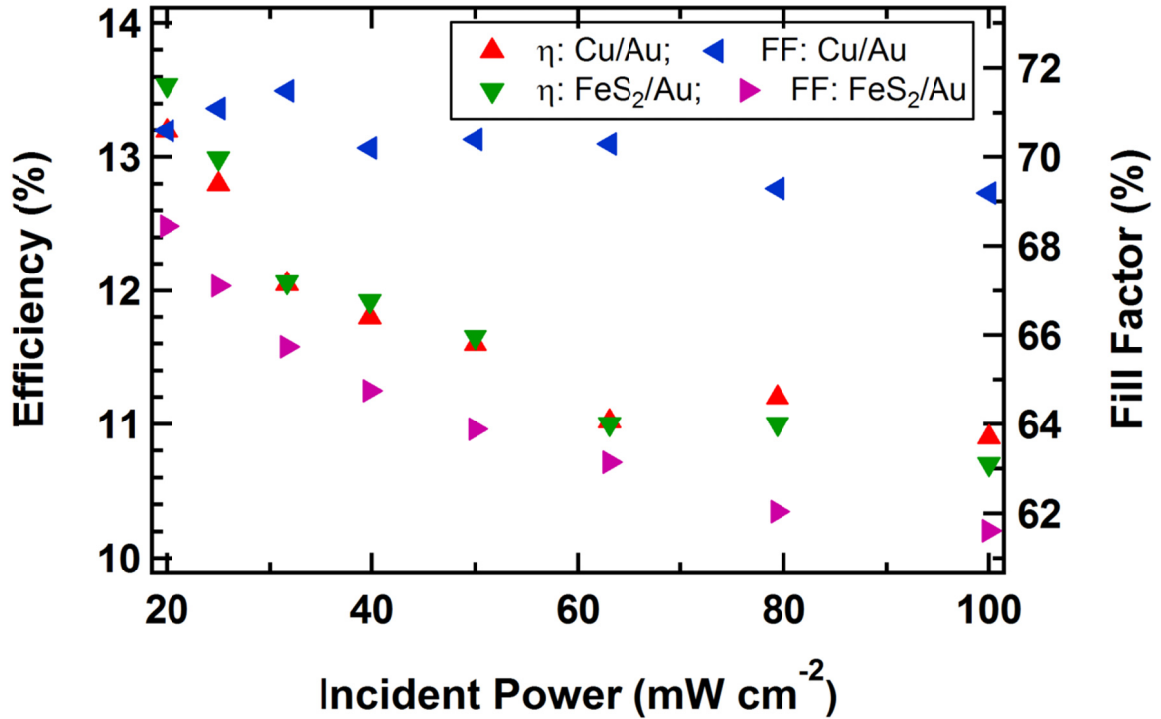


Figure 6-12. Effect of light intensity on the efficiency and fill factor of sputtered CdTe devices when Cu/Au and FeS₂/Au were used as back contacts.

6.3.2.5 Effect of surfactant on the performance of devices

To develop a better understanding of the electrical properties of the FeS₂ NC as a back contact, structural characteristics of the thin film need to be more thoroughly studied. The properties of the FeS₂ NC layer are significantly different from those of bulk metal or semiconductor layers. During the synthesis of these NCs, a long-chain C-H molecule (trioctylphosphine oxide, TOPO) has been used. TOPO controls the growth rate, determines the size of the NCs, and caps the NC surface. The length of these TOPO molecules is about 11 Å, and the solvated end of the molecule is hydrophobic.[287] Therefore, an estimate of the maximum separation between two neighboring NCs in the as-deposited film is ~2 nm, which creates an insulating film and clearly inhibits charge

transport through the FeS₂NC film/contact. Cube-shaped FeS₂ NCs capped with TOPO molecules, imaged by scanning electron microscopy, are shown in Figure 6-13a. When FeS₂ NC films are treated with hydrazine, these long molecules are removed. One of the applications of hydrazine is to remove oxygen from a reaction medium. In our case it reacts with TOPO to remove oxygen; since TOPO binds to FeS₂ through an oxygen, the result is to dissociate TOPO from the pyrite NCs. In addition, hydrazine may remove all the dissolved oxygen from the suspension where FeS₂ NCs are present. Any oxygen attached to pyrite NCs will be removed by hydrazine as well, potentially inhibiting any subsequent film oxidation. However, depending on the concentration of the NC solution and the resulting single-cycle layer thickness, the hydrazine treatment time should be varied. In the case where TOPO remains in the FeS₂ NC film, one can observe evident dramatic effects on current-voltage curves as shown in Figure 6-13b. Figure 6-13b presents J-V curves for sputtered CdTe solar cells prepared with back contacts of untreated FeS₂-NC layers with Au. The untreated film shows a clear S-shape signature, indicative of a transport barrier formed at the back contact. Similar “S-kink” shapes have been previously observed under illumination in CIS and also in organic solar cells (OSCs) when a charge buildup occurs at one contact.[288-290] Inflection points in the forward bias region of J-V curves observed in some organic solar cells are attributed to charge transport layers energetically misaligned to the energy levels of the active materials in planar heterojunction solar cells. In this present work, the proposed charging behavior is attributed to the residual barrier at the CdTe/FeS₂-NC interface (possibly exacerbated by the low-mobility of the FeS₂ NC film) resulting in the S-kink behavior. It is noted that the S-kink shape also appears, albeit subtly, in the illuminated J-V curves for

the two thickest FeS₂-NC contact devices in Figure 6-5. The quantity d^2J/dV^2 dips briefly to negative values in the power generating quadrant for nearly all FeS₂-NC/Au back contact devices (see Appendix).

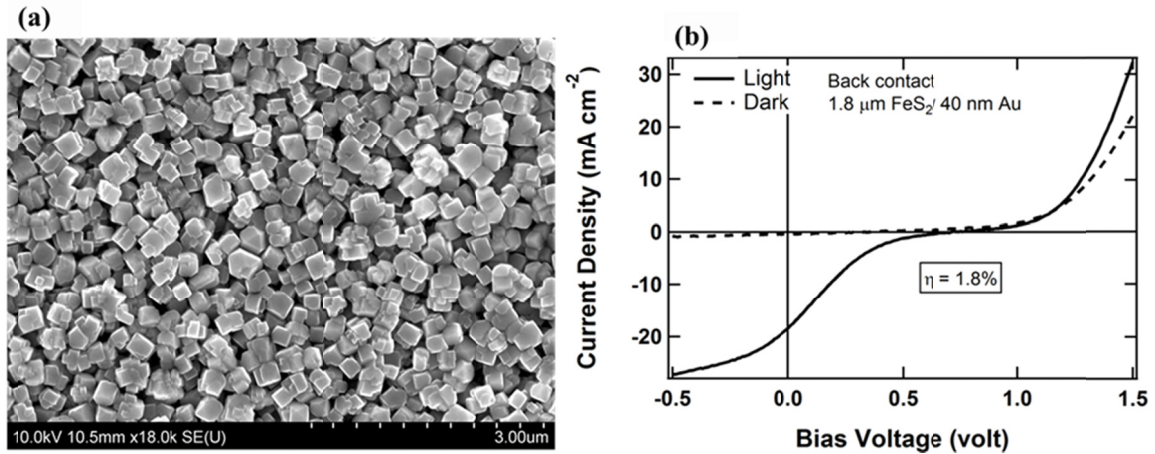


Figure 6-13. (a) SEM image of FeS₂ NCs at 10 kV accelerating potential; (b) J-V curves when untreated FeS₂ NC was used as a back contact for sputtered CdTe solar cells.

As discussed previously, hole mobility within CdTe is $\sim 100 \text{ cm}^2 \text{ V}^{-1} \text{ s}^{-1}$, and hole mobility within the FeS₂ NC film is $< 1 \text{ cm}^2 \text{ V}^{-1} \text{ s}^{-1}$. When electron hole pairs are generated within the CdTe, they are separated and move to their respective electrodes. Because of the low hole mobility, the transport of holes in the CdTe to the cathode (back contact) is impeded by the FeS₂ layer. This is due to the insulating layer between NCs and poor transport occurs especially when the FeS₂ layer is untreated or only partially treated with hydrazine. In such a case, holes may accumulate in the FeS₂ layer rather than swiftly transferring to the Au layer. Since the work function of FeS₂ and CdTe do not exactly match, there may already be a barrier for holes which can cause a reduction of the electric field at the CdS/CdTe interface. As the electric field at the interface of CdS/CdTe is decreased, the field dependent carrier generation efficiency at the CdS/CdTe interface

is reduced. This facilitates the carrier recombination at or near the CdTe/FeS₂ interface resulting in an S-kink. The consequence of all of this is the formation of S-shaped J-V behavior. The S-shaped J-V characteristics exhibited in cells depend on the thickness of the FeS₂ film as well. The thicker the film, the more S-like is the behavior. Therefore, the S-kink is likely due to a combination of a residual potential barrier and the unbalanced hole mobilities in CdTe and FeS₂ NC layers.

6.3.2.6 Role of FeS₂ NC film as an interface layer to CdTe device

To understand the contribution of FeS₂ to deformed JV curves, two sets of devices were fabricated where three layers of back contacts were deposited: 3 nm Cu/1 μm FeS₂/45 nm Au. This experiment was done for both sputtered and CSS CdTe devices. In this case, the performance of the Cu/FeS₂/Au devices was found to improve over that of the standard Cu/Au back contact devices as shown in Figure 6-14. The J-V curves in Figure 6-14 represent best cells performance.

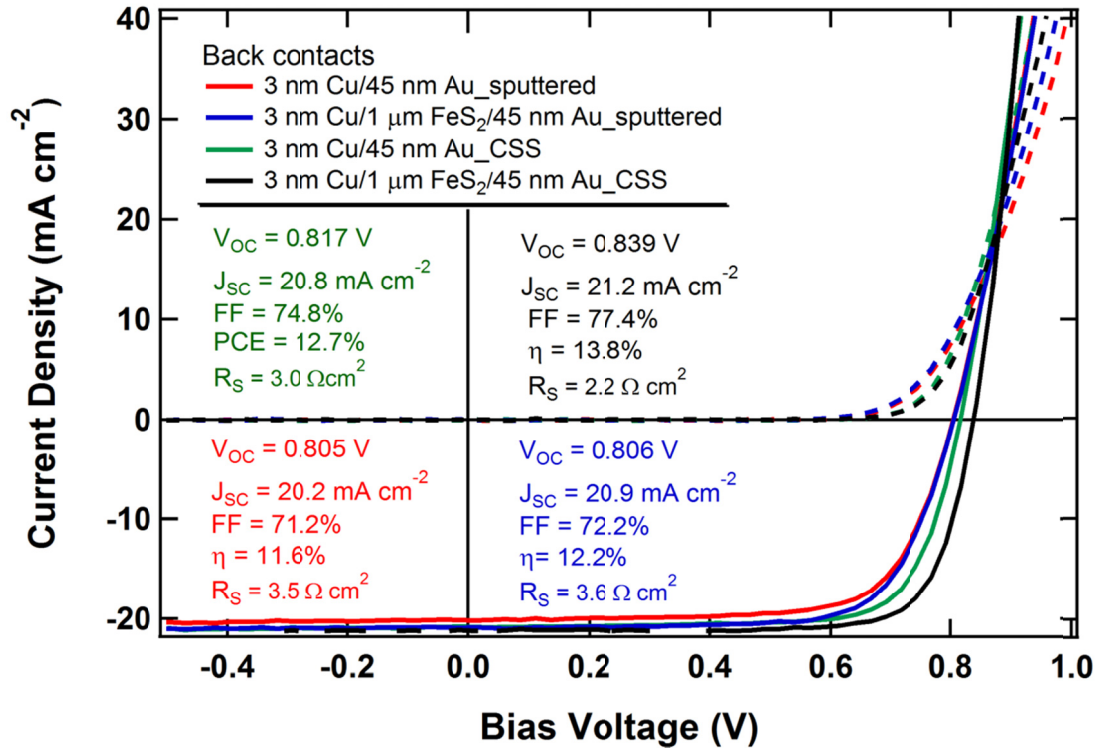


Figure 6-14. Current density voltage characteristics of CdTe devices, when the back contact is deposited as a combination of Cu/FeS₂/Au for both sputtered and CSS CdTe devices.

As shown in Figure 6-14, the presence of the FeS₂ NC layer improved the performance of the devices compared with that of the standard Cu/Au back contact devices. The statistics of 20 cells in each case are provided in Table 6-3. The thin layer of Cu utilized in the standard Cu/Au back contact improves performance by increasing the CdTe free hole concentration, one effect of which is a narrowing of the residual back barrier and improved hole tunneling efficiency. However, this does not completely make the barrier ohmic. When a layer of FeS₂ NC is deposited onto Cu-diffused CdTe, and the device is completed by evaporation of a Au layer, the device efficiency increases. As described above, Cu narrows the barrier width, and FeS₂ reduces the shunt resistance and

increases V_{OC} , perhaps because the FeS_2 NC layer serves as a p+ buffer layer with a relatively high work function. The performance of the FeS_2 interface layer may reflect the back surface field associated with the p+ layer at the back (p) contact within c-Si solar cells, reducing back-contact recombination by “reflecting” electrons away from the contact interface.

Table 6.3: Average of 20 cells (two different back contacts in two device fabrication condition: sputtered and CSS)

Sputtered CdS/CSS CdTe devices

Back contact	V_{OC} (volt)	J_{SC} ($mA\ cm^{-2}$)	FF (%)	η (%)	R_S ($\Omega\ cm^2$)	R_{Sh} ($\Omega\ cm^2$)
Cu/Au	0.809±0.008	20.7±0.3	74.7±1.1	12.5±0.2	2.6±0.7	2947±976
Cu/ FeS_2 /Au	0.836±0.002	21.4±0.4	75.0±0.8	13.4±0.3	2.9±1.0	4589±178

Sputtered CdS/CdTe device

Back contact	V_{OC} (volt)	J_{SC} ($mA\ cm^{-2}$)	FF (%)	η (%)	R_S ($\Omega\ cm^2$)	R_{Sh} ($\Omega\ cm^2$)
Cu/Au	0.786±0.01	20.4±0.3	68.8±1.1	11.1±0.4	4.1±0.7	2308±287
Cu/ FeS_2 /Au	0.796±0.01	21.3±0.6	69.2±1.7	11.7±0.4	3.6±0.8	2608±698

The purpose of utilizing a relatively thick layer of FeS_2 NC layer is to minimize the effective density of pin-holes present in the FeS_2 films, and to block the possibility that Au will diffuse or penetrate to the CdTe film. The thick NC layer passivates any shunting pathways from the back contact which is also clear from the high shunt resistance. One of the reasons of high V_{OC} and FF is due to the improvement in shunt resistance as shown in Table 6-3. The EQE measurement was repeated here for Cu/Au and Cu/ FeS_2 /Au back contact cases. The long wavelength cut off in EQE was again obtained at lower wavelength even though Cu and Au are present in both cases. The EQE

of CdTe devices with and without the FeS₂ NC layer are shown in Figure 6-15. The experimental evidence discards the possibility that hydrazine may alter the cell performance independent of the function of FeS₂. Although the hypothesis remains untested, one effect which may explain the blue-shift of the EQE long wavelength cutoff concerns the possibility that the CdTe/FeS₂ interface is a poor reflector of near-infrared light of wavelengths which the CdTe absorbs only quite weakly. If the reflection at the CdTe/FeS₂ interface is far reduced compared with the reflection coefficient for a Cu/Au contact, then the longest wavelengths would effectively experience weaker absorption due to an effective single pass instead of a double-pass through the CdTe layer.

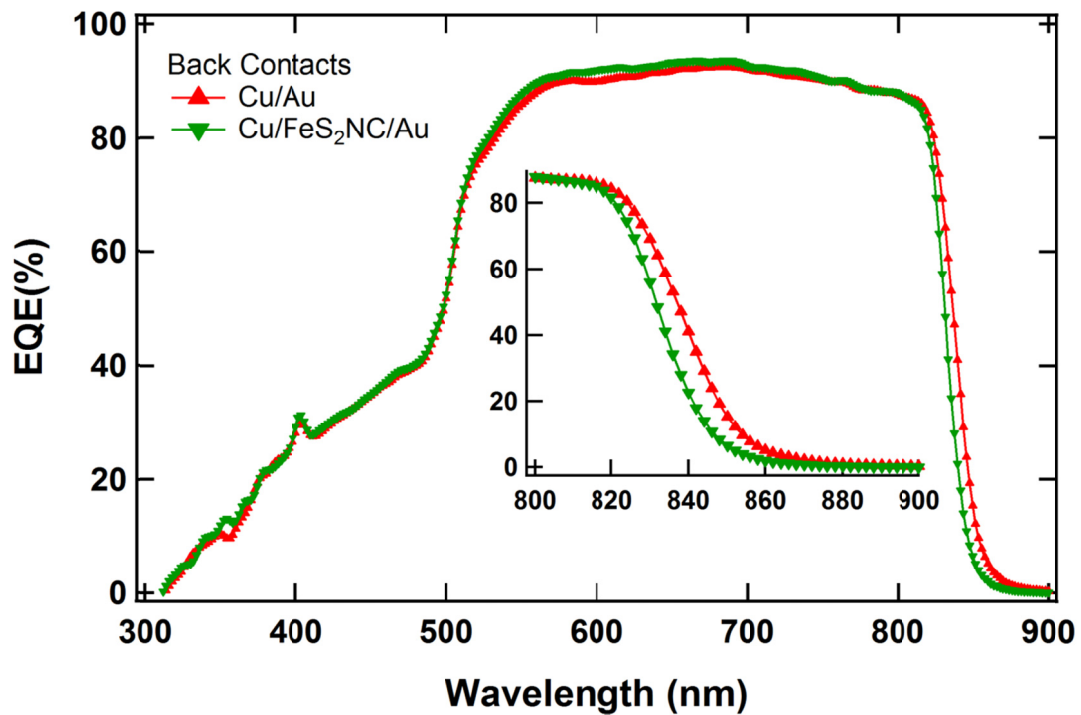


Figure 6-15. Typical external quantum efficiency (EQE) of cells before and after involving FeS₂ NC as an interface layer for CSS deposited CdTe devices. Inset provides a zoomed view of EQE at the long wavelength cutoff region.

6.3.2.7 Temperature dependent JV characteristics

Figure 6-16 to 6-18 show temperature dependent J-V characteristics of CdS/CdTe solar cells when three different types of back contacts were used. These measurements were conducted by Paul Roland at UT. They were done under excitation from a Kodak Projector light source for which it is difficult to establish and control an AM1.5G equivalent illumination. As such, the current densities reported here result from slightly higher or lower illumination intensity and should not be considered as intrinsic device characteristics. These results are reported for qualitative comparison of the temperature-dependent photocurrent and photo-voltage. Figure 6-16 shows J-V curves when the standard Cu/Au was used as the back contact and Figure 6-17 and 6-18 show J-V behaviors when FeS₂ NC films (hydrazine-treated and as-synthesized) were used along with Au as the back contact. In each of these cases, a clear temperature dependence is visible. At room temperature, the Cu/Au back contact device shows very nice diode behavior but the back barrier influence becomes evident at decreasing temperature. The devices having untreated-FeS₂/Au as the back contact were influenced significantly by temperature (Figure 6-18) whereas influences in the performance can also be seen in hydrazine treated-FeS₂/Au back contact devices (Figure 6-17) with good diode behavior at room temperature and an increasingly prominent S-kink behavior for decreasing temperature.

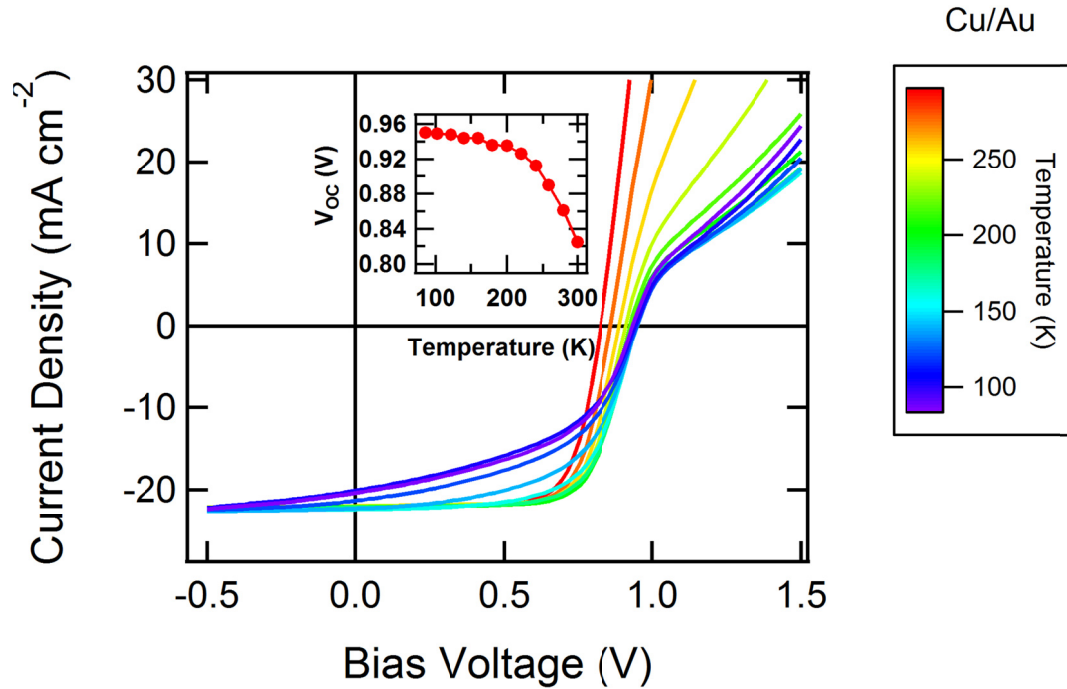


Figure 6-16. Temperature dependent J-V characteristics when standard Cu/Au is used as back contact for sputtered CdTe solar cell. Inset gives temperature dependent V_{oc} .

It is known that semiconductors exhibit a temperature-dependent band gap through the temperature dependence of the crystalline structural parameters.[291, 292] Typically, semiconductors show an increasing band gap energy as temperature is reduced.[293] Both single crystalline and thin film CdTe have been studied, and found to show a decreasing band gap with increasing temperature.[294-297] Using the Manoogian-Wooley (M-W) equation [298] with the coefficients obtained by Fonthal et al.[297], band gap of CdTe was calculated at 80 K and 300 K (the extremes of our temperature range); these values were determined to be $E_g(80\text{ K}) = 1.59\text{ eV}$, and $E_g(300\text{ K}) = 1.51\text{ eV}$. The change in band gap energy is 0.08 eV and the expected decrease in J_{sc} when temperature drops from 300 to 80 K is $\sim 2.6\text{ mA cm}^{-2}$. This expected change in J_{sc} is calculated assuming that all the photons above the given band gap energy contribute

one electron to the photocurrent. Due to a decrease in the intrinsic carrier concentration and the concomitant reduction in reverse saturation current, V_{OC} is expected to increase at decreasing temperatures. Figure 6-16 shows behavior in accord with these typical behaviors, although it is clear that a rapidly-decreasing FF exhibits substantial influence on the behavior of J_{SC} . When Cu is omitted and effectively replaced by untreated NC-FeS₂, J_{SC} is more strongly affected at low temperature as shown in Figure 6-18. Poor mobility expected within the untreated NC-FeS₂ contact layer yields complicated behavior, with a poorly-defined V_{OC} influenced strongly both by the nature of the effective barrier associated with the insulating ligands left intact between neighboring FeS₂ NCs, and by the resulting S-kink J-V behavior. Lattice vibrations decrease with decreasing temperature from room temperature. Reduced lattice scattering tends to increase the mobility with decreasing temperature. However, at lower temperatures the lower average thermal velocity leads to an increased impurity scattering, which decreases mobility.

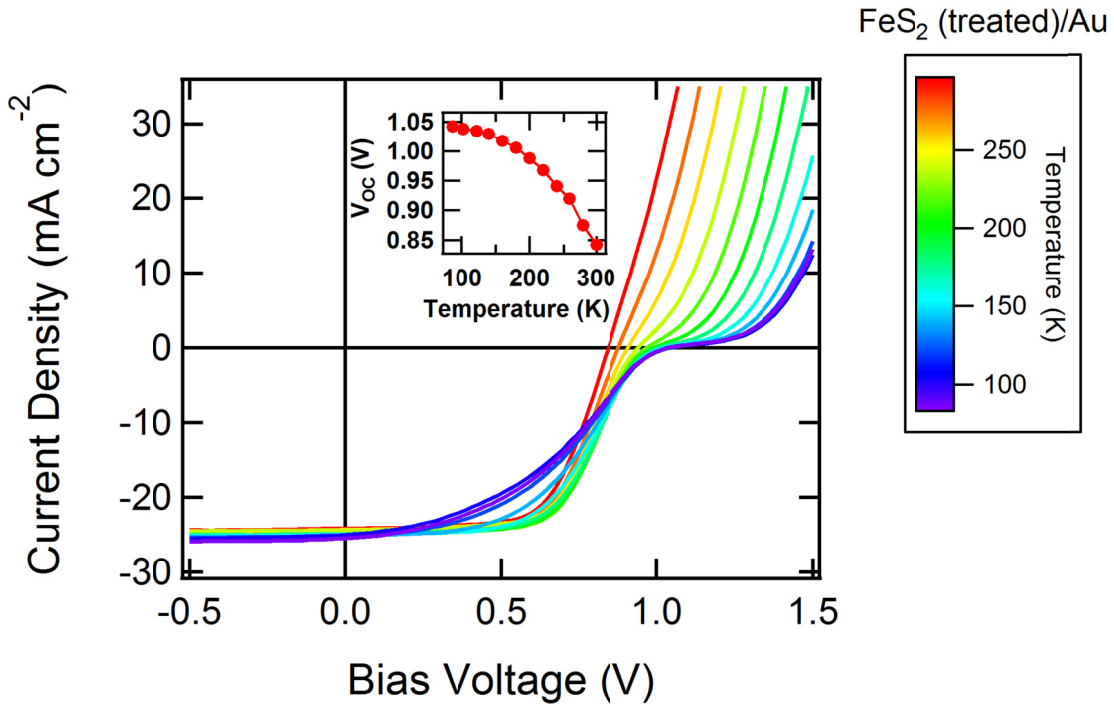


Figure 6-17. Temperature dependent JV characteristics when FeS₂/Au is used as back contact for sputtered CdTe solar cell. FeS₂ used here was treated with hydrazine. Inset gives temperature dependent V_{OC}.

As shown in Figure 6-16, J_{SC} has decreased by 2 mA cm⁻² when the temperature is decreased from 300 K to 80 K, which is close to the expected decrease in J_{SC} (2.6 mA cm⁻²). This decrease in J_{SC} may also be due to the apparent reduction in shunt resistance and increase in series resistance. In Figure 6-18, the decrease in J_{SC} is 10 mA cm⁻², which is higher than the expected value in for a CdS/CdTe solar cell. This decrease in J_{SC} likely arises from significantly reduced mobility in the untreated FeS₂ NC film. When the back contact consists of hydrazine-treated FeS₂/Au (Figure 6-17), J_{SC} is rather increased by ~1 mA cm⁻² when the temperature is decreased from 300K to 80K. Although additional testing of this behavior is merited, these initial results indicate that the hydrazine treated

FeS₂ NC back contact maintains the constant J_{SC} despite the increasing CdTe bandgap energy.

As shown in Figure 6-16, at low temperature, the forward current is severely limited by the back-contact-barrier developed at the CdTe/Au interface. The band gap is increased by 0.08 eV at low temperature but without additional experiments, it is not possible to determine conclusively whether there is a change in electron affinity or work function of the CdTe due to this band gap change. For n-InP, when the temperature was increased from 0 to 400 K, band gap was decreased by 0.2 eV and electron affinity was also increased by the same amount with the similar behavior observed for GaAs.[299] In this case, based on the experimental results, a change in work function is expected. For this, the valence band edge position shifts down when the temperature decreases from 300 K to 80 K by increasing the work function of CdTe. An increase in the CdTe band gap at low temperature further increases the barrier height for holes to transport to the Au layer. The barrier height developed at low temperature is shown by Julian Perrenoud in his PhD thesis. [300] Perrenoud's data showed that the barrier results in current "roll-over" in the forward bias region. However, when the CdTe/Cu/Au interface is replaced by a CdTe/FeS₂ and FeS₂/Au interfaces, the "roll-over" effect at the highest forward bias is absent (Figure 6-17). This is because the work functions of FeS₂ and Au are approximately equal, and an ohmic contact is maintained at the semiconductor-metal (FeS₂/Au) interface. The S-shaped J-V behavior developed in the FeS₂/Au back contact case may arise due to the freezing of carriers (no electrons from the valence band are raised into the acceptor states, freezing of carriers means negligible K_BT) at low temperature as the mobility of FeS₂ is already very small.

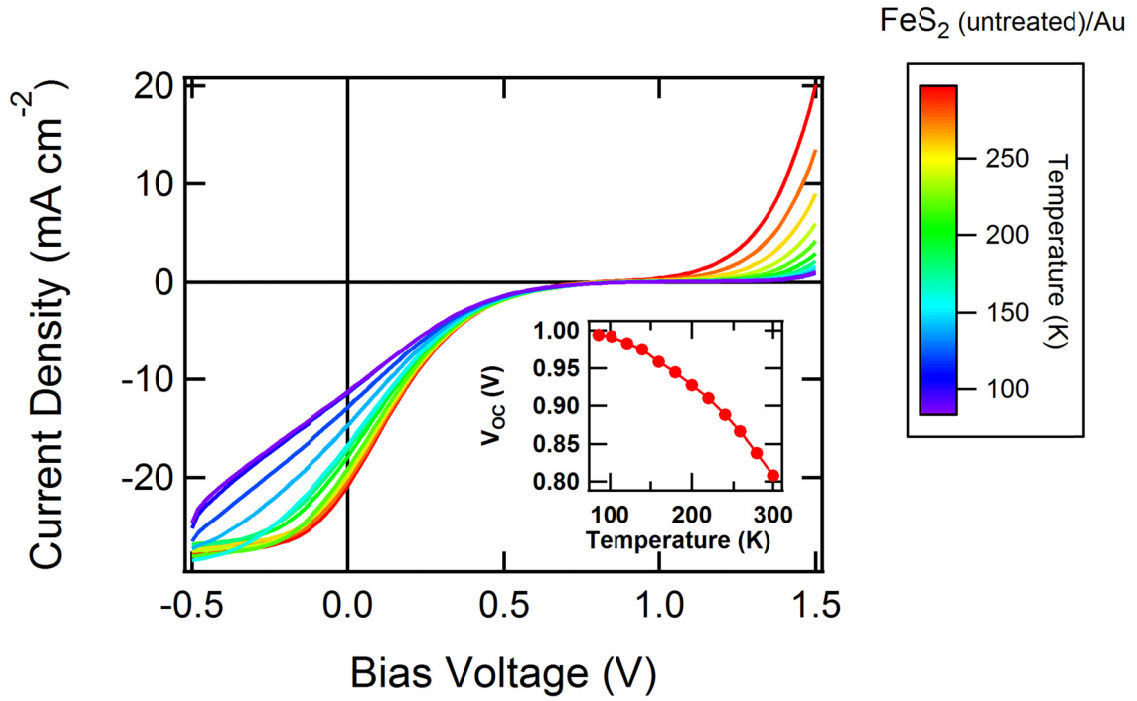


Figure 6-18. Temperature dependent JV characteristics when FeS₂/Au is used as back contact for sputtered CdTe solar cell. The FeS₂ NC contact layer used here was untreated and was used as obtained after synthesis. Inset gives temperature dependent V_{OC} .

Figures 6-16 to 6-18 clearly show the temperature dependence of V_{OC} in all three kinds of back contacts cases. When the temperature is reduced from 300 K to 80 K, V_{OC} was increased by 14%, 22% and 25% for Cu/Au, treated-FeS₂/Au and untreated-FeS₂/Au back contacts respectively. As said earlier, V_{OC} depends on the band gap of the semiconductor. When the band gap increases, V_{OC} also increases. In order to reveal more of the underlying physics responsible for the observed temperature dependence of V_{OC} , it is instructive to analyze the V_{OC} of a conventional p-n junction solar cell,[301, 302] given in Eq. 6-1.

$$V_{OC} = \frac{Ak_B T}{q} \ln \left(\frac{J_{sc}}{J_0} + 1 \right) \quad (6.1)$$

where, A is the diode quality factor, and J_0 is the reverse saturation current density. From this relation, V_{OC} depends on the J_{SC} and J_0 (other parameters are constant). When the back contact is treated-FeS₂/Au, J_{SC} remains constant with temperature (Figure 6-17) and V_{OC} depends only on J_0 . However, V_{OC} depends on both J_{SC} and J_0 when the back contacts are Cu/Au and untreated-FeS₂/Au (Figure 6-16 and 6-18). The J_0 is due to the recombination in the quasi-neutral region of the device. The J_0 is highly sensitive to temperature changes and increases exponentially with increasing temperature. The increase in V_{OC} in Figure 6-16 and 6-18 is therefore due to the resulting effects of J_{SC} and J_0 . Constant J_{SC} does not support increasing nature of J_0 with decreasing temperature. From this it is clear that J_0 did not increase significantly when the temperature decreased from 300 K to 80 K for when treated FeS₂/Au was used as back contact. Hence, for treated-FeS₂/Au case, increase in V_{OC} is only due to the increase in band gap of the absorbing layer. However, as the V_{OC} increases, the fill factor decreases such that ultimately overall device performance decline substantially. As indicated above, we attribute the decreased FF to the low mobility of holes in FeS₂ layer.

6.4 Conclusions

The author has demonstrated a high degree of control over the crystallinity and stoichiometry of iron pyrite nanocubes, and the high work function of FeS₂ and the high free hole concentration of our FeS₂ NC films have enabled the implementation of NC FeS₂ as a low-barrier back contact to CdTe within a Cu-free architecture. This work presents the first illustration of using an FeS₂ NC film as a low barrier electrical contact to thin film solar cells without the intentional preparation of a p+ highly-doped CdTe or

Cu_{2-x}Te layer that would serve to narrow any barrier width and facilitate tunneling. These FeS_2 NC films could not be used as the absorber layer in solar cell fabrication because of their conductive nature. The temperature dependent study of current voltage characteristics of CdS/CdTe solar cells with FeS_2/Au back contact reveals ohmic behavior for the CdTe/ FeS_2/Au interface.

Although the material studied to date consists principally of FeS_2 , related materials can be fabricated by stoichiometric or nonstoichiometric elemental substitution for either Fe or S.[224] For example, Co^{2+} or Ni^{2+} may substitute for Fe^{2+} , and other Group VI elements such as Se or Te can substitute for S. Indeed, free carrier concentration and possibly stability can potentially be controlled through such substitutions. Certainly, the exploration of FeTe_2 [303] represents one important potential pathway toward a material with improved compatibility with CdTe.

Chapter 7

Kelvin probe and photoelectron spectroscopy study of the electronic structure of metal and semiconductor thin films

7.1 Introduction

In this chapter, characterization techniques for determining the work function of metals and semiconductors, to locate the valence band maxima for some of the semiconductors, and to calculate the valence and conduction band offsets at semiconductor heterojunctions are described. To accomplish these materials measurements, Kelvin probe force microscopy (KPFM) and photoelectron spectroscopy (PS) measurements were employed. An overview, as well as the working principles and detailed applications of these techniques are described below.

7.2 Kelvin Probe force microscopy

7.2.1 Theory and working principle

In metals, work function (Φ_m) is defined as the minimum energy required to remove an electron, from the surface of a metal, initially at zero velocity at the Fermi energy. In metals, the valence bandfill with electrons up to the Fermi energy, and the

work function equals to the ionization energy. The work function (Φ_s) in a semiconductor is analogously defined. The position of the Fermi energy in semiconductors depends on the doping density. In non-degenerate semiconductors, the Fermi level is located within the band gap. Depending on the doping density, the Fermi level moves either towards the conduction band (n-type) or toward the valence band (p-type) of the semiconductors. Since the work function in a semiconductor is not an intrinsic quantity, people prefer to use the electron affinity (χ) instead. In a degenerate semiconductor, the Fermi level lies within a localized band and behaves similar to metals.

In Kelvin probe force microscopy (KPFM) measurement, a conducting atomic force microscopy (AFM) tip and sample are brought into electrical contact using an external wire. In this case, electrons will flow from the one contact side with lower work function to the one with higher work function until the Fermi energy is brought into equilibrium across the contact. After this charge sharing process, the contact side with a smaller work function becomes positively charged and one with a larger work function becomes negatively charged -- creating an electric potential between them. The potential established between the tip and the sample is called the contact potential difference (CPD). To measure the CPD, an external potential, so called counter potential, is applied with an opposing sign until the surface charges disappear. The amount of applied external bias that cancels out the electrical force due to the CPD is equal to the work function difference between the tip and sample. When the tip work function is known, the sample's work function can be calculated by the formula,

$$\text{CPD} = - (\Phi_{\text{tip}} - \Phi_{\text{sample}})/e$$
, where Φ_{tip} and Φ_{sample} are the work function of tip and the sample, and e the electronic charge.[304] The schematic of the KPFM measurement

technique is shown in Figure 7-1. Before electrical contact is made, the vacuum levels are aligned but Fermi energy levels are different; after electrical contact is made, the Fermi energy levels are aligned but the vacuum energy levels are different.

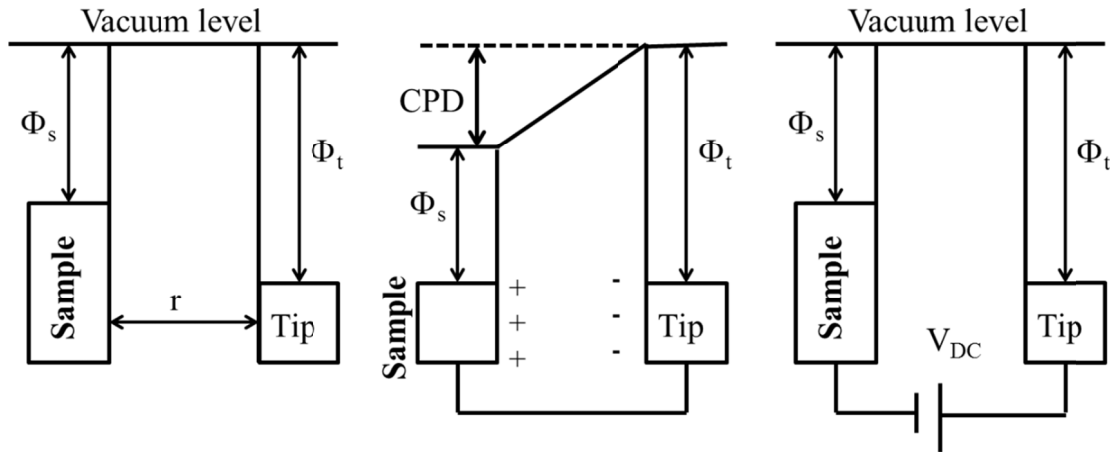


Figure 7-1. (Left) Work functions of the sample and the conducting tip before they are in contact; (middle) work functions of sample and tip when they are in contact; and (right) an external bias V_{DC} is applied to cancel the CPD.

Kelvin probe atomic force microscopy measurement has been used to obtain the CPD of wide varieties of samples such as Si[305], GaAs [306], and CuGaSe₂[307] There are various ways of detecting this charge free state in a Kelvin probe measurement. An AC voltage with a frequency ω is applied between tip and sample for the detection of electrostatic force. Frequency modulation (FM) or amplitude modulation (AM) detection modes can be employed for the measurement. In AM mode, the amplitude of the cantilever (tip) oscillation is measured which is proportional to the electrostatic force, and in FM mode the oscillation frequency shift is measured, which is proportional to the gradient of the electrostatic force. [308]

7.2.2 Sample preparation

Kelvin probe force microscopy measurements were performed to measure the work functions of Au, thin film CdS, and PbS-QD thin films. These three samples were prepared on soda lime glass substrates of size 2" x 2". A ~100 nm Au film was deposited by thermal evaporation onto three glass substrates. Onto two of the Au coated films was deposited ~70 nm CdS film by RF magnetron sputtering at a sputter power of 50 W in an argon atmosphere. Prior to the deposition, the substrate was heated to 270 °C for 30 minutes to yield a crystalline CdS film. Finally, onto one of the Au/CdS composite films was deposited a PbS-QD film using a solution-based layer-by-layer hand dipping method. [15, 16] The band gap of the PbS-QD thin film was ~1.6 eV, in accord with the QD diameter of ~2.5 nm; the PbS-QD film was ~200 nm thick. In LbL deposition, oleic acid (~18 Å capping ligand length) was replaced by 1,2-ethanediol (~0.25 nm capping ligand length) to make the film more conducting.[133, 309]

7.2.3 Results and discussion

In KPFM measurement the actual work function is obtained by calibrating the conducting tip of the instrument. It is calibrated against a surface with known work function. Reliable work function values can only be obtained if the calibration is done in very high vacuum. If the creation of very high vacuum is difficult or if the experiment is performed in ambient pressure, a highly oriented pyrolytic graphite (HOPG) crystal is used for the calibration. Highly oriented pyrolytic graphite does not react easily with other contaminants found on the surfaces and hence its work function remains quite

stable at 4.6 – 4.7 eV. All KPFM data were recorded in national renewable energy laboratory (NREL) with the help of Dr. Jianbo Gao.

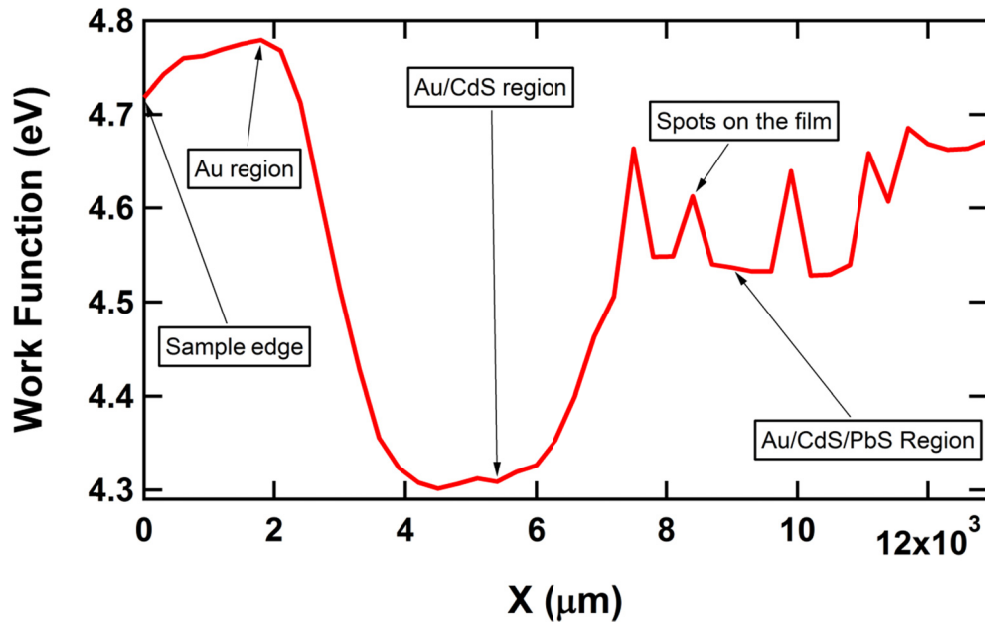


Figure 7-2. Work function of Au, CdS and PbS-QD films taken from KPFM measurement; Sample was scanned parallel to the edge. These data were collected in NREL with the help of Dr. Jianbo Gao.

Figure 7-2 displays work functions calculated by KPFM method for Au film deposited onto soda lime glass, bulk CdS film deposited onto Au and PbS-QD film deposited onto Au/CdS film. Work function data were gathered by scanning the sample parallel to the edge (parallel to the plane of the layers). In Figure 7-2, three regions belonging to Au, CdS and PbS are displayed with their work functions. The Au/CdS/PbS-QD region shows some positive peaks which corresponds to the spots on the cross-sectional surface of the film which increases the work function momentarily.

Figure 7-3 shows the average value of work function of Au, CdS and PbS-QD perpendicular to the edge. As shown in Figure 7-3, the average work function of Au is

4.7 ± 0.1 eV, the average work function of CdS is about 4.4 ± 0.1 eV and that of the PbS-QD film is about 4.5 ± 0.1 eV respectively. All results were measured by considering HOPG work function as a standard value. These results are slightly smaller than expected values.

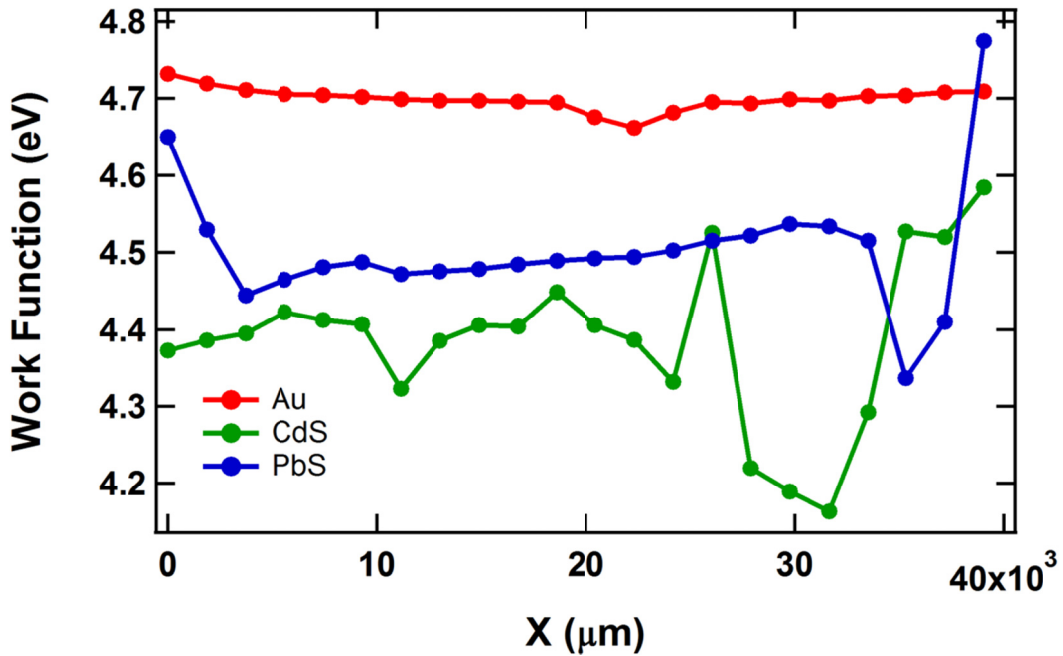


Figure 7-3. Work function measured by KPFM through atomic steps on Au, bulk-CdS and PbS-QD films respectively. These data were collected at NREL (Golden, Colorado) with the help of Dr. Jianbo Gao.

In the Au line profile (Figure 7-3), the dip at ~22 mm scanning distance is due to a scratch in the film. In the CdS film, the dip at ~30 mm distance is because the film was wiped off, and the increase in work function at ~40 mm is due to the bare gold at the edge of the sample. Similarly, in the PbS-QD film, the initial rise is due to the edge effect and the dip at 35 mm distance is caused by the bare film (all layers were delaminated leaving just the bare glass)(sample was wiped off).

7.3 Ultraviolet Photoelectron Spectroscopy (UPS)

7.3.1 Introduction

In photoelectron spectroscopy (PES), the surface of a sample is illuminated with high ultraviolet, and x-ray radiation. Electrons bound in the solid absorb incident photons emitting photoelectrons from the surface of the sample. Intensity and the kinetic energy of these emitted photoelectrons are recorded. The kinetic energy of the emitted photoelectron is related to the binding energy of the electron and the energy of the incident photon as given in equation 7-1. The PES is a direct measure of the material's density of state because emitted photoelectrons are directly counted in a spectrometer.

$$KE = h\nu - BE \quad (7-1)$$

In Ultraviolet Photoemission Spectroscopy (UV-PES), the sample is irradiated with light in the vacuum ultraviolet region of the spectrum. The photon source for these measurements is from a gas discharge tube. Typical sources employed include Helium-I (21.22 eV), Helium-II (40.8 eV), Neon-I (16.7 eV) and Neon-II (26.9 eV) respectively. These energies are of the same order of magnitude as the binding energies for valence shell electrons of molecules and for the valence band states of condensed systems. Hence, UV-PES gives information of only the valence orbitals in the molecular systems and possibly the valence band of solids. From the valence band emissions, the density of states of the investigated materials can be measured which allows the determination of the valence band maximum (VBM) of the materials.

7.3.2 Physical principle of UPS

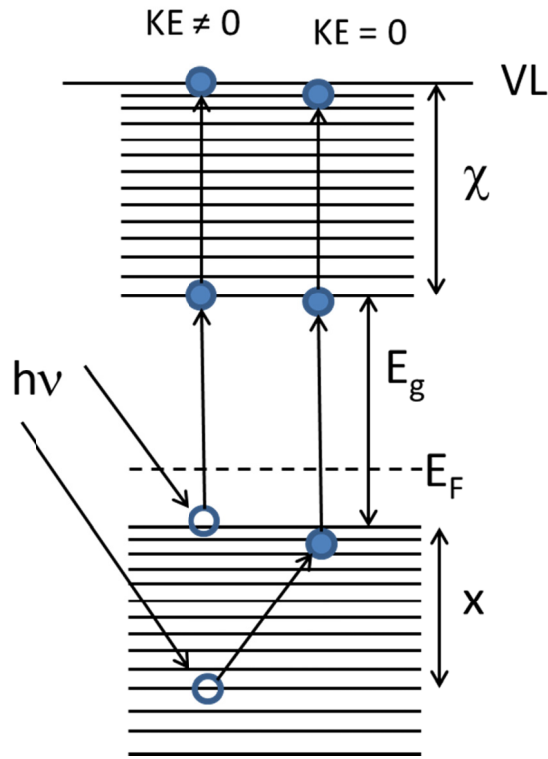


Figure 7-4. Schematic showing the physics of ultraviolet photoelectron spectroscopy (UPS). In Case 1, an electron is emitted from x depth below the valence band maximum (VBM) with zero KE; in Case 2, an electron is emitted from the valence band edge with maximum KE.

When He-I radiation of energy $h\nu$ is incident on a semiconductor of band gap E_g , the maximum kinetic energy is possessed by the electron emitted from the top of the valence band while zero kinetic energy is possessed by the electron emitted from a distance of x beneath the top of the valence band. In the second case, the excited electron cannot leave the sample and returns back to the top of the valence band. These two statements are expressed in equations as following:

$$h\nu = x + E_g + \chi \quad (7-2)$$

$$h\nu = E_g + \chi + E_{Max}^{KE} \quad (7-3)$$

Solving these two equations we get $x = E_{Max}^{KE}$ and $\Phi \cong 21.22 - x$. In equations (7-2) and (7-3), χ is known as the electron affinity of the semiconductor. Hence the work function of a material is the difference between the energy of the incident photon and the maximum kinetic energy of the emitted photoelectrons. However, the work function calculation using UPS spectra is slightly different as given in section 7.2.3.2.

7.3.3 Sample preparation

Samples were prepared using exactly the same procedure described in the KPFM method. All films were deposited onto 1" x 1" soda lime glass substrates. CdS films ~70 nm thick were deposited onto the ~80 nm thick Au layers, and PbS-QD layers were deposited onto the CdS layer. In summary, for UPS/XPS measurement, Au/CdS and Au/CdS/PbS QD films were prepared and were then transferred into the UPS/XPS spectrometer. All spectra were collected at room temperature in an ultrahigh vacuum photoelectron spectrometer equipped with an electron energy analyzer (CAE) with He-I radiation ($h\nu = 21.22$ eV) as UV source and Al $K\alpha$ ($h\nu = 1486.6$ eV) anode operated at 150 W, as X-ray source.

7.3.4 Electron energetics of semiconductor thin films

Figure 7-5 shows UPS spectra of the bulk CdS film deposited on Au. In figure 7-5, a distinctive peak (a) at ~14.5 eV originates from the Cd 3d core level emission and a

broad peak (b) at ~ 8.0 eV is due to the valence band emission from Cd 5S, and S 3p. Point (c) represents valence band edge of CdS. The valence band emission, inelastically scattered electrons and secondary electron cutoff regions are labeled.

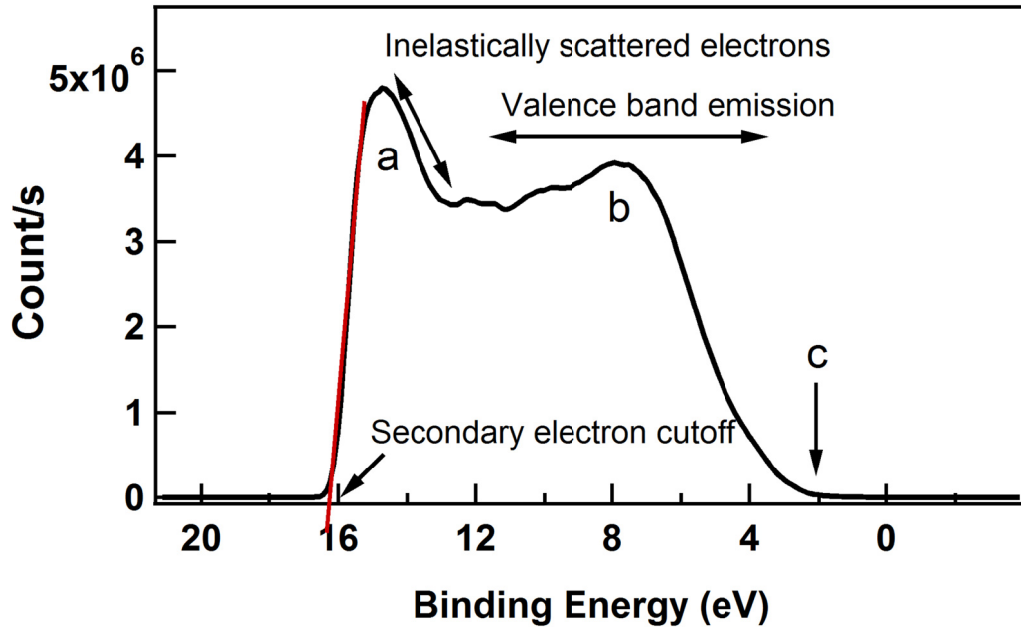


Figure 7-5. UPS spectra for CdS film deposited on gold substrate. $E = 0$ on the Binding Energy axis corresponds to the Fermi energy, E_F .

These values are at higher binding energies than CdS quantum dots given by V. L. Colvin et al. [310]. These authors have assigned 3d peaks for Cd at 11.66 - 12.52 eV and the valence band peak at 6 eV. In Figure 7-5, the valence band emission region spreads from about 2.0 to 12 eV. Then there is a high binding energy (BE) cutoff (also called the secondary edge) where the spectrum ends. Photoelectrons right at the edge have zero KE after leaving the surface. The electrons responsible for the secondary edge and the upward sloping tail before the edge are inelastically scattered electrons, which were initially emitted from valence band states but lost energy through scattering on their way

to the sample surface. The secondary electron cutoff allows the determination of the work function of the sample. The work function is defined as the energy difference between the Fermi energy and the vacuum level and is obtained by just subtracting the energy corresponding to the secondary electron cutoff from the incident photon energy (21.22 eV).

Figure 7-6 represents the analytical comparison of UPS spectra of the PbS QD films and the CdS films. Figure 7-6 also shows thickness dependent UPS measurement study for PbS QD films. PbS QD films were deposited onto the CdS film by solution LbL deposition method. The thickness of the QD films is about 50 and 100 nm. Secondary electron cutoff points for both CdS and PbS lie close to each other, exhibiting nearby work function values for both materials as shown in Figure 7-6. However, due to the different compositions and thicknesses of the films, intensities of inelastically scattered and valence band emission regions are different. The higher electron intensity from the 50 nm thick PbS-QD film is because most of the electrons absorbing a photon's energy managed to escape.

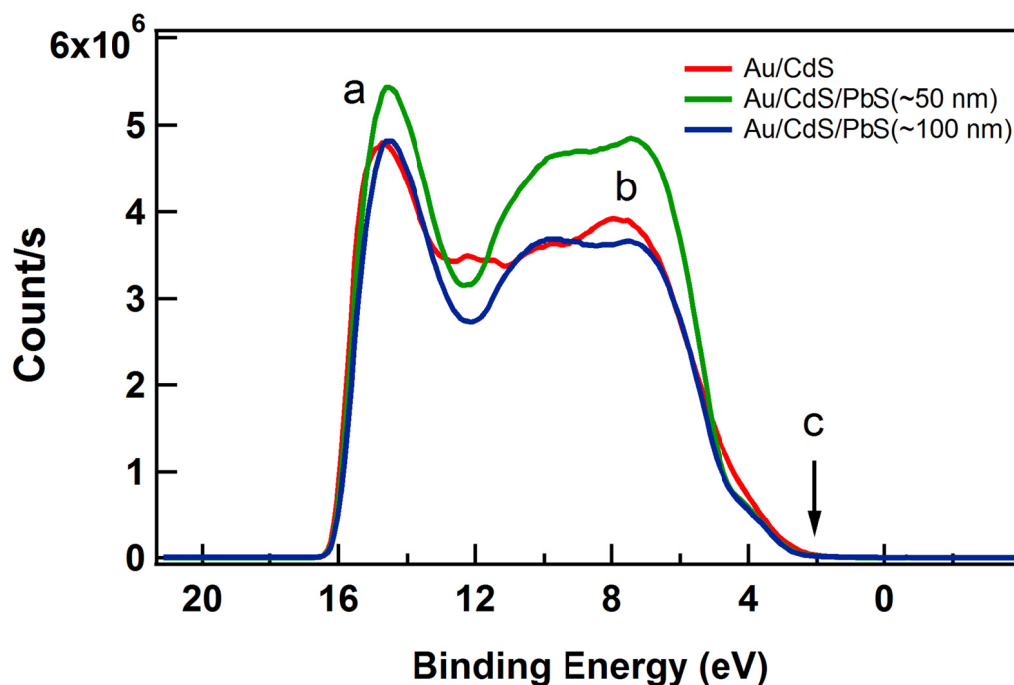


Figure 7-6. UPS spectra for CdS on Au and PbS QDs (diameter = 2.5 nm) on CdS for the qualitative analysis of emission behavior in two cases. $E = 0$ eV on binding energy scale corresponds to Fermi energy E_F .

7.3.4.1 Valence band maximum of CdS and PbS-QD films

The valence band maximum (VBM) is calculated for both a bulk CdS film and a PbS QD film by drawing a tangent on the linear portion of their spectrum as shown in Figure 7-7. This analysis indicates that the VBM for CdS lies 2.0 ± 0.1 eV below the Fermi level. As the band gap of CdS is at 2.42 eV, the Fermi level is 0.42 ± 0.1 eV below the conduction band level. This makes sense because the CdS layer is n-type such that the Fermi level resides in the gap but closer to the conduction band edge.

The VBM level of the PbS QD film is determined by linearly extrapolating the leading edge of the valence band emission within the spectrum where photoemission

intensity from the valence band decreases and merges into the low intensity background assigned to defects. We found the VBM of PbS QDs of diameter 2.5 nm to be at about 0.6 ± 0.1 eV from the Fermi level. Given the optical gap of $E_g = 1.6$ eV for these QDs, and the PbS are p-type semiconductors, with a Fermi level close to the valence band edge.

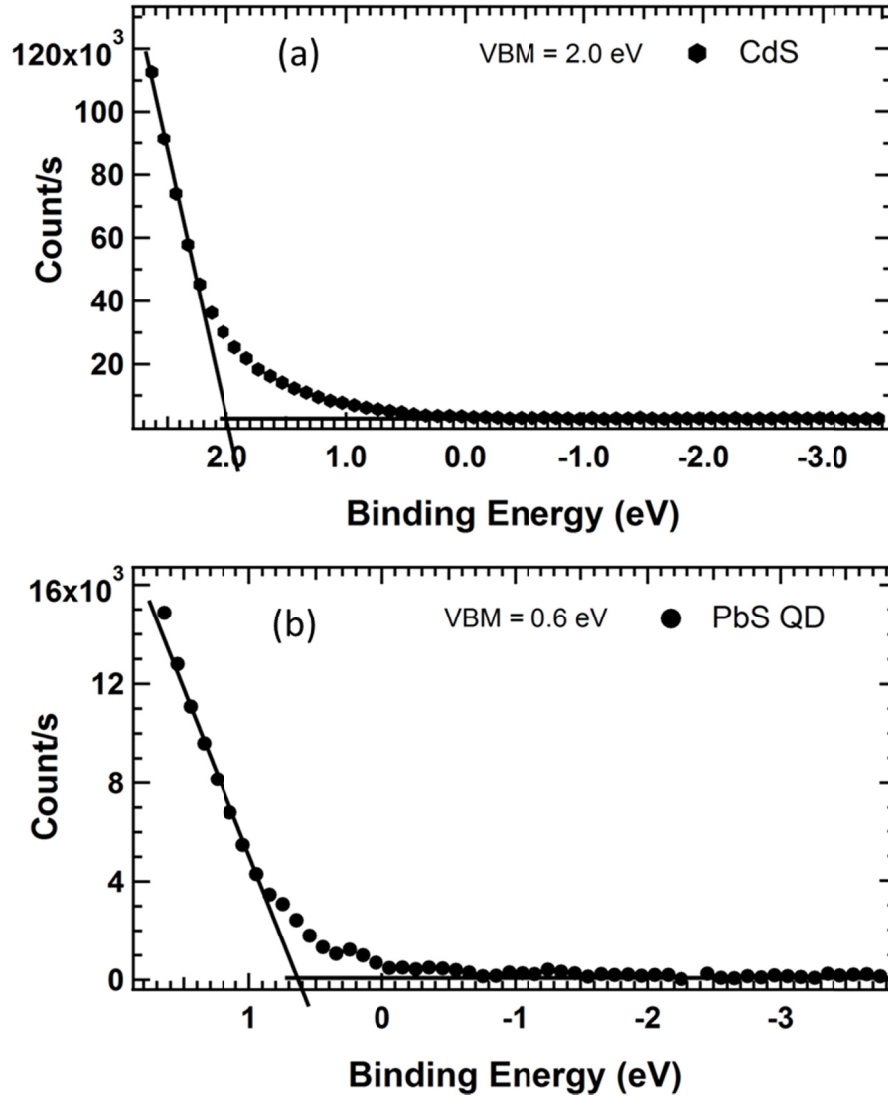


Figure 7-7. The VBM position for CdS is at 2.0 ± 0.1 eV and for PbS QD is at 0.6 ± 0.1 eV.

7.3.4.2 Work functions of Au, CdS and PbS-QD

In contrast with Kelvin probe measurements, UPS provides absolute work function values. However, while performing UPS measurement one can, in general, face the following two problems. The first is the buildup of positive charge on the surface of the sample during the measurement due to incomplete replacement of the emitted photoelectrons, and the second problem concerns the occurrence of photochemical modification of the sample surface due to the impinging UV radiation. Both of these problems occur instantaneously upon UV exposure to the sample, resulting in a shift of the secondary electron cutoff to higher binding energy, which decreases the accuracy of the work function measurement. Charging results in a shift of emission features across the complete spectral range and may be easier to detect, but the detection of photochemical modification is more challenging.

If the UPS spectrum is plotted as count/s vs. kinetic energy, then according to the Einstein equation, $E_{KE}^{Max.} = h\nu - \Phi$ or $E_{KE}^{Max.} = h\nu - IE$, where IE is the ionization energy. From this relation, the work function of the material can be calculated. In contrast to Kelvin probe measurements (which only yield the contact potential difference between sample and probe) UPS is able to deliver absolute work function values. This method does not depend on any experimental parameters except for the photon energy of UV source which is known very accurately.[311] Also the measurement is performed in ultra-high vacuum that excludes any possibility of altering surface properties due to contamination during the measurement.

Figure 7-8 shows a typical He-I UPS spectrum for CdS in kinetic energy scale. The spectrum width, E_{KE}^{Max} , is determined from the distance between the sample inelastic cutoff and the Fermi edge. The determination of the position of inelastic cutoff was unambiguous for all samples while the Fermi edge did not readily show up for some samples. However, this did not pose a problem because the Fermi edge is the reference point of the energy scale in photo-electron spectroscopy and should not change from sample to sample as long as the samples remain grounded. The work function of the CdS from this method is found to be 4.5 ± 0.1 eV which is very similar to the value (4.7 eV) determined by Guangming et al [312]. Work functions of the PbS-QD films (Figure 7-9) deposited onto the CdS film were similarly determined and found to be 4.92 ± 0.1 eV and 4.86 eV when the thicknesses of the PbS-QD films were ~ 100 and ~ 50 nm respectively. The work function of CdS obtained from UPS measurement is higher than our Kelvin probe measurement (KPM) where it was 4.4 eV. Similarly, the work function of PbS QDs given by UPS is also higher than KPM where it was 4.5 eV. These values are summarized in Table 7-1.

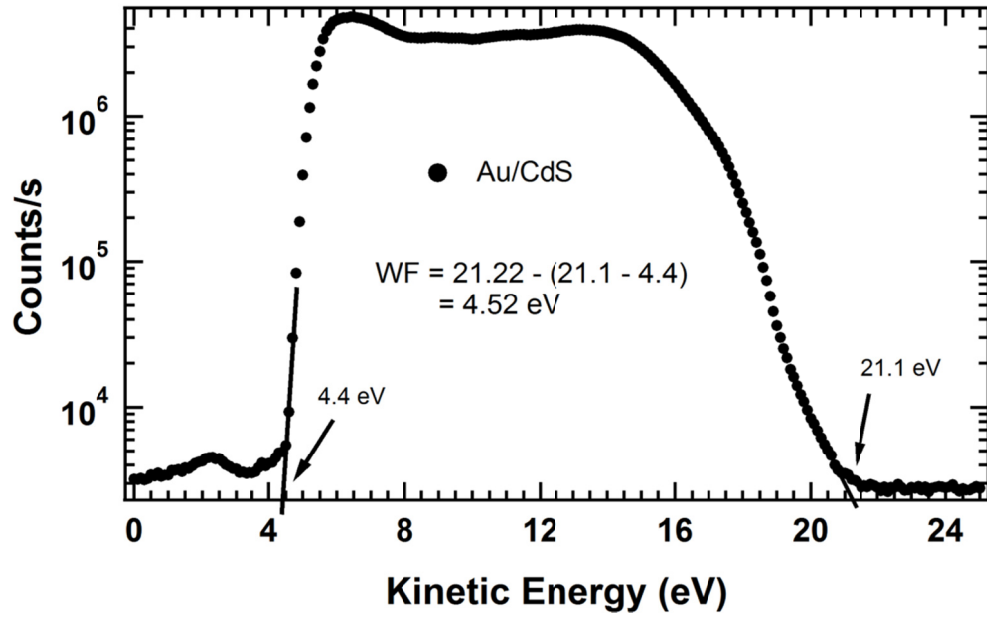


Figure 7-8. UPS spectrum of CdS plotted as counts/s with respect to kinetic energy. The relation between spectrum width, $h\nu$ and work function (WF) is numerically illustrated.

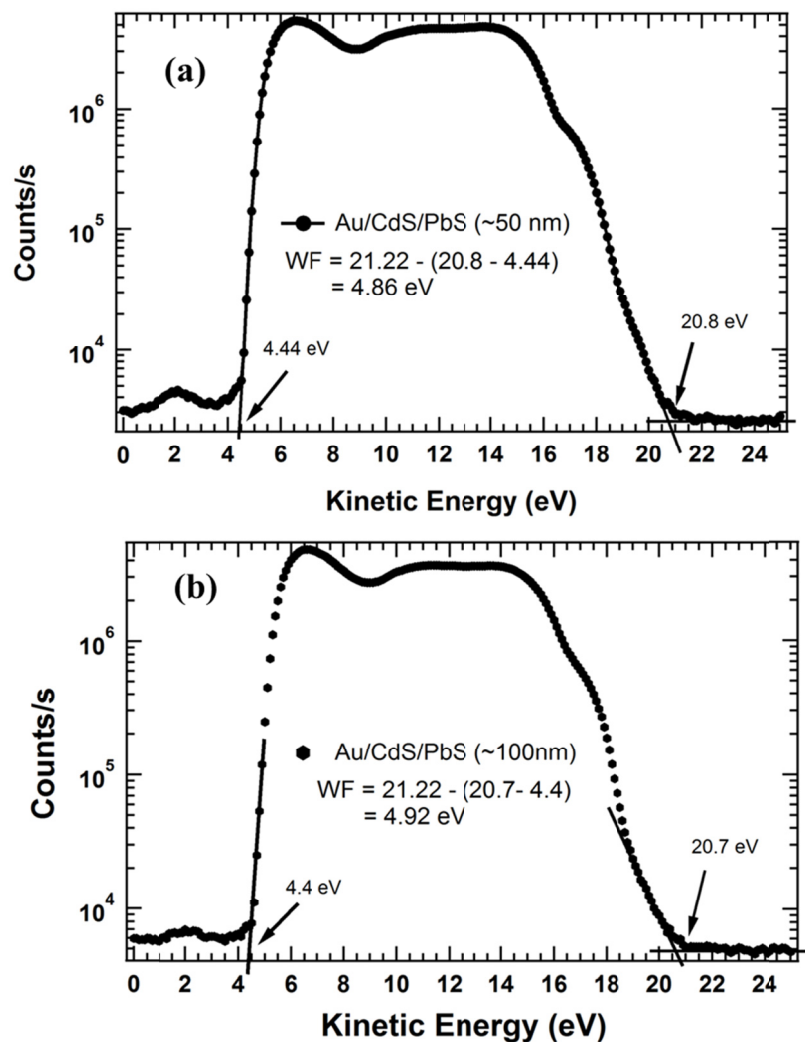


Figure 7-9. UPS spectra of PbS-QD film of two different thicknesses (a) ~50 nm and (b) ~100 nm plotted as counts/s with respect to kinetic energy. The relation between spectrum width, $h\nu$ and work function (WF) is numerically illustrated.

Table 7.1: Work function measurement

Methods	CdS	PbS QDs	Au
KPM	4.4 ± 0.1 eV	4.5 ± 0.1 eV	4.7 ± 0.1 eV
UPS	4.5 ± 0.1 eV	$4.92 \pm 0.1, 4.86 \pm 0.1$ eV	N/A

7.4 X-ray photoelectron spectroscopy

7.4.1 Introduction

X-ray photoelectron spectroscopy (XPS) is the most widely used surface-sensitive characterization technique that is used for elemental identification and the chemical states of element, for the relative composition of a compound in the surface region, and for valence band structure.[313] In an XPS measurement, a sample is irradiated with a beam of x-rays; the kinetic energy of photoelectrons emitted from the sample are measured along with their relative intensity (number of photoelectrons that escape from the sample per second). XPS measurement is done in high or ultra-high vacuum conditions to minimize the contamination of the sample. In XPS spectrum number of electrons detected (per unit time) is plotted with respect to their binding energies. Each element produces characteristic peaks in the spectrum at specific binding energy values. These characteristic spectral peaks correspond to the electrons configuration within the atom such as 1s, 2s, 2p, 3s and so on.

7.4.2 Sample preparation

For XPS studies, two sets of samples were prepared using a procedure to that described for the UPS method. The first sets of samples were used for their elemental analysis, and the second sets of samples were used to calculate band offsets between two semiconductors of opposite carrier type. For the elemental analysis, a CdS film was deposited onto an Au-coated glass substrate and PbS-QD films were prepared on the Au/CdS films. For these studies, PbS QDs of diameter ~ 2.5 nm (first exciton absorption

peak at ~ 1.6 eV) was used. For the band offsets study, the CdS film was prepared on a TEC-15 transparent conducting oxide (TCO) ($\text{SnO}_2/\text{SiO}_2/\text{SnO}_2:\text{F}$) coated glass substrate, and similarly the PbS-QD films were prepared on TCO/CdS coated substrates. In this case, PbS QDs of diameter ~ 2.8 nm corresponding to the first exciton peak at ~ 1.4 eV were used. In all cases, the size of the substrate was 1" x 1". In the second case, PbS-QD films of various thicknesses were prepared to see the evolution of band bending in the heterojunction between n-CdS and p-PbS.

7.4.3 Elemental analysis on surfaces of CdS and PbS-films

The core level XPS results for the EDT capped PbS quantum dot (QD) films are shown in Figure 7-10 for the S 2p (1a and 1b), O 1s (2a and 2b) and Pb 4f (3a and 3b) respectively. The QDs used in this study were 2.5 nm diameter, corresponding to a first exciton optical absorption peak at 1.6 eV. Similarly, the core level XPS results for the sputtered CdS films are shown in Figure 7-10 for the S 2p (1c), O 1s (2c) and Cd 3d (4a) respectively. The spectra show some of the peaks from ligands. Because QDs were capped with 1,2-ethanedithiol (EDT), we did not see any C peaks but we did see O peaks which can be due to the adsorption of some gaseous molecules such as H_2O on the QD surface, CdS film and on the substrate. Before making XPS and UPS measurements, PbS QD and CdS films were stored for a long period of time in air. So, we cannot neglect H_2O adsorption as a source of oxygen. The results indicate that the ~ 100 nm thick QD films are more susceptible to oxidation than 50 nm thick QD films, and that the sputtered CdS films are also affected, but less so than the PbS QD films.

The S (2p) region indicates that the majority of the sulfur in the samples is sulfide, S^{2-} with peaks at 160.8 ± 0.05 eV and 161.8 ± 0.05 eV for the $2p_{3/2}$ and $2p_{1/2}$ spin-orbit splitting features shown in Figure 1a for ~ 50 nm PbS QD film and slightly higher values in Figure 1b for ~ 100 nm thick films. The binding energies of these peaks are very close to values previously reported in literature.[125, 314] The nature of the species on the surface of the QD was also probed by XPS. Figure 1a and 1b show high-resolution spectra of the S (2p) photoelectrons from monolayers of ethanedithiol (EDT). The $S(2p_{3/2})$ peak in the XPS spectrum of EDT appears at 163.5 ± 0.05 eV for ~ 50 nm film and at 163.6 ± 0.05 for ~ 100 nm thick film.[315] Gold is considered a non-toxic material because of its well-known stability, non-reactivity and bio inertness. However, gold can easily react with thiol (-SH) derivatives to form the Au-S bond.[316] Thiolate is formed due to the adsorption of thiol on the gold surface with an XPS peak near 162 eV.[317] The intense peaks at 167.6 ± 0.05 and 167.9 ± 0.05 eVs are due to the contributions from oxidized sulfur atoms, SO_3^{2-} or SO_4^{2-} for the S ($2p_{3/2}$).[125, 314]

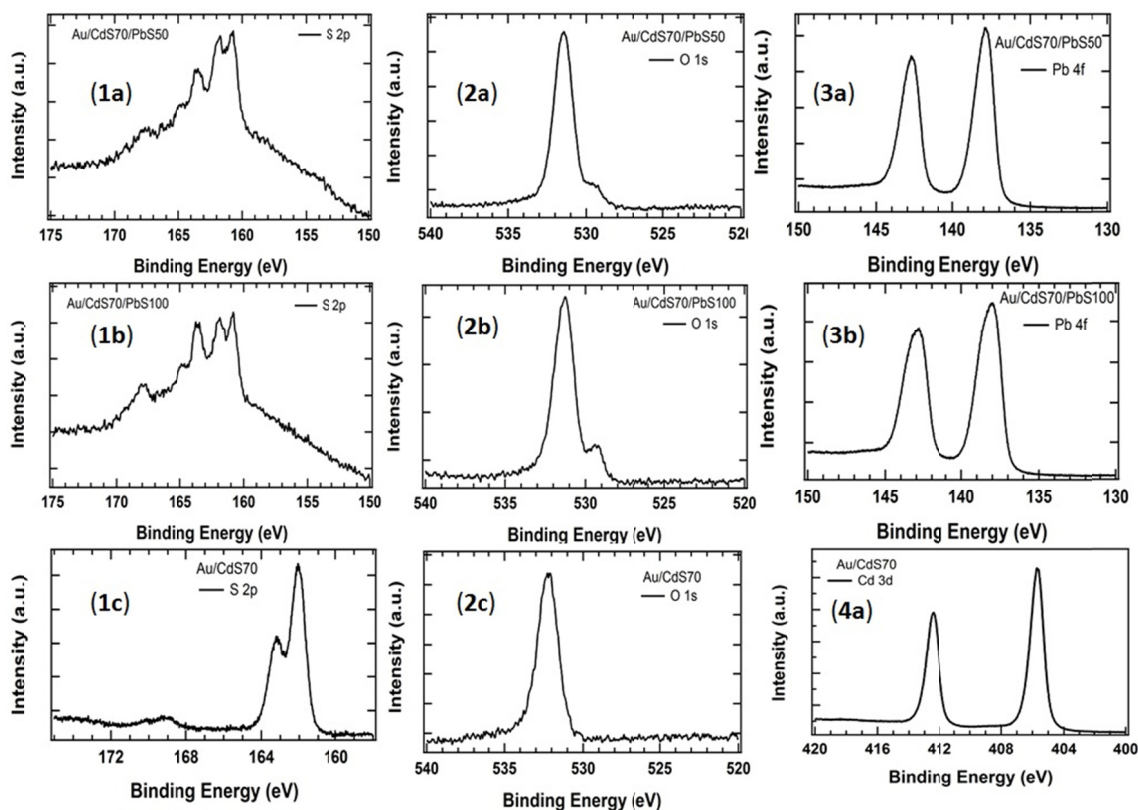


Figure 7-10. The S 2p (1a and 1b), O 1s (2a and 2b) and Pb 4f (3a and 3b) XPS spectra for the ~50 nm and ~100 nm thick EDT capped PbS quantum dot films respectively. Similarly, the S 2p (1c), O 1s (2c) and Cd 3d (4a) XPS spectra for the ~70 nm thick sputtered CdS film deposited onto gold coated substrates. Before depositing CdS and PbS, an 81 nm thick layer of gold was evaporated onto the glass substrates to facilitate current transport.

The 100 nm thick QD sample has significantly more intensity producing the shoulder in the S ($2p_{3/2}$). The spin-orbit splitting features S ($2p_{3/2}$) and S ($2p_{1/2}$) of S for CdS film are at slightly different binding energies. These peaks appear at binding energies of 162.05 ± 0.05 and 163.2 ± 0.05 eVs respectively. The oxidized sulfur peak has also been shifted to higher energy at 169.2 ± 0.05 eV. The small shift in peaks of binding energies for the PbS QD film is due to the capping ligand. The greater the

electronegativity of the ligands, the greater will be the binding energy of the core electron of the ligated atom [318]. The standard deviations in each case were obtained by fitting the corresponding peaks using Gaussian curve fitting.

The core level oxygen O 1s features in ~50 nm and ~100 nm PbS-QD films can be seen at binding energies 531.5 ± 0.05 and 531.3 ± 0.05 eV. These are the binding energy positions of the peak maxima as shown in Figure 2a and 2b. In each case, there also exists a shoulder at 529.64 eV and 529.4 eV respectively which may be due to the small contributions of oxidized sulfur, S-O-Pb.[314] The position of the O 1s in the CdS thin film is at 532.2 ± 0.05 eV with no shoulder peak. This binding energy matches very well with the XPS work done by Lee *et al* on CdS QD films.[319]

The Pb 4f core level spectra for these samples (Figures 3a and 3b) reveal the existence of two components with a binding energy difference of ~4.9 eV. In the 50 nm thick PbS QD film, the Pb contribution for PbS is centered at 137.9 ± 0.05 eV for the Pb ($4f_{7/2}$) peak and 142.85 ± 0.05 eV for the Pb ($4f_{5/2}$) peak respectively. Similarly, in the 100 nm thick PbS QD film, the Pb contributions appear at the slightly higher binding energies of 138.08 ± 0.05 , 142.9 ± 0.05 eV. These core level binding energies for Pb in PbS QDs are similar to those on previous work on PbS nanoparticle-polymer composites[314], oleic acid and TOP capped PbS NCs [125], and bulk PbS.[320] In ref. [320], the authors reported contributions of Pb in PbS centered at 137.6 eV for Pb ($4f_{7/2}$) and 142.4 eV for Pb ($4f_{5/2}$). These observed core level binding energies are close to the values of Pb-O bonding of 138.4 eV and 143.3 eV.[321] The shift to higher binding energy may be due to the fact that the O atoms are bound to the more electronegative sulfur of EDT molecules.

Figure 4a shows the core level spectra of Cd in a CdS thin film sample. These values of 405.7 ± 0.05 eV and 412.5 ± 0.05 eV compare closely with 405.0 eV and 411.5 eV binding energies obtained by Dicastro and Polzonetti in their XPS study of Cadmium oxidation in air.[322]

7.4.4 Determination of the valence and conduction band offsets between CdS bulk and PbS QDs using XPS

7.4.4.1 Introduction

A heterojunction interface is formed at the boundary between two dissimilar semiconductors. Optimizing the performance of a heterojunction typically requires configuring the material compositions to achieve matching of the lattice constants, or minimizing the lattice mismatch. The valence band offset for lattice matched heterojunctions has been very well studied.[323, 324] However, there are materials with considerable lattice mismatch, resulting in lateral tensile and/or compressive strain originating at the interface.[312, 325] It has been pointed out that core level (CL) to valence band edge binding energies are functions of strain due to the lattice mismatch.[326] In such systems, strain initiates both a shift and splitting of the core and valence bands, with the resulting band discontinuities depending explicitly on which material is under strain.[327] The conduction and valence band discontinuities ΔE_C and ΔE_V that occur at a heterojunction interface, due to the lattice mismatch and abrupt band gap change ΔE_g , can be used to improve the design of solid state electronic devices.[323, 324, 328] Accurate knowledge of valence band offset (ΔE_V) at an interface, and the

factors that influence its magnitude, are thus of both fundamental and practical interest. In this paper, the CdS/PbS-QD system is chosen for analysis for several reasons. First, PbS displays a relatively high room-temperature lattice mismatch ($\sim 11.6\%$) with CdS. This value was calculated by using the lattice constant ($a = 4.136 \text{ \AA}$, $c = 6.714 \text{ \AA}$) of CdS [329, 330], and the lattice constant ($a = 5.936 \text{ \AA}$) of PbS.[62] Second, to date there is no information available on the band offsets between bulk CdS and PbS-QD thin films.[49] Third, an accurate knowledge of the valence band offset ΔE_V and conduction band offset ΔE_C at the CdS/PbS-QD heterojunction interface owing to the band gap (E_g) difference between hexagonal wurtzite CdS ($E_g = 2.42 \text{ eV}$)[155] and rock salt PbS QD[331] is important for device design, modeling and performance prediction. So, this paper discusses how photoelectron spectroscopy, both ultraviolet photoemission spectroscopy (UPS) and x-ray photoelectron spectroscopy (XPS) can be applied to directly, contactlessly and quantitatively, to measure the ΔE_V at abrupt heterojunction interfaces between CdS/PbS QDs system.

7.4.4.2 Results and Discussion

The XPS core level (CL) spectra were acquired from bulk CdS film and PbS-QD film each deposited onto TCO coated glass substrates. All these data were collected at the Korea Institute of Machinery and Materials, Daejeon, South Korea, in collaboration with Dr. Sohee Jeong. The CL spectra were also acquired when PbS-QD films of seven different thicknesses were deposited onto the CdS film of fixed thickness. To begin with, core level survey scans were performed in order to scrutinize the surfaces of the films, to

determine elemental composition and their abundance. For most of the samples analyzed in this work, spectra of 0-800 eV were taken, because no peaks were present at energies higher than 800 eV. Very high resolution spectra, zooming in on a specific feature, were then acquired in order to determine the binding energy of specific elements observed in the survey spectra. The XPS core level survey spectra of 70 nm-thick CdS substrate, 200 nm-thick PbS-QD film and a 12 nm-thick PbS-QD/CdS samples are presented in Figure 7-11.

Figure 7-12 shows CL spectra of Cd 3d and Pb 4f when the thickness of the CdS layer is 70 nm and the thickness of PbS-QD film deposited onto CdS is varied from monolayer (3 nm) to 200 nm. There is an evident but comparatively small shift of the Cd 3d CL (toward larger BE) and Pb 4f CL (toward smaller BE) lines as the PbS-QD layer thickness is increases to higher values, which may indicate the formation of a depletion region (band bending) in PbS-QD layer. As the thickness of the PbS-QD layer increases, the Cd 3d emission peak intensity gradually decreases and vanishes, and the Pb 4f emission gradually increases in intensity. For PbS-QD layer thicknesses ranging from 0 to 12 nm, the CL binding energies of Cd 3d_{3/2} and Cd 3d_{5/2} peaks shift to higher BE by an average of 0.32 eV. Similarly, the CL binding energies of Pb 4f_{5/2} and Pb 4f_{7/2} peaks were shifted to higher BE by an average of 0.17 eV when the thickness of PbS-QD layer was discretely decreased from 200 nm 12 nm. These small shifts in binding energies are due to the similarity of carrier concentrations in CdS and PbS-QD (CdS: $9.95 \times 10^{15} \text{ cm}^{-3}$ vs PbS-QD = $5.6 \times 10^{16} \text{ cm}^{-3}$). [15] At 30 nm QD layer thickness, the Cd 3d_{5/2} emission is completely suppressed whereas Cd 3d_{3/2} emission is still in observable when the QD layer thickness reaches ~200 nm as shown in Figure 7-12. Even though sulfur is

contained in both the substrate and deposited layers, the S 2p spectra vary depending on the presence of organic thiol molecules on the QD surface. Moreover, Pb 4f shifts are in parallel with the shifts of Cd 3d but not with S 2p shifts due to the different chemical environment in the two materials.

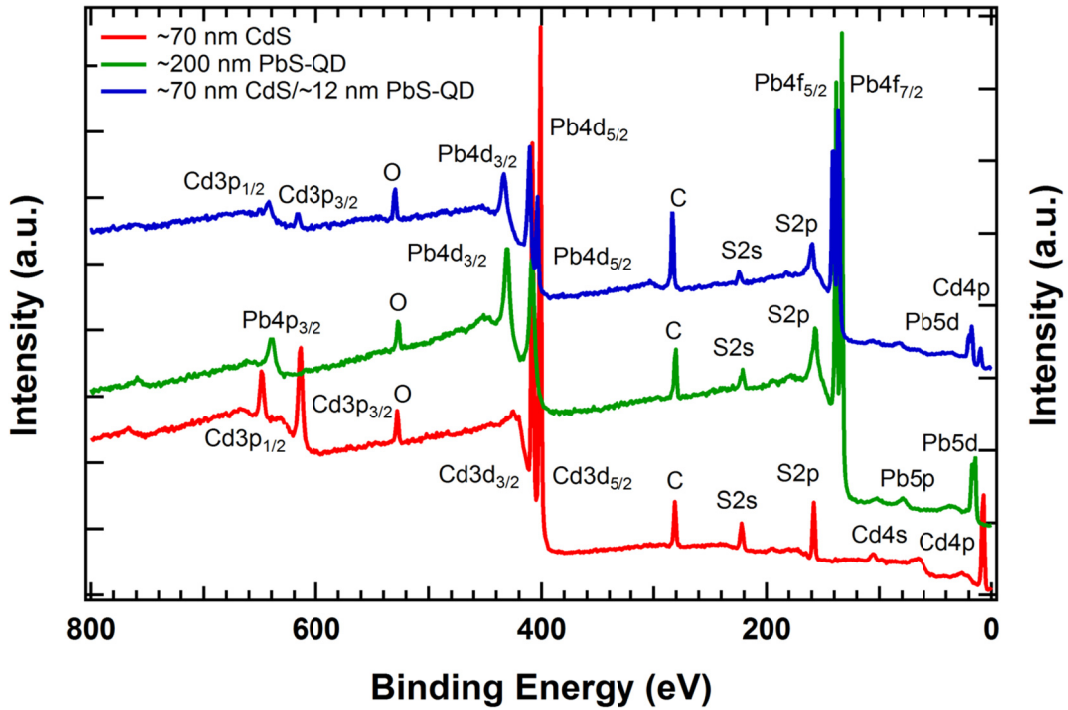


Figure 7-11. Core level survey spectra of 70 nm layer of CdS, 200 nm PbS-QD and 70 nm CdS/12 nm PbS-QD composite films each of them were deposited on TEC15 glass substrate.

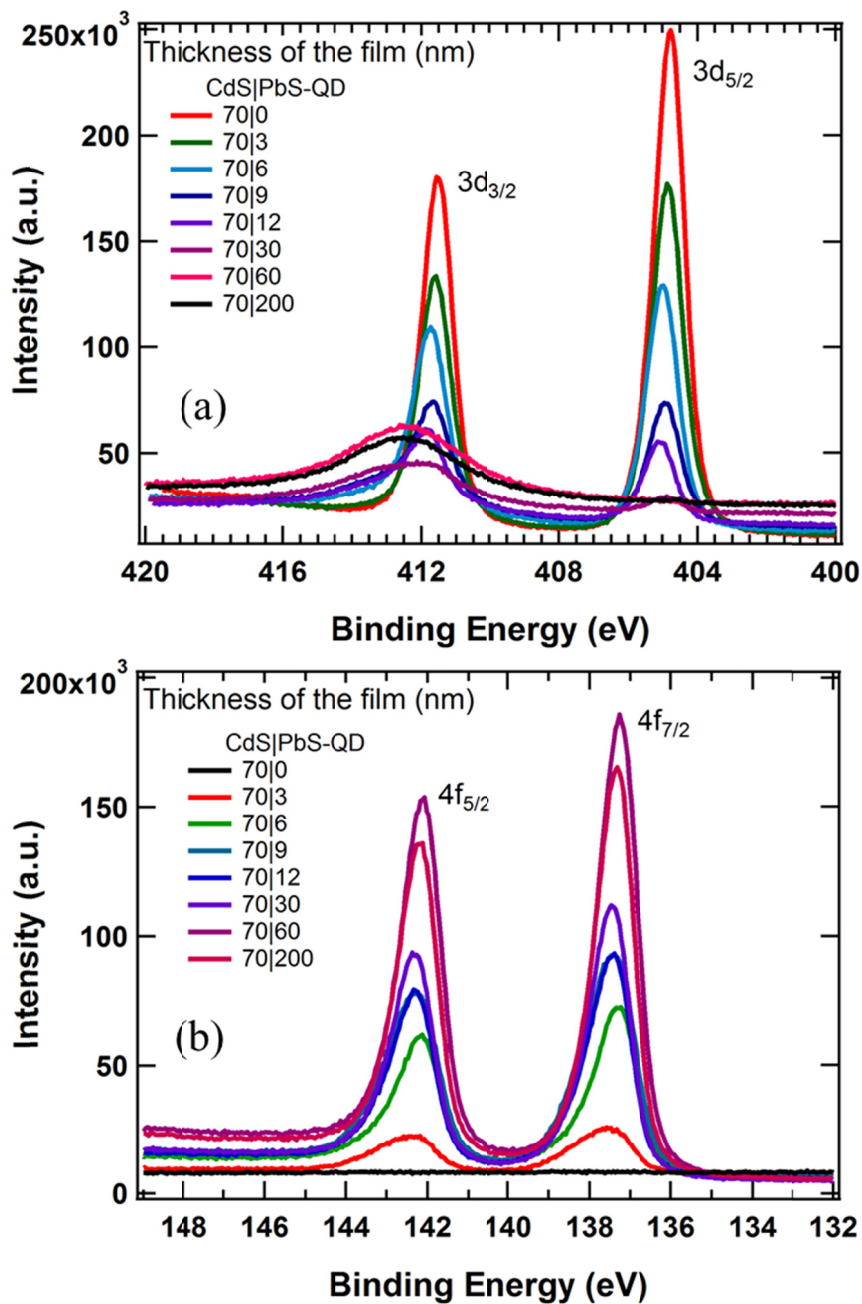


Figure 7-12. Photoemission spectra of Cd and Pb core levels measured after each layer of PbS-QD deposition onto the CdS thin film; the broad peaks near 412.5 eV for PbS-QD layer thickness of 30, 60, and 200 nm are not attributed to the Cd $3d_{3/2}$ transition. These peaks may be due to the contamination in the sample.

A CL photoemission-based method was used to determine the valence band offset.[302, 323, 332, 333] Appropriate CL peaks were referenced to the top of the valence band for the CdS and PbS-QD films, where the top of the valence band (VBM, E_v) was determined using a linear extrapolation of the leading edge of the valence band region in the UPS spectra.[15] Referring to the CdS/PbS-QD band diagram shown in Figure 7-13, the ΔE_v in terms of a binding energy difference ΔE_{CL} between CLs from each side of the interface is

$$\Delta E_v = \Delta E_{CL} + (E_{Pb4f}^{PbS} - E_v^{PbS}) - (E_{Cd3d}^{CdS} - E_v^{CdS}) \quad (7-4)$$

where ΔE_{CL} is the binding energy difference between the CLs of CdS and PbS QDs,

$\Delta E_{CL} = (E_{Cd3d}^{CdS} - E_{Pb4f}^{PbS})$. Core levels were located with Gaussian curve fits to the XPS spectra by a fitting procedure using Igor Pro software.

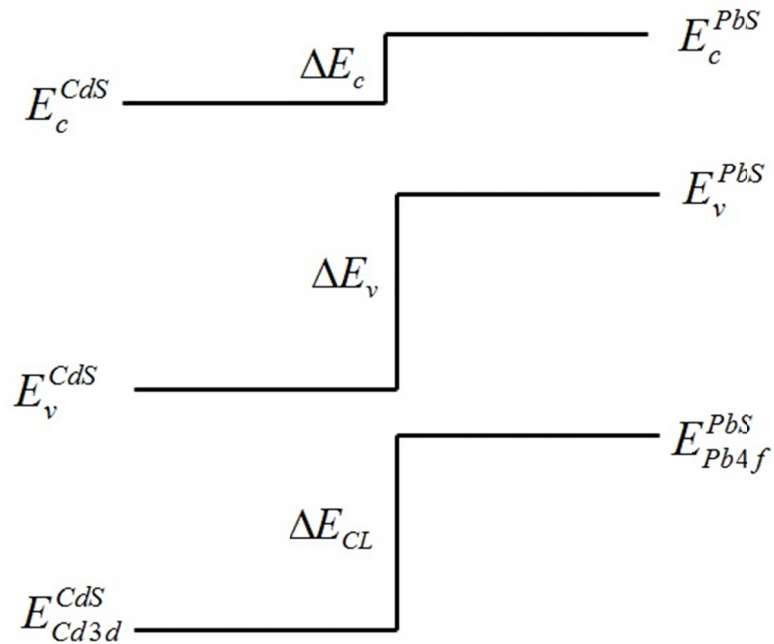


Figure 7-13. The schematic band diagram of the interface between CdS and PbS-QD film. The CL binding energies of CdS and PbS-QD film are also shown.

XPS data for both CdS and PbS-QDs are presented in Figures 7-14, with data shown for the Cd 3d core level peaks from the CdS layer and the Pb 4f core level peaks from PbS-QD layer. Figure 7-14a provides Cd 3d and Pb 4f spectra before the heterojunction is formed between CdS and PbS-QD films (i.e., for two separate samples, one of CdS and one of PbS-QD). The CdS film shows two significant Cd spectral lines – namely the Cd 3d_{3/2} at binding energy 411.54 ± 0.05 eV and the Cd 3d_{5/2} at binding energy 404.81 ± 0.05 eV. Similarly, Pb has two significant spectral lines -- namely the Pb 4f_{5/2} at binding energy 142.16 ± 0.05 eV and the Pb 4f_{7/2} at binding energy 137.3 ± 0.05 eV. The spin-orbit splitting is not evident with s-levels ($l = 0$), but are observed with p, d, and f core-levels which all show characteristic spin-orbit doublets. The spin-orbit separation (Δ) in Cd 3d lines is 6.73 ± 0.05 eV and in Pb 4f lines is 4.86 ± 0.05 eV respectively. Similarly, Figure 7-14b shows Cd 3d and Pb 4f core level binding energy spectra after the heterojunction is formed between CdS and PbS-QD layers. These spectra are used to calculate the CL binding energy difference between the two materials.

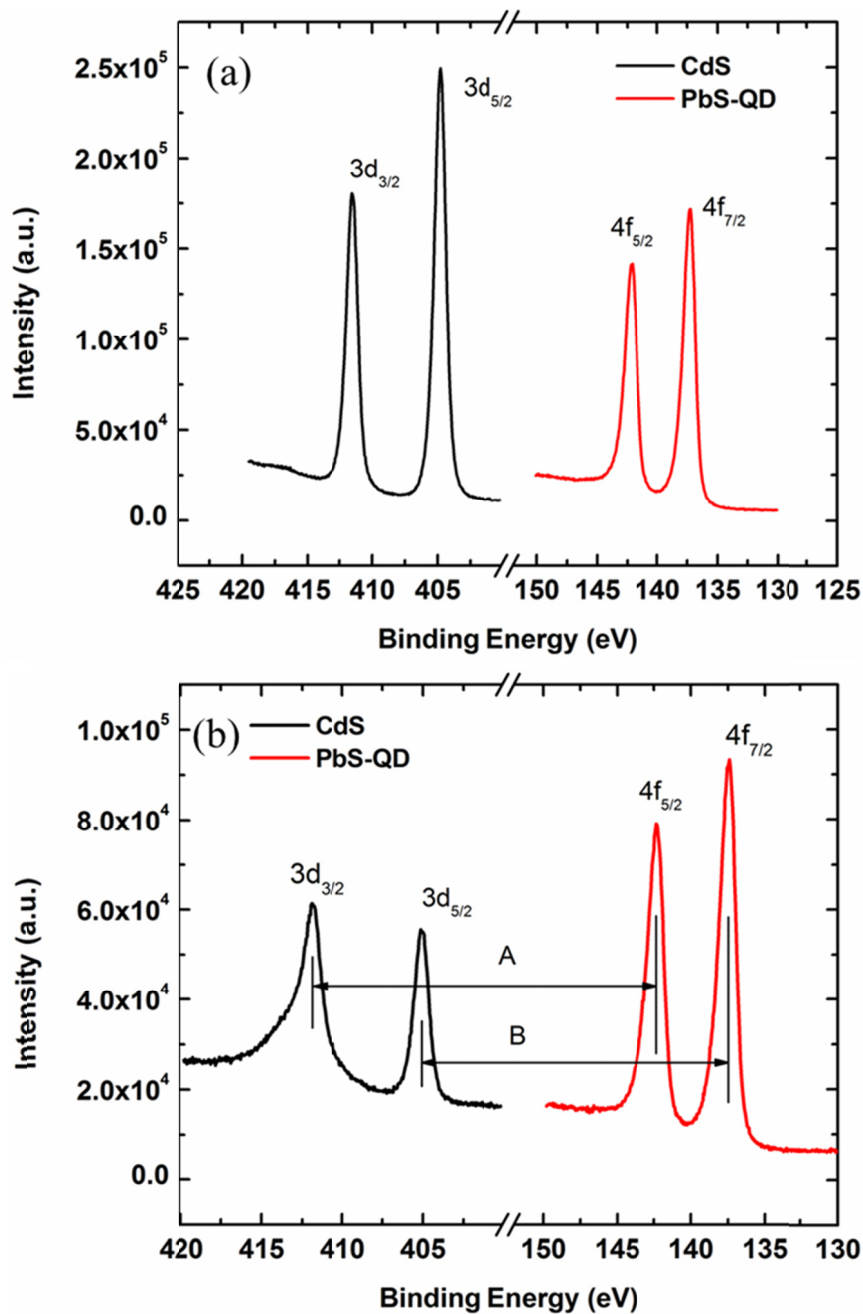


Figure 7-14. (a) XPS binding energy spectra of separate CdS-bulk and PbS-QD film samples, each deposited onto NSG TECTM15 coated glass substrates. (b) XPS binding energy spectrum of PbS-QD/CdS-bulk heterojunction sample in the region of the Pb 4f and Cd 3d core levels, when the PbS-QD layer thickness is ~12 nm. A and B represent the binding energy difference between the core levels of Cd and Pb.

In the Figure 7-14b, A and B denote the CL energy difference (ΔE_{CL}) between Cd 3d and Pb 4f states. The values of A and B are calculated to be 269.56 ± 0.05 eV and 267.63 ± 0.05 eV, respectively. The valence band maximum, E_v , was obtained from the UPS spectra as shown above. We found E_V for CdS at 2.0 eV below the Fermi level, which lies within the range of previously reported values.[334-336] As the band gap of CdS is at 2.42 eV, the Fermi level is 0.42 eV below the conduction band level. This makes sense because the CdS is an n-type semiconductor and the Fermi level is close to the conduction band of the spectrum. We found the VBM of PbS QDs of diameter 2.8 nm located 0.42 ± 0.1 eV from the Fermi level. Given the optical gap of $E_g = 1.4$ eV for the QD films, and the fact that the PbS-QD films show p-type majority carrier population, the Fermi level lies close to the valence band edge as expected.

The second and third terms in equation 7-4 can be calculated with the help of Figures 7-15 and 7-16. In Figure 7-15, the difference between the Cd 3d_{3/2} and VBM is denoted by 'a' and Cd 3d_{5/2} and VBM is denoted by 'b'. Substituting these CL and VBM values, the values of *a* and *b* are determined to be 409.54 ± 0.1 eV and 402.81 ± 0.1 eV respectively.

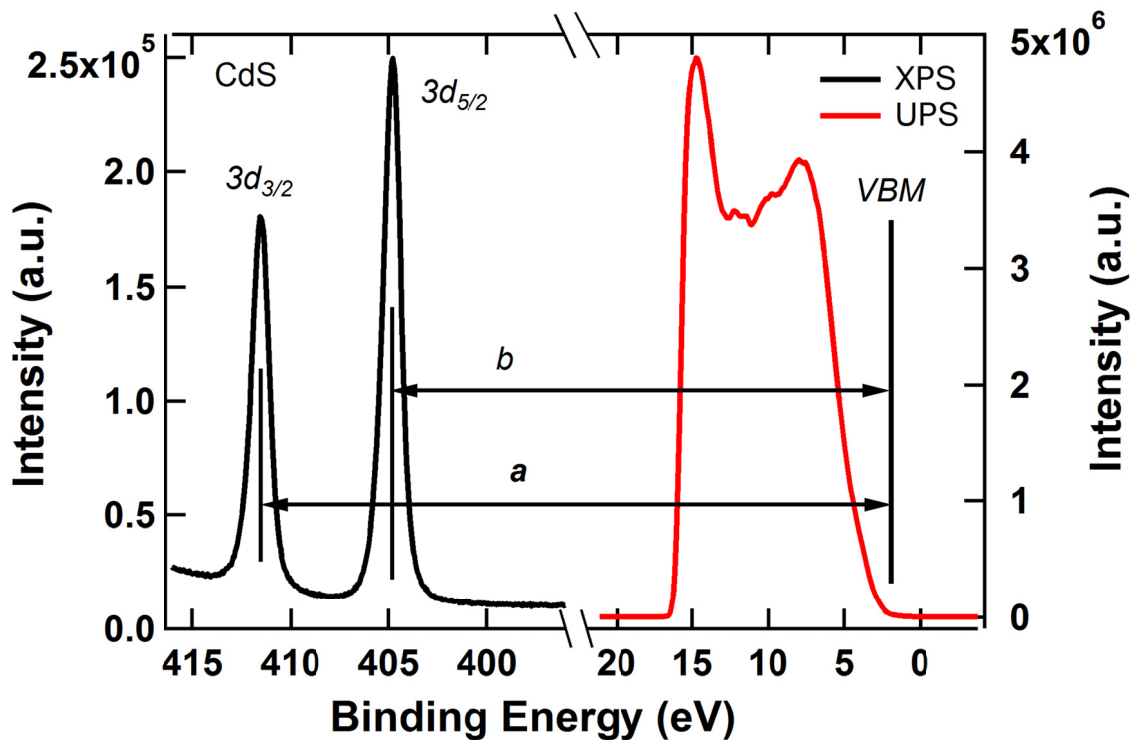


Figure 7-15. XPS and UPS binding energy spectra for CdS. Letters 'a' and 'b' represent the BE difference between the Cd 3d core level and the VBM.

In Figure 7-16, the difference between Pb $4f_{5/2}$ and the VBM is denoted by 'c' and Pb $4f_{7/2}$ and the VBM is denoted by 'd'. Substituting these CL and VBM values, *c* and *d* are determined to be 141.74 ± 0.1 eV and 136.88 ± 0.1 eV respectively.

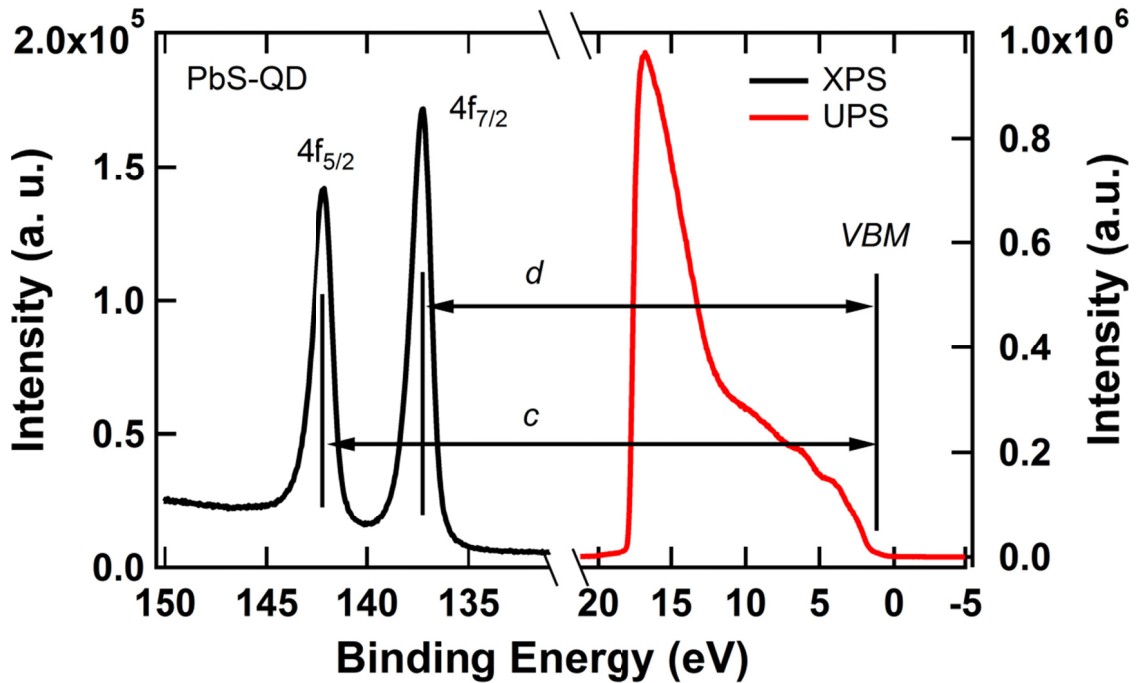


Figure 7-16. XPS and UPS binding energy spectra for PbS-QD. Letters 'c' and 'd' denote the BE difference between Pb 4f CL and the VBM.

Now all required information to calculate valence band offset ΔE_v in equation 4 are collected, for convenience, in Table 7-2.

Table 7.2: Calculated parameters to satisfy equation (7.4)

Core Level	ΔE_{CL}	$E_{Pb4f}^{PbS} - E_v^{PbS}$	$E_{Cd3d}^{CdS} - E_v^{CdS}$	Valence band
Cd3d _{5/2} Pb4f _{7/2}	269.56±0.05	141.74 ± 0.1	409.54 ± 0.1	1.76 ± 0.1
Cd3d _{3/2} Pb4f _{5/2}	267.63±0.05	136.88 ± 0.1	402.81 ± 0.1	1.7 ± 0.1

The average value of the valence band offset was then calculated to be 1.73 eV. Given that the band gap of CdS is 2.42 eV and that of the PbS-QD film is 1.4 eV, the conduction band offset ΔE_c is calculated to be 0.71 eV.

Figure 7-17 shows schematic of the energy band lineup in the CdS/PbS-QD heterojunction, with all of the energy scales included. The observed conduction band offset facilitates electron transfer from the top of the PbS-QD film to the CdS film.

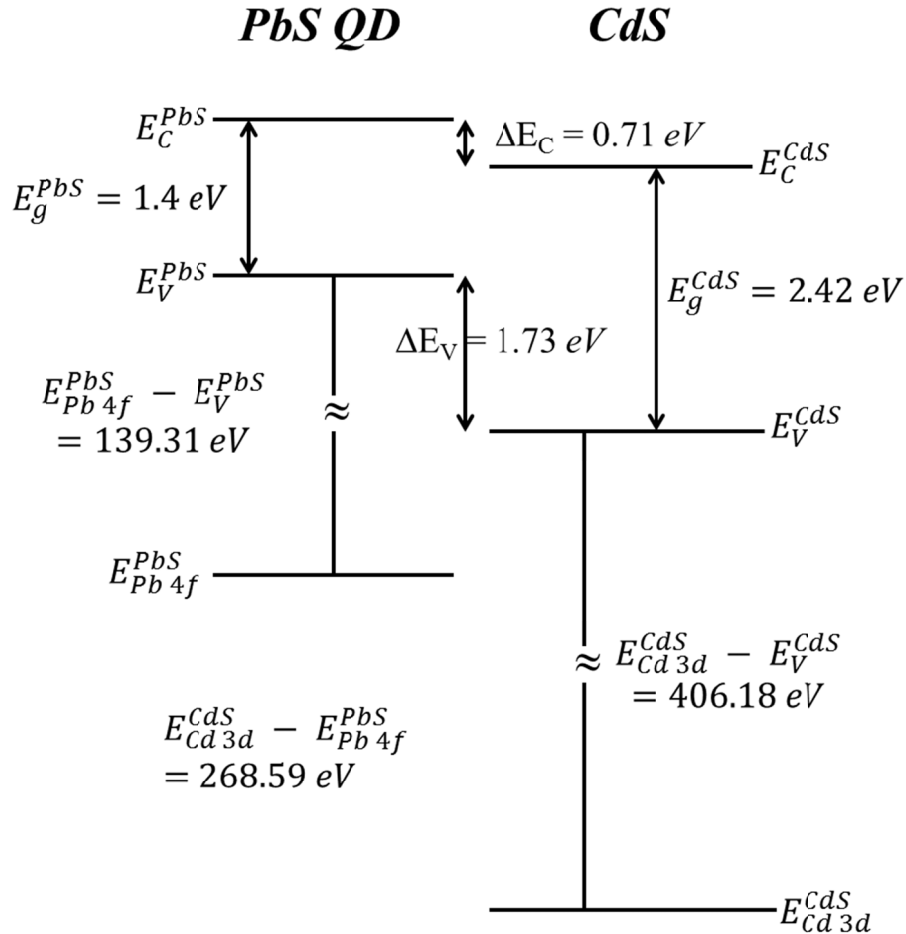


Figure 7-17. Energy band diagram of CdS/PbS-QD heterojunction interface. All parameters as obtained from the measurement are labeled and expressed in eV.

We have measured the valence band offset in CdS/PbS QDs heterojunction. For this heterojunction system, our measurements yield a valence band offset of 1.73 ± 0.1 eV and a conduction band offset of 0.71 ± 0.1 eV. These values are compatible with

reasonably efficient electron injection from PbS-QDs into CdS. This shows that excellent valence and conduction band offsets can be obtained in this semiconductor system.

7.5 Conclusions

I have used two important and widely used methods to determine the work functions of metal and semiconductor thin films. I used the KPFM method to determine the work functions of Au, CdS and PbS-QD with values of 4.7 eV, 4.4 eV and 4.5 eV respectively. Then I used UPS to determine the work functions of CdS and PbS-QD films (QD diameter = 2.5 nm) to be 4.5 eV and 4.9 eV, respectively. The UPS method was also used to calculate valence band maxima of CdS and PbS-QD. The VBM locations were measured with respect to the Fermi level (equivalent to the zero BE). The VBM for CdS is 2.0 eV and for thin film PbS-QD (2.5 nm diameter) is 0.6 eV, respectively. Finally, band offsets were calculated using both UPS and XPS methods. The valence band offset between CdS/PbS-QD was 1.7 eV and the conduction band offset was calculated with the help of band gap to be 0.71 eV.

The band offset values depend on the type of heterojunction. Band offset is large if band gap of one of the semiconductor is large. Band offset is still large if a small band gap semiconductor is making a junction with oxides of very large band gap. Hence, an optimal band offset value depends on the nature of the heterojunction between two materials. According to common anion rule, materials with the same anions should have very small valence band offsets because valence band is related to anionic states. This work represents the first known measurement of the band edge offsets for a CdS/PbS-QD

heterojunction, and will serve as a reference point for any future work on this material system.

Chapter 8

Life cycle assessment (LCA) study of photovoltaic systems

8.1 Introduction

In recent years, the continuous emissions and pollutants from conventional energy sources have led to the research and implementation of environmentally-friendly options such as solar energy. With low environmental impact, cost reduction measures and the development of more efficient photovoltaic modules, production of photovoltaic technologies has increased more than 45-fold over the last decade.[272] However, despite the increased emphasis and improvements made to photovoltaic technologies, photovoltaic devices lag far behind fossil fuels in several key areas such as intermittent energy output, electricity output, and capital recovery period. In fact, the capital recovery periods for some photovoltaic systems exceed 20 years.[337] In order to continue funding the build-out of photovoltaic electricity generation, an assessment of the energy payback time, power generation output, as well as multiple environmental factors should be

considered to gain a better understanding of the limitations, benefits, and potential areas of improvement.[338]

This chapter presents a review of literature research focused on the evaluation and assessment of energy and emissions costs and benefits of PV modules. The study aims to provide comparisons of crystalline silicon (mono-crystalline) and thin film (a:Si, CdTe and CIGS) PV modules. These modules are compared based on energy input/output over the course of a PV module's lifetime. The goal of the assessment for each technology is to determine whether future research and development should continue, possible areas for improvement, and how the technologies compare among the different impact categories.

Recently Peng et al.[339] compiled some of the published energy payback time (EPBT) and energy return on energy invested (EROI) data for different types of PV systems. However, since the different studies use different modeling assumptions, the results were not directly comparable across studies. This issue can be overcome using meta-analysis that 'harmonizes' the results from different studies. Meta-analysis and systematic reviews are often found in health sciences and clinical research but are gradually entering into the life cycle assessment (LCA) literature as well. [340, 341] The goal of this study was to do a meta-analysis of the literature data on EPBT and EROI of PV systems to be able to more accurately evaluate and compare the energy performance of different types of PV technologies. To achieve this goal, a thorough literature review was conducted. Energy performance of PV systems is sensitive to embedded energy, module efficiency, solar insolation and system lifetime.[342] EPBT and EROI data collected from the literature were harmonized for these parameters. I am grateful to

Jennifer Collier who has helped extensively with the inventory, assessment and interpretation of data used in the project that is the topic of this chapter.

A life cycle assessment primarily consists of 4 steps which include: a goal and scope definition, inventory analysis, impact assessment, and interpretation of the resulting data.[343] It is necessary to define the impact categories (greenhouse gas emissions, energy payback time, or acidification, etc..) that are taken into consideration, and also what processes (transportation, electricity, material extraction, etc..) contribute to these categories.[343] Then, the magnitude for each category is assessed. Here, the relative scores are measured for each impact category per functional unit. A functional unit is related to the function for a product, and it is a standard unit of measure that is used to calculate values for each impact category (e.g., a suitable functional unit of power generation system is 1 kWh of electricity).[343] Next, the calculated values are normalized, which is basically a computation of the calculated values based on a reference situation, such as the processes over a given period of time at a given location. Lastly, the data is interpreted based on the assessment of the processes per impact category for different products/types of products. This should ultimately produce comparisons and decisions related to the sustainability of a product or process.

8.2 PV System Description

8.2.1 Classification of PV System

The central goal of this work/chapter is to present a review of life cycle assessment of five different types of PV modules: single crystalline silicon, polycrystalline silicon, amorphous silicon, cadmium telluride and copper indium gallium

diselenide PV systems. Overall grouping of these PV modules is shown in Figure 8-1. The recent market share values of these PV systems are also expressed in percentage. These market share values were published in a report presented by Fraunhofer Institute for Solar Energy System ISE in October 2014.[344]

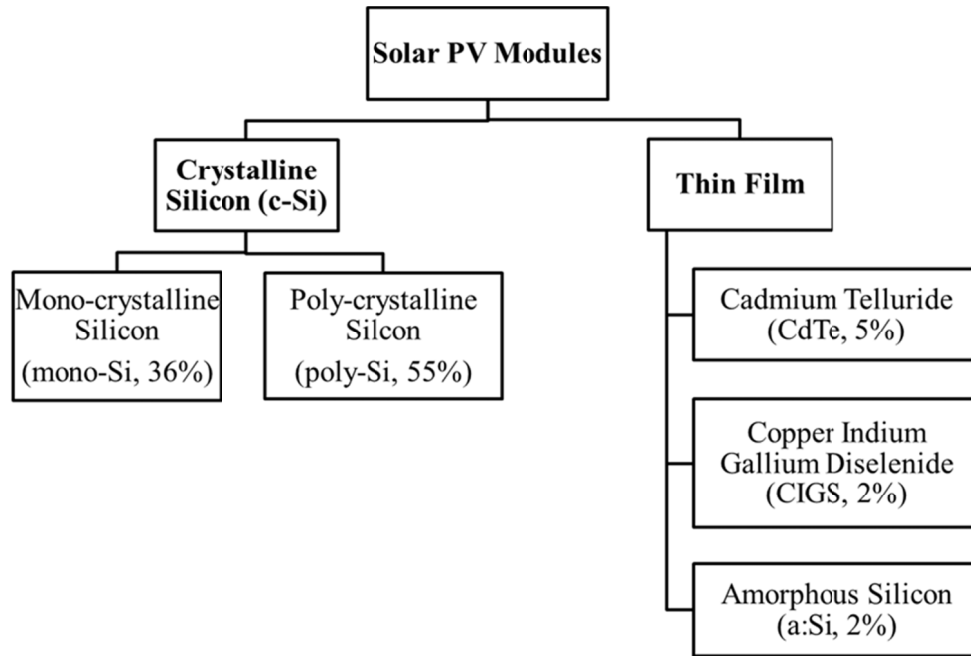


Figure 8-1. Technologies included in this study and their estimated percentage of market share. These market share percentages were published in 2013.[344]

8.2.2 Fabrication of the light-absorbing films used in photovoltaic cells and modules

Silicon is prepared by heating silicon dioxide and carbon in an electric furnace, using carbon electrodes. The first product obtained in this process is called metallurgical grade silicon (MG-Si), which is 98% pure. Further purification is required to get solar grade or higher grade silicon. The Czochralski (CZ) process [99] is used to produce single crystals of silicon for solid-state and semiconductor devices. The main idea behind the CZ process is to grow a single crystal from a melt by pulling a seed crystal very

slowly within a well regulated thermal environment.[345] Polycrystalline silicon is made up of small grains of monocrystalline silicon. For this, cube shaped ingots are made using molten silicon and cut into wafers similar to monocrystalline wafers. Thin films of hydrogenated amorphous silicon (a-Si:H) are grown using plasma enhanced chemical vapor deposition (PECVD) process.[346, 347] a-Si:H films can be grown under a wide variety of conditions but the best films are typically grown in low-power radio frequency (RF) discharges in pure silane or silane diluted with hydrogen.[348]

Cadmium is a byproduct of zinc, lead and copper production, and is collected from the emissions and waste streams of these major metals. Tellurium is a by-product of copper production, and is also collected from waste streams. High purity Cd and Te are used in synthesizing high purity (five 9s, 99.999% to six 9s, 99.9999%) CdTe for PV cells. According to industry sources, electrolytic purification does not produce any emissions and all waste is recycled.[349] There are various ways of depositing CdTe thin films such as physical vapor deposition (PVD), close-space sublimation (CSS), vapor transport deposition (VTD), sputter deposition and so on. The sputter deposition technique has been investigated by groups at the University of Toledo [350] and NREL [351] and has been used for the commercial production of thin PV modules.

High purity copper indium gallium diselenide (CIGS) films are deposited using sputtering and thermal evaporation method as well as solution based deposition method. In the first method films are grown in three stages.[352] In the first stage an $(\text{InGa})_2\text{Se}_3$ layer is deposited reacting it with Cu and Se. In the second stage, compositional control is achieved when the film reaches from Cu-poor to Cu-rich transition. In the third stage In and Ga are evaporated in the presence of Se.

8.2.3 Methods of growing

Crystalline silicon solar cells are homojunction devices, meaning that p-type and n-type crystalline silicon layers are interfaced to produce a p-n junction. Front and back contacts are chosen and deposited to complete the device. Amorphous silicon thin film solar cells use both p-i-n and n-i-p structures. [353] A three layer architecture is created, with a middle intrinsic layer between an n-type and a p-type layer as shown in Figure 8-2. Amorphous silicon is abundant and non-toxic and requires a low processing temperature. As the amorphous structure has a higher absorption rate of light than crystalline silicon, the complete light spectrum can be absorbed with a very thin layer of absorbing material.

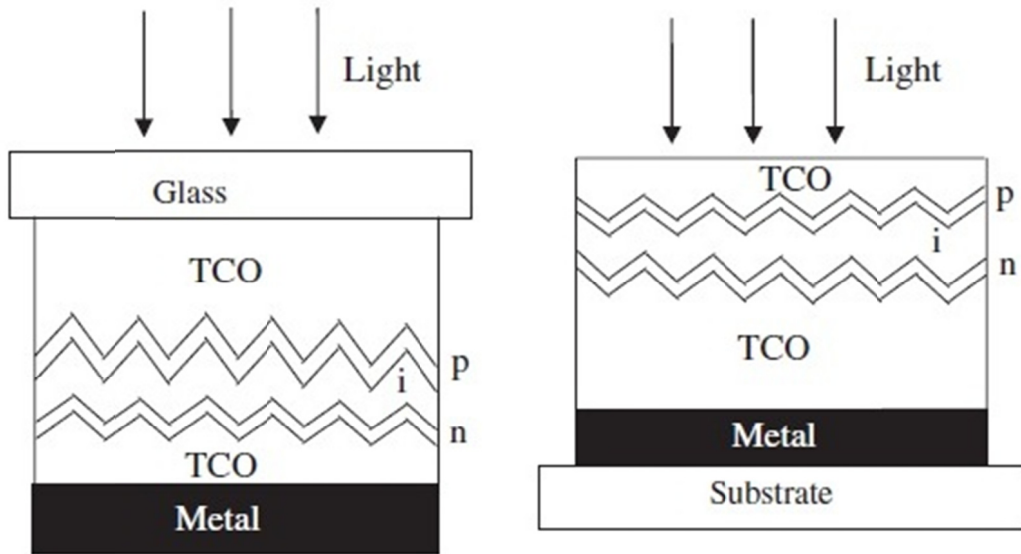


Figure 8-2. (Left) a-Si solar cell in "superstrate" (p-i-n) configuration, and (Right) "substrate" (n-i-p) configuration.[353]

Cadmium telluride solar cells can be fabricated in either substrate or superstrate configurations, as shown in Figure 8-3, but the highest efficiency is achieved in the

superstrate configuration.[354] The CdS/CdTe layers for superstrate configuration are grown on transparent conducting oxide (TCO) coated glass substrates. Solar cells in superstrate configuration have given the highest efficiency of up to 21%.[21] For substrate configuration, CdTe is deposited on metal-covered glass substrate, or a metal-coated flexible substrate such as polyimide. The highest efficiency in this scheme is 11.6% on a Mo/Cu coated glass substrate.[355] Commonly used back contacts are Cu/Au, Cu/graphite, and Cu/Mo combinations.[284] Recently, Bhandari et al. developed iron pyrite nanocrystal as a back contact for CdTe solar cell thin film solar cells.[39, 356]

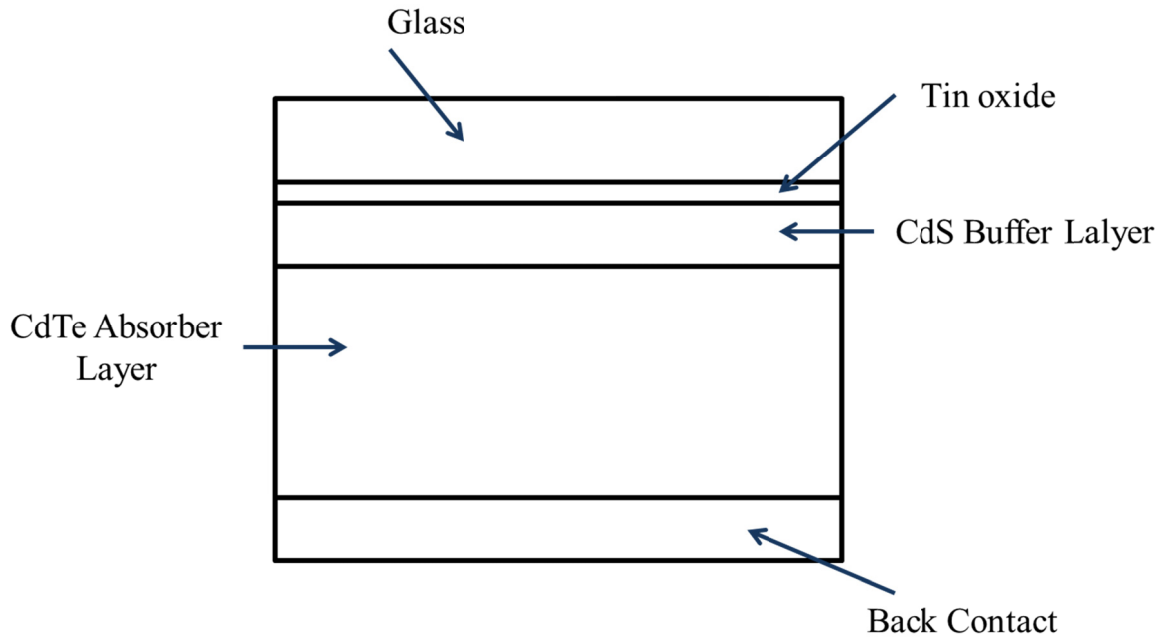


Figure 8-3. Schematic of a typical CdTe solar cell in superstrate configuration. [357]

In general, CIGS solar cells are grown in a substrate configuration as shown in figure 8-4. Optimal performance has been achieved with this configuration owing to favorable process conditions and material compatibility. However, an additional encapsulation layer and /or glass is required to protect the cell surface. The CIGS

absorber layer is grown on soda-lime glass substrate coated with a sputter-deposited Mo layer. Atop the CIGS layer, a CdS layer is prepared via chemical bath deposition. Aluminum doped ZnO (AZO) is deposited onto the CdS layer, and Ni/Al grids are deposited by electron beam evaporation to form the back contact.[357] Similar techniques of deposition work for CIS devices as well.

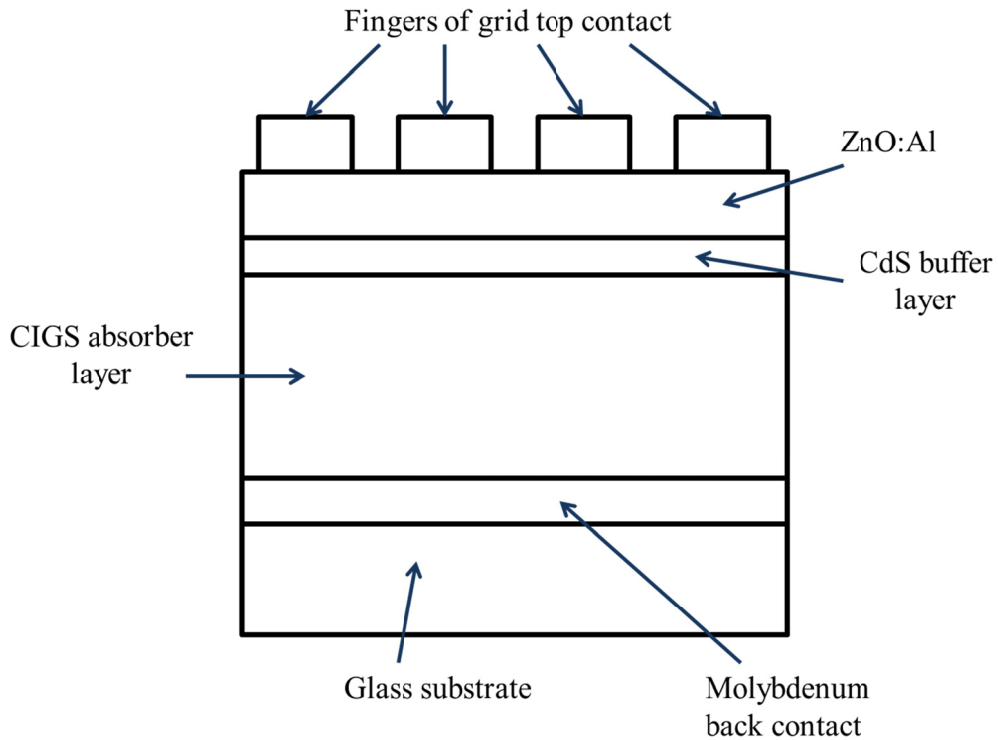


Figure 8-4. A schematic cross-sectional view of a typical substrate configuration CIGS solar cell.[357]

8.2.4 Module design

Photovoltaic (PV) modules use light energy from the sun to generate electricity through the photovoltaic effect. A PV module consists of a number of interconnected solar cells encapsulated into a single, long-lasting, stable unit. The majority of modules

use wafer-based crystalline silicon cells or thin film cells based on CdTe or silicon. The conducting wires that take the current off the panels may contain silver, copper or other non-magnetic conductive transition metals. To achieve a desired output voltage and current, electrical connections are made between cells within a module, and modules within an array, in series and/or in parallel. Many different types of PV modules exist and module structure is often different for different types of solar cells. The design of a PV module is based on system type, site location, and applications. One c-Si module contains about 50-60 cells and each module may have three to five column of cells in series as shown in figure 8-5.

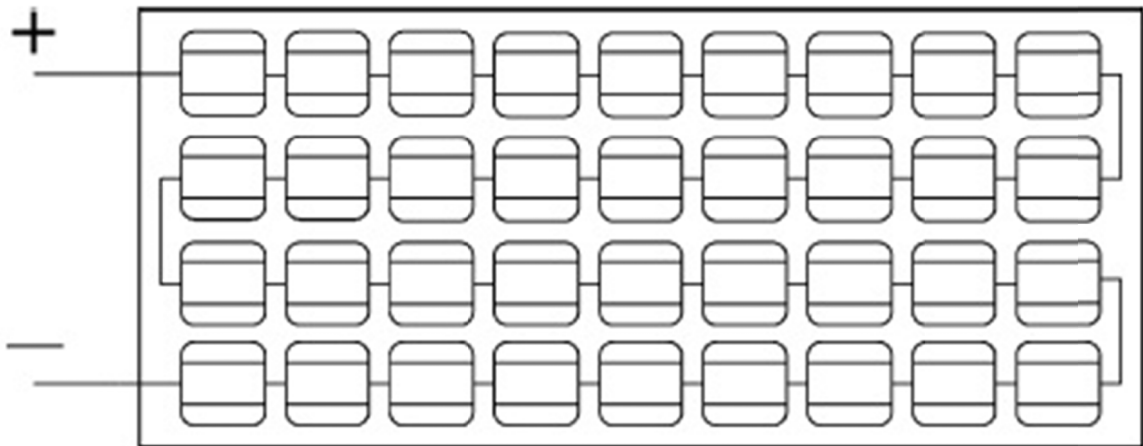


Figure 8-5. A schematic representation of a module showing 36 crystalline silicon PV cells connected in series. [357]

8.2.5 Relevant Parameters

8.2.5.1 Module Efficiency

Solar cell efficiency (photo-conversion efficiency, PCE or $\eta\%$) is the ratio of the electrical energy output of a solar cell to the light energy incident on the solar cells. This is calculated by dividing output power of a cell at its maximum power point ($P_{\text{mpp}} = I_{\text{mpp}} \times V_{\text{mpp}}$) in Watts by the power of the radiation incident on the cell (in W). A module is the package of large number of cells (for example, 60 cells is common in present-day crystalline Si modules). There can be a large difference between solar cell efficiency and fully packaged module efficiency. In general, three types of losses can be seen in a module: loss due to the physical layout of the module including framing area and gaps between cells, optical loss from reflection and absorption associated with encapsulation, and electrical loss due to series resistance developed from cell interconnections.

The module efficiency reported by manufacturers represents the initial efficiency of the module under STC, accounting for the entire area of the module and including the frame. Environmental influences such as moisture penetration, temperature fluctuation, and weathering of the encapsulation layers result in a gradual degradation of module efficiency which limits module lifetime. [358, 359] However, this degradation does not have a large effect on the EPBT calculation. For example, a module with initial 15.0 % conversion efficiency exhibiting performance degradation at a rate of 0.5 % annually would result after 30 years in only a 2.0 % absolute efficiency reduction to 13.0 % efficiency, and an average life time efficiency of 14.0 %. In harmonization, the author has adopted the average life time efficiency values that were used by Hsu, et al.[360] and

Kim, et al.[361] to harmonize the greenhouse gas emission from PV systems (Table 8.1). These values were calculated based on a 0.5 % per year degradation over a 30 year life time.

8.2.5.2 Performance Ratio

Performance ratio (PR) is the ratio of the actual to the theoretical energy output of a PV module. It reveals how well a module behaves under actual conditions. The PR consists of all inefficiencies in actual energy output, including the effects of variations in insolation, reduced efficiency associated with elevated module temperature, shading, soiling or snow-cover, and inverter inefficiency. The PR measures a location-independent quality of a PV module or system. The PR is expressed as a percentage such that a PR of 75% means that approximately 25% of the theoretical energy generation is lost due to such factors as snow or other environmental factors, or reduced conversion efficiency associated with elevated module temperature, or system down time.[362]

When calculating the EPBT for scenarios from studies that did not state the PR of the system, a PR of 75% for roof top and 80% for ground mount installations were assumed.[363, 364] For harmonization, a value of 75% was chosen for consistency. In practice, today's new PV systems can attain PR values as high as 90%.[365]

8.2.5.3 Solar Insolation

Solar insolation is a measure of solar radiation energy received per unit area over a given time interval. It is commonly expressed as average irradiance in kiloWatt-hours per square meter per year ($\text{kWh m}^{-2} \text{yr}^{-1}$). As annual insolation increases, EPBT decreases

(equation 8.1). The “universal” insolation value used here for harmonization is 1700 kWh m⁻² yr⁻¹. According to Phylipsen and Alsema [366], this insolation value is representative of the average global insolation, and has also been used for the insolation of Southern Europe and the Netherlands. [367, 368] To provide an idea of how insolation affects EPBT, annual insolation values of four other places (Los Angeles, CA; Trenton Mercer County, NJ; Las Vegas, NV; and average US) are reported.

8.3 Methods

8.3.1 Collection of Literature

A thorough literature review was conducted using www.google.com, scholar.google.com, and www.webofscience.com using keywords/phrases “energy payback time”, “mono-crystalline silicon”, “poly-crystalline silicon”, “amorphous silicon”, “CdTe”, “CIGS”, and “photovoltaics”. As indicated earlier, this study focused on the most relevant commercial technologies, falling into the categories of mono-crystalline silicon (mono-Si), poly-crystalline silicon (poly-Si), amorphous silicon (a:Si), cadmium telluride (CdTe), and copper indium gallium diselenide (CIGS). As of 2013 (Figure 8-1), these five technologies make up essentially 100 % of the current market share in the world, and while the thin film industry is only about 9 %, the growth in thin film industry has been reported to be faster than in the crystalline silicon industry.[369, 370] Any data, harmonization, and discussion of ribbon crystalline silicon, organic solar cells, dye-sensitized solar cells, solar concentrator systems, or quantum dot based cells are omitted because these technologies at present do not play a significant role in the commercial market.

After reviewing each article's abstract, it was determined to obtain the full article if the abstract discussed energy, payback times, sustainability, or environmental issues or impacts of photovoltaic systems. Additional articles were also obtained using the ancestry approach and the citation index. A total of 329 references were collected. From this total, only 7 (11 scenarios) papers on mono-Si, 6 (11) on poly-Si, 3 (7) on a:Si, 6 (11) on CdTe, and 5 (8) on CIGS passed screening used here. Here the number, for example, 7 represents number of papers referenced for mono-Si. Sometimes each paper has more than one scenario described pertaining to mono-Si, therefore, (11) represents number of scenarios on the mono-Si PV technology system. It is not uncommon in meta-analysis to discard over 90% of the studies from the initial list.[361]

8.3.2 Criteria for Inclusion

Kim et al. [361] used rigorous screening in their harmonization effort for thin film PV systems. In contrast, Hsu et al. [360] used less screening and aimed to capture more articles. Here, the method used by Kim et al.[361] has been followed whereby multiple criteria were set for screening references for inclusion in the analysis.

Several criteria were used in determining which studies to include in the analysis. All studies that did not discuss one of the five PV system types (mono-Si, poly-Si, a:Si, CdTe, CIGS) that dominate today's commercial market were eliminated. A PV system consists of the PV modules and the balance of system (BOS) components. The module encompasses the component that converts the solar radiant energy to electrical energy. The BOS components encompass all other supporting infrastructure and can include the wiring, switches (for connecting to the existing electric grid), support racks, and inverter

(to convert direct current to alternating current). The life cycle stages of a PV system include raw material acquisition and processing, manufacturing of the module and other components, operation, and end of life management. All papers that did not explicitly report the cradle to gate energy (raw material through manufacturing stages) from both the module and the BOS were eliminated. To be included in the analysis, the paper also had to report original data for both the BOS and the module. Some papers reported original data for the module but not the BOS. These studies were eliminated.

Each paper must have provided data on the EPBT of at least one specific type of PV system and it must have stated the stages considered in the calculation of embedded energy to be included in our harmonization. Also, the author(s) had to have made their own contribution. In other words, if the EPBTs reported were directly from other papers, that paper was eliminated and the original papers cited were obtained as the source of data. If the paper was unable to be attained in English, it also was not included. These criteria eliminated the majority of the references collected.

As another criterion, different scenarios were reviewed that a study might have modeled. The word 'scenario' here refers to the different analyses some papers did where they varied some of the parameters such as efficiency, performance ratio, insolation, and embedded energy to see its effect on EPBT. Some papers analyzed EPBT of multiple scenarios by varying the parameters that affect annual energy generation (i.e. efficiency, insolation, performance ratio) while keeping the embedded energy value constant. In such cases, harmonized EPBT value would be the same for all scenarios that have the same embedded energy. Therefore, data from only one scenario were recorded for each embedded energy value provided by a study.

In subsequent screening, those papers were eliminated that (a) did not directly state the information required for calculating the EPBT, or (b) failed to provide sufficient information to make accurate assumptions. In addition, each EPBT value was independently calculated using the embedded energy, insolation, efficiency, and performance ratio provided in the studies. If the calculated EPBT value differed by ~10 % (± 0.3 years) from the EPBT value reported in the study, that particular scenario or study was not included. Using this approach, the EPBT values of most of the studies were verified and only three data points were excluded in which case the calculated EPBT could not match the EPBT value reported in the study.

A cradle to gate system boundary (life cycle assessment study which covers from resource extraction to the factory gate) was selected for the analysis because there is limited and widely varying data available for the distribution, operation, maintenance, and end of life management of PV systems. Another reason of limiting this study in cradle to gate analysis is because the energy consumption in these stages are either low or negligible [337, 371] and most of the papers did not incorporate these phases. Also, the disposal stage would have added more uncertainty to our results as each study may have considered a different process, such as disposing the modules in a landfill or recycling. Some existing data for transportation and end of life management show that these stages do not contribute significantly to the life cycle energy demand. [337, 371-374]

Finally, the author aimed to define an objective criterion for screening the papers that would be using outdated technology based on the information provided by the studies such as the thickness of absorbing semiconductor layer, efficiency, module manufacturing processes and design. However, some studies that passed screening from

other criteria did not provide comprehensive information on these parameters. Therefore, ‘modernity’ of technology is chosen as final screening criterion based on the year the study was published. By applying this screening, several papers that passed other screening criteria were eliminated because they were published prior to 2000. Ultimately, our screening resulted in 11 papers (38 scenarios) to be included in the EPBT harmonization dataset [368, 375-384] and 23 papers to be included in the embedded energy dataset. All of the papers included in the study were published in between 2000 – 2013.

8.3.3 EPBT and EROI Calculation

EPBT and EROI were calculated using equations (8.1) and (8.2), respectively:

$$\begin{aligned}
 EPBT(year) &= \frac{\text{Embedded (primary) energy (MJ m}^{-2}\text{)}}{\text{Annual (primary) energy generated by the system (MJ m}^{-2}\text{ year}^{-1}\text{)}} \\
 &= \frac{W_1(\text{MJ m}^{-2})}{W_2(\text{MJ m}^{-2}\text{ year}^{-1})} = \frac{W_1}{\frac{I \times \eta \times PR}{\varepsilon}}
 \end{aligned} \tag{8.1}$$

EROI = lifetime energy output/Embedded energy

$$= \frac{W_3(\text{MJ m}^{-2})}{W_1(\text{MJ m}^{-2})} = \frac{W_2(\text{MJ m}^{-2}) \times LT(\text{year})}{W_2(\text{MJ m}^{-2}\text{ year}^{-1}) \times EPBT(\text{year})} = \frac{LT(\text{year})}{EPBT(\text{year})} \tag{8.2}$$

where, W_1 = embedded (primary) energy (MJ m⁻²);

W_2 = annual energy generated by the system expressed as primary energy (MJ m⁻² year⁻¹);

W_3 = total energy generated by the system over its lifetime expressed as primary energy (MJ m⁻²);

ε = electrical to primary energy conversion factor;

I = total solar insolation incident on the unit-surface, per year ($\text{MJ m}^{-2} \text{ year}^{-1}$);

η = average module efficiency (%);

PR = system performance ratio (%);

LT = lifetime of the system (year)

In equation (8.1), product $I \times \eta \times \text{PR}$ is the area-normalized annual electrical energy generated from the system, which is converted to primary energy equivalent using the electrical to primary energy conversion efficiency factor (ϵ). This conversion factor depends on a country's electricity mix. Some studies either reported the energy values in primary energy units or they specified the conversion efficiency factor from electrical to primary. For several studies, a conversion factor of $\epsilon = 0.35$ has been considered for primary to electrical energy. [379, 380, 385, 386] Similarly, a conversion factor of 0.39 was assumed for thermal to electrical energy conversion. An example can be taken from the work of Muneer et al. in which they reported embedded energy values of $230 \text{ MWh}_{\text{th}}$ and 5 MWh_e for a total module area of 125.5 m^2 . [376] Two conversion factors are applied as following to express embedded energy in MJ m^{-2} .

$$\left(\frac{230 \text{ MWh}_{\text{th}}}{125.5 \text{ m}^2} \times \frac{0.39 \text{ MWh}_e}{1 \text{ MWh}_{\text{th}}} + \frac{5 \text{ MWh}_e}{125.5 \text{ m}^2} \right) \times \frac{1 \text{ MWh}_{\text{prim}}}{0.35 \text{ MWh}_e} \times \frac{1000 \text{ kWh}_{\text{prim}}}{1 \text{ MWh}_{\text{prim}}} \times \frac{3.6 \text{ MJ}_{\text{prim}}}{1 \text{ kWh}_{\text{prim}}} = 7761 \text{ MJ}_{\text{prim}} \text{ m}^{-2}$$

Since EROI may also be calculated with the lifetime and EPBT, both of these metrics are highly dependent on the embedded energy value; the lower the embedded energy, the lower the EPBT and the higher the EROI. For this study, embedded energy (W_1), also known as the embodied energy, is the total primary energy required to manufacture the modules and BOS for the PV system being analyzed. For a more accurate calculation of EPBT, the numerator of equation (8.1) could be set equal to the

total energy required for the entire life cycle of the PV system. Our approach of using only the energy required for manufacturing underestimates the EPBT value but this error is expected to be insignificant. Embedded energy is reported using either MJ m⁻² or kWh kW_p⁻¹ and in collecting the embedded energy data from references, all data were converted to MJ m⁻² using equation (8.3).

$$\text{Power Rating } (W_p) = (1000 \text{ W m}^{-2}) \times \text{module efficiency } (\%) \times \text{module area } (\text{m}^2) \quad (8.3)$$

where standard test conditions (STC: incident sunlight with a spectral distribution defined by AM1.5G and an integrated intensity of 1000 W m⁻², and module temperature equal to 25°C (77°F)) are applied, and efficiency is expressed as a fraction (i.e., 15% efficiency is written as 0.15). In this way, a 15% module efficiency yields an areal peak power rating (at STC) of 150 W_p m⁻². To convert a module's efficiency to an areal rated power density (W_p m⁻²), one needs only to multiply the fractional efficiency by 1000 W_p m⁻².

As an example, Schaefer and Hagedorn [387] reported a value of 20,500 kWh kW_p⁻¹ for the embedded energy of a mono-Si PV power station with a module efficiency of 14%.

Following the conversions described above, we performed the following calculations:

$$\frac{20,500 \text{ kWh}}{1 \text{ kW}_p} \times \frac{3.6 \text{ MJ}}{1 \text{ kWh}} \times \frac{0.14 \text{ kW}_p}{\text{m}^2} = 10,332 \text{ MJ.m}^{-2}$$

Equation (8.1) was evaluated with the values reported by each reference in order to verify the reported EPBT (screening stage). If there was a small discrepancy (less than ±0.3 years) between the calculated EPBT and the reported EPBT, the reported EPBT value was used as an unharmonized value. Most of the papers did not calculate EROI. Equation (8.2) was used to calculate the unharmonized EROI based on the reported lifetime and EPBT. Once the unharmonized EPBT and EROI values were determined,

the harmonization parameter values of module efficiency, performance ratio, insolation, and lifetime were used to calculate the harmonized EPBT and EROI. The embedded energy value was not changed for the harmonization calculation. This parameter is considered to be already harmonized since only studies that considered the same stages (including only module manufacturing and BOS) were included in our analysis. The harmonized results only apply to the conditions determined here, but they may easily be changed since all of the factors are linear. For example, to change insolation from 1700 kWh m⁻² year⁻¹, to 2400 kWh m⁻² year⁻¹, one need only multiply the EPBT by 2400 and divide by 1700.

8.4 Results and Discussion

The module efficiency reported by manufacturers represents the initial efficiency of the module under STC. Environmental influences such as moisture penetration and temperature fluctuation result in module efficiency degradation over its lifetime.[358, 359] As a result, it is not accurate to use the initial efficiency when calculating EPBT and EROI. In the harmonization calculation, the average lifetime (30 years) efficiency values were used that were calculated based on a 0.5% per year degradation (Table 8.1). The same values have been used by Hsu, et al.[360] and Kim, et al.[361] on harmonization of greenhouse gas emissions from PV systems.

Table 8.1: Module efficiencies used for harmonization

Module Type	mono-Si	poly-Si	a:Si	CdTe	CIGS
Average Lifetime Efficiency (%)	13	12.3	6.3	10.9	11.5

8.4.1 Embedded Energy

The embedded energy data had a more than ten-fold variation with highest (13,428 MJ/m²) and lowest (894 MJ/m²) values reported for mono-Si and CdTe, respectively. The large variation in embedded energy observed here parallels the large variation in life cycle GHG emissions reported by Kim et al. [361] and Hsu et al.[360] A larger variation in the embedded energy of crystalline Si was observed than of thin film technologies (Figure 8-6). In general, the author would expect part of this variation to be due to improvements in PV technology that would reduce the embedded energy from improvements in existing processes, introduction of new processes and use of less material to make solar cells. This time-based improvement was evident in the statistically significant correlation ($p < 0.05$) between the embedded energy and publication date of all PV datasets as shown in Figure 8-7. Contrary to our expectations, PV types did not have a significant correlation between time and embedded energy. It is noted that the dataset used here is not large, and the statistical correlation (or lack thereof) should be interpreted within this context. In addition, it is also noted that the choice of units MJ/m² includes the efficiency of the module in the value reported for embedded energy since efficiency is used in converting MJ/kW_p to MJ/m² (see example calculation above). This would have strengthened the correlation between embedded energy and time if the efficiencies were

increasing with time. It can be seen that contrary to the observation from a larger dataset used here, Fthenakis et al. [383] used a smaller dataset (and use MJ/kW_p) but noted a drop in CdTe in embedded energy by more than 20% between 2005 and 2008.

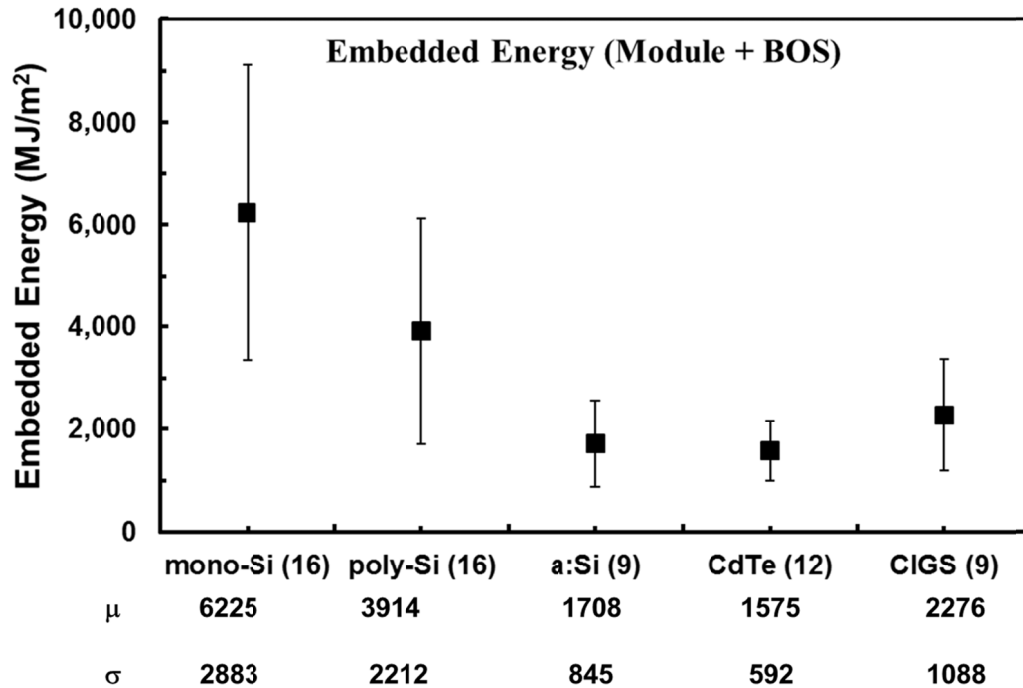


Figure 8-6 . Module and BOS mean (μ) and standard deviation (σ) of embedded primary energy with error bars representing one standard deviation. The number of values for each module type is indicated in parentheses.

In the mono-Si dataset, the large variation of the embedded energy is mainly due to the high values reported by Bizzari and Morini [377] (11,153 MJ/m²) and Garcia-Velverde et al.[379] (13,428 MJ/m²) and the low value (1708 MJ/m²) reported by Ito et al.[388] The same two references [377] (9,101 MJ/m²) and Ito et al.[388] (1008-1322 MJ/m²) also caused the large variation in the poly-Si dataset. Excluding these three references reduces the variation in

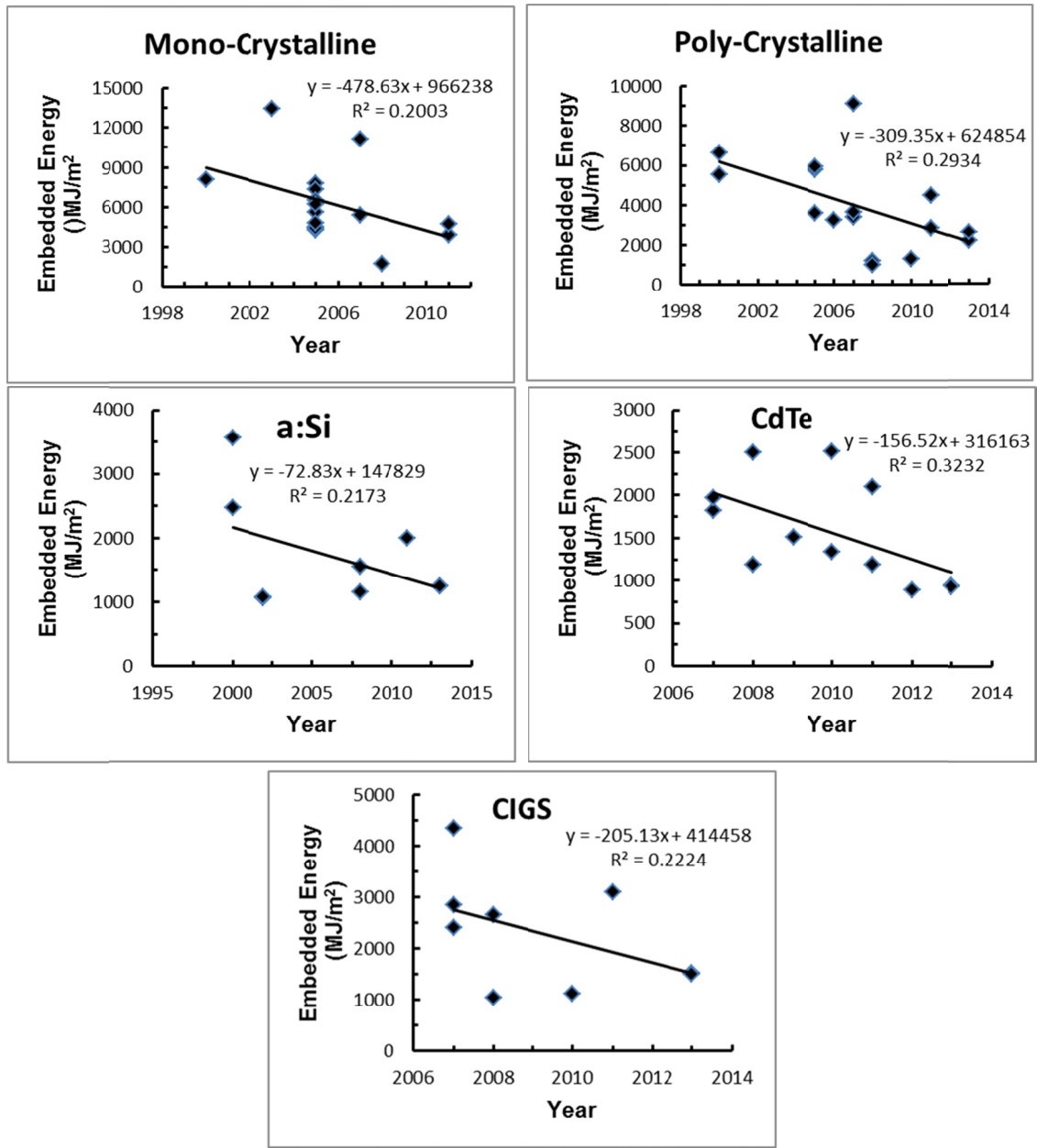


Figure 8-7. Correlation between the embedded energy and publication date of various PV types.

embedded energy to about two fold difference for mono-Si and three fold difference for poly-Si (to about 4000-8000 MJ/m² for mono-Si and 2200-6600 MJ/m² for poly-Si dataset). In general, the author would expect the large variation reported by different

studies to not be due to manufacturing energy differences among manufacturers since the competitive nature of the PV industry promotes a ‘race to the bottom’, which causes costs to be minimized. Since energy demand would correlate with costs of the PV module, there is indirectly a ‘race to the bottom’ on embedded energy as well. Irrespective of differences in different companies, there can still be some difference in embedded energy of a module manufactured by the same company but in different locations. For example, Fthenakis et al.[383] reported that that the embedded energy of a module manufactured in Frankfurt, Germany was about 10% lower than the same unit manufactured in Perrysburg, USA.

The inclusion of BOS in the analysis could explain some of the variation in the embedded energy shown in Figure 8-6 since BOS can contribute to a large portion of the total embedded energy. [389] The mean and standard deviations of the ground and roof BOS embedded energy are shown in Figure 8-8. The BOS embedded energy varied by almost 50 times with the lowest value (44 MJ/m^2) reported by Meijer and Kulchinski [390] for an unframed roof installation and the highest value (2300 MJ/m^2) reported by Alsema [368] for a framed ground installation. Ground-based system BOS requires more materials for mounting, and therefore the embedded energy was significantly higher than that of roof BOS only when data prior to year 2000 was included (t-test, $p < 0.05$). The BOS itself is often not well described in studies. For example, PV modules may or may not have a solar tracker, power functioning unit, or power optimizer (smart module) -- all of which would have affected the BOS embedded energy. These and other module-specific (e.g. thickness or specific manufacturing process) technology details should be

provided in future studies to better understand the variability of embedded energy across published data.

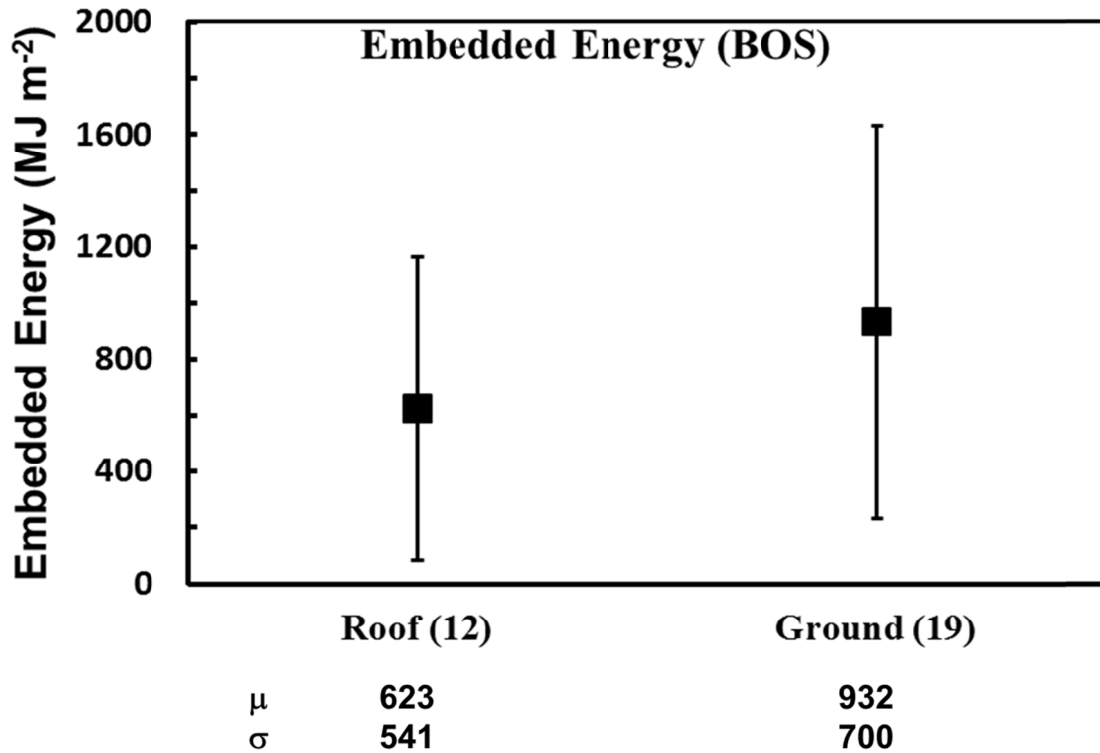


Figure 8-8. Mean embedded energy values reported by the collected references with error bars representing one standard deviation for the manufacturing of BOS. The number of scenarios included is shown in parentheses after the technology name. The BOS data were grouped by installation type and not by module type because some references stated different values for different module types while others reported the same value for every module type.

While choice of units (per m^2 versus per kW_p), geographical differences, and inclusion of BOS contributed to the variation of the embedded energy reported across studies, the primary reason that caused the observed variation in our dataset is the lack of transparency and the choice of data sources used by the different authors. The detailed

life cycle inventories were not reported in many of the studies included in our dataset. By nature, LCA models often use a mix of original data, published data, and calculations/interpretations derived from both. This can hold true even if a primary dataset for LCA is collected directly from the manufacturing facility. This aspect of LCA modeling applied to the PV LCA papers we reviewed as well, which is likely the primary cause of the variation in the dataset.

The mean values of embedded energy from the five different PV types were statistically different (ANOVA test, $p < 0.05$). The embedded energies of mono-Si and poly-Si were anticipated to be significantly higher than those of thin film due to the high energy requirements for producing solar-grade silicon [382] as well as the larger material requirements ($>100 \mu\text{m}$ absorber layer thickness for crystalline silicon versus $<5 \mu\text{m}$ for thin film technologies). However, post-hoc Tukey's test ($\alpha = 0.05$) confirmed this hypothesis only when studies published prior to year 2000 were included in the analysis. When only data published after 2000 is included the embedded energy values for poly-Si, a:Si, and CIGS were not significantly different from one another but were all significantly higher than that of CdTe (Tukey's test, $\alpha = 0.05$).

8.4.2 Energy Payback Time (EPBT)

Figure 8-9 and 8-10 demonstrate EPBT with respect to the PV module type and publication date from 2000 to 2013. The EPBT dataset contains fewer scenarios than the embedded energy dataset since it only includes the studies that report an EPBT value (verified by the author) within 10 % error. Across all technologies, the mean harmonized EPBT ranged from 1.0 to 4.1 years. From lowest to highest EPBT, the module types

ranked in the following order: CdTe, CIGS, a:Si, poly-Si, and mono-Si . This was the same order as the most recent data reported by De Wild-Scholten. [381] The ranking of the PV types was also similar to the order observed for embedded energy with one exception. In EPBT, a:Si was higher than CIGS; in embedded energy CIGS was higher than a:Si. The reason can be explained by analyzing the parameters used in calculating the EPBT. The only parameters that varied in the harmonized EPBT calculation were the embedded energy and the efficiency since performance ratio and insolation values were the same across different PV types. The efficiency of a:Si was only 55% of that of CIGS which caused the change in ranking of the EPBT.

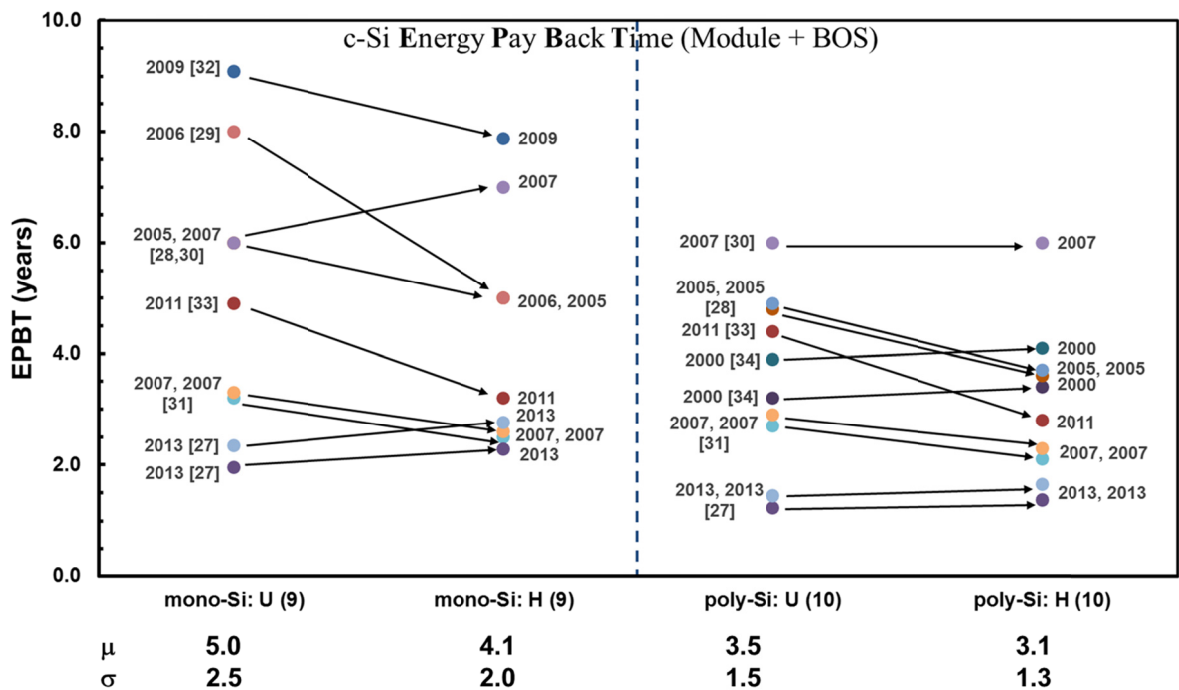


Figure 8-9. Unharmonized (U) and harmonized (H) EPBT for crystalline silicon solar cells. The number of scenarios included is shown in parentheses after the technology name. Mean (μ) and standard deviation (σ) are shown below the graph. Numbers in square brackets next to the data points indicate the reference for which this data comes from.

As a result of the harmonization, the ranges of EPBT for each technology narrowed and the mean shifted down. This shift was caused primarily by the change in the insolation value between the unharmonized and harmonized calculations. Table 8.2 provides the mean values of the unharmonized and harmonized parameters. Depending on the technology, the harmonized PR (0.75) was about 2.6% lower than the unharmonized PR values used in the studies. Such a small difference between the harmonized and unharmonized PR value does not have a large impact on the EPBT. Also, the change in the module efficiency ranged between a decrease of 8.7% and an increase of 9%. This would not account for the consistent decrease in EPBT since a lower module efficiency for harmonization would increase the EPBTs while a higher efficiency would decrease them. On the contrary, the insolation consistently increased, between 10% and 28%. The changes observed here are larger than those among the PR values and they would always contribute to lowering the EPBT, unlike the efficiency. In some cases, such as for CdTe, the change in module efficiency and the change in insolation worked together to decrease the EPBT while in others, such as mono-Si, they worked against each other (see Table 8.2). However, the insolation generally had the greater impact and is the primary reason for the reduction in the mean EPBT. Table 8.3 displays the variation of mean harmonized EPBT with respect to insolation by keeping other parameters constant. In this example, five different insolation values (in units of $\text{kWh m}^{-2} \text{ year}^{-1}$) -- 1700 (global average), 1800 (US average), 1824 (Los Angeles, CA), 1436 (Trenton Mercer County, NJ) and 2032 (Las Vegas, NV) -- were considered. These locations were chosen because they were in the top three states in solar installation in 2010.[391] It is clear from Table 8.1 that increasing solar insolation decreases the EPBT

for all type of PV systems. This result is similar to the findings of Hsu et al.[360] who attributed the reduction in the median of the harmonized life cycle emissions to insolation and module lifetime.

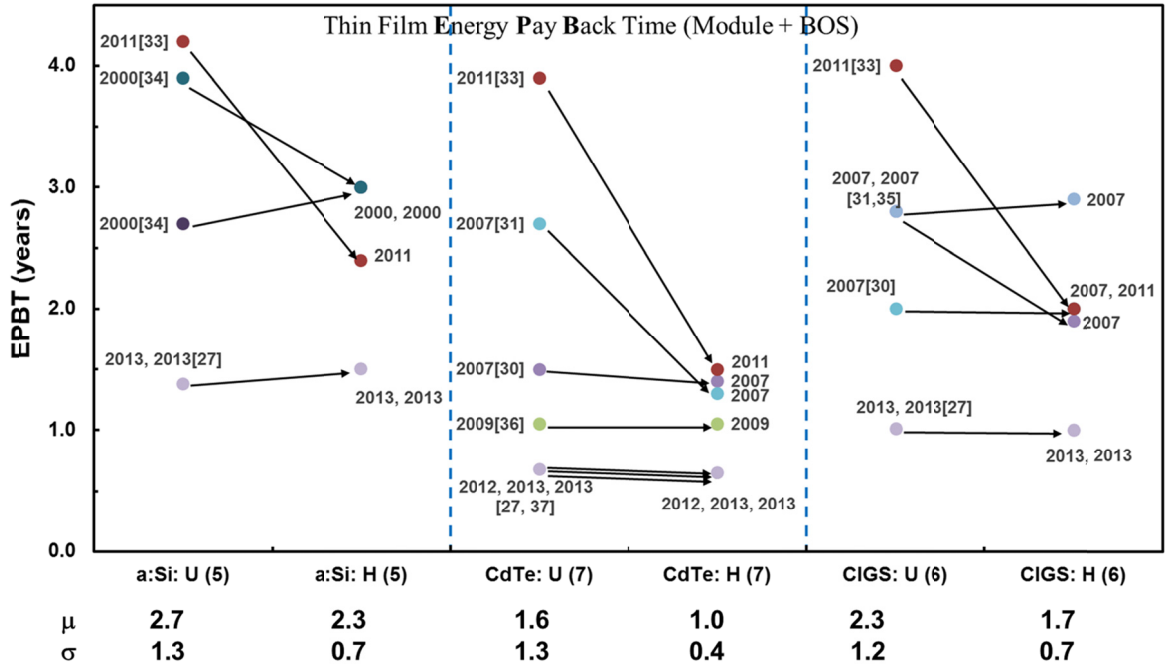


Figure 8-10. Unharmonized (U) and harmonized (H) EPBT for thin film solar cells. The number of scenarios included is shown in parentheses after the technology name. Mean (μ) and standard deviation (σ) are shown on the bottom. Numbers in brackets next to the data points indicate the reference for which this data comes from.

Future EPBT values will depend on the improvements in embedded energy, efficiency and performance ratio. Performance ratios have reached to the range of 75 % to 85 %. There is room for improvement for only ~10 % more. The embedded energy data did not show significant correlations with time (year of publication) except for poly-Si PV. However, the embedded energy of the most recent data from de Wild-Scholten [381] were much lower than the mean embedded energy of the other studies resulting in

the 2013 harmonized EPBT data to be 1.5 to 3 times lower (1.8 for mono-Si, 2.9 for poly-Si, 1.5 for a:Si, 1.5 for CdTe, 1.7 for CIGS) than the mean harmonized EPBT of the entire EPBT dataset. A theoretical embedded energy for PV has not yet been established. However, the global learning curve for PV suggests a 22 % price reduction for each doubling of cumulative volume since 1979.[392] Since price and embedded energy would be expected to be correlated, the future reductions in embedded energy would depend on the cumulative PV installation volume.

Table 8.2: Mean unharmonized (U) and harmonized (H) parameters for each photovoltaic technology with the percentage difference.

Parameter	Module Efficiency (%)		Performance Ratio		Insolation (kWh m ⁻² year ⁻¹)		Lifetime (years)	
	U (H)	% Diff	U (H)	% Diff	U (H)	% Diff	U (H)	% Diff
mono-Si	14.2 (13)	-8.4%	0.75 (0.75)	0%	1328 (1700)	28%	28.9 (30)	3.8%
poly-Si	13.3 (12.3)	-7.5%	0.77 (0.75)	-2.6%	1372 (1700)	24%	29.5 (30)	1.7%
a:Si	6.9 (6.3)	-8.7%	0.76 (0.75)	-1.3%	1550 (1700)	10%	30 (30)	0%
CdTe	10.0 (10.9)	9.0%	0.77 (0.75)	-2.6%	1525 (1700)	11%	28.3 (30)	6.0%
CIGS	11 (11.5)	4.5%	0.77 (0.75)	-2.6%	1450 (1700)	17%	26.7 (30)	12.4%

An analysis of the efficiency data is presented in Figure 8-11. There was a large amount of scatter among published efficiency values. The efficiency data among the screened studies show a significant correlation ($p < 0.05$) with publication date for mono-

Si and poly-Si only when studies before 2000 are included. Actual and expected efficiencies reported by de Wild-Scholten are also plotted in Figure 8-11. These show a clear increasing trend. The mean efficiencies from this study and from De Wild-Scholten [381] were 1.4-1.9 times lower than the current best lab efficiencies [393] and 2.2 to 3.4 times lower than the theoretical maximum efficiencies. [394] There is therefore about 1.5 to 3.5 times more room for efficiency improvement, which would further lower the EPBT of PV technology.

Table 8.3: Mean harmonized EPBT and EROI for Multiple Insolation values.

Mono-Si	World Average	US Average	Los Angeles	New Jersey	Nevada
Insolation (kWh m ⁻² yr ⁻¹)	1700	1800	1824	1436	2032
Mean EPBT (years)	4.11	3.88	4.05	5.22	2.90
Mean EROI	8.73	8.2	9.1	11.2	4.9
Poly-Si					
Insolation (kWh m ⁻² yr ⁻¹)	1700	1800	1824	1436	2032
Mean EPBT (years)	3.06	2.89	3.02	3.89	2.16
Mean EROI	11.62	11.0	12.1	15.0	6.5
a:Si					
Insolation (kWh m ⁻² yr ⁻¹)	1700	1800	1824	1436	2032
Mean EPBT (years)	2.28	2.16	2.25	2.90	1.61
Mean EROI	14.45	13.6	15.1	18.6	8.0
CdTe					
Insolation (kWh m ⁻² yr ⁻¹)	1700	1800	1824	1436	2032
Mean EPBT (years)	1.02	0.96	1.00	1.29	0.72
Mean EROI	34.18	32.3	35.7	44.0	19.0
CIGS					
Insolation (kWh m ⁻² yr ⁻¹)	1700	1800	1824	1436	2032
Mean EPBT (years)	1.73	1.64	1.71	2.20	1.23
Mean EROI	19.94	18.8	20.8	25.7	11.1

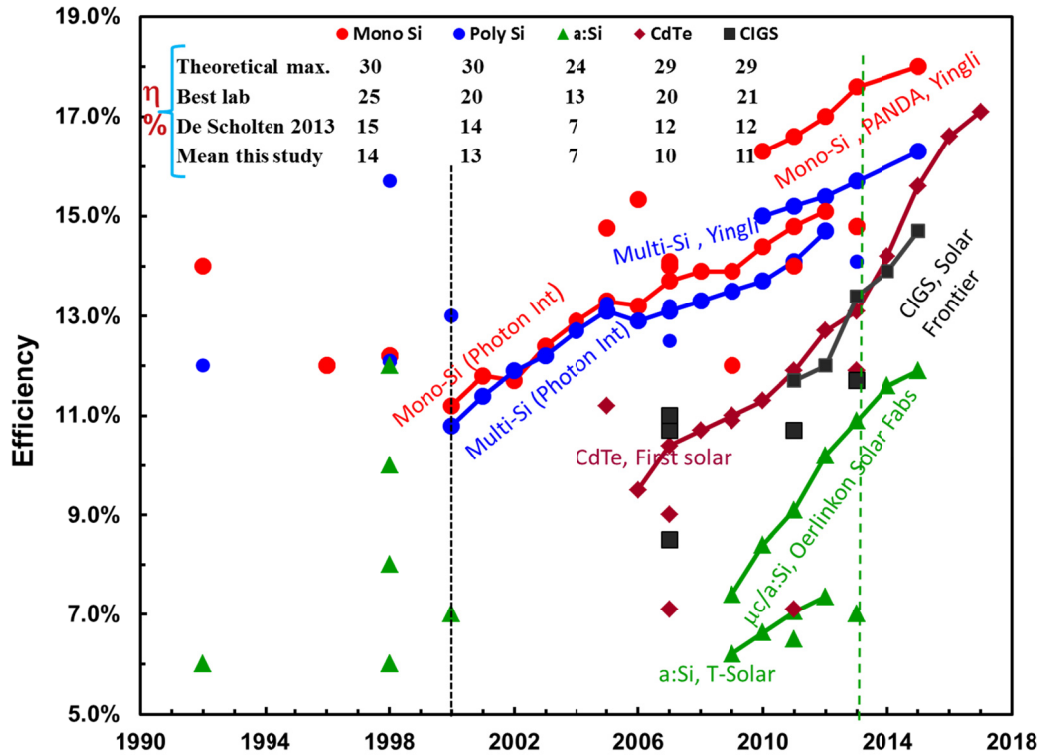


Figure 8-11. Efficiency values from the studies that passed all screening as well as the ones that did not pass the year 2000 cutoff criteria (the modernity criterion). A vertical line (black) placed in year 2000 is used to indicate that data to the right of this line is considered ‘modern’ and passed our screening. Most recent data published by de Wild-Scholten is shown as solid lines. [381] The vertical line (green) at 2013 separates the actual achieved and expected (predicted) efficiencies from PV power plants. [381] Best lab efficiencies were obtained from NREL.[393] Graph shows theoretical max. efficiencies [394] and mean efficiencies from this study (also shown in table 8.2) are calculated from the EPBT dataset (years 2000-2013).

Embedded energy and efficiency will determine which PV technology achieves the best EPBT in the future. Across different types of PV, the variation in embedded energy is greater than the variation in efficiency. Among the screened studies, the embedded energy varied over more than a factor of ten. In the recent data from de Wild-

Scholten [381], the embedded energy varied more than a factor of four among different types of technologies. In contrast, the mean conversion efficiencies varied by a factor of two across different types of PV and the theoretical maximum conversion efficiencies for all five PV types are similar. Among different types of technologies, the differences in embedded energy are greater than the differences in efficiency (and theoretical maximum efficiency). The implication of this finding is that, until the differences in embedded energy among different types of PV are significantly reduced, any increases in module efficiency will not play a dominant role in determining EPBT. The relative ranking of the EPBT of different PV technologies depends primarily on their embedded energy and not their conversion efficiency.

8.4.3 Energy Return on Energy Invested (EROI)

The mean harmonized EROI varied from 8.7 to 34.2 and the EROI of the different technologies ranked in the reverse order as was observed for EPBT (Figure 8-12). This is due to EROI being calculated by dividing the lifetime by the embedded energy. As embedded energy and corresponding EPBT increases, the EROI decreases. Because EPBT and EROI are interrelated, EROI also depends strongly on insolation as shown in Table 8.3. The higher the insolation, higher will be the EROI.

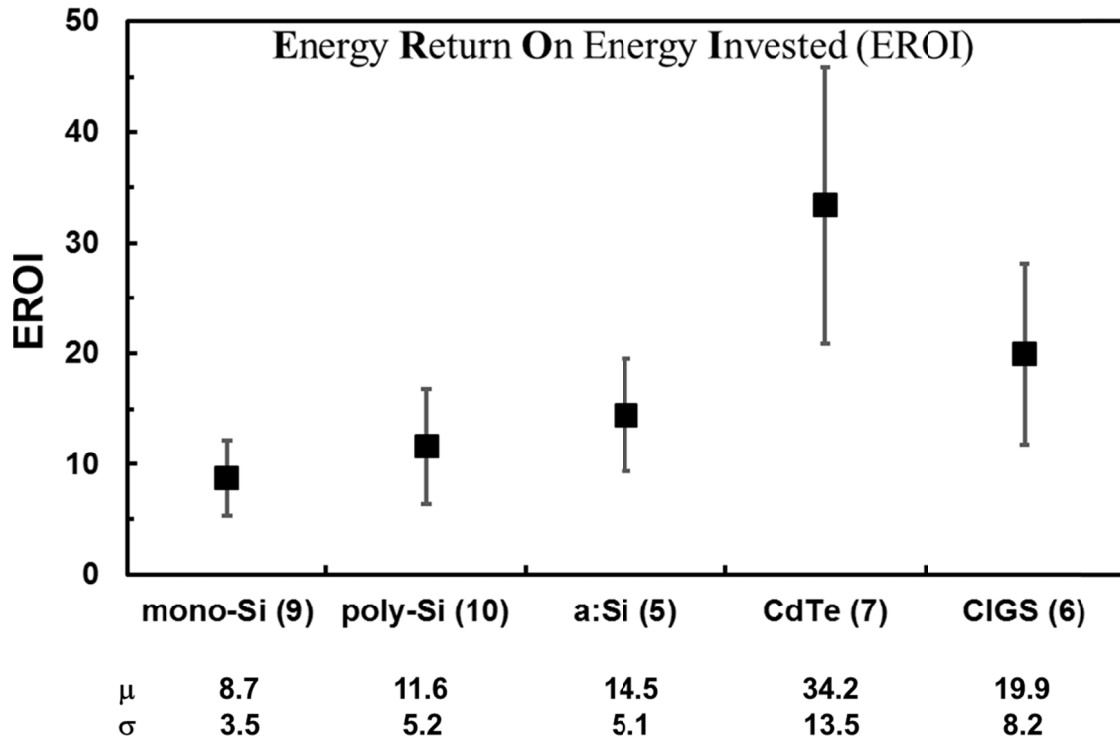


Figure 8-12. Mean harmonized EROI with error bars representing standard deviation. The number of values for each module type is included in parentheses. Mean (μ) and standard deviation (σ) are shown at the bottom of the graph.

Raugeti et al.[395] discussed the intricacies in comparing PV EROI to the EROI from fossil fuel sources and noted that the meaningful comparison would be to compare the PV EROI calculated from Equation (8.2) to the EROI of fuel which is calculated as the ratio of energy in a given amount of the extracted and delivered fuel to the total primary energy used in the supply chain including the construction of the power plants. Based on this calculation, Raugei estimated the EROI of mono Si and Poly Si PV as about 20 and of CdTe as about 40. The mean values estimated in this study were lower than Raugei’s estimate. Similarly, Raugei estimated the maximum oil and coal EROI as 30 and 80, respectively. Based on the efficiency and embedded energy improvement

potentials discussed in this paper, it is likely for PV technology to catch up to the maximum EROI from coal in the future.

8.5 Conclusions

A systematic review and meta-analysis of embedded energy, energy payback time and energy return on energy invested were conducted for the crystalline silicon and thin film photovoltaic systems. Out of 232 references collected, 7 (11) papers on mono-Si, 6 (11) on poly-Si, 3 (7) on a:Si, 6 (11) on CdTe, and 5 (8) on CIGS passed our screening for EPBT (embedded energy). Photovoltaic module parameters such as performance ratio, system lifetime, module efficiency and insolation were harmonized to calculate the less disturbed EPBT/EROI values, and these values were compared with values before harmonization. Our study showed that the embedded energy reported in the literature varies greatly with a minimum of 894 MJ/m² for thin film to 13,428 MJ/m² for mono-crystalline silicon. The author expected newer studies to report lower embedded energy. However, statistical correlation between publication time and embedded energy was found only for the poly-Si dataset. Other PV technologies did not have a significant correlation likely because of the small sample population of the dataset and the variations in geographical location, BOS energy, and LCA data sources across included studies. Here, the unit MJ/m² was considered for the embedded energy analysis since this set of units has been more commonly used in more recent papers. It is noted that for comparing different studies, kW_p based units instead of m² based units (e.g. MJ/kW_p instead of MJ/m²) would be more appropriate since efficiency is incorporated into the embedded energy in the area based (MJ/m²) unit.

The harmonization narrowed the range of the published EPBT values. The mean harmonized EPBT varied from 1.0 to 4.1 years; from lowest to highest, the module types ranked in the following order: cadmium telluride (CdTe), copper indium gallium diselenide (CIGS), amorphous silicon (a:Si), poly-crystalline silicon (poly-Si), and mono-crystalline silicon (mono-Si). The mean harmonized EROI varied from 8.7 to 34.2. Among different types of PV, the variation in embedded energy was greater than the variation in efficiency and performance ratio suggesting that the relative ranking of the EPBT of different PV technology today and in the future depends primarily on their embedded energy and not their efficiency.

Chapter 9

Conclusion and future work

9.1 Conclusions

The properties of nanostructured semiconducting nanomaterials differ significantly from those of the bulk materials. Semiconducting nanocrystal size and shape can be controlled, depending on the nature and type of the semiconductors, by the type and amount of chemicals used in synthesis and by the methods of synthesis. For example, the size of the FeS₂ nanocubes the author synthesizes here typically ranges from 50 nm to 150 nm. Synthesis was done using thermal injection method using trioctylphosphine oxide as a surfactant, Iron (II) bromide as iron precursor, elemental sulfur as sulfur source, and oleylamine as non-coordinating solvent. On the other hand, PbS quantum dots synthesized for this thesis are significantly smaller, with diameters from ~2 nm to ~5 nm. The synthesis method was similar to that used to prepare FeS₂, but for PbS QDs, oleic acid was used as surfactant, PbO as Pb precursor TMS as S precursor and octadecene as non-coordinating solvent. The shape of these nanocrystals depends on their crystal structure and amount of surfactant used and nucleation and growth rate

during synthesis. Rock salt PbS QDs in this size range are typically spherical in shape whereas FeS₂ NCs possess cubical shape. Spherical QDs have the smallest number of total surface atoms and are thermodynamically the most stable. These are called equilibrium nanocrystals with minimum surface area. Equilibrium nanocrystals are obtained when the growth rate is small and uniform in all directions. At higher growth rate an astonishing variety of highly anisotropic shapes are obtained such as rods, and disks etc.

The size of the nanocrystals and their bulk exciton Bohr radius determine possible quantum confinement effect in the nanocrystals. In PbS QDs, the quantum confinement effect plays a substantial role in determining the optoelectronic properties because the achievable diameters of the QD samples is much smaller than the exciton Bohr radius ($r_{ex} = 18 \text{ nm}$ [396]), whereas in FeS₂ NCs (the exciton Bohr radius for FeS₂ pyrite is $r_{ex} = 1.3 \text{ nm}$ [397]) the nanocube size (length of each side of a cube) is dramatically larger than r_{ex} and hence the quantum confinement effect does not influence the effective bandgap. In quantum confined QDs, the energy levels are modeled to first order using a particle in a box model in which the energy of different states depends on the length of the box. Quantum dots are considered strongly confined if the nanocrystal radii are smaller than the Bohr exciton radius. Nanocrystals with dimensions smaller than r_{ex} demonstrate strongly size-dependent absorption and fluorescence spectra with discrete electronic transitions which are somewhat atomic-like.

Lead sulfide has the rock salt crystal structure where the space lattice is face-centered cubic, with a basis of one Pb⁺⁺ ion and one S⁻ ion associated with each lattice

point. Iron pyrite, which is Earth's most abundant sulfur mineral, holds face centered cubic crystal structure where each Fe atom is surrounded by 6 S atoms and each S atom is coordinated with 1 neighboring S atom and 3 neighboring Fe atoms.

In chapter 3, the dependence of PbS quantum dot (QD) solar cell performance on the QD bandgap energy, window layer materials and their thicknesses, and light-soaking effects were studied. Our best device, based on a ZnO/PbS-QD heterojunction design, demonstrates V_{OC} of 0.6 V, J_{SC} of 15.6 mA cm^{-2} , FF of 44% and photovoltaic conversion efficiency of 4.1%. The current vs. voltage characteristics of these devices show a QD size (bandgap) dependent behavior. Light soaking studies show improvement in the performance of Schottky junction and heterojunction devices. The light-soaking-induced enhancement is greatest in heterojunction devices, and reverses upon termination of light soaking. Preliminary assessment indicates that light soaking improves the QD-QD interfaces through photochemical passivation.

In chapter 4, heterojunction PbS quantum dot (QD) solar cells using CdS as the n-type window layer were studied. These solar cells generate large open circuit voltage, higher than the case when ZnO was used as window layer for similar QD diameter. The open circuit voltage obtained from these devices was as high as 0.65 V, attaining short circuit current up to 12 mA-cm^{-2} , and efficiencies reaching 3.3%. Our investigations of this device design show an optimized CdS film thickness of 70 nm and an optimized PbS QD diameter of $\sim 2.5 \text{ nm}$, corresponding to a bandgap energy of $\sim 1.56 \text{ eV}$.

Chapter 5 describes the synthesis and characterization of stable, phase pure and highly crystalline cubic iron pyrite (FeS_2) cube-shaped nanocrystals with size varying from ~ 50 to 150 nm. Synthesis was performed using a solution-based hot injection

method. In the synthesis process, iron (II) bromide was for the first time used as an iron precursor, elemental sulfur as a sulfur source, trioctylphosphine oxide (TOPO) and 1,2-hexanediol as capping ligands and oleylamine as non-coordinating solvent. In the film fabrication process, hydrazine was used to remove long chain hydrocarbon molecules from the surface of the NCs and sintered the NC films at 500⁰C – 550⁰C for various time periods to make pinhole free NC films. From four point probe and Hall measurements, the author found that the pyrite films are highly conductive and not suitable for the solar cell applications. Carrier concentration of FeS₂ NC, hydrazine treated but unsintered, was of the order of 10¹⁹ cm⁻³ and resistivity was 100 Ω cm respectively.

Demonstration and development of nanocrystalline FeS₂ thin films as the back contact for CdTe solar cells was shown in chapter 6. The FeS₂ NC layer is prepared from solution directly onto the CdCl₂-treated CdTe surface using drop-casting and hydrazine treatment at ambient temperature and pressure, in a process that requires no thermal treatment. Solar cells prepared by applying the NC FeS₂ back contact onto CdTe, without the typical introduction of Cu within the back-contact, yield efficiencies reaching ~95% that of the standard Cu/Au back contact devices. The FeS₂ back contact solar cells show very little degradation under initial thermal stress (at open circuit, though nominally unilluminated). Although the Cu/Au back contact shows poor long-term stability, owing to its simplicity and repeatability, it has been used as a standard back contact for CdTe devices in which Cu incorporation facilitates hole transfer at the back contact. In this dissertation, Cu has been replaced with a layer of nanocrystalline FeS₂. The author has also tested the use of an FeS₂ NC layer while still including the usual Cu treatment. In this case, a layer of FeS₂ is deposited onto the Cu-annealed CdTe device, and the device

is then finished by evaporating the Au layer. From this, the improvement in the device performance was clearly visible. Using VAT-deposited devices, we obtained V_{OC} as high as 0.842 V, J_{SC} up to 22 mA cm^{-2} , and FF as high as 77%; the optimum device efficiency exceeded 14%.

Chapter 7 is devoted to PV materials and interface studies based on photoelectron spectroscopy and Kelvin probe measurements. Photoelectron spectroscopy was used to measure the energy discontinuity in the valence band (ΔE_v) of CdS/PbS QD heterostructures in which the PbS QDs was grown using solution based layer-by-layer (LbL) dip coating method on top of rf magnetron sputtered CdS. Ultraviolet photoelectron spectroscopy was used to find the top of the valence band with respect to the Fermi level, and x-ray photoelectron spectroscopy was used to find the core level binding energies of Cd 3d and Pb4f core level positions. Using these two types of information, a value of valence band offset at the interface between two heterojunctions, $\Delta E_v = 1.73 \text{ eV}$ was obtained. Given the band gap energies of CdS and PbS QD, a conduction band offset ΔE_c was determined to be 0.71 eV. Photoelectron spectroscopy was also used to find the work function of thin films of Au, CdS and PbS. The work function values of these materials were also determined using Kelvin Probe measurement.

In chapter 8 a review of life cycle assessment of photovoltaic (PV) system is provided. In this review crystalline silicon (monocrystalline silicon and polycrystalline silicon) PV and thin film (CdTe, CIGS and a:Si) PV are included. The data used in the analysis are from 2000 to 2013. Meta-analysis of the literature data on embedded energy, EPBT and EROI of PV systems to produce more accurate evaluations and comparisons

of the energy performance of different types of PV systems are included. In this study, harmonization of the EPBT and EROI metrics are provided including the analysis of the embedded energy metric.

9.2 Future work

There are numerous interesting future research topics the author has in mind, some of which have already begun and for which continuation of the work is expected. These future works are summarized point-wise as following.

9.2.1 Electron injection from colloidal PbS QDs into sputtered CdS thin films

Size tunable band gap of PbS QDS allows selection of QDs that optimize the energy level alignment with various n-type materials such as ZnO, TiO₂. Here, the author has begun a study of electron transport from colloidal QDs (caped with organic ligand with short C-H bonds, 1,2 ethandithiol) films to CdS film. This work is motivated by the potential of the lead-salt QDs for bulk CdS solar cells. Figure 9-1 shows energy levels (valence band and conduction band) of various sizes PbS QDs and bulk CdS. According to Figure 9-1, efficient charge transfer from PbS QDs to bulk CdS film is possible only if the size of the QDs is smaller than 4.6 nm. Injection of photoexcited electrons from colloidal PbS QDs into TiO₂ nanoparticles has been investigated.[47] However, similar work for the heterostructure of PbSQD/CdS interface has not been seen yet. .

This study was begun by taking two different diameters PbS QDs: one 4.7 nm for which electron transfer is not expected and another about 3 nm from which electron transfer is expected. Two QDs films were made from each size QDs using layer by layer

(LbL) dip coating method onto glass and CdS film as substrates. Thickness of CdS film deposited by sputtering method on glass substrate was about 35 nm. Transmission and reflection percentages of these films were measured using UV/VIS/NIR Spectrophotometer and absorbance (A) was calculated using these results.

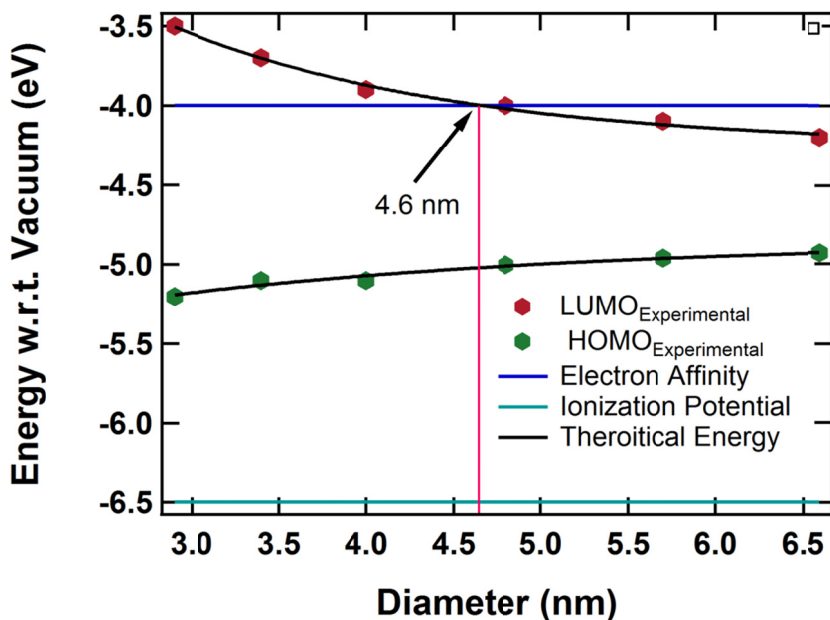


Figure 9-1. Valence and conduction band levels of various sizes of PbS QDs and CdS films with respect to vacuum level. Horizontal lines are energy levels of bulk CdS film and curved lines for PbS QDs. [47]

The optical absorbance spectra of the QD-CdS composite film are essentially identical to that of the QDs film alone as shown in Figure 9-2. Absorption decreases slightly for QD-CdS composite films from about 500 nm to 1500 nm. In higher energy region composite film has higher absorption. The first exciton absorption peaks in both cases are located at the same place.

Steady state photoluminescence (PL) measurement of these films offers the possibility to understand the charge separation and electron transport of photoexcited

carriers from PbS QD film to CdS film. If electron transport is poor, emission quenching from Pbs QD-CdS composite film is negligible. Steady state PL has not been performed yet and this is considered as one of the future works to accomplish this study.

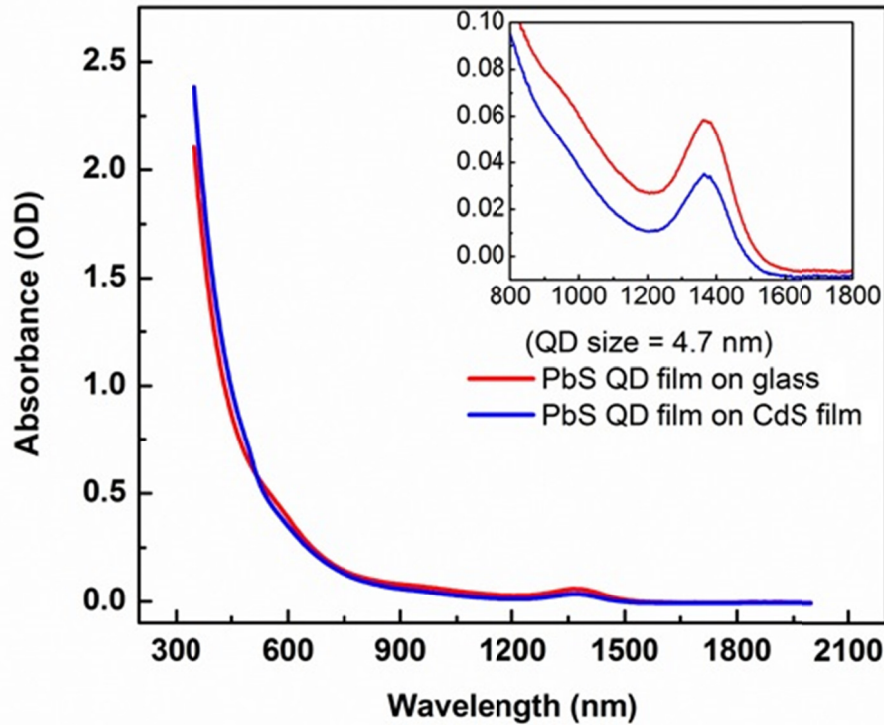


Figure 9-2. The absorbance spectra of PbS QDs (solid green lines), with diameter of 4.7 nm, and the PbS QD-CdS composite (solid blue lines).

Another experimental topic to address is the time resolved photoluminescence (TRPL) study to monitor the dynamics of the electron population in the QDs. To accomplish this, a comparative study of the fluorescence of larger and smaller than 4.6 nm PbS QD films with and without CdS films can be performed. From the larger size dot, fluorescence decay of the QD-CdS composite is expected to be identical to that of the QD film alone. If the type of decay and fluorescence lifetime of QD-CdS composite and QD alone films are identical, that indicates that there is no or negligible charge transfer from

the QD film to the CdS film. From the QD film with QD diameter less than 4.6 nm coupled to CdS film, it would be expected to observe evidence of charge transfer. The fluorescence decay of the composite should be much faster than non-composite film.

The absorption spectra of 2.9 nm diameter PbS QD film and PbS QD-CdS composite film are shown in Figure 9-3. Absorption spectra almost match each other. That means that the composite film absorbs very well. Theoretically the emission peak must be quenched dramatically for the composite film. Fluorescence quenching would be the signature of electron injection from smaller dots into CdS film. These studies will be performed in future to establish the charge transfer phenomenon from PbS-QD film to the CdS film.

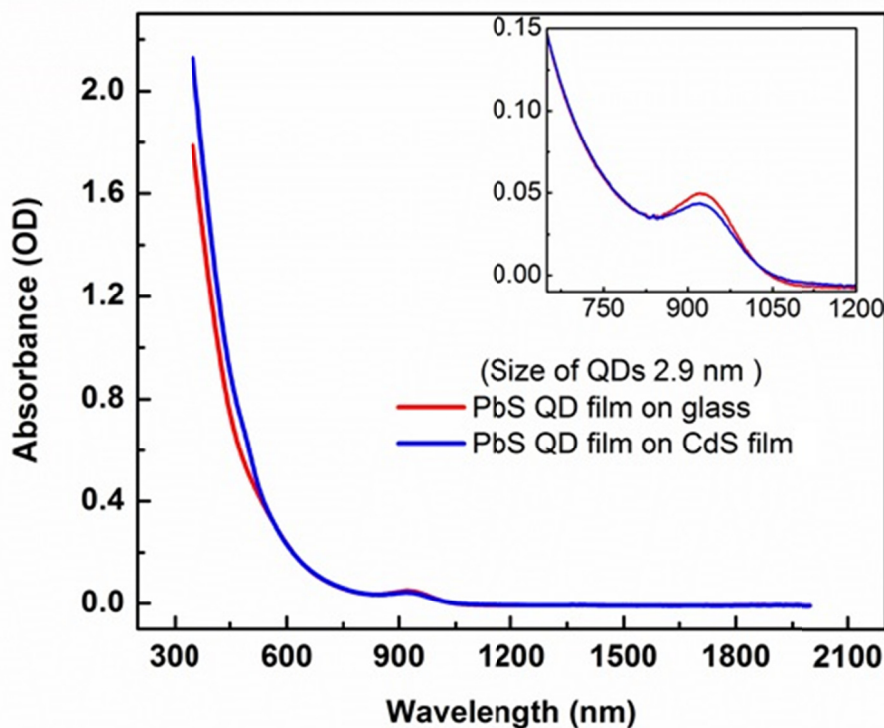


Figure 9-3. The absorbance spectra of PbS QDs (solid green lines), with diameter of 3.0 nm, film and the PbS QD-CdS composite film (solid blue lines).

9.2.2 Doping of PbS QDs using metal impurities

Colloidal semiconductor quantum dots (QDs) possess size dependent optical and electronic properties. Fabrication of competitive solid state devices from solution-processed colloidal quantum dots remains challenging. In QDs, transport of charge carriers is dominated by the inter-particle medium. During the synthesis, surface ligands stabilize the colloidal quantum dots, mediating growth and preventing aggregation. These surface ligands are hydrocarbon organic molecules with long hydrocarbon chains [119, 398]. These molecules create highly insulating barriers around each QD. Thus, the promise of these quantum dots as technological material, for applications like wavelength tunable lasers [399], bio-imaging [400] and solar cells [14, 105], may ultimately depend on altering their behavior through doping. Impurities can strongly modify electronic, optical and magnetic properties of bulk and QD semiconductors. However, impurity doping in such colloidal QDs is remains challenging [401, 402]. QDs undergo 'self purification' meaning that impurity solubility is much lower in the bulk [403]. QDs are hard to dope for thermodynamic reasons because impurities are generally efficiently expelled to the surface.

One of the routes of doping semiconductor nanoparticles is thorough the use of carrier-donating binding ligands on the nanoparticle surface or electrochemical carrier injection.[404, 405] Magnetically active Mn atoms act as substitution doping impurities for many NCs. [401, 406, 407] Transition metal ions such as Cu, Ag and Au have shown promising expectation for permanent incorporation of charges into the NCs. [238, 402, 408, 409] Here, the author present preliminary work of doping of lead sulfide (PbS) QDs of various sizes using transition metal atoms Cu and Ag. This doping method is a slightly

modified version of Mocatta et al., who successfully implemented it for the doping of InAs NCs[238]. Doping method is a simple and can be conducted at room temperature.

To dope the QDs by silver, 10 mg of silver salt (AgNO_3), 80 mg of dodecylamine (DDA), and 120 mg (149 μL) of didodecyldimethylammonium bromide (DDAB) were dissolved in 10 mL of toluene. The dissolved salt solution was added drop by drop into the stirred 2 mL solution of PbS QDs in toluene. After about 10 -15 minutes, the mixture of two solutions was centrifuged for about 15 -20 minutes by adding certain amount of acetone. For precipitation, ethanol (EtOH) or methanol (MeOH) can also be used. The decanted solution was removed and the sediment was dispersed again in hexane. A similar procedure was performed for copper-doping, with the only difference that the AgNO_3 was replaced by same amount of CuCl_2 . For a typical case, the concentration of the QD solution was ~ 30 mg/mL. A few minutes of ultrasonication or/and heating ($<100^\circ\text{C}$) was required to dissolve the metal salts into the toluene.

In the doping process, the author believes that Cu and Ag atoms diffused into the QDs in solution. To accomplish this process, the QD solution and the metal salt solution are both prepared in toluene; the two solutions are mixed by adding the metal; salt solution drop-wide into the stirred QD solution. In Figure 9-4, absorbance and photoluminescence (PL) spectra are plotted with respect to wavelength in nm. For Figure 9-4(a), three samples were prepared: the first from silver doped QDs, the second from the QDs treated with DDA and DDAB but not silver and the third one from the as-synthesized QDs. The second and third cases were used to understand the contributions of metal in the results and which is clear from Figure 9-4(a). Differences in the first

exciton peak positions between the second and the third cases is only ~ 4 nm and which can be due to the difference in concentration of the QDs. The red shift of the doped QDs is 34 nm. Red shift is also obtained in their photoluminescence spectra as shown in Figure 9-4(b). The red shifts in the first exciton peaks and PL peaks in two cases in 9-4(b) are 37 and 27 nm respectively.

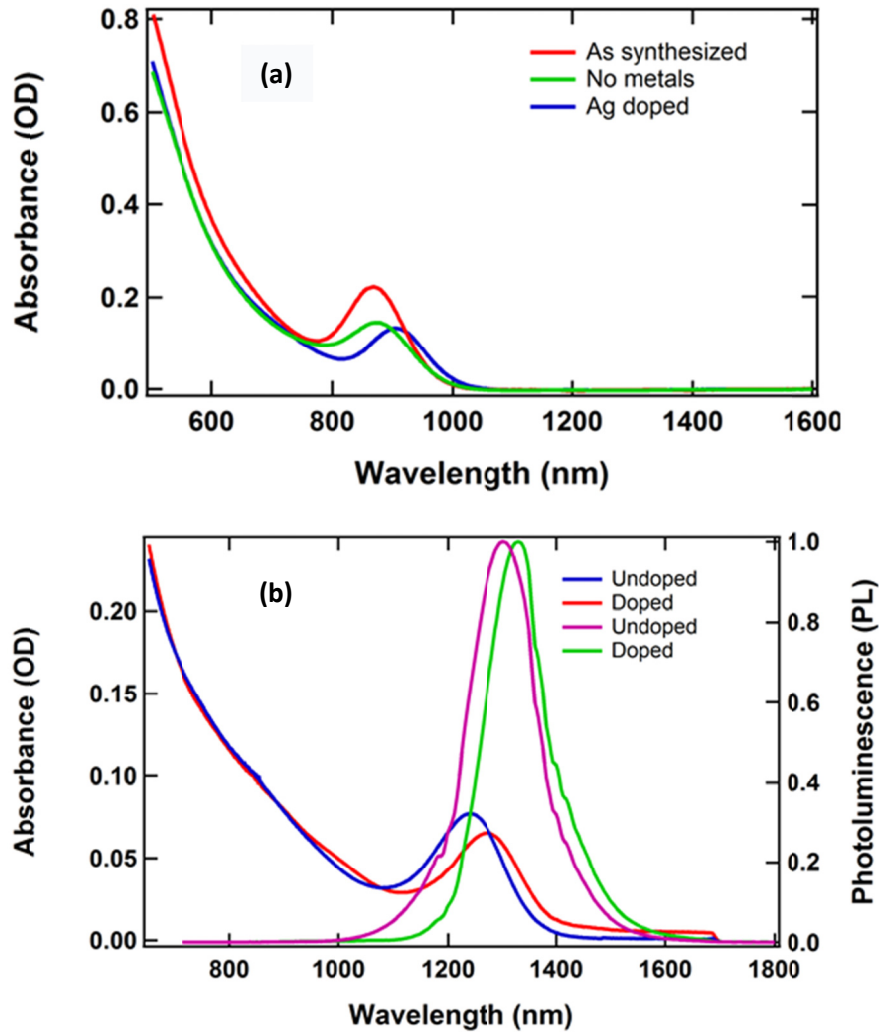


Figure 9-4. (a) Absorbance spectra of silver doped and undoped PbS QDs of first exciton peak at ~ 870 nm, (b) absorbance and photoluminescence spectra of silver doped and undoped PbS QDs of first excitation peak at ~ 1238 nm.

Ag atom replaces Pb atom because ionic radius of Ag is 128 pm and cannot sit at the interstitial site and makes more p type: deficiency of electrons. When an atom (Ag) replaces another compositional atom (Pb), this is referred to as substitutional doping. Since the ionic radius of Cu is 91 pm, they can enter and reside at an interstitial site yielding a surplus of electrons giving n-type behavior. PbS is a p-type semiconductor. At certain doping levels, the acceptor states merge with the valence band and form a valence band tail extending into the energy gap. Similarly, when the electron concentration increases, electron states appear immediately below the conduction band. At certain doping levels, these electron states merge with the conduction band and form conduction band tail reaching into the energy gap.[410] In either case, the Fermi level moves from within the gap into either the valence or conduction band. For p-type doping, absorption and emission are red shifted and for n-type doping, the absorption is blue shifted and emission is red shifted.[238] The first exciton peak and PL peaks of the copper doped PbS QDs are blue shifted as in Figure 9-5. The blue shift in the exciton peaks is 28 nm and PL peaks is 29 nm respectively. The first exciton peak of these dots was at 870 nm.

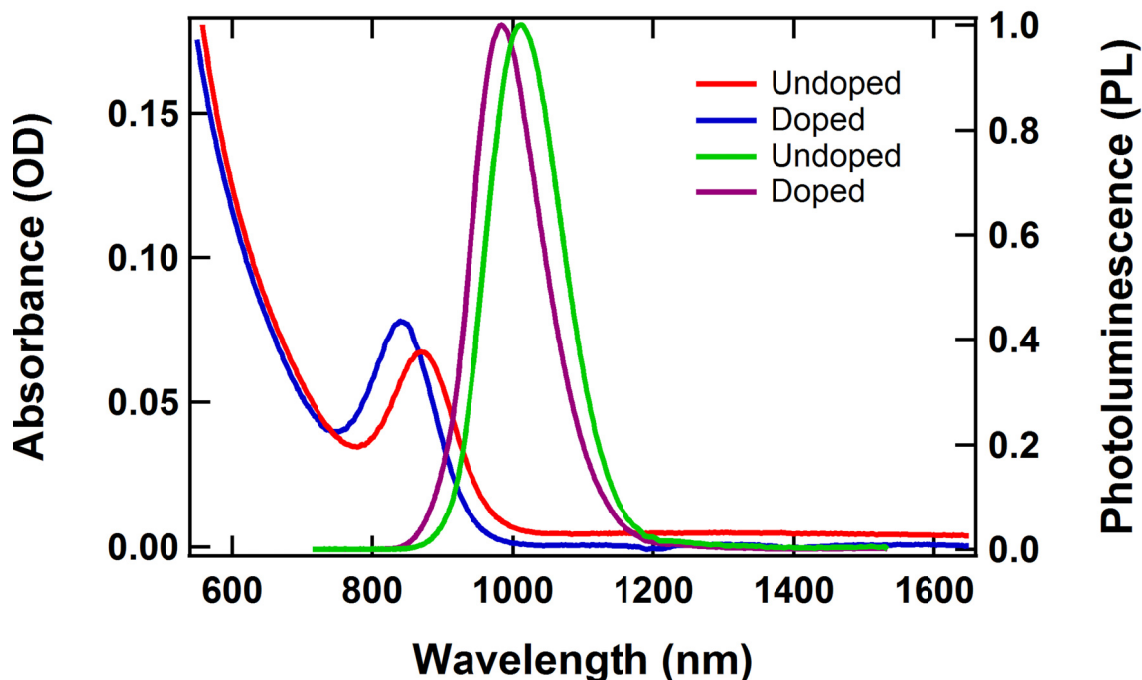


Figure 9-5. Absorbance spectra of doped (copper) and undoped PbS 870 size QDs.

Energy dispersive X-ray Spectroscopy (EDS) is used to identify the elemental composition of a sample or small area of interest on the sample. During EDS, a sample is exposed to an electron beam inside the scanning (transmission) electron microscopy (S(T)EM). These electrons collide with the electrons within the sample causing some of them to be knocked out of their orbitals. The vacated positions are filled by higher energy electrons which emit x-rays in the process. By analyzing the emitted x-rays, the elemental composition of the sample can be determined. Both qualitative and quantitative analysis are made from the spectra obtained from EDS. Qualitative analysis involves the identification of the lines in the spectrum and quantitative analysis (determination of the concentrations of the elements present) entails measuring line intensities for each element in the sample and for the same elements in calibration standard of known composition.

Figure 9-6 provides corresponding EDS spectra. To accomplish EDS study, three samples (PbS QD films) were prepared: one from silver (Ag) doped, one from copper (Cu) doped and one from control, where all ingredients except metal salts were added. QD films were deposited on gold coated glass substrates by simply drop casting method. These QDs were capped with long hydrocarbon molecules. The size of these QDs is about 3.3 nm, with the first exciton absorption peak at ~1000 nm. Films were deposited on gold substrates to minimize the charge formation on the sample. These samples were fixed on aluminum (Al) sample holder. To make a good contact between gold and aluminum, carbon paste (graphite) was used.

In Figure 9-6(a), no traces of Ag and Cu can be seen. In EDX, all of the energies of the characteristic X-rays incident on the detector are measured simultaneously and data acquisition is therefore very rapid across the entire spectrum. However, due to the very low spectral resolution of EDX detector (that is x-ray lines from different elements may not be resolvable if their energies are similar), Pb and S peaks are seen overlapped. That's why people use wavelength dispersive spectroscopy (WDS) instead of EDS. Similarly, Figure 9-6(b) and 9-6(c) provide EDX spectra for Ag doped and Cu doped PbS QDs. In both cases, a very distinct peak of Al in the spectrum which might be due to the sample holder can be seen. Interestingly, Al peak could not be seen for control QD sample. In control case, Al is somehow not exposed to the detector. Both Ag and Cu peaks can be seen in the spectra and which confirms the existence of these metal impurities in the QDs. Cu peaks are not as distinct as Ag peaks in the spectrum. This is due to the low film thickness on the selected regions.

To further confirm the existence of Ag and Cu in the PbS QDs, HyperMap analysis was performed. The HyperMap provides the maps of individual element as well as the mixing of elements in mixing modes. In the control sample, existence of individual element (Pb, S, Au), in the selected regions, as well as the existence of all elements together, based on their availability, are shown in mixing map in Figure 9-6(a). Similar maps in Ag and Cu doped samples are shown in Figures 9-6(b) and 9-6(c) respectively. In mixing mode, color appears with respect to layer position for example for control PbS QDs, Pb and S appear on the top and gold on the bottom.

X-Ray Diffraction Spectroscopy (XRD) measurement was performed for both doped and undoped PbS QDs. X-ray diffraction images are shown in Figure 9-7. XRD measurement did not provide much information about the doping. However, from the spectra it is clearly seen that in both the Cu and Ag doped samples, the main PbS reflections are present which indicates that the PbS crystal structure (rock salt) is generally preserved even after doping. It should be noted that evidence for disorder is seen in slight broadening of the peaks at higher angles.

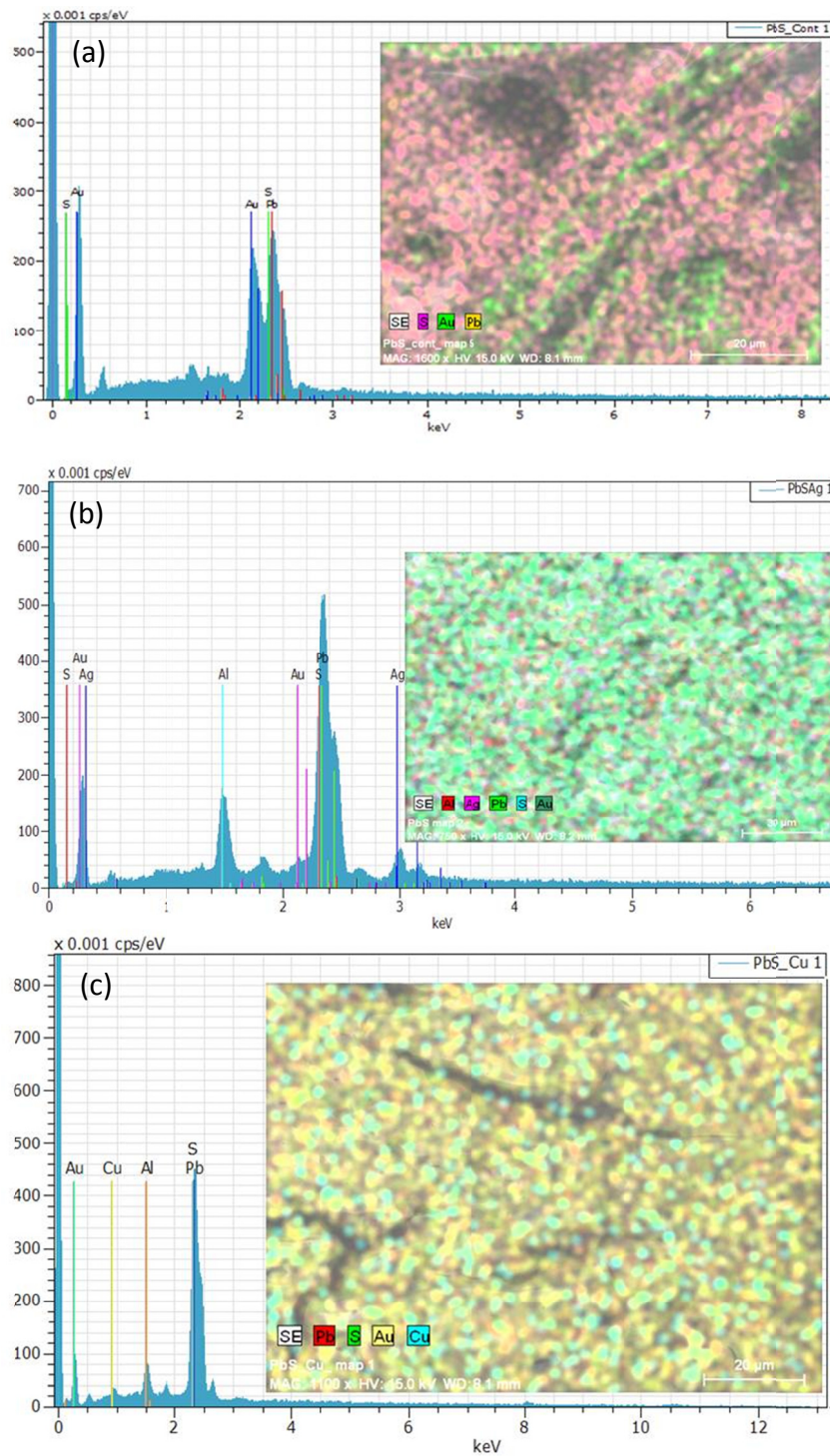


Figure 9-6. EDS Spectra for doped and undoped PbS QDs. Horizontal axis is energy in keV.

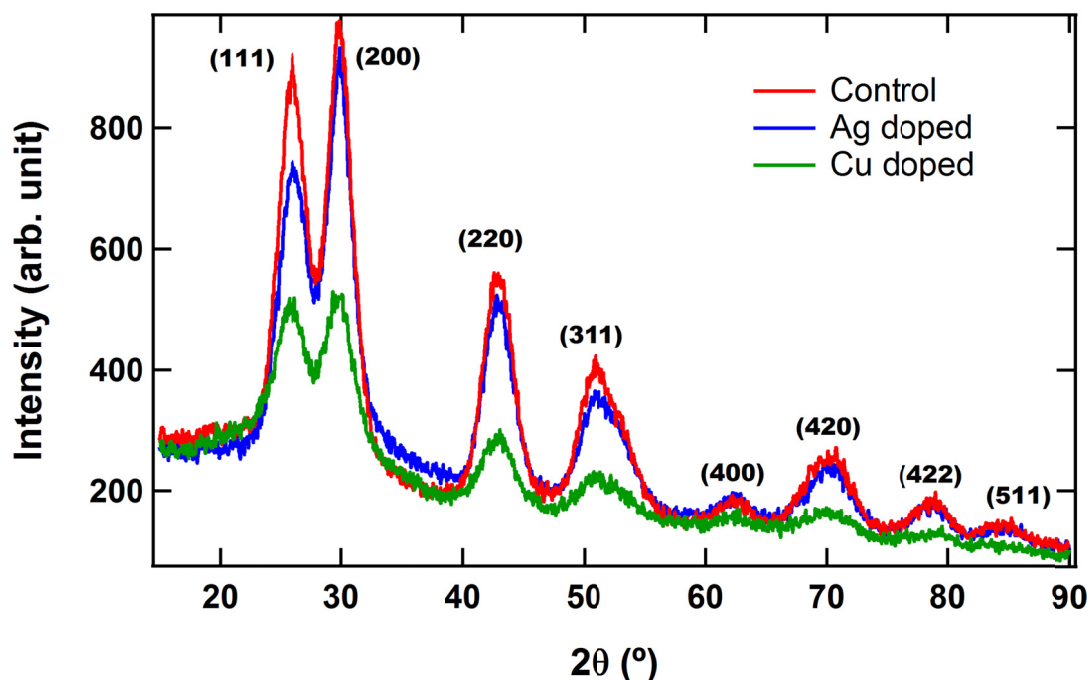


Figure 9-7. XRD diffractograms for both doped and undoped QD films; The PbS QDs crystal structure corresponds to the PbS bulk fcc rock salt structure.

Results presented here are promising but they are preliminary and do not represent a conclusive study. Even with EDS, the results do not proven that the metals are truly core-doping the QDs. **As future work**, some other experimental tests should be conducted to confirm the doping of QDs. For example, x-ray photoelectron spectroscopy (XPS) measurement can be done for elemental analysis, inductively plasma enhanced mass spectroscopy (ICP-MS) can be done again to find out number of impurity atoms in each QDs, homo-junction solar cells can be made to increase the performance of the devices. ICP-MS has already been done but the results are not quite clear.

9.2.3 Multijunction (tandem) solar cells from PbS-QDs of different sizes

One of the best applications of semiconductor QDs is to make tandem solar cells because of their size tunable properties.[140, 411] This work will be started making a double junction solar cells and based on the performance other layer can be added to make it multijunction. In order to harvest as many photons of the solar spectrum as possible, the tandem solar cell consists of two subcells with complementary absorption spectra. These two subcells are separated by a composite middle electrode. This middle electrode acts as a charge recombination center and also protects the first cell while preparing the second cell. To cover the whole visible spectrum, the top cell absorbs low-energy photons and bottom cell absorbs high-energy photons if the light is passing through the bottom cell. The middle electrode is very thin and can be made by depositing 0.5 nm of LiF and 0.5 nm of Al. The middle electrode is not found in case of inorganic tandem solar cell.

The two subcells are stacked in series the current extracted from the tandem cell follows the lowest of the currents generated in the bottom and top cell. When light is passing through the bottom cells then the top cell absorbs the light that is not absorbed by the bottom cell and is illuminated under lower light intensities. As a result the top cell produces lower photocurrents. When the bottom cell generates more current than the top cell, the excess current cannot recombine with the holes from the top cell. This condition helps charging of the middle electrode. The charging of the middle electrode compensates the built in voltage across the bottom cell until the current of the bottom cell matches the current of the top cell. The V_{OC} of the tandem cell is equal to the sum of the

V_{OC} s of both individual cells. The J_{SC} of the tandem cell is limited by the lower J_{SC} of the two individual cells. For maximum performance of the tandem cell, the J_{SC} of each subcell has to be matched.

The structure of the tandem solar cells should be Glass/ITO/ZnO/large band gap quantum dot layer/thin layer of LiF/Al/smaller band gap quantum dot/back contact (Au). To construct a tandem cell, LiF/Al layer can also be replaced by another ZnO layer as shown in Figure 9-8. Both absorbing layers are prepared from PbS quantum dots of different band gap using layer by layer depositing methods. In this process, ligand exchange will be done to make QD film more conductive.

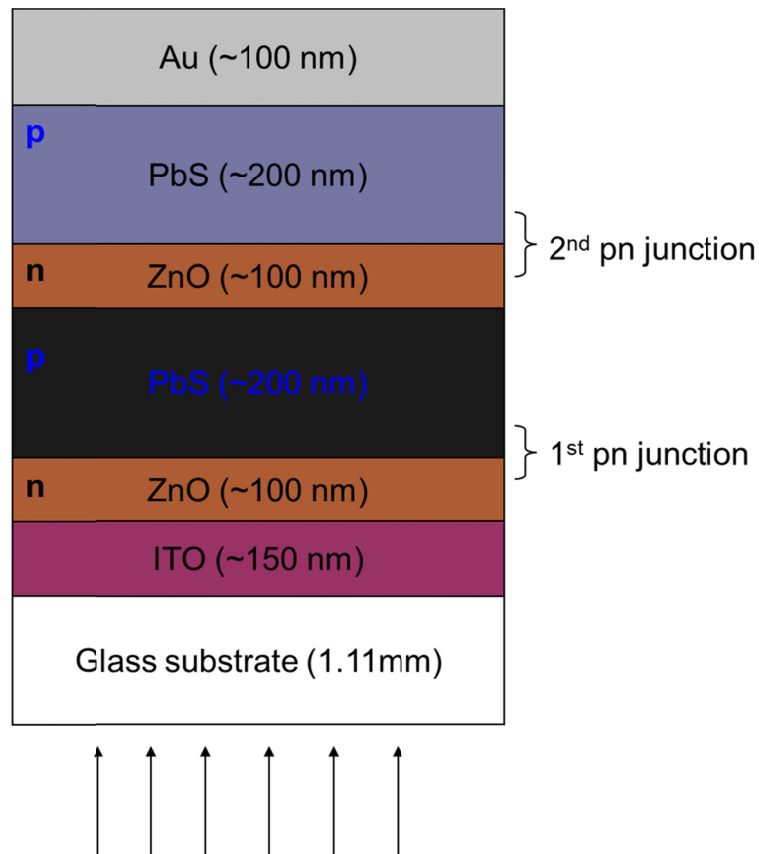


Figure 9-8. Multijunction quantum dot solar cell device structure.

The important parameters of the bottom cells are the transmitted light intensity, J_{SC} , V_{OC} , and FF. In general the bottom cell has to have large band gap and higher mobility of the charge carriers. Using materials with higher motilities causes a higher generated photocurrent in the device. In this way using a proper material the photocurrent of the bottom cells can be tuned. To determine the photocurrent that can be generated from the top cell, a reference top cell can be made that mimics the top cell in the tandem cells.

9.2.4 FeS₂ NC and low work function metal as back contact for CdTe solar cells

Because of very high work function of CdTe, none of the metal is able to make ohmic contact with it. So the Schottky junction formed between the CdTe and the back contact metal brings obstacle to the photogenerated holes to reach to the back contact. The magnitude of the work function difference between these two materials determines the extent of difficulty in hole motion. One way of solving this problem is by inserting any semiconducting layer between the CdTe and back contact metal. The thin layer of semiconducting material should have high carrier concentration and helps to reduce the barrier height opposing the hole motion. In this respect, instead of using comparatively high work function metal, low work function metals such as Al and Ag can also be utilized with same performance as that was obtained with Au. This work has already been started and some of the fruitful results have already been achieved. Optimization of this work is remaining as a future work. Figure 9-9 provided JV curves using FeS₂/Al as a back contact to CdS/CdTe devices.

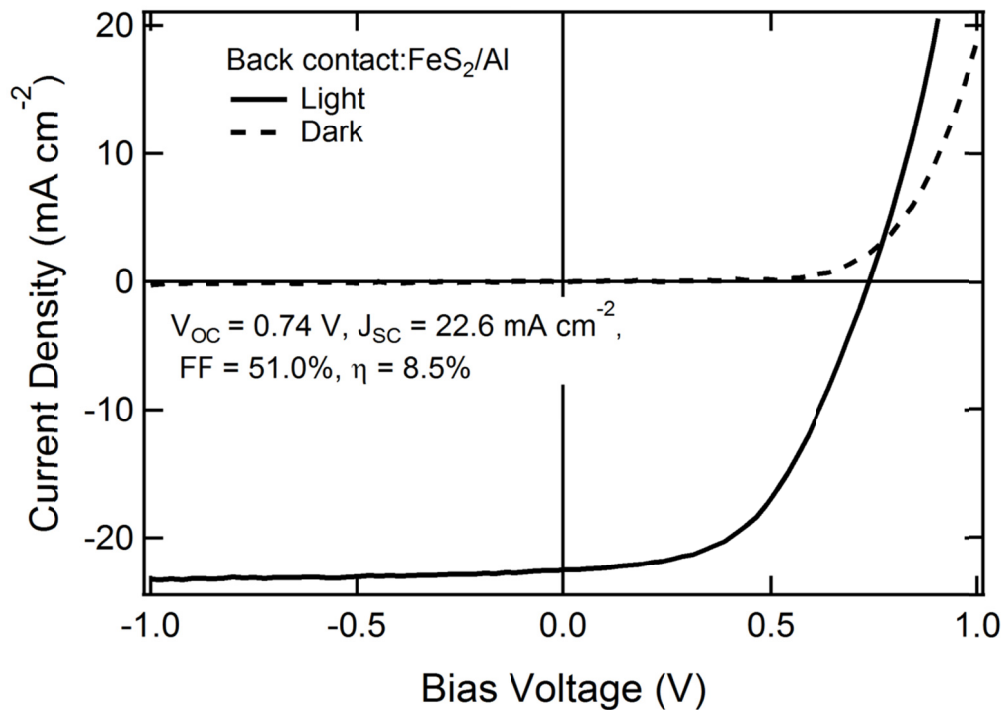


Figure 9-9. Current voltage characteristics of CdS/CdTe solar cells when FeS₂ NC/Al is used as a back contact.

9.2.5 Size dependent study of FeS₂ NCs using TRPL and TA

In this project FeS₂ NCs of different sizes can be synthesized. The size variation can be from 50 nm to 150 nm with the increment of 20-30 nm. Then the NC solution and film can be studied using time resolved photoluminescence and transient absorption.

9.2.6 Synthesis and applications of other pyrite materials such as FeTe₂ and FeSe₂

Similar procedure used in synthesizing FeS₂ NC may be used to make these different pyrite materials. If similar procedure does not work then some other techniques can be utilized to accomplish the task.

References

- [1] P.V. Kamat, Meeting the Clean Energy Demand: Nanostructure Architectures for Solar Energy Conversion, *The Journal of Physical Chemistry C*, 111 (2007) 2834-2860.
- [2] International Energy outlook 2013 with projections to 2040, US Energy Information Administration (access at [http://www.eia.gov/forecasts/ieo/pdf/0484\(2013\).pdf](http://www.eia.gov/forecasts/ieo/pdf/0484(2013).pdf)), (2013) 312.
- [3] M. Zeman, Introduction to Photovoltaic Solar Energy, Solar Cells, collegematerial, (2003).
- [4] United Nation News center, <http://www.un.org/apps/news/story.asp?NewsID=45165#.VEPebBZQDvo>, (2013).
- [5] S.A. Kalogirou, Solar thermal collectors and applications, *Progress in energy and combustion science*, 30 (2004) 231-295.
- [6] International Energy Agency-photovoltaic power systems programme, 2014 http://www.iea-pvps.org/fileadmin/dam/public/report/statistics/PVPS_report_-_A_Snapshot_of_Global_PV_-_1992-2013_-_final_3.pdf.
- [7] Global market outlook for photovoltaics 2014 - 2018, European Photovoltaic Industry Association, <http://www.epia.org/news/publications/>.

- [8] J.M. Pearce, Photovoltaics—a path to sustainable futures, *Futures*, 34 (2002) 663-674.
- [9] A. Goetzberger, J. Knobloch, B. Voss, R. Waddington, *Crystalline silicon solar cells*, Wiley Chichester, 1998.
- [10] A.G. Aberle, Surface passivation of crystalline silicon solar cells: a review, *Progress in Photovoltaics: Research and Applications*, 8 (2000) 473-487.
- [11] A. Shah, P. Torres, R. Tscharnner, N. Wyrsh, H. Keppner, *Photovoltaic Technology: The Case for Thin-Film Solar Cells*, *Science*, 285 (1999) 692-698.
- [12] K.W. Johnston, Schottky-quantum dot photovoltaics for efficient infrared power conversion, *Appl. Phys. Lett.*, 92 (2008) 151115.
- [13] P.V. Kamat, Quantum Dot Solar Cells. Semiconductor Nanocrystals as Light Harvesters†, *The Journal of Physical Chemistry C*, 112 (2008) 18737-18753.
- [14] J. Tang, K.W. Kemp, S. Hoogland, K.S. Jeong, H. Liu, L. Levina, M. Furukawa, X. Wang, R. Debnath, D. Cha, K.W. Chou, A. Fischer, A. Amassian, J.B. Asbury, E.H. Sargent, Colloidal-quantum-dot photovoltaics using atomic-ligand passivation, *Nat Mater*, 10 (2011) 765-771.
- [15] K.P. Bhandari, P.J. Roland, H. Mahabaduge, N.O. Haugen, C.R. Grice, S. Jeong, T. Dykstra, J. Gao, R.J. Ellingson, Thin film solar cells based on the heterojunction of colloidal PbS quantum dots with CdS, *Solar Energy Materials and Solar Cells*, 117 (2013) 476-482.
- [16] K.P. Bhandari, H. Mahabaduge, J. Gao, R.J. Ellingson, PbS quantum dot thin film solar cells using a CdS window layer, in, 2013, pp. 88240I-88240I-88249.

- [17] D. Swanson, The role of modeling in SunPower's commercialization efforts. Presented at challenges in PV Science, Technology, and Manufacturing: A workshop on the role of theory, modeling and simulation, Purdue University, August 2 - 3, 2012, (2012).
- [18] M.A. Green, K. Emery, Y. Hishikawa, W. Warta, E.D. Dunlop, Solar cell efficiency tables (version 42), Progress in Photovoltaics: Research and Applications, 21 (2013) 827-837.
- [19] Best research Cell Efficiency, National Renewable Energy Laboratory (NREL), http://www.nrel.gov/ncpv/images/efficiency_chart.jpg.
- [20] ZSW, http://www.pv-tech.org/news/zsw_sets_21.7_cigs_cell_record.
- [21] First Solar <http://investor.firstsolar.com/releasedetail.cfm?ReleaseID=864426>.
- [22] First Solar Builds the Highest Efficiency Thin Film PV Cell on Record(accessed at <http://investor.firstsolar.com/releasedetail.cfm?ReleaseID=864426>). (2014).
- [23] A. Nozik, Quantum dot solar cells, Physica E: Low-dimensional Systems and Nanostructures, 14 (2002) 115-120.
- [24] R.D. Schaller, V.I. Klimov, High efficiency carrier multiplication in PbSe nanocrystals: implications for solar energy conversion, Physical review letters, 92 (2004) 186601.
- [25] B. O'regan, M. Grfitzeli, A low-cost, high-efficiency solar cell based on dye-sensitized, nature, 353 (1991) 737-740.
- [26] E. H Sargent, Infrared quantum dots, Advanced Materials, 17 (2005) 515-522.
- [27] A.J. Nozik, Multiple exciton generation in semiconductor quantum dots, Chemical Physics Letters, 457 (2008) 3-11.

- [28] R.J. Ellingson, M.C. Beard, J.C. Johnson, P. Yu, O.I. Micic, A.J. Nozik, A. Shabaev, A.L. Efros, Highly efficient multiple exciton generation in colloidal PbSe and PbS quantum dots, *Nano letters*, 5 (2005) 865-871.
- [29] P. Guyot-Sionnest, M. Shim, C. Matranga, M. Hines, Intraband relaxation in CdSe quantum dots, *Physical Review B*, 60 (1999) R2181-R2184.
- [30] V.I. Klimov, A.A. Mikhailovsky, D.W. McBranch, C.A. Leatherdale, M.G. Bawendi, Mechanisms for intraband energy relaxation in semiconductor quantum dots: The role of electron-hole interactions, *Physical Review B*, 61 (2000) R13349-R13352.
- [31] K. Jain, M. Klosner, M. Zemel, S. Raghunandan, Flexible Electronics and Displays: High-Resolution, Roll-to-Roll, Projection Lithography and Photoablation Processing Technologies for High-Throughput Production, *Proceedings of the IEEE*, 93 (2005) 1500-1510.
- [32] M.A. Green, *Third generation photovoltaics: advanced solar energy conversion*, Springer, 2006.
- [33] J.B. Guinée, R. Heijungs, Life Cycle Assessment, in: *Kirk-Othmer Encyclopedia of Chemical Technology*, John Wiley & Sons, Inc., 2000.
- [34] A. Azapagic, Life cycle assessment and its application to process selection, design and optimisation, *Chemical Engineering Journal*, 73 (1999) 1-21.
- [35] K.P. Bhandari, J.M. Collier, R.J. Ellingson, D.S. Apul, Energy payback time (EPBT) and energy return on energy invested (EROI) of solar photovoltaic systems: A systematic review and meta-analysis, *Renewable and Sustainable Energy Reviews*, 47 (2015) 133-141.

- [36] V. Fthenakis, H. Kim, M. Held, M. Raugei, J. Krones, Update of PV energy payback times and life-cycle greenhouse gas emissions, in: 24th European Photovoltaic Solar Energy Conference and Exhibition, 2009, pp. 21-25.
- [37] H. Şengül, T.L. Theis, An environmental impact assessment of quantum dot photovoltaics (QDPV) from raw material acquisition through use, *Journal of Cleaner Production*, 19 (2011) 21-31.
- [38] A.B. Phillips, R.R. Khanal, Z. Song, R.M. Zartman, J.L. DeWitt, J.M. Stone, P.J. Roland, V.V. Plotnikov, C.W. Carter, J.M. Styancho, R.J. Ellingson, A.D. Compaan, M.J. Heben, Wiring-up Carbon Single Wall Nanotubes to Polycrystalline Inorganic Semiconductor Thin Films: Low-Barrier, Copper-Free Back Contact to CdTe Solar Cells, *Nano Letters*, 13 (2013) 5224-5232.
- [39] K.P. Bhandari, R.R. Khanal, N.R. Paudel, P. Koirala, P.J. Roland, T. Kinner, Y. Yan, R.W. Collins, M.J. Heben, R. Ellingson, Performance of nanocrystalline iron pyrite as the back contact to CdS/CdTe solar cells, in: *Photovoltaic Specialist Conference (PVSC), 2014 IEEE 40th, IEEE, 2014*, pp. 2293-2298.
- [40] U.V. Desnica, Doping limits in II–VI compounds — Challenges, problems and solutions, *Progress in Crystal Growth and Characterization of Materials*, 36 (1998) 291-357.
- [41] T.C. Anthony, A.L. Fahrenbruch, M.G. Peters, R.H. Bube, Electrical properties of CdTe films and junctions, *Journal of Applied Physics*, 57 (1985) 400-410.
- [42] T.L. chu, S.S. Chu, K.D. Han, Y.X. Han, Y.H. Liu, M.K. Mantravadi, Efficient thin film cadmium telluride heterojunction solar cells, *Solar Cells*, 24 (1988) 27-34.

- [43] J.M. Luther, M. Law, M.C. Beard, Q. Song, M.O. Reese, R.J. Ellingson, A.J. Nozik, Schottky Solar Cells Based on Colloidal Nanocrystal Films, *Nano Letters*, 8 (2008) 3488-3492.
- [44] G.I. Koleilat, L. Levina, H. Shukla, S.H. Myrskog, S. Hinds, A.G. Pattantyus-Abraham, E.H. Sargent, Efficient, Stable Infrared Photovoltaics Based on Solution-Cast Colloidal Quantum Dots, *ACS Nano*, 2 (2008) 833-840.
- [45] R. Vogel, P. Hoyer, H. Weller, Quantum-Sized PbS, CdS, Ag₂S, Sb₂S₃, and Bi₂S₃ Particles as Sensitizers for Various Nanoporous Wide-Bandgap Semiconductors, *The Journal of Physical Chemistry*, 98 (1994) 3183-3188.
- [46] I. Robel, M. Kuno, P.V. Kamat, Size-Dependent Electron Injection from Excited CdSe Quantum Dots into TiO₂ Nanoparticles, *Journal of the American Chemical Society*, 129 (2007) 4136-4137.
- [47] B.-R. Hyun, Y.-W. Zhong, A.C. Bartnik, L. Sun, H.D. Abruña, F.W. Wise, J.D. Goodreau, J.R. Matthews, T.M. Leslie, N.F. Borrelli, Electron Injection from Colloidal PbS Quantum Dots into Titanium Dioxide Nanoparticles, *ACS Nano*, 2 (2008) 2206-2212.
- [48] J.J. Choi, Y.-F. Lim, M.E.B. Santiago-Berrios, M. Oh, B.-R. Hyun, L. Sun, A.C. Bartnik, A. Goedhart, G.G. Malliaras, H.D. Abruña, F.W. Wise, T. Hanrath, PbSe Nanocrystal Excitonic Solar Cells, *Nano Letters*, 9 (2009) 3749-3755.
- [49] B.A. Timp, X.Y. Zhu, Electronic energy alignment at the PbSe quantum dots/ZnO(10 $\bar{1}$ 0) interface, *Surface Science*, 604 (2010) 1335-1341.
- [50] A. Li, Interaction of nanoparticles with radiation, *ASP conference series*, 000 (2003) 5.

- [51] H. Zogg, C. Maissen, J. Masek, S. Blunier, A. Fach, Photovoltaic lead-chalcogenide on silicon infrared sensor arrays, *OPTICE*, 33 (1994) 1440-1449.
- [52] H. Preier, Recent advances in lead-chalcogenide diode lasers, *Appl. Phys.*, 20 (1979) 189-206.
- [53] K. Kellermann, D. Zimin, K. Alchalabi, P. Gasser, N.A. Pikhtin, H. Zogg, Optically pumped lead-chalcogenide midinfrared lasers on Si substrates, *Journal of Applied Physics*, 94 (2003) 7053-7058.
- [54] T.K. Chaudhuri, A solar thermophotovoltaic converter using Pbs photovoltaic cells, *International Journal of Energy Research*, 16 (1992) 481-487.
- [55] J. An, A. Franceschetti, S. Dudyi, A. Zunger, The peculiar electronic structure of PbSe quantum dots, *Nano Letters*, 6 (2006) 2728-2735.
- [56] S. Kohn, P. Yu, Y. Petroff, Y. Shen, Y. Tsang, M. Cohen, Electronic band structure and optical properties of PbTe, PbSe, and PbS, *Physical Review B*, 8 (1973) 1477-1488.
- [57] S.-H. Wei, A. Zunger, Electronic and structural anomalies in lead chalcogenides, *Physical Review B*, 55 (1997) 13605-13610.
- [58] P.J. Lin, L. Kleinman, Energy Bands of PbTe, PbSe, and PbS, *Physical Review*, 142 (1966) 478.
- [59] U. Elfurawi, Optical and electronic properties of PbS colloidal nanocrystals, in, University of Nottingham, 2012.
- [60] D. Mitchell, R. Wallis, Theoretical energy-band parameters for the lead salts, *Physical Review*, 151 (1966) 581.

- [61] R. Dalven, A review of the semiconductor properties of PbTe, PbSe, PbS and PbO, *Infrared physics*, 9 (1969) 141-184.
- [62] I. Moreels, K. Lambert, D. Smeets, D. De Muynck, T. Nollet, J.C. Martins, F. Vanhaecke, A. Vantomme, C. Delerue, G. Allan, Z. Hens, Size-Dependent Optical Properties of Colloidal PbS Quantum Dots, *ACS Nano*, 3 (2009) 3023-3030.
- [63] Lead compounds: lead sulphide, https://www.webelements.com/compounds/lead/lead_sulphide.html.
- [64] Y. Wang, A. Suna, W. Mahler, R. Kasowski, PbS in polymers. From molecules to bulk solids, *The Journal of chemical physics*, 87 (1987) 7315-7322.
- [65] N. Shaffer, *Rocks and Minerals - pyrite* Indiana Geological Survey, <http://igs.indiana.edu/RocksAndMinerals/Pyrite.cfm>, (2011).
- [66] G.K. Brostigen, Arne, Redetermined Crystal Structure of FeS₂ (Pyrite), *Acta Chemica Scandinavica*, 23 (1969) 3.
- [67] T.A. Bither, R. Bouchard, W. Cloud, P. Donohue, W. Siemons, Transition metal pyrite dichalcogenides. High-pressure synthesis and correlation of properties, *Inorganic Chemistry*, 7 (1968) 2208-2220.
- [68] J.A. STROSCIO, D.M. EIGLER, Atomic and Molecular Manipulation with the Scanning Tunneling Microscope, *Science*, 254 (1991) 1319-1326.
- [69] C.M. Lieber, J. Liu, P.E. Sheehan, Understanding and Manipulating Inorganic Materials with Scanning Probe Microscopes, *Angewandte Chemie International Edition in English*, 35 (1996) 686-704.

- [70] A.P. Alivisatos, *Semiconductor Clusters, Nanocrystals, and Quantum Dots*, *Science*, 271 (1996) 933-937.
- [71] P. Moriarty, *Nanostructured materials*, *Reports on Progress in Physics*, 64 (2001) 297.
- [72] C. Kittel, P. McEuen, *Introduction to solid state physics*, Wiley New York, 1986.
- [73] N.W. Ashcroft, N.D. Mermin, *Solid state physics*, Saunders College, 1976.
- [74] M. Humar, *Jozef Stefan International Postgraduate School*, *Theory of Nanomaterials: excitons in Semiconductor Quantum Dots*, (2008).
- [75] J. Khatei, K.K. Nanda, *Various quantum mechanical concepts for confinements in semiconductor nanocrystals*, *Resonance*, 18 (2013) 771-776.
- [76] A.J. Nozik, M.C. Beard, J.M. Luther, M. Law, R.J. Ellingson, J.C. Johnson, *Semiconductor quantum dots and quantum dot arrays and applications of multiple exciton generation to third-generation photovoltaic solar cells*, *Chemical reviews*, 110 (2010) 6873-6890.
- [77] D.J. Norris, M.G. Bawendi, *Measurement and assignment of the size-dependent optical spectrum in CdSe quantum dots*, *Physical Review B*, 53 (1996) 16338-16346.
- [78] L. Bányai, S.W. Koch, *Semiconductor quantum dots*, World Scientific, 1993.
- [79] T. Basché, *Photoluminescence Intermittency of Semiconductor Quantum Dots in Dielectric Environments*.
- [80] L. Brus, *Electronic wave functions in semiconductor clusters: experiment and theory*, *The Journal of Physical Chemistry*, 90 (1986) 2555-2560.

- [81] Y. Wang, N. Herron, Nanometer-sized semiconductor clusters: materials synthesis, quantum size effects, and photophysical properties, *The Journal of Physical Chemistry*, 95 (1991) 525-532.
- [82] V.I. Klimov, *Semiconductor and metal nanocrystals: synthesis and electronic and optical properties*, CRC Press, 2003.
- [83] C. Murray, D.J. Norris, M.G. Bawendi, Synthesis and characterization of nearly monodisperse CdE (E= sulfur, selenium, tellurium) semiconductor nanocrystallites, *Journal of the American Chemical Society*, 115 (1993) 8706-8715.
- [84] Z.A. Peng, X. Peng, Nearly monodisperse and shape-controlled CdSe nanocrystals via alternative routes: nucleation and growth, *Journal of the American Chemical Society*, 124 (2002) 3343-3353.
- [85] I. Moreels, Y. Justo, B. De Geyter, K. Haestraete, J.C. Martins, Z. Hens, Size-tunable, bright, and stable PbS quantum dots: a surface chemistry study, *Acs Nano*, 5 (2011) 2004-2012.
- [86] L. Sun, J. Fang, J.C. Reed, L. Estevez, A.C. Bartnik, B.-R. Hyun, F.W. Wise, G.G. Malliaras, E.P. Giannelis, Lead-Salt Quantum-Dot Ionic Liquids, *Small*, 6 (2010) 638-641.
- [87] Y. Yin, A.P. Alivisatos, Colloidal nanocrystal synthesis and the organic-inorganic interface, *Nature*, 437 (2005) 664-670.
- [88] Z.A. Peng, X. Peng, Nearly Monodisperse and Shape-Controlled CdSe Nanocrystals via Alternative Routes: Nucleation and Growth, *Journal of the American Chemical Society*, 124 (2002) 3343-3353.

- [89] S.M. Shim, C. Liu, Y.K. Kwon, J. Heo, Lead sulfide quantum dots formation in glasses controlled by erbium ions, *Journal of the American Ceramic Society*, 93 (2010) 3092-3094.
- [90] S. Kudera, L. Carbone, L. Manna, W.J. Parak, Growth mechanism, shape and composition control of semiconductor nanocrystals, in: *Semiconductor nanocrystal quantum dots*, Springer, 2008, pp. 1-34.
- [91] E.A. Boer, Synthesis, passivation and charging of silicon nanocrystals, in, *California Institute of Technology*, 2001.
- [92] M. Fernee, A. Watt, J. Warner, S. Cooper, N. Heckenberg, H. Rubinsztein-Dunlop, Inorganic surface passivation of PbS nanocrystals resulting in strong photoluminescent emission, *Nanotechnology*, 14 (2003) 991.
- [93] M.A. Hines, P. Guyot-Sionnest, Synthesis and Characterization of Strongly Luminescing ZnS-Capped CdSe Nanocrystals, *The Journal of Physical Chemistry*, 100 (1996) 468-471.
- [94] B.O. Dabbousi, J. Rodriguez-Viejo, F.V. Mikulec, J.R. Heine, H. Mattoussi, R. Ober, K.F. Jensen, M.G. Bawendi, (CdSe)ZnS Core-Shell Quantum Dots: Synthesis and Characterization of a Size Series of Highly Luminescent Nanocrystallites, *The Journal of Physical Chemistry B*, 101 (1997) 9463-9475.
- [95] X. Peng, M.C. Schlamp, A.V. Kadavanich, A. Alivisatos, Epitaxial growth of highly luminescent CdSe/CdS core/shell nanocrystals with photostability and electronic accessibility, *Journal of the American Chemical Society*, 119 (1997) 7019-7029.

- [96] P. Reiss, J. Bleuse, A. Pron, Highly Luminescent CdSe/ZnSe Core/Shell Nanocrystals of Low Size Dispersion, *Nano Letters*, 2 (2002) 781-784.
- [97] T.M. Inerbaev, A.E. Masunov, S.I. Khondaker, A. Dobrinescu, A.-V. Plamadă, Y. Kawazoe, Quantum chemistry of quantum dots: Effects of ligands and oxidation, *The Journal of chemical physics*, 131 (2009) 044106.
- [98] G. Kalyuzhny, R.W. Murray, Ligand effects on optical properties of CdSe nanocrystals, *The Journal of Physical Chemistry B*, 109 (2005) 7012-7021.
- [99] A. Luque, S. Hegedus, *Handbook of Photovoltaic Science and Engineering*, John Wiley & Sons, 2011.
- [100] V.I. Klimov, Optical nonlinearities and ultrafast carrier dynamics in semiconductor nanocrystals, *The Journal of Physical Chemistry B*, 104 (2000) 6112-6123.
- [101] S.O. Kasap, *Principles of electronic materials and devices*, McGraw-Hill New York, NY, 2006.
- [102] K.S. Leschkies, T.J. Beatty, M.S. Kang, D.J. Norris, E.S. Aydil, Solar Cells Based on Junctions between Colloidal PbSe Nanocrystals and Thin ZnO Films, *ACS Nano*, 3 (2009) 3638-3648.
- [103] N. Zhao, T.P. Osedach, L.-Y. Chang, S.M. Geyer, D. Wanger, M.T. Binda, A.C. Arango, M.G. Bawendi, V. Bulovic, Colloidal PbS Quantum Dot Solar Cells with High Fill Factor, *ACS Nano*, 4 (2010) 3743-3752.
- [104] J.M. Luther, J. Gao, M.T. Lloyd, O.E. Semonin, M.C. Beard, A.J. Nozik, Stability Assessment on a 3% Bilayer PbS/ZnO Quantum Dot Heterojunction Solar Cell, *Advanced Materials*, 22 (2010) 3704-3707.

- [105] D. Zhitomirsky, I.J. Kramer, A.J. Labelle, A. Fischer, R. Debnath, J. Pan, O.M. Bakr, E.H. Sargent, Colloidal quantum dot photovoltaics: The effect of polydispersity, *Nano Letters*, 12 (2012) 1007-1012.
- [106] Z. Ning, Y. Ren, S. Hoogland, O. Voznyy, L. Levina, P. Stadler, X. Lan, D. Zhitomirsky, E.H. Sargent, All-Inorganic Colloidal Quantum Dot Photovoltaics Employing Solution-Phase Halide Passivation, *Advanced Materials*, (2012).
- [107] V. Sukhovatkin, S. Hinds, L. Brzozowski, E.H. Sargent, Colloidal Quantum-Dot Photodetectors Exploiting Multiexciton Generation, *Science*, 324 (2009) 1542-1544.
- [108] G. Konstantatos, E.H. Sargent, Nanostructured materials for photon detection, *Nat Nano*, 5 (2010) 391-400.
- [109] T.P. Osedach, N. Zhao, S.M. Geyer, L.-Y. Chang, D.D. Wanger, A.C. Arango, M.C. Bawendi, V. Bulović, Interfacial Recombination for Fast Operation of a Planar Organic/QD Infrared Photodetector, *Advanced Materials*, 22 (2010) 5250-5254.
- [110] F. Yoshino, A.A. Major, L. Levina, E.H. Sargent, Nonlinear refractive properties in lead sulfide (PbS) nanocrystals from 1200 to 1550 nm, in: *Quantum Electronics Conference, 2004. (IQEC). International, 2004*, pp. 527-529.
- [111] Z. Tan, F. Zhang, T. Zhu, J. Xu, A.Y. Wang, J.D. Dixon, L. Li, Q. Zhang, S.E. Mohney, J. Ruzyllo, Bright and Color-Saturated Emission from Blue Light-Emitting Diodes Based on Solution-Processed Colloidal Nanocrystal Quantum Dots, *Nano Letters*, 7 (2007) 3803-3807.

- [112] R.Y. Wang, J.P. Feser, J.-S. Lee, D.V. Talapin, R. Segalman, A. Majumdar, Enhanced Thermopower in PbSe Nanocrystal Quantum Dot Superlattices, *Nano Letters*, 8 (2008) 2283-2288.
- [113] J. Jasieniak, M. Califano, S.E. Watkins, Size-Dependent Valence and Conduction Band-Edge Energies of Semiconductor Nanocrystals, *ACS Nano*, 5 (2011) 5888-5902.
- [114] A. Kongkanand, K. Tvrdy, K. Takechi, M. Kuno, P.V. Kamat, Quantum Dot Solar Cells. Tuning Photoresponse through Size and Shape Control of CdSe–TiO₂ Architecture, *Journal of the American Chemical Society*, 130 (2008) 4007-4015.
- [115] R. Debnath, M.T. Greiner, I.J. Kramer, A. Fischer, J. Tang, D.A.R. Barkhouse, X. Wang, L. Levina, Z.-H. Lu, E.H. Sargent, Depleted-heterojunction colloidal quantum dot photovoltaics employing low-cost electrical contacts, *Applied Physics Letters*, 97 (2010) 023109-023103.
- [116] J. Gao, J.M. Luther, O.E. Semonin, R.J. Ellingson, A.J. Nozik, M.C. Beard, Quantum Dot Size Dependent J–V Characteristics in Heterojunction ZnO/PbS Quantum Dot Solar Cells, *Nano Letters*, 11 (2011) 1002-1008.
- [117] A.G. Pattantyus-Abraham, I.J. Kramer, A.R. Barkhouse, X. Wang, G. Konstantatos, R. Debnath, L. Levina, I. Raabe, M.K. Nazeeruddin, M. Grätzel, E.H. Sargent, Depleted-Heterojunction Colloidal Quantum Dot Solar Cells, *ACS Nano*, 4 (2010) 3374-3380.

- [118] C.-H.M. Chuang, P.R. Brown, V. Bulović, M.G. Bawendi, Improved performance and stability in quantum dot solar cells through band alignment engineering, *Nat Mater*, 13 (2014) 796-801.
- [119] M.A. Hines, G.D. Scholes, Colloidal PbS Nanocrystals with Size-Tunable Near-Infrared Emission: Observation of Post-Synthesis Self-Narrowing of the Particle Size Distribution, *Advanced Materials*, 15 (2003) 1844-1849.
- [120] L. Cademartiri, E. Montanari, G. Calestani, A. Migliori, A. Guagliardi, G.A. Ozin, Size-Dependent Extinction Coefficients of PbS Quantum Dots, *Journal of the American Chemical Society*, 128 (2006) 10337-10346.
- [121] T.J. McDonald, Near-infrared Fourier transform photoluminescence spectrometer with tunable excitation for the study of single-walled carbon nanotubes, *Rev. Sci. Instrum.*, 77 (2006) 053104.
- [122] H. Du, C. Chen, R. Krishnan, T.D. Krauss, J.M. Harbold, F.W. Wise, M.G. Thomas, J. Silcox, Optical Properties of Colloidal PbSe Nanocrystals, *Nano Letters*, 2 (2002) 1321-1324.
- [123] K.P. Bhandari, H. Mahabaduge, J. Gao, R.J. Ellingson, PbS quantum dot thin film solar cells using a CdS window layer, in: SPIE, SPIE, Digital Library, San Diego, California, United States, 2013, pp. 88240I-88240I-88249.
- [124] M.J. Fernée, E. Thomsen, P. Jensen, H. Rubinsztein-Dunlop, Highly efficient luminescence from a hybrid state found in strongly quantum confined PbS nanocrystals, *Nanotechnology*, 17 (2006) 956.
- [125] A. Lobo, T. Möller, M. Nagel, H. Borchert, S.G. Hickey, H. Weller, Photoelectron Spectroscopic Investigations of Chemical Bonding in Organically

- Stabilized PbS Nanocrystals, *The Journal of Physical Chemistry B*, 109 (2005) 17422-17428.
- [126] J. Zhang, X. Jiang, Confinement-dependent below-gap state in PbS quantum dot films probed by continuous-wave photoinduced absorption, *The Journal of Physical Chemistry B*, 112 (2008) 9557-9560.
- [127] C.J. Murphy, J.L. Coffey, *QuantumDots: A Primer*, (2002).
- [128] J.M. An, A. Franceschetti, A. Zunger, The Excitonic Exchange Splitting and Radiative Lifetime in PbSe Quantum Dots, *Nano Letters*, 7 (2007) 2129-2135.
- [129] J.M. Luther, M. Law, Q. Song, C.L. Perkins, M.C. Beard, A.J. Nozik, Structural, Optical, and Electrical Properties of Self-Assembled Films of PbSe Nanocrystals Treated with 1,2-Ethanedithiol, *ACS Nano*, 2 (2008) 271-280.
- [130] B.G. Jung, S.-H. Min, C.-W. Kwon, S.-H. Park, K.-B. Kim, T.-S. Yoon, Colloidal Nanoparticle-Layer Formation Through Dip-Coating: Effect of Solvents and Substrate Withdrawing Speed, *Journal of The Electrochemical Society*, 156 (2009) K86-K90.
- [131] P.A. Kralchevsky, V.N. Paunov, I.B. Ivanov, K. Nagayama, Capillary meniscus interaction between colloidal particles attached to a liquid—fluid interface, *Journal of Colloid and Interface Science*, 151 (1992) 79-94.
- [132] M. Law, J.M. Luther, Q. Song, B.K. Hughes, C.L. Perkins, A.J. Nozik, Structural, Optical, and Electrical Properties of PbSe Nanocrystal Solids Treated Thermally or with Simple Amines, *Journal of the American Chemical Society*, 130 (2008) 5974-5985.

- [133] J.J. Choi, J. Luria, B.-R. Hyun, A.C. Bartnik, L. Sun, Y.-F. Lim, J.A. Marohn, F.W. Wise, T. Hanrath, Photogenerated Exciton Dissociation in Highly Coupled Lead Salt Nanocrystal Assemblies, *Nano Letters*, 10 (2010) 1805-1811.
- [134] W. Yoon, J.E. Boercker, M.P. Lumb, D. Placencia, E.E. Foos, J.G. Tischler, Enhanced Open-Circuit Voltage of PbS Nanocrystal Quantum Dot Solar Cells, *Sci. Rep.*, 3 (2013).
- [135] C.J. Brabec, S.E. Shaheen, C. Winder, N.S. Sariciftci, P. Denk, Effect of LiF/metal electrodes on the performance of plastic solar cells, *Applied Physics Letters*, 80 (2002) 1288-1290.
- [136] E.-J. Guo, H. Guo, H. Lu, K. Jin, M. He, G. Yang, Structure and characteristics of ultrathin indium tin oxide films, *Applied Physics Letters*, 98 (2011) 011905-011903.
- [137] O. Madelung, *Semiconductors: Data Handbook*, Springer, 2004.
- [138] J. Gao, C.L. Perkins, J.M. Luther, M.C. Hanna, H.-Y. Chen, O.E. Semonin, A.J. Nozik, R.J. Ellingson, M.C. Beard, n-Type Transition Metal Oxide as a Hole Extraction Layer in PbS Quantum Dot Solar Cells, *Nano Letters*, 11 (2011) 3263-3266.
- [139] K.P. Bhandari, P.J. Roland, G. Jianbo, R.J. Ellingson, Bandgap, window layer thickness, and light soaking effects on PbS quantum dot solar cells, in: *Photovoltaic Specialists Conference (PVSC), 2013 IEEE 39th*, 2013, pp. 0258-0263.

- [140] J.J. Choi, W.N. Wenger, R.S. Hoffman, Y.-F. Lim, J. Luria, J. Jasieniak, J.A. Marohn, T. Hanrath, Solution-Processed Nanocrystal Quantum Dot Tandem Solar Cells, *Advanced Materials*, 23 (2011) 3144-3148.
- [141] S. Nezu, G. Larramona, C. Choné, A. Jacob, B. Delatouche, D. Péré, C. Moisan, Light Soaking and Gas Effect on Nanocrystalline TiO₂/Sb₂S₃/CuSCN Photovoltaic Cells following Extremely Thin Absorber Concept, *The Journal of Physical Chemistry C*, 114 (2010) 6854-6859.
- [142] J. Tang, X. Wang, L. Brzozowski, D.A.R. Barkhouse, R. Debnath, L. Levina, E.H. Sargent, Schottky Quantum Dot Solar Cells Stable in Air under Solar Illumination, *Advanced Materials*, 22 (2010) 1398-1402.
- [143] A.H. Ip, S.M. Thon, S. Hoogland, O. Voznyy, D. Zhitomirsky, R. Debnath, L. Levina, L.R. Rollny, G.H. Carey, A. Fischer, K.W. Kemp, I.J. Kramer, Z. Ning, A.J. Labelle, K.W. Chou, A. Amassian, E.H. Sargent, Hybrid passivated colloidal quantum dot solids, *Nat Nano*, 7 (2012) 577-582.
- [144] S. Ito, P. Chen, P. Comte, M.K. Nazeeruddin, P. Liska, P. Péchy, M. Grätzel, Fabrication of screen-printing pastes from TiO₂ powders for dye-sensitised solar cells, *Progress in Photovoltaics: Research and Applications*, 15 (2007) 603-612.
- [145] D. Lincot, G. Hodes, Chemical Solution Deposition of Semiconducting and Non-Metallic Films: Proceedings of the International Symposium, Electrochemical Society, 2006.
- [146] N. Romeo, A. Bosio, R. Tedeschi, A. Romeo, V. Canevari, A highly efficient and stable CdTe/CdS thin film solar cell, *Solar Energy Materials and Solar Cells*, 58 (1999) 209-218.

- [147] K.D. Dobson, I. Visoly-Fisher, G. Hodes, D. Cahen, Stability of CdTe/CdS thin-film solar cells, *Solar Energy Materials and Solar Cells*, 62 (2000) 295-325.
- [148] K. Ramanathan, M.A. Contreras, C.L. Perkins, S. Asher, F.S. Hasoon, J. Keane, D. Young, M. Romero, W. Metzger, R. Noufi, J. Ward, A. Duda, Properties of 19.2% efficiency ZnO/CdS/CuInGaSe₂ thin-film solar cells, *Progress in Photovoltaics: Research and Applications*, 11 (2003) 225-230.
- [149] R. Scheer, H.W. Schock, *Chalcogenide Photovoltaics: Physics, Technologies, and Thin Film Devices*, John Wiley & Sons, 2011.
- [150] H. Uda, H. Yonezawa, Y. Ohtsubo, M. Kosaka, H. Sonomura, Thin CdS films prepared by metalorganic chemical vapor deposition, *Solar Energy Materials and Solar Cells*, 75 (2003) 219-226.
- [151] J.-H. Lee, D.-J. Lee, Effects of CdCl₂ treatment on the properties of CdS films prepared by r.f. magnetron sputtering, *Thin Solid Films*, 515 (2007) 6055-6059.
- [152] J.Y. Choi, K.-J. Kim, J.-B. Yoo, D. Kim, Properties of cadmium sulfide thin films deposited by chemical bath deposition with ultrasonication, *Solar Energy*, 64 (1998) 41-47.
- [153] S.L. Wang, X.J. Wang, W.Z. Wang, C.J. Liang, Z. Wang, Z. Qi, Comparative study on thin films of cadmium sulfide prepared by chemical bath deposition and radio frequency magnetron sputtering, *Guang Pu Xue Yu Guang Pu Fen Xi*, 32 (2012) 1094-1097.
- [154] B.W. Kempshall, L.A. Giannuzzi, B.I. Prentzer, F.A. Stevie, S. X. Da, Comparative evaluation of protective coatings and focused ion beam chemical

- vapor deposition processes, *Journal of Vacuum Science & Technology B: Microelectronics and Nanometer Structures*, 20 (2002) 286-290.
- [155] Y.H. Sun, Y.J. Ge, W.W. Li, D.J. Huang, F. Chen, L.Y. Shang, P.X. Yang, J.H. Chu, Structural and optical analysis of CdS thin films grown by magnetron sputtering technique, *Journal of Physics: Conference Series*, 276 (2011) 012187.
- [156] K. Subba Ramaiah, R. Pilkington, A. Hill, R. Tomlinson, A.-K. Bhatnagar, Structural and optical investigations on CdS thin films grown by chemical bath technique, *Materials Chemistry and Physics*, 68 (2001) 22-30.
- [157] A. Guinier, X-ray diffraction in crystals, imperfect crystals, and amorphous bodies, Courier Dover Publications, 1994.
- [158] E. da Silva, D. Strauch, U. Rößler, Numerical Data and Functional Relationships in Science and Technology: Group 3: Condensed Matter. Vol. 44. Semiconductors. New Data and Updates for Several III-V (including Mixed Crystals) and II-VI Compounds/Ed.: U. Rössler. Authors: ECF Da Silva and D. Strauch, Springer, 2012.
- [159] P.R. Brown, R.R. Lunt, N. Zhao, T.P. Osedach, D.D. Wanger, L.-Y. Chang, M.G. Bawendi, V. Bulović, Improved Current Extraction from ZnO/PbS Quantum Dot Heterojunction Photovoltaics Using a MoO₃ Interfacial Layer, *Nano Letters*, 11 (2011) 2955-2961.
- [160] A.K. Rath, M. Bernechea, L. Martinez, G. Konstantatos, Solution-Processed Heterojunction Solar Cells Based on p-type PbS Quantum Dots and n-type Bi₂S₃ Nanocrystals, *Advanced Materials*, 23 (2011) 3712-3717.

- [161] G. Zhai, A. Bezryadina, A.J. Breeze, D. Zhang, G.B. Alers, S.A. Carter, Air stability of TiO₂/PbS colloidal nanoparticle solar cells and its impact on power efficiency, *Applied Physics Letters*, 99 (2011) 063512-063513.
- [162] L. Etgar, T. Moehl, S. Gabriel, S.G. Hickey, A. Eychmüller, M. Grätzel, Light Energy Conversion by Mesoscopic PbS Quantum Dots/TiO₂ Heterojunction Solar Cells, *ACS Nano*, 6 (2012) 3092-3099.
- [163] L.A.A. Pettersson, L.S. Roman, O. Inganäs, Modeling photocurrent action spectra of photovoltaic devices based on organic thin films, *Journal of Applied Physics*, 86 (1999) 487-496.
- [164] M. Law, M.C. Beard, S. Choi, J.M. Luther, M.C. Hanna, A.J. Nozik, Determining the Internal Quantum Efficiency of PbSe Nanocrystal Solar Cells with the Aid of an Optical Model, *Nano Letters*, 8 (2008) 3904-3910.
- [165] V. Plotnikov, Fabrication of ultra thin CdS/CdTe solar cells by magnetron sputtering, in, University of Toledo, 2009.
- [166] J. Tang, E.H. Sargent, Infrared Colloidal Quantum Dots for Photovoltaics: Fundamentals and Recent Progress, *Advanced Materials*, 23 (2011) 12-29.
- [167] G. Vigil, O. n, A. Arias-Carbajal, P. Mendoza, R. rez, R. Santana, G. guez, H. Sastre, J. ndez, J.C. Alonso, G. Moreno, E. a, G. Contreras-Puente, A. Morales-Acevedo, Improving the efficiency of CdS/CdTe solar cells by varying the thiourea/CdCl₂ ratio in the CdS chemical bath, *Semiconductor Science and Technology*, 20 (2005) 819-822.

- [168] J.L. Peña, O. Arés, V. Rejón, A. Rios-Flores, J.M. Camacho, N. Romeo, A. Bosio, A detailed study of the series resistance effect on CdS/CdTe solar cells with Cu/Mo back contact, *Thin Solid Films*, 520 (2011) 680-683.
- [169] S.M. Willis, C. Cheng, H.E. Assender, A.A.R. Watt, Modified Mott-Schottky Analysis of Nanocrystal Solar Cells, <http://arxiv.org/abs/1112.1623>, (2011).
- [170] D.K. Schroder, Semiconductor material and device characterization, in, Wiley, 1990.
- [171] G. Garcia-Belmonte, A. Munar, E.M. Barea, J. Bisquert, I. Ugarte, R. Pacios, Charge carrier mobility and lifetime of organic bulk heterojunctions analyzed by impedance spectroscopy, *Organic Electronics*, 9 (2008) 847-851.
- [172] S.M. Willis, C. Cheng, H.E. Assender, A.A.R. Watt, The Transitional Heterojunction Behavior of PbS/ZnO Colloidal Quantum Dot Solar Cells, *Nano Letters*, 12 (2012) 1522-1526.
- [173] A.G. Pattantyus-Abraham, I.J. Kramer, A.R. Barkhouse, X.H. Wang, G. Konstantatos, R. Debnath, L. Levina, I. Raabe, M.K. Nazeeruddin, M. Gratzel, E.H. Sargent, Depleted-Heterojunction Colloidal Quantum Dot Solar Cells, *Acs Nano*, 4 (2010) 3374-3380.
- [174] J.P. Clifford, K.W. Johnston, L. Levina, E.H. Sargent, Schottky barriers to colloidal quantum dot films, *APPLIED PHYSICS LETTERS*, 91 (2007) 3.
- [175] H. Chavez, M. Jordan, J.C. McClure, G. Lush, V.P. Singh, Physical and electrical characterization of CdS films deposited by vacuum evaporation, solution growth and spray pyrolysis, *J. Mater. Sci.-Mater. Electron.*, 8 (1997) 151-154.

- [176] S.G. Hur, E.T. Kim, J.H. Lee, G.H. Kim, S.G. Yoon, Characterization of photoconductive CdS thin films prepared on glass substrates for photoconductive-sensor applications, *J. Vac. Sci. Technol. B*, 26 (2008) 1334-1337.
- [177] A. Ashour, The physical characteristics of Cu₂S/CdS thin-film solar cell, *J. Optoelectron. Adv. Mater.*, 8 (2006) 1447-1451.
- [178] P.P. Altermatt, T. Kieseewetter, K. Ellmer, H. Tributsch, Specifying targets of future research in photovoltaic devices containing pyrite (FeS₂) by numerical modelling, *Solar Energy Materials and Solar Cells*, 71 (2002) 181-195.
- [179] C. Wadia, Y. Wu, S. Gul, S.K. Volkman, J. Guo, A.P. Alivisatos, Surfactant-Assisted Hydrothermal Synthesis of Single phase Pyrite FeS₂ Nanocrystals, *Chemistry of Materials*, 21 (2009) 2568-2570.
- [180] L. Yu, S. Lany, R. Kykyneshi, V. Jieratum, R. Ravichandran, B. Pelatt, E. Altschul, H.A.S. Platt, J.F. Wager, D.A. Keszler, A. Zunger, Iron Chalcogenide Photovoltaic Absorbers, *Advanced Energy Materials*, 1 (2011) 748-753.
- [181] K. Ellmer, C. Höpfner, On the stoichiometry of the semiconductor pyrite (FeS₂), *Philosophical Magazine A*, 75 (1997) 1129-1151.
- [182] A. Ennaoui, H. Tributsch, Iron sulphide solar cells, *Solar Cells*, 13 (1984) 197-200.
- [183] A. Ennaoui, S. Fiechter, C. Pettenkofer, N. Alonso-Vante, K. Büker, M. Bronold, C. Höpfner, H. Tributsch, Iron disulfide for solar energy conversion, *Solar Energy Materials and Solar Cells*, 29 (1993) 289-370.

- [184] Y. Bi, Y. Yuan, C.L. Exstrom, S.A. Darveau, J. Huang, Air Stable, Photosensitive, Phase Pure Iron Pyrite Nanocrystal Thin Films for Photovoltaic Application, *Nano Letters*, 11 (2011) 4953-4957.
- [185] J. Puthussery, S. Seefeld, N. Berry, M. Gibbs, M. Law, Colloidal Iron Pyrite (FeS₂) Nanocrystal Inks for Thin-Film Photovoltaics, *Journal of the American Chemical Society*, 133 (2010) 716-719.
- [186] S.V. Parag, P.D. Tara, Thin Film Solar Cells Using Earth-Abundant Materials, in, *Solar Cells-Research and Application*, 2013.
- [187] A. Kirkeminde, R. Scott, S. Ren, All inorganic iron pyrite nano-heterojunction solar cells, *Nanoscale*, 4 (2012) 7649-7654.
- [188] H.A. Macpherson, C.R. Stoldt, Iron Pyrite Nanocubes: Size and Shape Considerations for Photovoltaic Application, *ACS Nano*, 6 (2012) 8940-8949.
- [189] J.M. Lucas, C.-C. Tuan, S.D. Lounis, D.K. Britt, R. Qiao, W. Yang, A. Lanzara, A.P. Alivisatos, Ligand-Controlled Colloidal Synthesis and Electronic Structure Characterization of Cubic Iron Pyrite (FeS₂) Nanocrystals, *Chemistry of Materials*, 25 (2013) 1615-1620.
- [190] M. Akhtar, J. Akhter, M.A. Malik, P. O'Brien, F. Tuna, J. Raftery, M. Helliwell, Deposition of iron sulfide nanocrystals from single source precursors, *Journal of Materials Chemistry*, 21 (2011) 9737-9745.
- [191] K.P. Bhandari, P.J. Roland, T. Kinner, Y. Cao, H. Choi, S. Jeong, R.J. Ellingson, Analysis and characterization of iron pyrite nanocrystals and nanocrystalline thin films derived from bromide anion synthesis, *Journal of Materials Chemistry A*, (2015).

- [192] N.G. Larsen, P.D.W. Boyd, S.J. Rodgers, G.E. Wuenschell, C.A. Koch, S. Rasmussen, J.R. Tate, B.S. Erler, C.A. Reed, Bis-benzimidazole-appended binucleating porphyrin ligands: synthesis, characterization, and x-ray structure, *Journal of the American Chemical Society*, 108 (1986) 6950-6960.
- [193] J.P. Collman, R.R. Gagne, C. Reed, T.R. Halbert, G. Lang, W.T. Robinson, Picket fence porphyrins. Synthetic models for oxygen binding hemoproteins, *Journal of the American Chemical Society*, 97 (1975) 1427-1439.
- [194] Sigma Aldrich, <http://www.sigmaaldrich.com/safety-center.html>.
- [195] A. Yamamoto, M. Nakamura, A. Seki, E.L. Li, A. Hashimoto, S. Nakamura, Pyrite (FeS₂) thin films prepared by spray method using FeSO₄ and (NH₄)₂Sx, *Solar Energy Materials and Solar Cells*, 75 (2003) 451-456.
- [196] Y.Z. Dong, Y.F. Zheng, H. Duan, Y.F. Sun, Y.H. Chen, Formation of pyrite (FeS₂) thin nano-films by thermal-sulfurating electrodeposition films at different temperature, *Materials Letters*, 59 (2005) 2398-2402.
- [197] L. Huang, F. Wang, Z. Luan, L. Meng, Pyrite (FeS₂) thin films deposited by sol-gel method, *Materials Letters*, 64 (2010) 2612-2615.
- [198] S. Seefeld, M. Limpinsel, Y. Liu, N. Farhi, A. Weber, Y. Zhang, N. Berry, Y.J. Kwon, C.L. Perkins, J.C. Hemminger, R. Wu, M. Law, Iron Pyrite Thin Films Synthesized from an Fe(acac)₃ Ink, *Journal of the American Chemical Society*, 135 (2013) 4412-4424.
- [199] C. Raisin, Y. Bertrand, SnS₂ and SnSe₂ photoemission studies, *Journal of Physics C: Solid State Physics*, 15 (1982) 1805.

- [200] R. Schlaf, O. Lang, C. Pettenkofer, W. Jaegermann, Band lineup of layered semiconductor heterointerfaces prepared by van der Waals epitaxy: Charge transfer correction term for the electron affinity rule, *Journal of Applied Physics*, 85 (1999) 2732-2753.
- [201] E. Lifshitz, Z. Chen, L. Bykov, Optical spectroscopy of 1T-tin disulfide single crystal, *The Journal of Physical Chemistry*, 97 (1993) 238-242.
- [202] C. Wang, K. Tang, Q. Yang, Y. Qian, C. Xu, Hydrothermal Synthesis and Characterization of SnS₂ Nanocrystals, *Chemistry Letters*, 30 (2001) 1294-1295.
- [203] D. Ma, W. Zhang, Q. Tang, R. Zhang, W. Yu, Y. Qian, Large-Scale Hydrothermal Synthesis of SnS₂ Nanobelts, *Journal of Nanoscience and Nanotechnology*, 5 (2005) 806-809.
- [204] C.S.H.a.E.O. Schlemper, The crystal and molecular structure of tetrakis-(N,N-diethyldithiocarbamate)-tin (IV), *Acta crystallographica*, 27 (1971) 1964-1969.
- [205] X.-L. Gou, J. Chen, P.-W. Shen, Synthesis, characterization and application of SnS_x (x=1, 2) nanoparticles, *Materials Chemistry and Physics*, 93 (2005) 557-566.
- [206] T.E. Webber, Synthesis of Iron Pyrite and Tin (VI) Sulfide Nanoparticles for Potential Application in Solar Cells, in, University of Nebraska at Kearney, Kearney, 2010.
- [207] M.A. Hines, P. Guyot-Sionnest, Bright UV-Blue Luminescent Colloidal ZnSe Nanocrystals, *The Journal of Physical Chemistry B*, 102 (1998) 3655-3657.

- [208] J.-w. Seo, J.-t. Jang, S.-w. Park, C. Kim, B. Park, J. Cheon, Two-Dimensional SnS₂ Nanoplates with Extraordinary High Discharge Capacity for Lithium Ion Batteries, *Advanced Materials*, 20 (2008) 4269-4273.
- [209] J. Jasieniak, B.I. MacDonald, S.E. Watkins, P. Mulvaney, Solution-Processed Sintered Nanocrystal Solar Cells via Layer-by-Layer Assembly, *Nano Letters*, 11 (2011) 2856-2864.
- [210] Q. Guo, S.J. Kim, M. Kar, W.N. Shafarman, R.W. Birkmire, E.A. Stach, R. Agrawal, H.W. Hillhouse, Development of CuInSe₂ Nanocrystal and Nanoring Inks for Low-Cost Solar Cells, *Nano Letters*, 8 (2008) 2982-2987.
- [211] Q. Guo, G.M. Ford, W.-C. Yang, B.C. Walker, E.A. Stach, H.W. Hillhouse, R. Agrawal, Fabrication of 7.2% Efficient CZTSSe Solar Cells Using CZTS Nanocrystals, *Journal of the American Chemical Society*, 132 (2010) 17384-17386.
- [212] M. Birkholz, S. Fiechter, A. Hartmann, H. Tributsch, Sulfur deficiency in iron pyrite (FeS_{2-x}) and its consequences for band-structure models, *Physical Review B*, 43 (1991) 11926-11936.
- [213] G. Smestad, A. Ennaoui, S. Fiechter, H. Tributsch, W.K. Hofmann, M. Birkholz, W. Kautek, Photoactive thin film semiconducting iron pyrite prepared by sulfurization of iron oxides, *Solar Energy Materials*, 20 (1990) 149-165.
- [214] I.J. Ferrer, D.M. Nevskaja, C. de las Heras, C. Sánchez, About the band gap nature of FeS₂ as determined from optical and photoelectrochemical measurements, *Solid State Communications*, 74 (1990) 913-916.

- [215] N.M. Ravindra, V.K. Sritastava, Temperature dependence of the energy gap in pyrite (FeS₂), *physica status solidi (a)*, 65 (1981) 737-742.
- [216] C. de las Heras, G. Lifante, Optical parameters of pyrite thin films, *Journal of Applied Physics*, 82 (1997) 5132.
- [217] C.d.l. Heras, I.J. Ferrer, C. Sanchez, Temperature dependence of the optical absorption edge of pyrite FeS₂ thin films, *Journal of Physics: Condensed Matter*, 6 (1994) 10177.
- [218] A.M. Karguppikar, A.G. Vedeshwar, Electrical and optical properties of natural iron pyrite (FeS₂), *physica status solidi (a)*, 109 (1988) 549-558.
- [219] W.W. Kou, M.S. Seehra, Optical absorption in iron pyrite (FeS₂), *Physical Review B*, 18 (1978) 7062-7068.
- [220] D.A.R. Barkhouse, O. Gunawan, T. Gokmen, T.K. Todorov, D.B. Mitzi, Device characteristics of a 10.1% hydrazine-processed Cu₂ZnSn(Se,S)₄ solar cell, *Progress in Photovoltaics: Research and Applications*, 20 (2012) 6-11.
- [221] T.K. Todorov, J. Tang, S. Bag, O. Gunawan, T. Gokmen, Y. Zhu, D.B. Mitzi, Beyond 11% Efficiency: Characteristics of State-of-the-Art Cu₂ZnSn(S,Se)₄ Solar Cells, *Advanced Energy Materials*, 3 (2013) 34-38.
- [222] S.N. White, Laser Raman spectroscopy as a technique for identification of seafloor hydrothermal and cold seep minerals, *Chemical Geology*, 259 (2009) 240-252.
- [223] A. Kleppe, A. Jephcoat, High-pressure Raman spectroscopic studies of FeS₂ pyrite, *Mineralogical Magazine*, 68 (2004) 433-441.

- [224] M. Eghbalnia, Electrochemical and Raman investigation of pyrite and chalcopyrite oxidation, (2012).
- [225] M. Blanchard, M. Alfredsson, J. Brodholt, G.D. Price, K. Wright, C.R.A. Catlow, Electronic structure study of the high-pressure vibrational spectrum of FeS₂ pyrite, *The Journal of Physical Chemistry B*, 109 (2005) 22067-22073.
- [226] A. Boughriet, R.S. Figueiredo, J. Laureyns, P. Recourt, Identification of newly generated iron phases in recent anoxic sediments: ⁵⁷Fe Mossbauer and microRaman spectroscopic studies, *Journal of the Chemical Society, Faraday Transactions*, 93 (1997) 3209-3215.
- [227] C. Rémazeilles, M. Saheb, D. Neff, E. Guilminot, K. Tran, J.-A. Bourdoiseau, R. Sabot, M. Jeannin, H. Matthiesen, P. Dillmann, P. Refait, Microbiologically influenced corrosion of archaeological artefacts: characterisation of iron(II) sulfides by Raman spectroscopy, *Journal of Raman Spectroscopy*, 41 (2010) 1425-1433.
- [228] N. Alonso-Vante, G. Chatzitheodorou, S. Fiechter, N. Mgoduka, I. Poullos, H. Tributsch, Interfacial behavior of hydrogen-treated sulphur deficient pyrite (FeS_{2-x}), *Solar Energy Materials*, 18 (1988) 9-21.
- [229] S. Fiechter, M. Birkholz, A. Hartmann, P. Dulski, M. Giersig, H. Tributsch, R.J.D. Tilley, The microstructure and stoichiometry of pyrite FeS_{2-x}, *Journal of Materials Research*, 7 (1992) 1829-1838.
- [230] S. Kment, H. Kmentova, A. Sarkar, R.J. Soukup, N.J. Ianno, J. Krysa, Z. Hubicka, J. Olejnicek, C.L. Exstrom, S.A. Darveau, A novel sol-gel route to

- pinhole-free iron sulfide thin films, in: Photovoltaic Specialists Conference (PVSC), 2011 37th IEEE, 2011, pp. 001287-001291.
- [231] G. Smestad, A. Da Silva, H. Tributsch, S. Fiechter, M. Kunst, N. Mezziani, M. Birkholz, Formation of semiconducting iron pyrite by spray pyrolysis, *Solar Energy Materials*, 18 (1989) 299-313.
- [232] A. Monshi, M.R. Foroughi, M.R. Monshi, Modified Scherrer equation to estimate more accurately nano-crystallite size using XRD, *World Journal of Nano Science and Engineering*, 2 (2012) 154.
- [233] G. Golan, A. Axelevitch, B. Gorenstein, V. Manevych, Hot-Probe method for evaluation of impurities concentration in semiconductors, *Microelectronics Journal*, 37 (2006) 910-915.
- [234] L.Y. Huang Liuyi, Meng Liang, Pyrite Films Growth by Sulfurizing precursive Iron of Different Crystallizing Status, *J. Mater. Sci. Technol.*, 25 (2009) 5.
- [235] J. Hu, Y. Zhang, M. Law, R. Wu, First-principles studies of the electronic properties of native and substitutional anionic defects in bulk iron pyrite, *Physical Review B*, 85 (2012) 085203.
- [236] M. Cabán-Acevedo, M.S. Faber, Y. Tan, R.J. Hamers, S. Jin, Synthesis and Properties of Semiconducting Iron Pyrite (FeS₂) Nanowires, *Nano Letters*, 12 (2012) 1977-1982.
- [237] S.S. Li, *Semiconductor physical electronics*, Springer Science & Business Media, 2007.
- [238] D. Mocatta, G. Cohen, J. Schattner, O. Millo, E. Rabani, U. Banin, Heavily Doped Semiconductor Nanocrystal Quantum Dots, *Science*, 332 (2011) 77-81.

- [239] J.Y.W. Seto, The electrical properties of polycrystalline silicon films, *Journal of Applied Physics*, 46 (1975) 5247-5254.
- [240] J. Werner, Origin of curved Arrhenius plots for the conductivity of polycrystalline semiconductors, *Solid State Phenomena*, 37 (1994) 213-218.
- [241] N. Hamdadou, A. Khelil, J. Bernede, Pyrite FeS₂ films obtained by sulphuration of iron pre-deposited films, *Materials chemistry and physics*, 78 (2003) 591-601.
- [242] J. Ares, A. Pascual, I. Ferrer, C. Sanchez, Lattice intrinsic defects and electrical resistivity in pyrite thin films, *Thin Solid Films*, 451 (2004) 233-236.
- [243] Y.C. Zhang, Z.N. Du, K.W. Li, M. Zhang, Size-controlled hydrothermal synthesis of SnS₂ nanoparticles with high performance in visible light-driven photocatalytic degradation of aqueous methyl orange, *Separation and Purification Technology*, 81 (2011) 101-107.
- [244] G. Said, P.A. Lee, Electrical conduction mechanisms in tin disulphide, *physica status solidi (a)*, 15 (1973) 99-103.
- [245] C. Wang, K. Tang, Q. Yang, Y. Qian, Raman scattering, far infrared spectrum and photoluminescence of SnS₂ nanocrystallites, *Chemical physics letters*, 357 (2002) 371-375.
- [246] A. Ennaoui, H. Tributsch, Energetic characterization of the photoactive FeS₂ (pyrite) interface, *Solar Energy Materials*, 14 (1986) 461-474.
- [247] A. Ennaoui, S. Fiechter, W. Jaegermann, H. Tributsch, Photoelectrochemistry of Highly Quantum Efficient Single-Crystalline n - FeS₂ (Pyrite), *Journal of The Electrochemical Society*, 133 (1986) 97-106.

- [248] B. Rezig, H. Dahman, M. Kenzari, Iron pyrite FeS₂ for flexible solar cells, *Renewable Energy*, 2 (1992) 125-128.
- [249] K. Bükler, N. Alonso-Vante, H. Tributsch, Photovoltaic output limitation of n-FeS₂ (pyrite) Schottky barriers: A temperature-dependent characterization, *Journal of Applied Physics*, 72 (1992) 5721-5728.
- [250] G. Chatzitheodorou, S. Fiechter, R. Könenkamp, M. Kunst, W. Jaegermann, H. Tributsch, Thin photoactive FeS₂ (pyrite) films, *Materials Research Bulletin*, 21 (1986) 1481-1487.
- [251] T.E. Webber, Synthesis of Iron Pyrite and Tin (VI) Sulfide Nanoparticles for Potential Application in Solar Cells.
- [252] A. Kirkeminde, B.A. Ruzicka, R. Wang, S. Puna, H. Zhao, S. Ren, Synthesis and Optoelectronic Properties of Two-Dimensional FeS₂ Nanoplates, *ACS Applied Materials & Interfaces*, 4 (2012) 1174-1177.
- [253] D.-Y. Wang, Y.-T. Jiang, C.-C. Lin, S.-S. Li, Y.-T. Wang, C.-C. Chen, C.-W. Chen, Solution-Processable Pyrite FeS₂ Nanocrystals for the Fabrication of Heterojunction Photodiodes with Visible to NIR Photodetection, *Advanced Materials*, 24 (2012) 3415-3420.
- [254] M. Gong, A. Kirkeminde, Y. Xie, R. Lu, J. Liu, J.Z. Wu, S. Ren, Iron Pyrite (FeS₂) Broad Spectral and Magnetically Responsive Photodetectors, *Advanced Optical Materials*, 1 (2013) 78-83.
- [255] A. Kirkeminde, S. Ren, Thermodynamic control of iron pyrite nanocrystal synthesis with high photoactivity and stability, *Journal of Materials Chemistry A*, 1 (2013) 49-54.

- [256] W. Ki, H.W. Hillhouse, Earth-Abundant Element Photovoltaics Directly from Soluble Precursors with High Yield Using a Non-Toxic Solvent, *Advanced Energy Materials*, 1 (2011) 732-735.
- [257] K. Woo, Y. Kim, J. Moon, A non-toxic, solution-processed, earth abundant absorbing layer for thin-film solar cells, *Energy & Environmental Science*, 5 (2012) 5340-5345.
- [258] K. Hui-Seon, L. Chang-Ryul, I. Jeong-Hyeok, L. Ki-Beom, M. Thomas, M. Arianna, M. Soo-Jin, H.-B. Robin, Y. Jun-Ho, E.M. Jacques, G. Michael, P. Nam-Gyu, Lead Iodide Perovskite Sensitized All-Solid-State Submicron Thin Film Mesoscopic Solar Cell with Efficiency Exceeding 9%, *Scientific Reports*, 2 (2012).
- [259] D. Rickard, G.W. Luther, Chemistry of Iron Sulfides, *Chemical Reviews*, 107 (2007) 514-562.
- [260] K.P. Bhandari, P. Koirala, N.R. Paudel, R.R. Khanal, A.B. Phillips, Y. Yan, R.W. Collins, M.J. Heben, R.J. Ellingson, Iron pyrite nanocrystal film serves as a copper-free back contact for polycrystalline CdTe thin film solar cells, *Solar Energy Materials and Solar Cells*, 140 (2015) 108-114.
- [261] First Solar hits cost reduction milestone, 2013 http://www.pv-tech.org/news/has_first_solar_retaken_the_lowest_cost_pv_manufacturer_mantle (2013).
- [262] C.R. Corwine, A.O. Pudov, M. Gloeckler, S.H. Demtsu, J.R. Sites, Copper inclusion and migration from the back contact in CdTe solar cells, *Solar Energy Materials and Solar Cells*, 82 (2004) 481-489.

- [263] T.J. Bernard, D.S. Albin, B. To, J.W. Pankow, M. Young, S.E. Asher, Effects of Cu at the device junction on the properties of CdTe/CdS photovoltaic cells, *Journal of Vacuum Science & Technology B*, 22 (2004) 2423-2428.
- [264] S.H. Demtsu, D.S. Albin, J.R. Sites, W.K. Metzger, A. Duda, Cu-related recombination in CdS/CdTe solar cells, *Thin Solid Films*, 516 (2008) 2251-2254.
- [265] K.K. Chin, T. Gessert, S.-H. Wei, The roles of Cu impurity states in CdTe thin film solar cells, in: *Photovoltaic Specialists Conference (PVSC)*, 2010 35th IEEE, IEEE, 2010, pp. 001915-001918.
- [266] S.-H. Wei, S.B. Zhang, Chemical trends of defect formation and doping limit in II-VI semiconductors: The case of CdTe, *Physical Review B*, 66 (2002) 155211.
- [267] D. Albin, D. Levi, S. Asher, A. Balcioglu, R. Dhere, J. Hiltner, Precontact surface chemistry effects on CdS/CdTe solar cell performance and stability, in: *IEEE 29th Photovoltaic Specialists Conference (PVSC)*, Sept 15-22, 2000, Anchorage, AK, 2000, pp. 583-586.
- [268] J. Liang, H. Bi, D. Wan, F. Huang, Novel Cu Nanowires/Graphene as the Back Contact for CdTe Solar Cells, *Advanced Functional Materials*, 22 (2012) 1267-1271.
- [269] T. Lin, F. Huang, J. Liang, Y. Wang, A facile preparation route for boron-doped graphene, and its CdTe solar cell application, *Energy & Environmental Science*, 4 (2011) 862-865.
- [270] V. Plotnikov, X. Liu, N. Paudel, D. Kwon, K.A. Wieland, A.D. Compaan, Thin-film CdTe cells: Reducing the CdTe, *Thin Solid Films*, 519 (2011) 7134-7137.

- [271] A. Bosio, N. Romeo, S. Mazzamuto, V. Canevari, Polycrystalline CdTe thin films for photovoltaic applications, *Progress in Crystal Growth and Characterization of Materials*, 52 (2006) 247-279.
- [272] K.V. Krishna, V. Dutta, Effect of in situ CdCl₂ treatment on spray deposited CdTe/CdS heterostructure, *Journal of Applied Physics*, 96 (2004) 3962-3971.
- [273] H. Dahman, M. Khalifa, M. Brunel, B. Rezig, Iron pyrite films prepared by sulfur vapor transport, *Thin Solid Films*, 280 (1996) 56-60.
- [274] M.A. Islam, M.S. Hossain, M.M. Aliyu, M.R. Karim, T. Razykov, K. Sopian, N. Amin, Effect of CdCl₂ treatment on structural and electronic property of CdTe thin films deposited by magnetron sputtering, *Thin Solid Films*, 546 (2013) 367-374.
- [275] A.J. Al-Douri, F.Y. Al-Shakily, A.A. Alnajjar, M.F.A. Alias, The Role of Dopant Concentration on Conductivity and Mobility of CdTe Thin Films, *Advances in Condensed Matter Physics*, 2011 (2011).
- [276] S. Trigwell, M.K. Mazumder, R. Pellissier, Tribocharging in electrostatic beneficiation of coal: Effects of surface composition on work function as measured by x-ray photoelectron spectroscopy and ultraviolet photoelectron spectroscopy in air, *Journal of Vacuum Science & Technology A*, 19 (2001) 1454-1459.
- [277] T.J. Bernard, D.S. Albin, B. To, J.W. Pankow, M. Young, S.E. Asher, Effects of Cu at the device junction on the properties of CdTe/CdS photovoltaic cells, *Journal of Vacuum Science & Technology B*, 22 (2004) 2423-2428.

- [278] D. Rioux, D.W. Niles, H. Höchst, ZnTe: A potential interlayer to form low resistance back contacts in CdS/CdTe solar cells, *Journal of applied physics*, 73 (1993) 8381-8385.
- [279] N. Strevel, L. Trippel, C. Kotarba, I. Khan, Improvements in CdTe module reliability and long-term degradation through advances in construction and device innovation, *Photovoltaic international*, (2014).
- [280] K. Durose, P.R. Edwards, D.P. Halliday, Materials aspects of CdTe/CdS solar cells, *Journal of Crystal Growth*, 197 (1999) 733-742.
- [281] R.J. Hager, E.S. Johnson, W. Scott, E.L. Stelzer, Ohmic contacts to p-type mercury cadmium telluride, in, *Google Patents*, 1976.
- [282] S. Demtsu, J. Sites, Effect of back-contact barrier on thin-film CdTe solar cells, *Thin Solid Films*, 510 (2006) 320-324.
- [283] M. Köntges, R. Reineke-Koch, P. Nollet, J. Beier, R. Schäffler, J. Parisi, Light induced changes in the electrical behavior of CdTe and Cu (In, Ga) Se 2 solar cells, *Thin Solid Films*, 403 (2002) 280-286.
- [284] D.L. Bätzner, R. Wendt, A. Romeo, H. Zogg, A.N. Tiwari, A study of the back contacts on CdTe/CdS solar cells, *Thin Solid Films*, 361–362 (2000) 463-467.
- [285] N.R. Paudel, Y. Yan, Fabrication and characterization of high-efficiency CdTe-based thin-film solar cells on commercial SnO₂:F-coated soda-lime glass substrates, *Thin Solid Films*, 549 (2013) 30-35.
- [286] R. Mauer, I.A. Howard, F. Laquai, Effect of Nongeminate Recombination on Fill Factor in Polythiophene/Methanofullerene Organic Solar Cells, *The Journal of Physical Chemistry Letters*, 1 (2010) 3500-3505.

- [287] H. Graaf, M. Vieluf, C.v. Borczyskowski, Selective binding of dye molecules and CdSe nanocrystals on nanostructures generated by AFM lithography of silicon surfaces, *Nanotechnology*, 18 (2007) 265306.
- [288] I.L. Eisgruber, J.E. Granata, J.R. Sites, J. Hou, J. Kessler, Blue-photon modification of nonstandard diode barrier in CuInSe₂ solar cells, *Solar Energy Materials and Solar Cells*, 53 (1998) 367-377.
- [289] J.C. Wang, X.C. Ren, S.Q. Shi, C.W. Leung, P.K.L. Chan, Charge accumulation induced S-shape J–V curves in bilayer heterojunction organic solar cells, *Organic Electronics*, 12 (2011) 880-885.
- [290] W. Tress, K. Leo, M. Riede, Influence of Hole-Transport Layers and Donor Materials on Open-Circuit Voltage and Shape of I–V Curves of Organic Solar Cells, *Advanced Functional Materials*, 21 (2011) 2140-2149.
- [291] N. Peyghambarian, S.W. Koch, A. Mysyrowicz, Introduction to semiconductor optics, Prentice-Hall, Inc., 1994.
- [292] Y. Varshni, Temperature dependence of the energy gap in semiconductors, *Physica*, 34 (1967) 149-154.
- [293] B. Van Zeghbroeck, Principles of semiconductor devices, Colorado University, (2004).
- [294] G. Mahan, Temperature dependence of the band gap in CdTe, *Journal of Physics and Chemistry of Solids*, 26 (1965) 751-756.
- [295] D. Poelman, J. Vennik, The temperature dependence of the optical properties of thin CdTe films, *Journal of Physics D: Applied Physics*, 21 (1988) 1004.

- [296] X. Mathew, Band gap of CdTe thin films—The dependence on temperature, *Journal of materials science letters*, 21 (2002) 529-531.
- [297] G. Fonthal, L. Tirado-Mejía, J.I. Marín-Hurtado, H. Ariza-Calderón, J.G. Mendoza-Alvarez, Temperature dependence of the band gap energy of crystalline CdTe, *Journal of Physics and Chemistry of Solids*, 61 (2000) 579-583.
- [298] A. Manoogian, J. Woolley, Temperature dependence of the energy gap in semiconductors, *Canadian journal of physics*, 62 (1984) 285-287.
- [299] W. Mönch, N.J. Dinardo, Semiconductor surfaces and interfaces, *Physics Today*, 47 (2008) 66-67.
- [300] J.C. Perrenoud, Low temperature grown CdTe thin film solar cells for the application on flexible substrates, in, *Diss., Eidgenössische Technische Hochschule ETH Zürich*, Nr. 20460, 2012, 2012.
- [301] E. Katz, D. Faiman, S. Tuladhar, J. Kroon, M. Wienk, T. Fromherz, F. Padinger, C. Brabec, N. Sariciftci, Temperature dependence for the photovoltaic device parameters of polymer-fullerene solar cells under operating conditions, *Journal of Applied Physics*, 90 (2001) 5343-5350.
- [302] R.W. Meulenber, J.R.I. Lee, A. Wolcott, J.Z. Zhang, L.J. Terminello, T. van Buuren, Determination of the Exciton Binding Energy in CdSe Quantum Dots, *ACS Nano*, 3 (2009) 325-330.
- [303] M. Bouroushian, *Electrochemistry of metal chalcogenides*, Springer, 2010.
- [304] W. Melitz, J. Shen, A.C. Kummel, S. Lee, Kelvin probe force microscopy and its application, *Surface Science Reports*, 66 (2011) 1-27.

- [305] S. Kitamura, K. Suzuki, M. Iwatsuki, High resolution imaging of contact potential difference using a novel ultrahigh vacuum non-contact atomic force microscope technique, *Applied Surface Science*, 140 (1999) 265-270.
- [306] C. Sommerhalter, T.W. Matthes, T. Glatzel, A. Jäger-Waldau, M.C. Lux-Steiner, High-sensitivity quantitative Kelvin probe microscopy by noncontact ultra-high-vacuum atomic force microscopy, *Applied Physics Letters*, 75 (1999) 286-288.
- [307] S. Sadewasser, T. Glatzel, M. Rusu, A. Jäger-Waldau, M.C. Lux-Steiner, High-resolution work function imaging of single grains of semiconductor surfaces, *Applied Physics Letters*, 80 (2002) 2979-2981.
- [308] T. Glatzel, S. Sadewasser, M.C. Lux-Steiner, Amplitude or frequency modulation-detection in Kelvin probe force microscopy, *Applied Surface Science*, 210 (2003) 84-89.
- [309] J.J. Urban, D.V. Talapin, E.V. Shevchenko, C.B. Murray, Self-Assembly of PbTe Quantum Dots into Nanocrystal Superlattices and Glassy Films, *Journal of the American Chemical Society*, 128 (2006) 3248-3255.
- [310] V.L. Colvin, A.P. Alivisatos, J.G. Tobin, Valence-band photoemission from a quantum-dot system, *Physical Review Letters*, 66 (1991) 2786-2789.
- [311] Y. Park, V. Choong, Y. Gao, B.R. Hsieh, C.W. Tang, Work function of indium tin oxide transparent conductor measured by photoelectron spectroscopy, *Applied Physics Letters*, 68 (1996) 2699-2701.
- [312] G. Liu, T. Schulmeyer, J. Brötz, A. Klein, W. Jaegermann, Interface properties and band alignment of Cu₂S/CdS thin film solar cells, *Thin Solid Films*, 431-432 (2003) 477-482.

- [313] K.P. Bhandari, H. Choi, S. Jeong, H. Mahabaduge, R.J. Ellingson, Determination of heterojunction band offsets between CdS bulk and PbS quantum dots using photoelectron spectroscopy, *Applied Physics Letters*, 105 (2014) 131604.
- [314] D.J. Asunskis, L. Hanley, Valence band and core level X-ray photoelectron spectroscopy of lead sulfide nanoparticle–polymer composites, *Surface Science*, 601 (2007) 4648-4656.
- [315] C.D. Bain, H.A. Biebuyck, G.M. Whitesides, Comparison of self-assembled monolayers on gold: coadsorption of thiols and disulfides, *Langmuir*, 5 (1989) 723-727.
- [316] V. Švorčík, Z. Kolská, O. Kvítek, J. Siegel, A. Řezníčková, P. Řezanka, K. Záruba, "Soft and rigid" dithiols and Au nanoparticles grafting on plasma-treated polyethyleneterephthalate, *Nanoscale research letters*, 6 (2011) 1-7.
- [317] R.G. Nuzzo, B.R. Zegarski, L.H. Dubois, Fundamental studies of the chemisorption of organosulfur compounds on gold(111). Implications for molecular self-assembly on gold surfaces, *Journal of the American Chemical Society*, 109 (1987) 733-740.
- [318] L. Scudiero, www.wsu.edu/~scudiero.
- [319] W. Lee, H. Kim, D.-R. Jung, J. Kim, C. Nahm, J. Lee, S. Kang, B. Lee, B. Park, An effective oxidation approach for luminescence enhancement in CdS quantum dots by H₂O₂, *Nanoscale Research Letters*, 7 (2012) 1-5.
- [320] R.B. Shalvoy, G.B. Fisher, P.J. Stiles, Bond ionicity and structural stability of some average-valence-five materials studied by x-ray photoemission, *Physical Review B*, 15 (1977) 1680-1697.

- [321] K. Laajalehto, R.S.C. Smart, J. Ralston, E. Suoninen, STM and XPS investigation of reaction of galena in air, *Applied Surface Science*, 64 (1993) 29-39.
- [322] S. Ciampi, V. di Castro, G. Polzonetti, XPS study of cadmium oxidation in air, *Journal of Electron Spectroscopy and Related Phenomena*, 56 (1991) R1-R6.
- [323] J.R. Waldrop, R.W. Grant, S.P. Kowalczyk, E.A. Kraut, Measurement of semiconductor heterojunction band discontinuities by X-ray photoemission spectroscopy, *Journal of Vacuum Science & Technology A: Vacuum, Surfaces, and Films*, 3 (1985) 835-841.
- [324] E.T. Yu, D.H. Chow, T.C. McGill, Commutativity of the GaAs/AlAs (100) band offset, *Journal of Vacuum Science & Technology B: Microelectronics and Nanometer Structures*, 7 (1989) 391-394.
- [325] E.A. Douglas, A. Scheurmann, R.P. Davies, B.P. Gila, H. Cho, V. Craciun, E.S. Lambers, S.J. Pearton, F. Ren, Measurement of SiO₂/InZnGaO₄ heterojunction band offsets by x-ray photoelectron spectroscopy, *Applied Physics Letters*, 98 (2011) 242110-242113.
- [326] J. Tersoff, C.G. Van de Walle, Strain and the interpretation of band-lineup measurements, *Physical Review Letters*, 59 (1987) 946-946.
- [327] G.P. Schwartz, M.S. Hybertsen, J. Bevk, R.G. Nuzzo, J.P. Mannaerts, G.J. Gualtieri, Core-level photoemission measurements of valence-band offsets in highly strained heterojunctions: Si-Ge system, *Physical Review B*, 39 (1989) 1235-1241.
- [328] E.T. Yu, E.T. Croke, D.H. Chow, D.A. Collins, M.C. Phillips, T.C. McGill, J.O. McCaldin, R.H. Miles, Measurement of the valence band offset in novel

- heterojunction systems: Si/Ge (100) and AlSb/ZnTe (100), *Journal of Vacuum Science & Technology B: Microelectronics and Nanometer Structures*, 8 (1990) 908-915.
- [329] N.G. Stoffel, Experimental band structure of cadmium sulfide, *Physical Review B*, 28 (1983) 3306-3319.
- [330] O. Madelung, *Semiconductors: Other than group IV elements and III-V compounds*, Springer-Verlag, 1992.
- [331] I. Kang, F.W. Wise, Electronic structure and optical properties of PbS and PbSe quantum dots, *J. Opt. Soc. Am. B*, 14 (1997) 1632-1646.
- [332] E.A. Kraut, R.W. Grant, J.R. Waldrop, S.P. Kowalczyk, Semiconductor core-level to valence-band maximum binding-energy differences: Precise determination by x-ray photoelectron spectroscopy, *Physical Review B*, 28 (1983) 1965-1977.
- [333] J.R. Waldrop, R.W. Grant, Measurement of AlN/GaN (0001) heterojunction band offsets by x-ray photoemission spectroscopy, *Applied Physics Letters*, 68 (1996) 2879-2881.
- [334] A. Klein, C. Körber, A. Wachau, F. Säuberlich, Y. Gassenbauer, S.P. Harvey, D.E. Proffit, T.O. Mason, Transparent conducting oxides for photovoltaics: manipulation of Fermi level, work function and energy band alignment, *Materials*, 3 (2010) 4892-4914.
- [335] A. Santoni, F. Biccari, C. Malerba, M. Valentini, R. Chierchia, A. Mittiga, Valence band offset at the CdS/Cu₂ZnSnS₄ interface probed by x-ray

- photoelectron spectroscopy, *Journal of Physics D: Applied Physics*, 46 (2013) 175101.
- [336] K. Ellmer, A. Klein, B. Rech, *Transparent Conductive Zinc Oxide: Basics And Applications In Thin Film Solar Cells* (Springer Series In Materials Science, (2010).
- [337] F. Cucchiella, I. D'Adamo, Estimation of the energetic and environmental impacts of a roof-mounted building-integrated photovoltaic systems, *Renewable and Sustainable Energy Reviews*, 16 (2012) 5245-5259.
- [338] V. Fthenakis, Sustainability of photovoltaics: The case for thin-film solar cells, *Renewable and Sustainable Energy Reviews*, 13 (2009) 2746-2750.
- [339] J. Peng, L. Lu, H. Yang, Review on life cycle assessment of energy payback and greenhouse gas emission of solar photovoltaic systems, *Renewable and Sustainable Energy Reviews*, 19 (2013) 255-274.
- [340] M. Brandão, G. Heath, J. Cooper, What Can Meta-Analyses Tell Us About the Reliability of Life Cycle Assessment for Decision Support?, *Journal of Industrial Ecology*, 16 (2012) S3-S7.
- [341] R. Lifset, Toward Meta-Analysis in Life Cycle Assessment, *Journal of Industrial Ecology*, 16 (2012) S1-S2.
- [342] S. Pacca, D. Sivaraman, G.A. Keoleian, Parameters affecting the life cycle performance of PV technologies and systems, *Energy Policy*, 35 (2007) 3316-3326.
- [343] A. Meijer, M.A.J. Huijbregts, J.J. Schermer, L. Reijnders, Life-cycle assessment of photovoltaic modules: Comparison of mc-Si, InGaP and InGaP/mc-Si solar

- modules, *Progress in Photovoltaics: Research and Applications*, 11 (2003) 275-287.
- [344] Fraunhofer Institute for solar energy systems ISE, <http://www.ise.fraunhofer.de/de/downloads/pdf-files/aktuelles/photovoltaics-report-in-englischer-sprache.pdf>, in, 2013.
- [345] A. Armaou, P.D. Christofides, Crystal temperature control in the Czochralski crystal growth process, *AIChE Journal*, 47 (2001) 79-106.
- [346] M. Moravej, S.E. Babayan, G.R. Nowling, X. Yang, R.F. Hicks, Plasma enhanced chemical vapour deposition of hydrogenated amorphous silicon at atmospheric pressure, *Plasma Sources Science and Technology*, 13 (2004) 8.
- [347] O. Yan Ying, C. Bang Tao, E.H.T. Francis, I. Ciprian, Process Analysis and Optimization on PECVD Amorphous Silicon on Glass Substrate, *Journal of Physics: Conference Series*, 34 (2006) 812.
- [348] D.M. Tanenbaum, A.L. Laracuate, A. Gallagher, Surface roughening during plasma-enhanced chemical-vapor deposition of hydrogenated amorphous silicon on crystal silicon substrates, *Physical Review B*, 56 (1997) 4243-4250.
- [349] V.M. Fthenakis, Life cycle impact analysis of cadmium in CdTe PV production, *Renewable and Sustainable Energy Reviews*, 8 (2004) 303-334.
- [350] R. Wendt, A. Fischer, D. Grecu, A.D. Compaan, Improvement of CdTe solar cell performance with discharge control during film deposition by magnetron sputtering, *Journal of Applied Physics*, 84 (1998) 2920-2925.

- [351] F.A. Abou-Elfotouh, T.J. Coutts, RF PLANAR MAGNETRON SPUTTERING OF POLYCRYSTALLINE CdTe THIN-FILM SOLAR CELLS, *International Journal of Solar Energy*, 12 (1992) 223-231.
- [352] R. Kannan, J. Keane, R. Noufi, Properties of high-efficiency CIGS thin-film solar cells, in: *Photovoltaic Specialists Conference, 2005. Conference Record of the Thirty-first IEEE, 2005*, pp. 195-198.
- [353] T.M. Razykov, C.S. Ferekides, D. Morel, E. Stefanakos, H.S. Ullal, H.M. Upadhyaya, Solar photovoltaic electricity: Current status and future prospects, *Solar Energy*, 85 (2011) 1580-1608.
- [354] S.J.C. Irvine, V. Barrioz, D. Lamb, E.W. Jones, R.L. Rowlands-Jones, MOCVD of thin film photovoltaic solar cells—Next-generation production technology?, *Journal of Crystal Growth*, 310 (2008) 5198-5203.
- [355] L. Kranz, C. Gretener, J. Perrenoud, R. Schmitt, F. Pianezzi, F. La Mattina, P. Blösch, E. Cheah, A. Chirilă, C.M. Fella, Doping of polycrystalline CdTe for high-efficiency solar cells on flexible metal foil, *Nature communications*, 4 (2013).
- [356] K.P. Bhandari, P. Koirala, N.R. Paudel, R.R. Khanal, A.B. Phillips, Y. Yan, R.W. Collins, M.J. Heben, R.J. Ellingson, Iron pyrite nanocrystal film serves as a copper-free back contact for polycrystalline CdTe thin film solar cells.
- [357] R.W. Miles, Photovoltaic solar cells: Choice of materials and production methods, *Vacuum*, 80 (2006) 1090-1097.

- [358] M. Vázquez, I. Rey-Stolle, Photovoltaic module reliability model based on field degradation studies, *Progress in Photovoltaics: Research and Applications*, 16 (2008) 419-433.
- [359] J.H. Wohlgemuth, D.W. Cunningham, P. Monus, J. Miller, A. Nguyen, Long term reliability of photovoltaic modules, in: *Photovoltaic Energy Conversion, Conference Record of the 2006 IEEE 4th World Conference on*, IEEE, 2006, pp. 2050-2053.
- [360] D.D. Hsu, P. O'Donoghue, V. Fthenakis, G.A. Heath, H.C. Kim, P. Sawyer, J.-K. Choi, D.E. Turney, Life Cycle Greenhouse Gas Emissions of Crystalline Silicon Photovoltaic Electricity Generation, *Journal of Industrial Ecology*, 16 (2012) S122-S135.
- [361] H.C. Kim, V. Fthenakis, J.-K. Choi, D.E. Turney, Life Cycle Greenhouse Gas Emissions of Thin-film Photovoltaic Electricity Generation, *Journal of Industrial Ecology*, 16 (2012) S110-S121.
- [362] N. Strevel, L. Trippel, M. Gloeckler, Performance characterization and superior energy yield of First Solar PV power plants in high-temperature conditions, *Photovoltaics Int*, 17 (2012) 148-154.
- [363] V. Fthenakis, R. Frischknecht, M. Raugei, H. Kim, E. Alsema, M. Held, M. de Wild-Scholten, Methodology guidelines on life cycle assessment of photovoltaic electricity, *IEA PVPS Task*, 12 (2011).
- [364] E. Alsema, D. Fraile, R. Frischknecht, V. Fthenakis, M. Held, H. Kim, W. Pölz, M. Raugei, M. de Wild Scholten, Methodology guidelines on life cycle assessment of photovoltaic electricity, *IEA PVPS Task*, 12 (2009).

- [365] N.H. Reich, B. Mueller, A. Armbruster, W.G. Sark, K. Kiefer, C. Reise, Performance ratio revisited: is PR > 90% realistic?, *Progress in Photovoltaics: Research and Applications*, 20 (2012) 717-726.
- [366] G. Phylipsen, E. Alsema, Environmental life-cycle assessment of multicrystalline silicon solar cell modules, Department of Science, Technology and Society, Utrecht University, 1995.
- [367] E.A. Alsema, M.J. de Wild-Scholten, Environmental Impacts of Crystalline Silicon Photovoltaic Module Production, in: 13th CIRP Intern. Conf. on Life Cycle Engineering, Leuven, Belgium, 2006.
- [368] E.A. Alsema, Energy payback time and CO₂ emissions of PV systems, *Progress in Photovoltaics: Research and Applications*, 8 (2000) 17-25.
- [369] K. Ardani, R. Margolis, 2010 Solar Technologies Market Report, in, US Department of Energy, 2011, pp. 1-121.
- [370] R. Margolis, C. Coggeshall, J. Zuboy, SunShot Vision Study, in, US Department of Energy, 2012.
- [371] R. Battisti, A. Corrado, Evaluation of technical improvements of photovoltaic systems through life cycle assessment methodology, *Energy*, 30 (2005) 952-967.
- [372] L. Lu, H.X. Yang, Environmental payback time analysis of a roof-mounted building-integrated photovoltaic (BIPV) system in Hong Kong, *Applied Energy*, 87 (2010) 3625-3631.
- [373] M. Held, Life cycle assessment of CdTe module recycling, in: *Proceedings*, 2009, pp. 21-25.

- [374] A.F. Sherwani, J.A. Usmani, Varun, Siddhartha, Life cycle assessment of 50 kWp grid connected solar photovoltaic (SPV) system in India, *International Journal of Energy and Environment*, 2 (2011) 49-56.
- [375] N. Jungbluth, Life cycle assessment of crystalline photovoltaics in the Swiss ecoinvent database, *Progress in Photovoltaics: Research and Applications*, 13 (2005) 429-446.
- [376] T. Muneer, S. Younes, N. Lambert, J. Kubie, Life cycle assessment of a medium-sized photovoltaic facility at a high latitude location, *Proceedings of the Institution of Mechanical Engineers, Part A: Journal of Power and Energy*, 220 (2006) 517-524.
- [377] G. Bizzarri, G.L. Morini, A Life Cycle Analysis of roof integrated photovoltaic systems, *International Journal of Environmental Technology and Management*, 7 (2007) 134-146.
- [378] N. Jungbluth, R. Dones, R. Frischknecht, Life Cycle Assessment of Photovoltaics; Update of the ecoinvent Database, *MRS Online Proceedings Library*, 1041 (2007) null-null.
- [379] R. García-Valverde, C. Miguel, R. Martínez-Béjar, A. Urbina, Life cycle assessment study of a 4.2 kWp stand-alone photovoltaic system, *Solar Energy*, 83 (2009) 1434-1445.
- [380] R. Laleman, J. Albrecht, J. Dewulf, Life Cycle Analysis to estimate the environmental impact of residential photovoltaic systems in regions with a low solar irradiation, *Renewable and Sustainable Energy Reviews*, 15 (2011) 267-281.

- [381] M.J. de Wild-Scholten, Energy payback time and carbon footprint of commercial photovoltaic systems, *Solar Energy Materials and Solar Cells*, 119 (2013) 296-305.
- [382] M. Raugei, S. Bargigli, S. Ulgiati, Life cycle assessment and energy pay-back time of advanced photovoltaic modules: CdTe and CIS compared to poly-Si, *Energy*, 32 (2007) 1310-1318.
- [383] V. Fthenakis, H. Kim, M. Held, M. Raugei, J. Krones, Update of PV energy payback times and life-cycle greenhouse gas emissions, in: *24th European Photovoltaic Solar Energy Conference and Exhibition*, 2009, pp. 4412-4416.
- [384] H. Kim, K. Cha, B. Kim, V.M. Fthenakis, T. Hur, Life Cycle Assessment of CdTe Photovoltaic System, in: *Proceedings of EcoDesign 2011: 7th International Symposium on Environmentally Conscious Design and Inverse Manufacturing*, Springer, 2012, pp. 1018-1020.
- [385] E. Alsema, Energy requirements and CO₂ mitigation potential of PV systems, (1998).
- [386] E.A. Alsema, P. Frankl, K. Kato, Energy payback time of photovoltaic energy systems: present status and prospects, in: *2nd World Conference on Photovoltaic Energy Conversion*, Vienna, 1998.
- [387] H. Schaefer, G. Hagedorn, Hidden energy and correlated environmental characteristics of P.V. power generation, *Renewable Energy*, 2 (1992) 159-166.
- [388] M. Ito, K. Komoto, K. Kurokawa, Life-cycle analyses of very-large scale PV systems using six types of PV modules, *Current Applied Physics*, 10 (2010) S271-S273.

- [389] E.A. Alsema, Environmental aspects of solar cell modules: summary report, Department of Science, Technology and Society, University Utrecht, 1996.
- [390] P.J. Meier, Kulcinski, Life-Cycle Energy Costs and Greenhouse Gas Emissions for Building-Integrated Photovoltaics, in, 2002.
- [391] US Solar Market Insight, 2010 Year in Review, (2010).
- [392] D. Gielen, Renewable Energy Technologies: cost Analysis Series, Solar Photovoltaics, 1 (2012) 52.
- [393] <http://www.nrel.gov/ncpv/>, (2012).
- [394] W. Shockley, H.J. Queisser, Detailed Balance Limit of Efficiency of p-n Junction Solar Cells, Journal of Applied Physics, 32 (1961) 510-519.
- [395] M. Raugei, P. Fullana-i-Palmer, V. Fthenakis, The energy return on energy investment (EROI) of photovoltaics: Methodology and comparisons with fossil fuel life cycles, Energy Policy, 45 (2012) 576-582.
- [396] W. Ma, J.M. Luther, H. Zheng, Y. Wu, A.P. Alivisatos, Photovoltaic Devices Employing Ternary PbS x Se_{1-x} Nanocrystals, Nano letters, 9 (2009) 1699-1703.
- [397] J.P. Wilcoxon, P.P. Newcomer, G.A. Samara, Strong quantum confinement effects in semiconductors: FeS₂ nanoclusters, Solid State Communications, 98 (1996) 581-585.
- [398] C.B. Murray, C.R. Kagan, M.G. Bawendi, Synthesis and characterization of monodisperse nanocrystals and close-packed nanocrystal assemblies, Annual Review of Materials Science, 30 (2000) 545-610.
- [399] E. Lifshitz, M. Brumer, A. Kigel, A. Sashchiuk, M. Bashouti, M. Sirota, E. Galun, Z. Burshtein, A.Q. Le Quang, I. Ledoux-Rak, J. Zyss, Air-Stable PbSe/PbS and

- PbSe/PbSexS_{1-x} Core–Shell Nanocrystal Quantum Dots and Their Applications†, *The Journal of Physical Chemistry B*, 110 (2006) 25356-25365.
- [400] A. Fu, W. Gu, C. Larabell, A.P. Alivisatos, Semiconductor nanocrystals for biological imaging, *Current Opinion in Neurobiology*, 15 (2005) 568-575.
- [401] S.C. Erwin, L. Zu, M.I. Haftel, A.L. Efros, T.A. Kennedy, D.J. Norris, Doping semiconductor nanocrystals, *Nature*, 436 (2005) 91-94.
- [402] D.J. Norris, A.L. Efros, S.C. Erwin, Doped Nanocrystals, *Science*, 319 (2008) 1776-1779.
- [403] G.M. Dalpian, J.R. Chelikowsky, Self-Purification in Semiconductor Nanocrystals, *Physical Review Letters*, 96 (2006) 226802.
- [404] D.V. Talapin, C.B. Murray, PbSe Nanocrystal Solids for n- and p-Channel Thin Film Field-Effect Transistors, *Science*, 310 (2005) 86-89.
- [405] D. Yu, C. Wang, P. Guyot-Sionnest, n-Type Conducting CdSe Nanocrystal Solids, *Science*, 300 (2003) 1277-1280.
- [406] S.T. Ochsenbein, Y. Feng, K.M. Whitaker, E. Badaeva, W.K. Liu, X. Li, D.R. Gamelin, Charge-controlled magnetism in colloidal doped semiconductor nanocrystals, *Nat Nano*, 4 (2009) 681-687.
- [407] D.A. Bussian, S.A. Crooker, M. Yin, M. Brynda, A.L. Efros, V.I. Klimov, Tunable magnetic exchange interactions in manganese-doped inverted core-shell ZnSe-CdSe nanocrystals, *Nat Mater*, 8 (2009) 35-40.
- [408] D. Chen, R. Viswanatha, G.L. Ong, R. Xie, M. Balasubramanian, X. Peng, Temperature Dependence of “Elementary Processes” in Doping Semiconductor Nanocrystals, *Journal of the American Chemical Society*, 131 (2009) 9333-9339.

- [409] R. Viswanatha, S. Brovelli, A. Pandey, S.A. Crooker, V.I. Klimov, Copper-Doped Inverted Core/Shell Nanocrystals with “Permanent” Optically Active Holes, *Nano Letters*, 11 (2011) 4753-4758.
- [410] P. Van Mieghem, Theory of band tails in heavily doped semiconductors, *Reviews of modern physics*, 64 (1992) 755.
- [411] X. Wang, G.I. Koleilat, J. Tang, H. Liu, I.J. Kramer, R. Debnath, L. Brzozowski, D.A.R. Barkhouse, L. Levina, S. Hoogland, Tandem colloidal quantum dot solar cells employing a graded recombination layer, *Nature Photonics*, 5 (2011) 480-484.

Appendix A

Solar cell performance of iron pyrite

The author used (1) as-synthesized, (2) hydrazine treated, and (3) hydrazine treated and annealed FeS₂ NC films for the fabrication of Schottky junction and heterojunction solar cells employing FeS₂ as the absorber layer. In the efforts to create FeS₂ absorber layer heterojunction devices, the window layer (e.g. CdS, ZnO, NC-SnS₂) transmitted most of the solar spectrum, and those photons absorbed within the n-type window layer did not generate meaningful photocurrent. Figure A-1 shows current voltage characteristics of CdS/Fe_xS_y heterojunction solar cell.

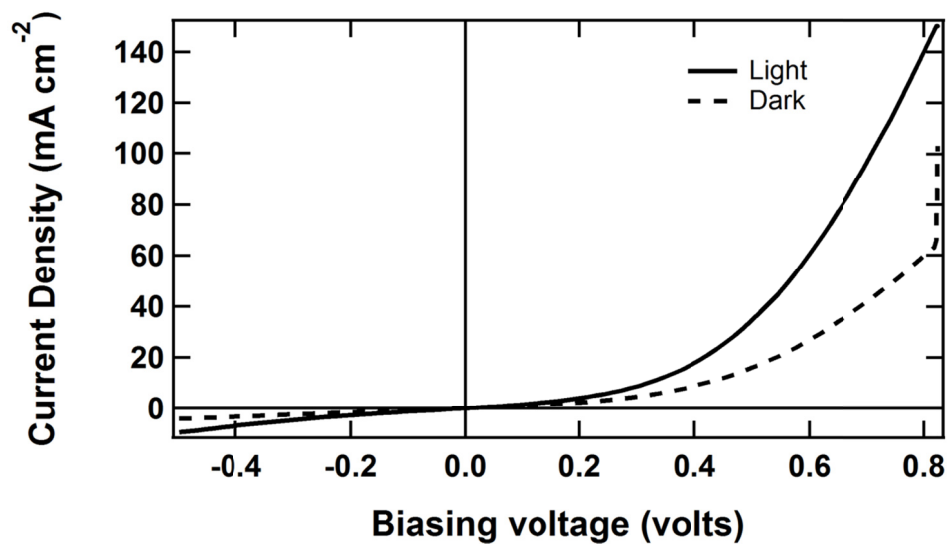


Figure A-1. Device structure ITO/CdS/Fe_xS_y/Au; Here Fe_xS_y was mixture of FeS and cubic FeS₂.

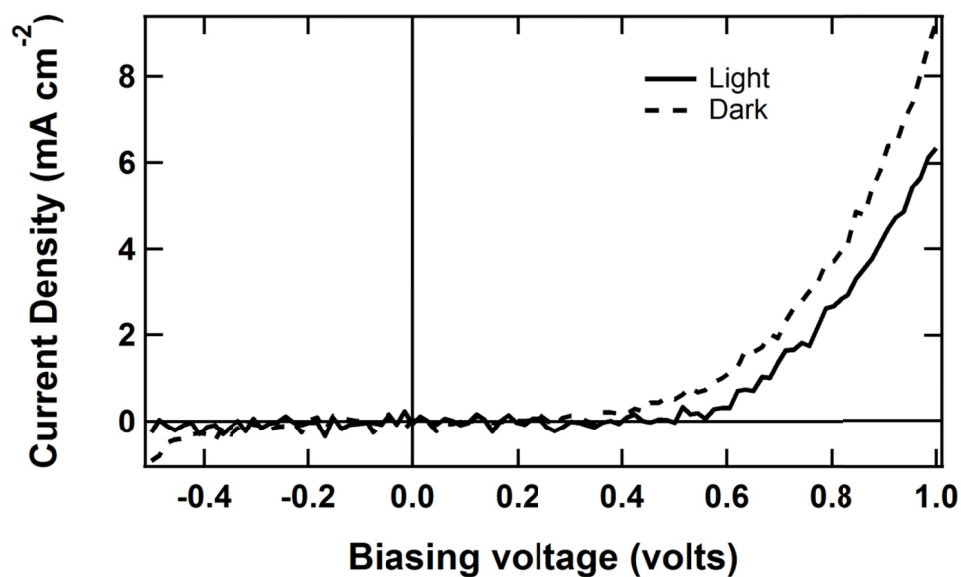


Figure A-2. Device structure: HRT/TEC15/FeS₂/Al; I rarely got this J-V curve out of numerous Schottky devices. Here, we can see a diode behavior even though the cell parameters are unbelievable. This was from a pure pyrite NCs.

In Figure A-2, V_{OC} was 0.298 volts, J_{SC} was 0.056 mA cm^{-2} , FF 368.8% and PCE was 0.061%. This device was made from 100% pure iron pyrite and during LbL process, ligand exchange was done with hydrazine (1M in EtOH)

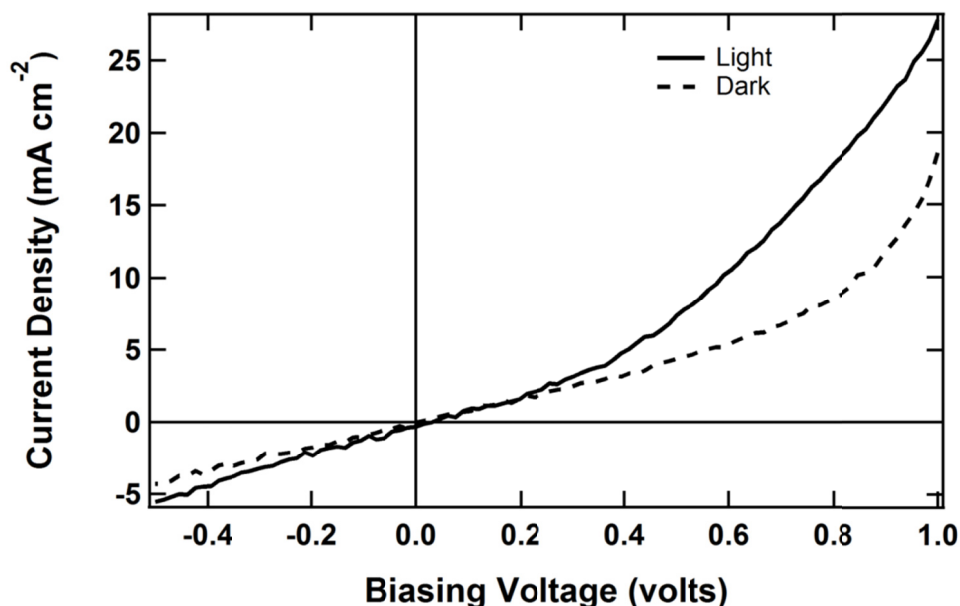


Figure A-3. Device structure: ITO/FeS₂/Al; this is the best device I have ever got from this structure. It is attempting to show diode behavior.

In Figure A-3, V_{OC} was 0.033 volts, J_{SC} was 0.363 mA cm^{-2} , FF 16.1% and PCE was 0.002%. This device was also made from pure pyrite film. During the LbL process, film was treated with hydrazine.

None of the heterojunction devices made from iron pyrite as an absorbing layer and ZnO, CdS or SnS₂ as a window layer showed any performance. I could not get even a diode behavior from these devices. Both ITO coated as well as HRT/TEC15 coated glasses were used as substrates. A representing current voltage characteristics curve from these devices look like as shown in Figure A-4.

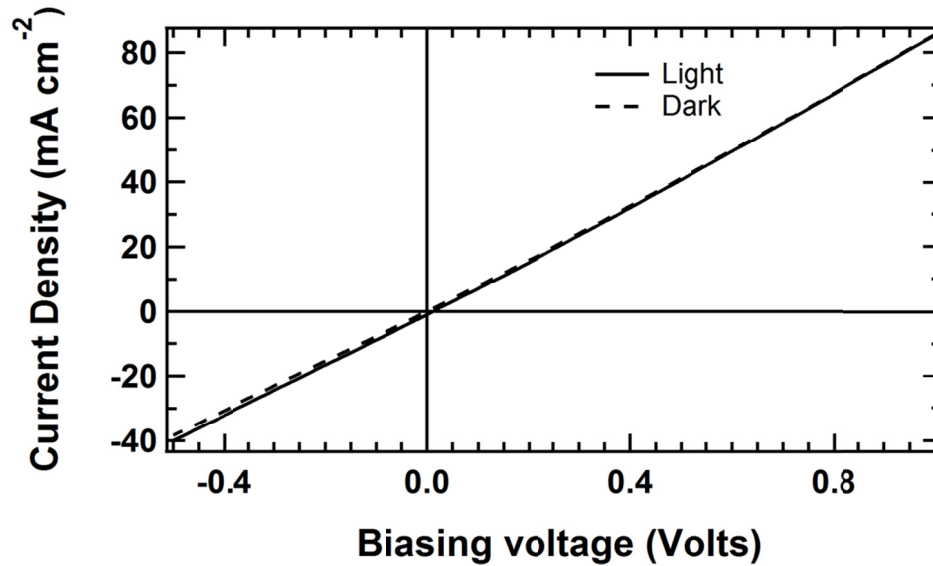


Figure A-4. Device structure: HRT/TEC-15 (or ITO)/CdS or ZnO or SnS₂/FeS₂/Au; FeS₂ film thickness did not bring any change in the results. Treatment of the film both by hydrazine and sintering also did not bring any change in the final results. In all these cases, I got straight line passing through the origin.

There was no any built in voltage in the heterojunction between the two semiconductors. The cause of this was later found to be the higher conductivity of pyrite films. Their exceeding high carrier concentration did not allow window layer to make a depletion region in the absorbing layer.

Appendix B

Second derivative of JV curves when FeS₂/Au and Cu/Au were used as back contacts for CdTe devices prepared from CSS deposition methods

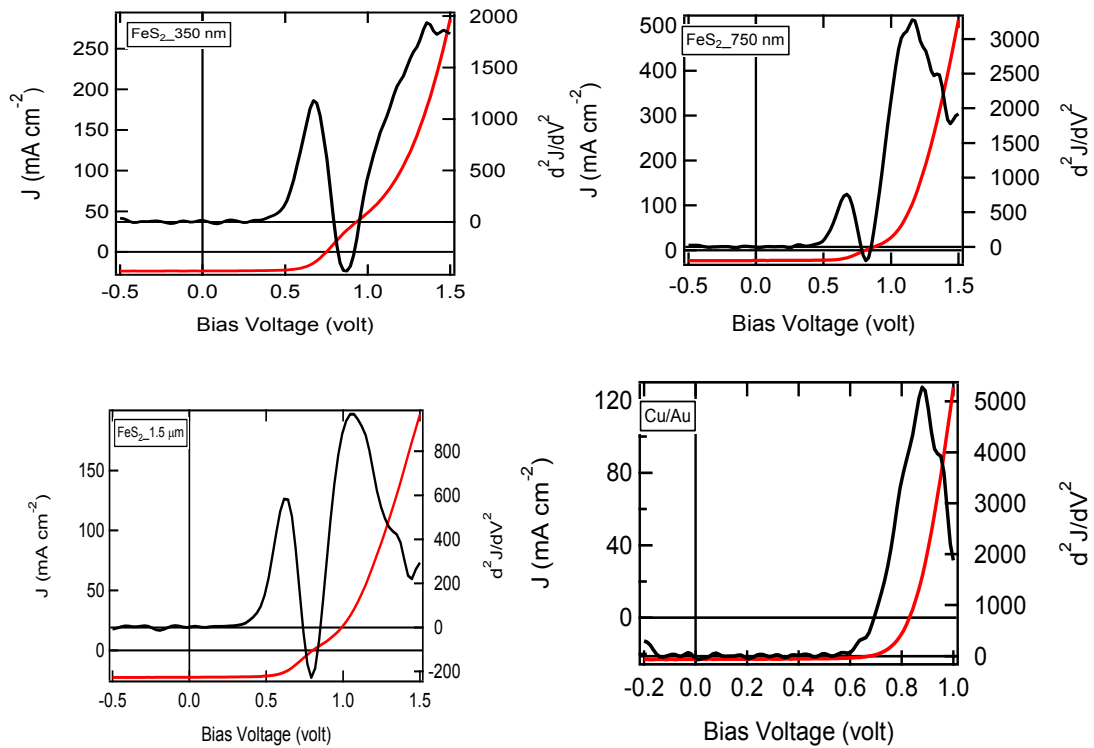
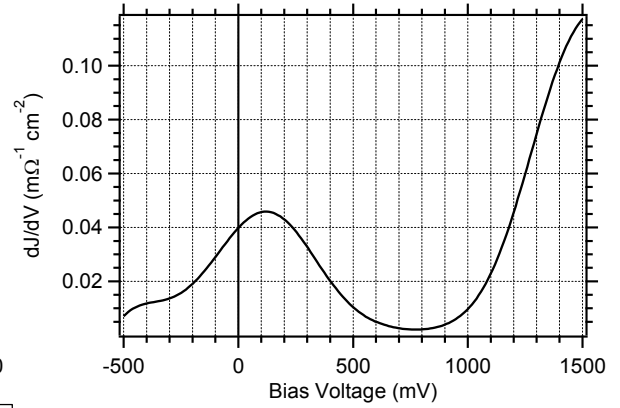
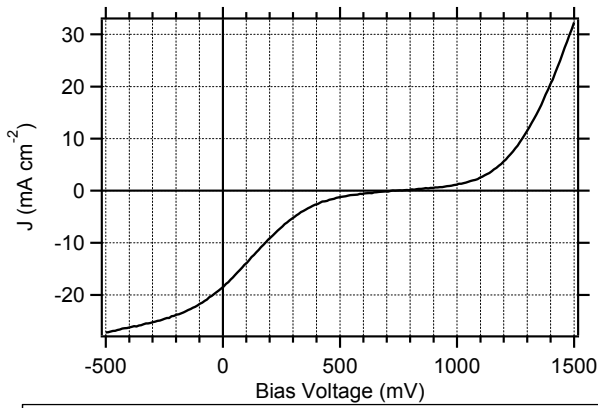


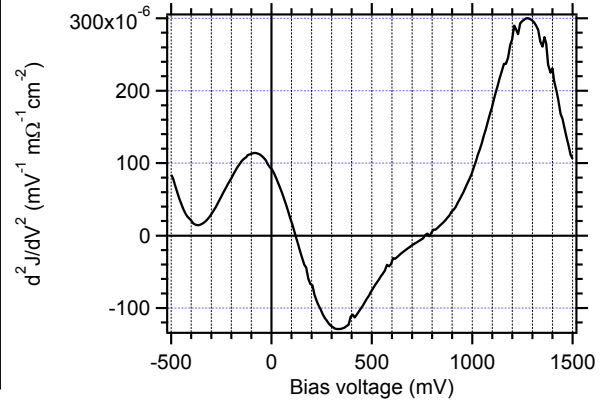
Figure B-1. Second derivative of JV curves obtained from high efficient CSS CdTe when Cu/Au and FeS₂/Au were used as back contacts.

Appendix C

Derivatives of JV curves (light) when FeS₂ (untreated)/Au, and FeS₂ (treated)/Au were used as back contacts for sputtered CdS/CdTe solar cells



These three graphs provide zero, first and second derivatives of current density with respect to bias voltage for CdS/CdTe device with FeS₂ NC (as synthesized)/Au back contact. Values of second derivative within the band gap of CdTe are all negative.



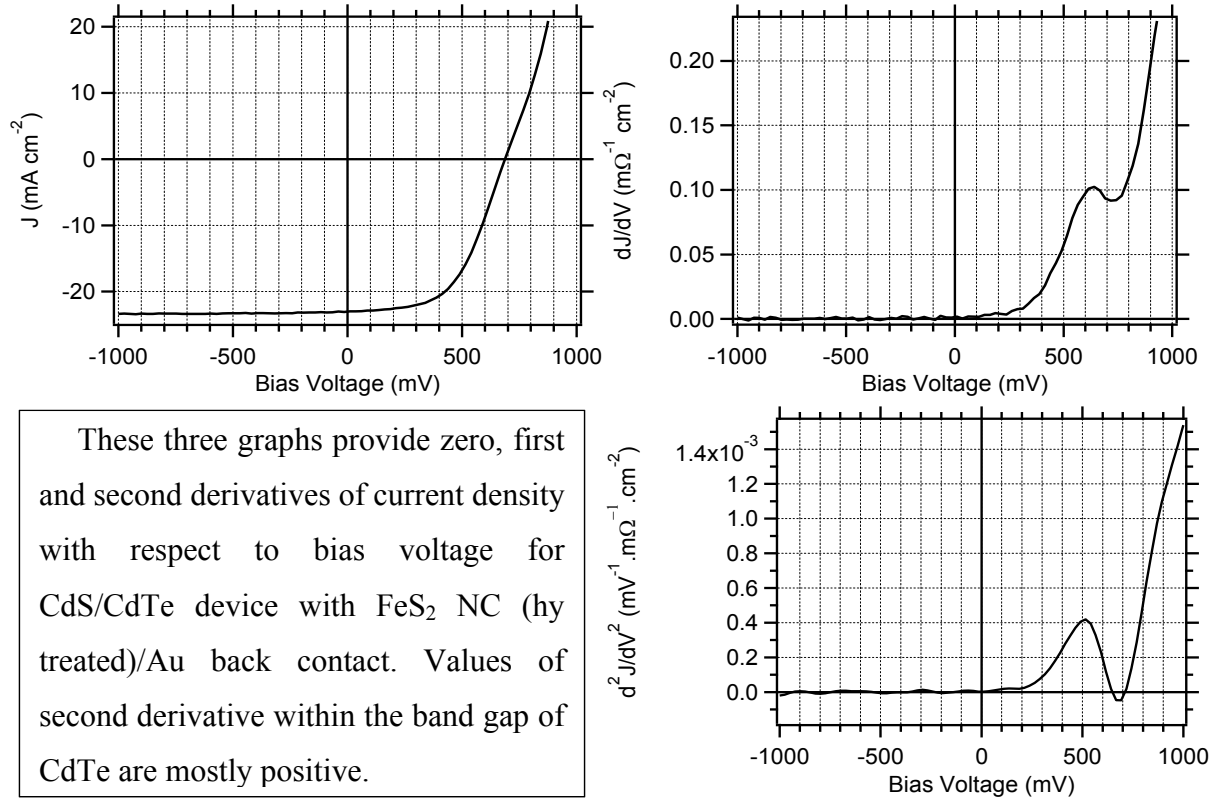


Figure C-1. Derivatives of JV curves in two different cases.